Krishna Mohan Singh
Sushanta Dutta
Sudhakar Subudhi
Nikhil Kumar Singh   *Editors*

Fluid Mechanics and Fluid Power, Volume 7

Select Proceedings of FMFP 2022

Springer

Lecture Notes in Mechanical Engineering

Lecture Notes in Mechanical Engineering (LNME) publishes the latest developments in Mechanical Engineering—quickly, informally and with high quality. Original research reported in proceedings and post-proceedings represents the core of LNME. Volumes published in LNME embrace all aspects, subfields and new challenges of mechanical engineering.

To submit a proposal or request further information, please contact the Springer Editor of your location:

Europe, USA, Africa: Leontina Di Cecco at Leontina.dicecco@springer.com
China: Ella Zhang at ella.zhang@springer.com
India: Priya Vyas at priya.vyas@springer.com
Rest of Asia, Australia, New Zealand: Swati Meherishi at swati.meherishi@springer.com

Topics in the series include:

- Engineering Design
- Machinery and Machine Elements
- Mechanical Structures and Stress Analysis
- Automotive Engineering
- Engine Technology
- Aerospace Technology and Astronautics
- Nanotechnology and Microengineering
- Control, Robotics, Mechatronics
- MEMS
- Theoretical and Applied Mechanics
- Dynamical Systems, Control
- Fluid Mechanics
- Engineering Thermodynamics, Heat and Mass Transfer
- Manufacturing Engineering and Smart Manufacturing
- Precision Engineering, Instrumentation, Measurement
- Materials Engineering
- Tribology and Surface Technology

Indexed by SCOPUS, EI Compendex, and INSPEC.

All books published in the series are evaluated by Web of Science for the Conference Proceedings Citation Index (CPCI).

To submit a proposal for a monograph, please check our Springer Tracts in Mechanical Engineering at https://link.springer.com/bookseries/11693.

Krishna Mohan Singh · Sushanta Dutta ·
Sudhakar Subudhi · Nikhil Kumar Singh
Editors

Fluid Mechanics and Fluid Power, Volume 7

Select Proceedings of FMFP 2022

Editors
Krishna Mohan Singh
Department of Mechanical and Industrial
Engineering
Indian Institute of Technology Roorkee
Roorkee, Uttarakhand, India

Sushanta Dutta
Department of Mechanical and Industrial
Engineering
Indian Institute of Technology Roorkee
Roorkee, Uttarakhand, India

Sudhakar Subudhi
Department of Mechanical and Industrial
Engineering
Indian Institute of Technology Roorkee
Roorkee, India

Nikhil Kumar Singh
Department of Mechanical and Industrial
Engineering
Indian Institute of Technology Roorkee
Roorkee, Uttarakhand, India

Contents

About the Editors

Prof. Krishna Mohan Singh is Professor in the Department of Mechanical and Industrial Engineering at Indian Institute of Technology (IIT) Roorkee. His research interests include the areas of computational mechanics, development of novel parallel algorithms, meshfree methods, shape and topology optimization, fluid dynamics, DNS/LES of turbulent flows, CAE, computer-aided analysis and design of thermo-fluid and multi-physics systems, computational fluid dynamics, modeling and simulation of flow and heat transfer in turbomachines, transport and energy systems.

Prof. Sushanta Dutta is Professor in the Department of Mechanical and Industrial Engineering at Indian Institute of Technology (IIT) Roorkee. His research interests are in the areas of experimental fluid mechanics, experimental heat transfer, optical measurement techniques, active and passive control of flow field, wake dynamics, turbulence study, Schlieren, HWA, PIV, LCT, PSP, microfluidics and heat transfer augmentation using phase change material.

Prof. Sudhakar Subudhi is Professor in the Department of Mechanical and Industrial Engineering at Indian Institute of Technology (IIT) Roorkee. His research interests are in the area of experimental heat transfer and fluid mechanics, heat transfer enhancement of natural and forced convection in water/nanofluids, natural ventilation and unconventional energy systems.

Dr. Nikhil Kumar Singh is Assistant Professor in the Department of Mechanical and Industrial Engineering at Indian Institute of Technology (IIT) Roorkee. His broad research interests include direct numerical simulations of two-phase flows and phase change, computational fluid dynamics and heat transfer, numerical methods and turbulent flows.

Renewable Energy

Performance Exploration of Impinging Jet Solar Air Heater: A Comparative Study

Amitesh Sharma, Sushant Thakur, Prashant Dhiman, and Rakesh Kumar

Abstract Given the imminent depletion of fossil fuels, the present scenario relies on capturing solar energy. The current study compares experimental trials of traditional SAH with alternative impinging jet ribbed solar air heater designs. The experimental investigation is investigated by increasing the Re from 4000 to 16,500 and comparing the results. The geometric parameters and jet parameters used in the investigation were $e/d_{\mathrm{hd}} = 0.043$, $P/e = 10$, $\alpha = 55°$, $X_{\mathrm{st}}/d_{\mathrm{hd}} = 0.40$, $Y_{\mathrm{sp}}/d_{\mathrm{hd}} = 0.84$, and $d_j/d_{\mathrm{hd}} = 0.064$. The impinging jet with multi-V-shaped ribs outperformed the V-shaped ribbed SAH, with a reported thermohydraulic efficiency of 3.301 compared to 2.05 for the V-shaped ribbed SAH and 1.83 for the impinging jet flat-plate solar air. It establishes that when active and passive heat transfer approaches are coupled, heat transfer enhancement and THEP are increased. The findings were also compared to traditional SAH.

Keywords Solar air heater · Artificial roughness · Jet impingement · THEP · Circular holes

Nomenclature

SAH	Solar air heater
A_o	Duct opening area, m^2
C_p	Specific heat at const. pressure, J kg^{-1} K^{-1}
d_{hd}	Hydraulic dia. of the channel, m
A_p	Absorber plate area, m^2
C_d	Coefficient of discharge of orifice plate

A. Sharma (✉) · S. Thakur · P. Dhiman
Mechanical Engineering Department, N.I.T, Hamirpur, India
e-mail: amitesh.jngec@gmail.com

A. Sharma · R. Kumar
Mechanical Engineering Department, M.G. Government Engineering College, Jeori Shimla, H.P, India

H	Vertical channel height, m
e	Wire roughness height, m
m	Flow rate of air, kg s^{-1}
L	Length of testing section, m
P	Roughness pitch, m
k_a	Air thermal conductivity, W m^{-1} K
h	Convective coefficient, W m^{-2} K
Q_f	Heat exchange rate, W
ΔP_d	Pressure decrement crosswise in the testing section, N m^{-2}
ΔP_o	Pressure decrement in orifice meter, N m^{-2}
T_{in}	Entry air temp. in the conduit, K
T_{out}	Exit air temp. in plenum, K
T_{mp}	Average plate temperature, K
T_{mf}	Mean temp. of air, K
V	Fluid speed, m s^{-1}
W	Conduit breadth, m Dimensionless factors/numbers
e/d_{hd}	Relative wire rib roughness height
f_s	Friction factor of conventional SAH
Nu	Nusselt number
Nu$_s$	Nusselt number of conventional SAH
P/e	Relative roughness pitch
w/W	Width ratio
Pr	Prandtl number
Re	Reynolds number
f_p	Friction penalty of a roughened surface
$X_{\text{st}}/d_{\text{hd}}$	Streamwise impinging jet pitch ratio
$Y_{\text{st}}/d_{\text{hd}}$	Spanwise impinging jet pitch ratio
THEP	Thermohydrodynamic efficiency parameter

Symbols: (Greek)

α	Attack angle
β	Fraction of hole distance corresponding of pipe width
ρ_{air}	The density of fluid, kg m^{-3}
ρ_{air}	Density of flowing air at mean temperature, kg m^{-3}
ϑ	Kinematic viscosity, m^2 s^{-1}

1　Introduction

Solar insolation is a pure, plentiful, and limitless source of power. Research on renewable energy is sorely needed in light of the present fossil fuel dilemma [1]. A solar air heater (SAH) is a tool for obtaining solar heat energy to be used in commercial and agricultural purposes [2]. Heating systems and air conditioning (SAH) are preferred over solar water heaters (SWH) due to their usage in a number of technical applications, such as the drying of paper and pulp, whereas SWH's uses are quite constrained. Second, the simple design, lack of scaling-fouling, corrosion, leakage problems, and safety features of SAHs make them safe to use [3]. Despite its numerous advantages, it has one disadvantage: poor performance due to air's low heat transfer coefficient [4].

Numerous techniques have been created to increase SAH efficiency and encourage heat exchange between the absorbing surface and air [5]. The techniques are categorized as active techniques, passive techniques, and combination of both active and passive techniques [6]. The absorber plate is suitable modified by arrangement of ribs underneath the absorber plate which results in distortion of laminar sublayer resulting in heat transfer augmentation [7]. Design modifications are done by the arrangement of extended surfaces [8, 9] incorporating baffles suitably on absorber plate [10] and utilizing the impingement of flowing fluid on the absorber plate for boosting the turbulence [11]. The jet impingement approach is a good way to improve heat transfer between air and a hot surface [12]. Several researchers investigated this process and reported on it in experimental and numerical investigations. Based on jet impingement physics, Chaudhary and Garg developed a mathematical model for solar air heaters, with findings indicating a 26% improvement in efficiency and a maximum temperature rise of 15.5 °C at airflow rates ranging from 50 to 250 kg/hm^2 with a 10 cm conduit depth and 2.0 m duct length [13]. Chauhan and Thakur conducted an experimental procedure of modified impinging jet SAH, with reported maximum efficiency of 70% recorded by adjusting jet hole diameter, streamwise jet pitch, and spanwise jet pitch [14]. The effectiveness of an unglazed SAH with an impinging jet was investigated by Belusko et al., and it was shown that jet-to-jet distance is paramount factor in increasing thermal efficiency [15]. Singh et al. evaluated impinging jet behavior in a dual-passage rectangular duct with a modified corrugated wavy impinging jet plate. The highest thermal performance improvement of roughly 94% was achieved with 0.48% perforation of the impinging jet plate and 98% bed porosity [16]. Maithani et al. used jet impingement on an absorber plate having hemispherical protrusions slightly below the jet holes in order to provide impingement over the protrusions and produce turbulence. The maximum thermal hydraulic efficiency measurement was 3.01 [17]. Kannan et al. conducted investigation under outdoor circumstances, a suitably adapted SAH with a pin–fin absorber plate, and compared this with a normal SAH, and the output air temperature was increased from 2° to 7 °C with improved energy, thermohydraulic, and exergy efficiency [18].

According to the prior research, the impinging jet method is extensively employed for enhancing heat transfer in a variety of applications. Only few works have

been conducted to investigate the interaction of cylindrical wire-shaped ribs with impinging air jet SAH. The current study fills this void by examining the thermal behavior of cylindrical wired ribs positioned underneath the absorber plate and applying a variety of geometric parameters for rib roughness in cylindrical wire-shaped ribs. The current experimental investigation is a comparison of the increased thermal behavior of an impinging jet on a flat-plate solar air heater and an impinging air ribbed solar air heater with ribs installed on a V-shaped pattern and a multi-V-shaped pattern with a conventional SAH.

2 Experimental Setup

An indoor test facility for assessing roughened absorber plate has been established in line with the ASHRAE standard [19]. A test facility has been built based on this idea, as illustrated in Fig. 1. It was an open-loop system with a rectangular route comprising components for entry, testing, and exit.

The test component of the rectangular channel has a cross-section of 300×25 mm and a length of 1400 mm. The entry and exit parts are respectively 600 and 400 mm in dimension, equivalent of $5\sqrt{W_d H_d}$ & $2.5\sqrt{W_d H_d}$ as per ASHRAE protocols. As a result, the flow may be presumed to be completely developed across the length of the test portion. A variac is used to govern a steady heat flow of approximately 1000 W/m^2. The mass flow through the conduit is measured using a U-tube. A digital micro-manometer of TSI made with a least count of 0.1 Pa was used to monitor the pressure change over the jet impingement test segment. The average temperature of
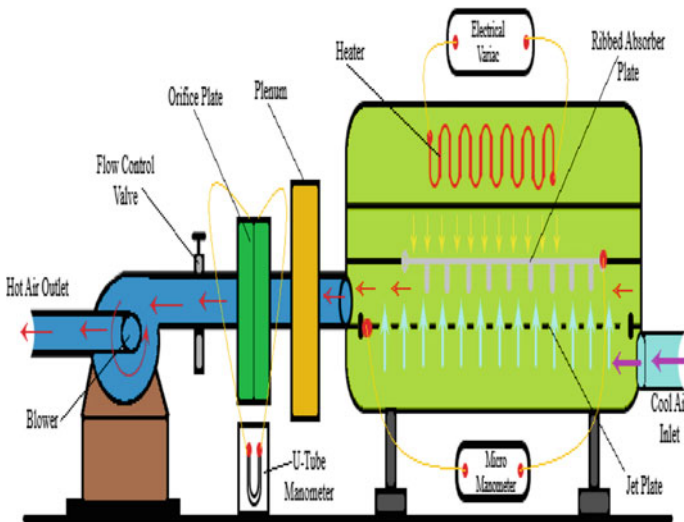
Fig. 1 Test rig

Table 1 Lists the parameters that were chosen for the experiment

S no.	Parameters of investigation	Range
1	Re	4000–16,500
2	Width ratio (w/W)	01 and 05
3	Relative roughness ht. (e/d_{hd})	0.043
4	Relative roughness pitch (P/e)	10
5	Attack angle (α)	55^0
6	Streamwise jet hole pitch ratio (X_{st}/d_{hd}),	0.40
7	Spanwise jet hole pitch ratio (Y_{sp}/d_{hd})	0.84
8	Jet hole diameter ratio (d_j/d_{hd})	0.064

air at the intake and exit portions, as well as the temperature of the absorbing surface, was measured at 18 places using calibrated J-type thermocouples with an accuracy of 0.1 °C. The air was blown through the rectangular conduit using a 3-HP centrifugal blower. The experiment was started by setting the appropriate set of geometric and flow parameters on the jet plate arrangement, and the operational conditions were assured by utilizing a gate valve to govern the mass flow rate of air.

The various parameters selected for the study are presented in Table 1.

3 Confirmation of the Experimental Procedure

The created setup facility was approved for a conventional SAH without any obstructions in the passage of the flow regimes, as required by the laws. The estimated results from an experimental run were equal to the projected values of the Nu and friction penalty determined using an empirical relationship well acknowledged by various researches for assessing classic SAH. The Dittus-Boelter correlation and Gnielinski equation as given in Eqs. (1, 2) for Nusselt number, the modified Blasius equation as represented in Eq. (3), and Petukhov equation as represented in Eq. (4) were used to obtain the projected values for conventional SAH in validating friction factor [7]. As shown in Fig. 2, the mean absolute deviation in this conformity for Nusselt number estimated using Gnielinski and Dittus-Boelter correlations was 5.06% and 6.8%, respectively. The mean absolute deviation of friction penalty from modified Blasius and Petukhov empirical correlations and experimental values were 3.5 and 6.1% as represented in Fig. 3**.** The lower percentage of mean absolute deviation proves the setup acceptability and validation of the experimental facility and its use in future test concerning planned study, leading to logical acceptance of the test rig.

$$Nu_s = 0.023 \text{Re}^{0.8} \text{Pr}^{0.4} \tag{1}$$
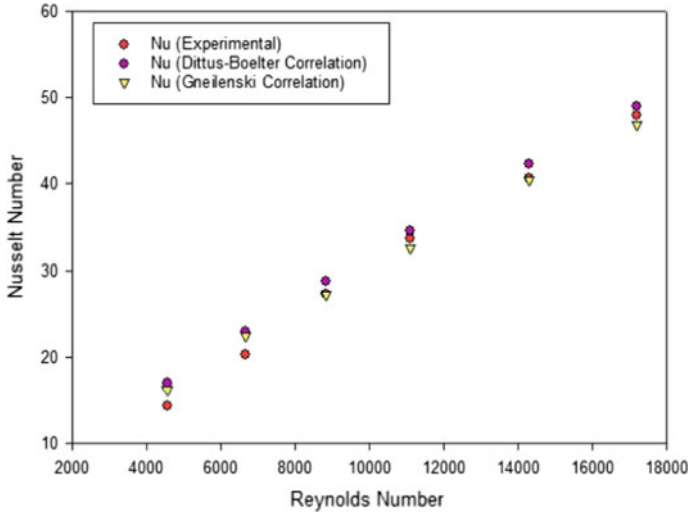
Fig. 2 Validation for Nu
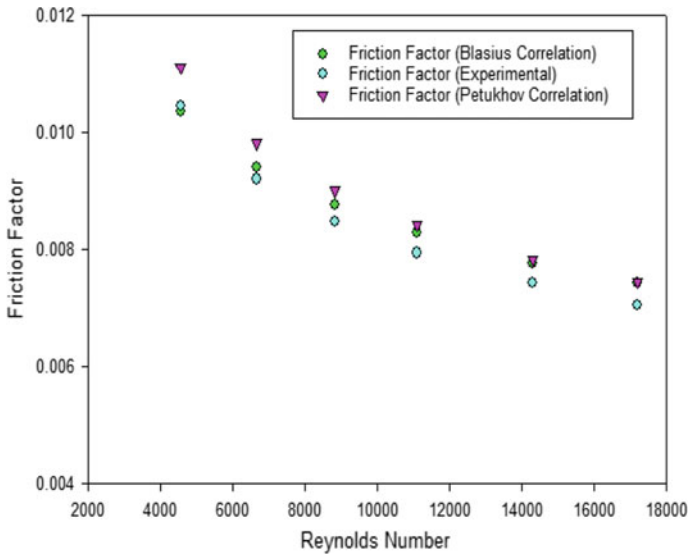
Fig. 3 Validation for friction factor

$$Nu_s = \frac{(f/2)(\mathrm{Re} - 1000)\,\mathrm{Pr}}{1 + 12.7\big([f/2]^{0.5}3\big)(\mathrm{Pr}^2 - 1)} \tag{2}$$

$$f_s = 0.085\,\mathrm{Re}^{-0.25} \tag{3}$$

$$f_s = (1.58 \ \ln \ \text{Re} - 3.82)^{-2} \tag{4}$$

3.1 Formula Used

1. Heat gain by fluid:

$$Q_f = \dot{m} C_p (T_{out} - T_{in})$$

2. Mass flow rate of working fluid:

$$\dot{m} = C_d A_o \left[\frac{2 \rho_{\text{air},0} \Delta P_o}{1 - \beta^4} \right]^{1/2}$$

3. Friction factor:

$$f = \frac{2(\Delta P)_d D_h}{4 \rho_{air} L V^2}$$

4. Convective heat transfer coefficient:

$$h = \frac{Q_a}{A_p (T_{mp} - T_{mf})}$$

5. $Nu := \frac{h D_h}{k_{air}}$.

3.2 THEP

A lot of studies have looked into the usage of turbulence promoters to improve the thermal behavior of SAH. This advantage, however, comes at the expense of a pressure loss, which needs a large pumping effort to move the air through the pipe. As a result, in order to establish the setup for effective performance, the heat transfer and friction characteristics must be examined concurrently, a process known as "thermohydraulic performance," [20] as mentioned in Eq. (5)

$$\eta_{\text{THEP}} = \left[(Nu_{\text{roughened}} / Nu_{\text{smooth}}) / (f_{\text{roughened}} / f_{\text{smooth}})^{\frac{1}{3}} \right] \tag{5}$$

4   Result and Discussion

This experimental comparative study determines the Nu symbolizing heat transfer increase, friction coefficient, and THEP for a given range of variables used in a redesigned impinging jet solar air heater.

4.1   Heat Gain

The augmentation in Nusselt number represents the heat gain. Figure 4 demonstrates the relationship between Nu and Re within a set of parameters. The fixed geometric and jet parameters were $w/W = 1$ and 5 (width ratio), $P/e = 10$ (relative roughness pitch), $e/d_{hd} = 0.043$ (relative rib roughness height), $\alpha = 55°$ (attack angle), $X_{st}/d_{hd} = 0.40$ (streamwise pitch), $Y_{st}/d_{hd} = 0.84$ (spanwise pitch), and jet hole diameter $(d_j/d_{hd}) = 0.064$. In typical solar air heaters, heat transmission to the air is limited by a viscous layer formed near the absorber plate, and the impinging jet causes turbulence and promotes heat transfer augmentation, stated to as the passive heat transfer enhancement strategy. As shown in the illustration Fig. 5, a modified absorber plate is used, with V-patterned ribs positioned beneath the absorber plate and a jet impinging from the bottom via the jet plate. This is an amalgamation of active and passive manners of heat transfer, and the results show that as Re increases, Nu increases for both impinging jet and impinging jet V patterned ribs, and the results are also compared to conventional solar air heaters, as shown in Fig. 4, with the maximum Nu reported for multi-V-patterned impinging jet SAH and secondly by V-patterned impinging jet SAH.

As a result, the arrangement in which the ribs were fastened throughout the whole length of the absorber plate was optimal for heat exchange. To push fluid from the cooler zone (internal core) toward the multi-V obstacle wall, the impingement jets have two separate rotating vortices. As a result, the lower impingement jets become entrained in the primary flow. Boundary layer development was halted due to heat transmission among the multi-V ribs, which was triggered by the mixing of inner stream with the main stream. With an increase in Re, the convective resistance in the boundary layer decreased, resulting in a thinner boundary layer and a greater Nu. As a result, there was significant turbulence where the impinging jets separated and merged with the main stream. This was located behind the ribs. There was a rise in HT from the absorber plate to the air as the number of vortices rose as in multi-V ribs in comparison with other designs.
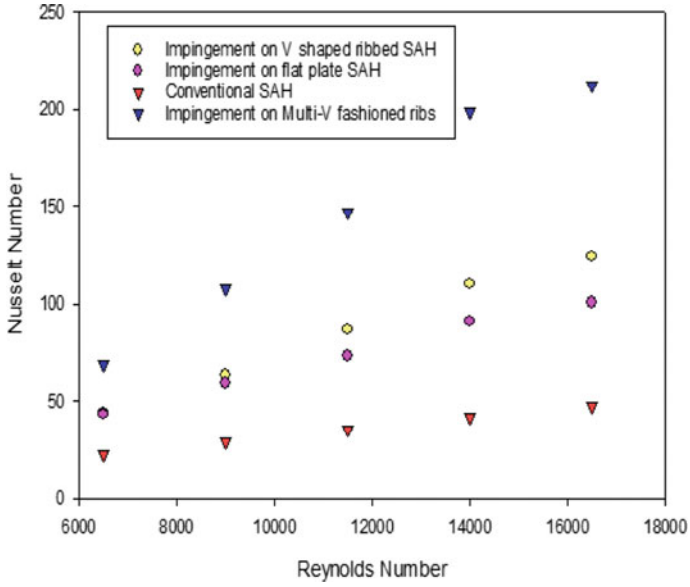
Fig. 4 Variation of Nusselt number with Re
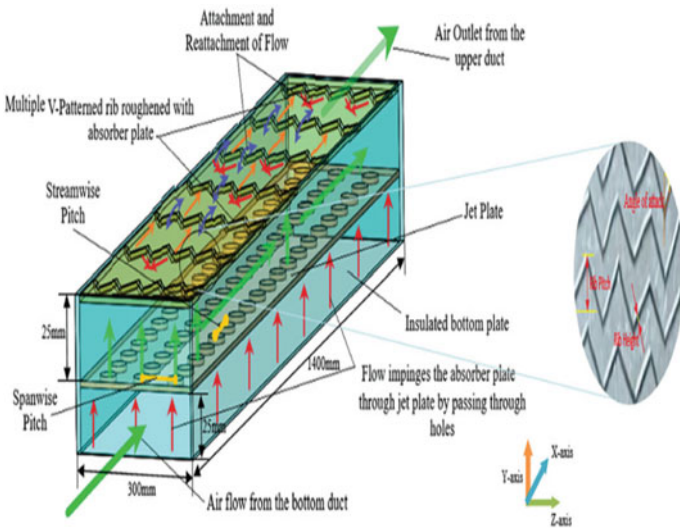
Fig. 5 Schematic diagram and flow pattern [5]
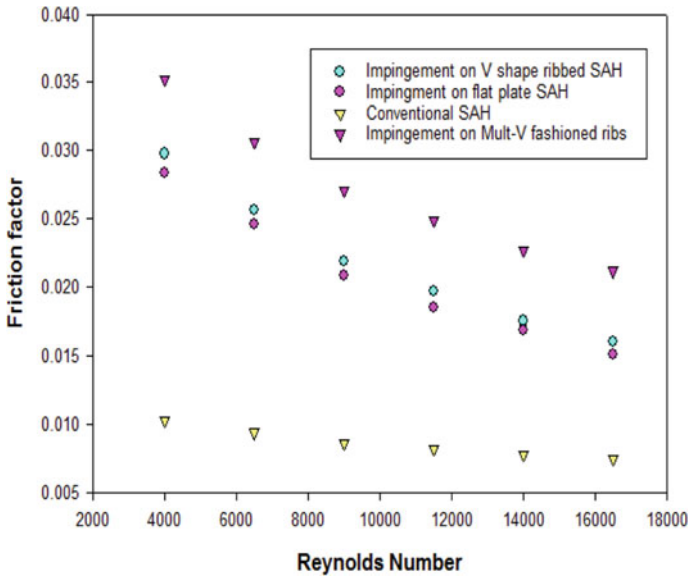
Fig. 6 Variation of Friction factor with Re

4.2 Frictional Characteristics

Figure 6 shows the relationship between f and Re for a set of selected parameters. With rising Re, the value of f continues to decrease. As Re increases, so does air penetration into the ribs, resulting in a continual reduction in pressure drop. Furthermore, the jet spacing is carefully selected to reduce jet interference. When the width-to-expansion value ratio was adjusted from 1 to 5, a corresponding rise in the number of secondary stream jets was observed. In this way, a sequence of V-shaped ribs on the absorber plates can increase the friction factor to a maximum value within the range of the design's specifications. The frictional cost introduced by the partitioning of the flow may be used to investigate the vortex structures. Nu rises when pressure builds up in the vortex. An increase in Nu, as is the case with most targets, occurs when the flow increases its pumping force around the SAH, as seen above. The frictional factor recorded for V-patterned ribbed impinging jet SAH is 0.0297. The highest value recorded for multi-V-patterned ribs signifies that augment in heat transfer leads to enhancement in pressure drop.

4.3 THEP

Thermohydraulic performance is dimensionless parameter that denotes performance of modified SAH. Figure 7 illustrates THEP variation with Re for fixed geometric
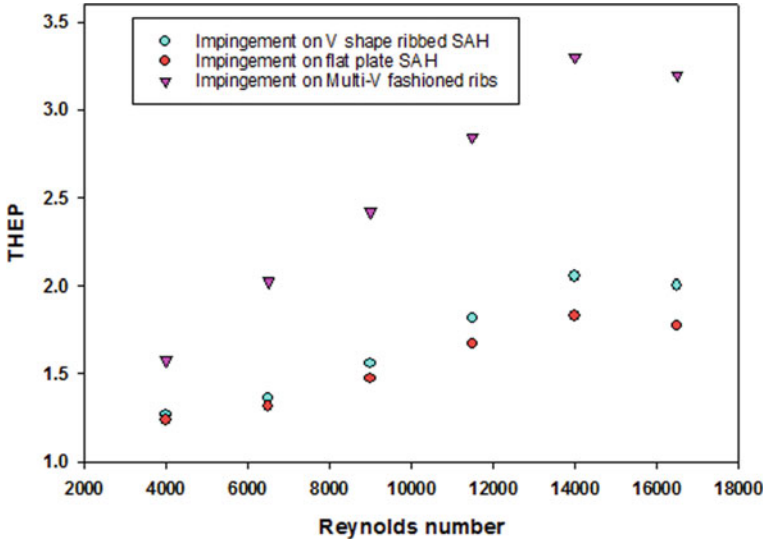
Fig. 7 Thermohydraulic efficiency parameter variation with Re

and jet parameters. The maximum THEP reported is for Reynolds number 14,500 for all designs, i.e., impinging jet SAH, impinging jet ribbed SAH (V and multi-V ribs) with maximum reported value of 3.301 for impinging jet multi-V-patterned ribs. The rise and fall that were seen in the findings of thermohydraulic efficiency may be attributed to an increase in the pumping power above the thermal gain at a certain value of mass flow rate in relation to the geometrical parameters, and this value offers the optimum value.

5 Conclusions

The present study is performed to conclude the comparison of impinging air and impinging air ribbed SAH, in which ribs are organized in V pattern. The fixed value of various parameter is $w/W = 1$ and 5, $P/e = 10$, $e/d_{hd} = 0.043$, $\alpha = 55°$, $X_{st}/d_{hd} = 0.40$ (streamwise pitch), $Y_{st}/d_{hd} = 0.84$, and jet hole diameter $(d_j/d_{hd}) = 0.064$. The results clearly showed that when jet impingement is combined with roughness, heat transfer augmentation increases with a certain rise in friction factor. The results clearly showed that when jet impingement is combined with roughness, heat transfer augmentation increases with a certain rise in friction factor. The study's findings may be summarized as follows:

- The highest THEP is reported as 3.301 for impinging jet multi-V-patterned ribbed modified SAH.

- When equated to usual conventional SAH, there is a 4.70 times enhancement in Nu and a 2.92 times augmentation in friction factor in this research in the option of impinging jet multi-V-patterned ribbed modified SAH with width ratio of 5.

References

1. Phu NM, Tuyen V, Ngo TT (2019) Augmented heat transfer and friction investigations in solar air heater artificially roughened with metal shavings. J Mech Sci Technol 33(7):3521–3529. https://doi.org/10.1007/s12206-019-0646-x
2. Singh I, Singh S, Vardhan S (2021) Heat transfer and fluid flow characteristics of solar air heater duct with non-uniform ribs. J Mech Sci Technol 35(1):343–350. https://doi.org/10.1007/s12206-020-1234-9
3. Sharma S, Das RK, Kulkarni K (2021) Computational and experimental assessment of solar air heater roughened with six different baffles. Case Stud Therm Eng 27:101350. https://doi.org/10.1016/j.csite.2021.101350
4. Kumar R, Goel V, Bhattacharyya S, Tyagi VV, Abusorrah AM (2022) Experimental investigation for heat and flow characteristics of solar air heater having symmetrical gaps in multiple-arc rib pattern as roughness elements. Exp Heat Transf 35(4):466–483. https://doi.org/10.1080/08916152.2021.1905752
5. Sharma A, Thakur S, Dhiman P (2022) Jet impingement in a V-rib roughened solar air heater: an experimental approach. Energy Sourc Part A Recover Util Environ Eff 44(3):6970–6984. https://doi.org/10.1080/15567036.2022.2105988
6. Mousavi Ajarostaghi SS, Zaboli M, Javadi H, Badenes B, Urchueguia JF (2022) A review of recent passive heat transfer enhancement methods. Energies 15(3):986. https://doi.org/10.3390/en15030986
7. Yadav SK (2021) Thermal performance evaluation of arc rib having symmetrical wide gaps and staggered elements and additional narrow gap in each arc segment used in absorber surface of solar air heater. Appl Sol Energy 57(3):192–197. https://doi.org/10.3103/S0003701X21030105
8. Josyula T, Singh S, Dhiman P (2018) Numerical investigation of a solar air heater comprising longitudinally finned absorber plate and thermal energy storage system. J Renew Sustain Energy 10(5):055901. https://doi.org/10.1063/1.5035136
9. Goel AK, Singh SN (2019) Performance studies of a jet plate solar air heater with longitudinal fins. Int J Ambient Energy 40(2):119–127. https://doi.org/10.1080/01430750.2017.1372808
10. Chamoli S, Thakur NS (2015) Effect of roughness height ratio in V down perforated baffle roughness on thermohydraulic performance of solar air heater: an experimental study. Int J Ambient Energy 36(5):242–247. https://doi.org/10.1080/01430750.2013.853206
11. Kumar R, Nadda R, Rana A, Chauhan R, Chandel SS (2020) Performance investigation of a solar thermal collector provided with air jets impingement on multi V-shaped protrusion ribs absorber plate. Heat Mass Transf 56(3):913–930. https://doi.org/10.1007/s00231-019-02755-2
12. Shukla AK, Dewan A (2017) Flow and thermal characteristics of jet impingement: comprehensive review. Int J Heat Technol 35(1):153–166. https://doi.org/10.18280/ijht.350121
13. Choudhury C, Garg HP (1991) Evaluation of a jet plate solar air heater. Sol Energy 46(4):199–209. https://doi.org/10.1016/0038-092X(91)90064-4
14. Chauhan R, Thakur NS (2014) Investigation of the thermohydraulic performance of impinging jet solar air heater. Energy 68:255–261. https://doi.org/10.1016/J.ENERGY.2014.02.059
15. Belusko M, Saman W, Bruno F (2008) Performance of jet impingement in unglazed air collectors. Sol Energy 82(5):389–398. https://doi.org/10.1016/J.SOLENER.2007.10.005
16. Singh S, Chaurasiya SK, Negi BS, Chander S, Nemś M, Negi S (2020) Utilizing circular jet impingement to enhance thermal performance of solar air heater. Renew Energy 154:1327–1345. https://doi.org/10.1016/j.renene.2020.03.095

17. Maithani R, Kumar A, Raghav G, Nagpal M, Kumar B (2021) Thermal analysis of jet impingement on hemispherical protrusion on heated surface. Exp Heat Transf 34(7):662–677. https://doi.org/10.1080/08916152.2020.1808117
18. Kannan C, Mohanraj M, Sathyabalan P (2021) Experimental investigations on jet impingement solar air collectors using pin-fin absorber. Proc Inst Mech Eng Part E J Process Mech Eng 235(1):134–146. https://doi.org/10.1177/0954408920935301
19. ASHRAE (1977) Method of testing to determine the thermal performance of solar collectors. (ASHRAE standard 93–7)
20. Webb RL, Eckert ERG, Goldstein RJ (1972) Generalized heat transfer and friction correlations for tubes with repeated-rib roughness. Int J Heat Mass Transf 15(1):180–184. https://doi.org/10.1016/0017-9310(72)90179-2

Performance Evaluation of Single Pass Solar Air Heater with Stepped-Type Arrangement of Metal Foam by a Numerical Study

Rawal Diganjit and N. Gnanasekaran

Abstract A solar air heater is easy to build and easy to use for drying applications, room heating purposes, etc. In the present study, single-pass forced convection rectangular-type solar air heater is studied numerically. The copper metal foam with 0.92 porosity is used for case (a) empty channel, cases (b) to (e) comprising of different stepped-type arrangements, and case (f) fully filled metal foam condition and studied numerically to obtain outlet temperature, pressure drop and the performance factor of the solar air heater. The Reynolds number is varied from 4401 to 5868. Based on this range of Reynolds number RNG k-ε model with enhanced wall function is adopted for numerical simulations. The local thermal equilibrium model is used to simulate the porous zone. The Rosseland radiation model has been chosen with solar ray tracing method. The case (c) is the best stepped-type arrangement to get same outlet temperature compared to fully filled metal foam case (f). Hence, the material cost is minimized. The temperature rise is 8.89% more compared to empty channel solar air heater. Case (c) has less pressure drop compared to other metal foam arrangements. The performance factor for case (c) is 2.03.

Keywords Single pass · Solar air heater (SAH) · Metal foam · Performance factor · Forced convection

Nomenclature

R_e	Reynolds number [-]
ε	Porosity [%]
T_s	Solid temperature [K]
T_f	Fluid temperature [K]
T_{out}	Outlet temperature [K]

R. Diganjit · N. Gnanasekaran (✉)
Department of Mechanical Engineering, National Institute of Technology, Mangalore, Karnataka 575025, India
e-mail: Gnanasekaran@nitk.edu.in

ΔP Pressure drop [Pa]
CFD   Computational fluid dynamics [-]
SAH   Solar air heater [-]
ρ Density [kg/m^3]
Cp Specific heat capacity [kJ/kg K]
k Thermal conductivity [W/m K]
μ Kinematic viscosity [Ns/m^2]

1 Introduction

Solar energy is easily available on earth. It has zero cost; so, there is a scope to utilize this solar energy for human comfort. The solar air heater has four main parts, i.e., absorber plate, transparent cover, insulation, and outer frame of the solar air heater. The absorber plate absorbs the solar radiation and heats the incoming air. The air passes through the space between the glass and absorber plate. The metal foam is used due to its low density, high superficial area-to-volume ratio, and high strength. The metal foam is used to maximize the heat transfer rate in solar air heater [1], heat exchangers [2], electronic cooling devices, etc.

2 Literature Review and Objectives

Saedodin et al. [1] performed numerical and experimental analyses using single-pass flow. They used porous metal foam having bed dimensions of 70 × 12 mm. The control volume method and local thermal equilibrium (LTE) model have been adopted through test channel to get thermal performance, and pressure drop. The numerical and experimental analyses of porous medium results give increased thermal efficiency and Nusselt number up to 18.5% and 82% respectively. Kansara et al. [3] investigated the performance of flat-plate collector using internal fins and porous media by using solar simulator. The rise in temperature of air with fins and porous media is 8.19% and 16.17%, respectively, than an empty channel. Maximum rise is 115.9 K for copper foam, and minimum is 110.4 K for steel foam. Anirudh et al. [4] studied performance improvement of a flat-plate solar collector with intermittent porous blocks by using numerical analysis of FPSC. The porous resistances are higher in amplitudes for low permeability. The values vary for Darcy–Brinkman compared to Extended Darcy–Brinkman–Forchheimer model. Singh et al. [5] performed experimental and numerical investigations of a single and double pass using porous serpentine wavy wire mesh in solar air heater. Best thermal and thermohydraulic efficiencies for 93% porous double-pass serpentine-packed bed solar air heater are achieved. The thermohydraulic performance for serpentine presents 24.33% than flat-packed bed solar air heater. Huang [6] reported a numerical study of enhanced forced convection

in a channel of solar water collector using multiple metal foam blocks. With the help of Darcy–Brinkman–Forchheimer flow model and local thermal non-equilibrium model, the study includes thermo-flow fields inside the porous media. Valizade et al. [7] studied experimentally the thermal behavior of direct absorption parabolic collector using copper metal foam. The maximum thermal efficiency for full metal foam and semi-metal foam are 171.2% and 119.6%, respectively, than free-channel metal foam. Wang et al. [8] worked on experimental study of latent thermal energy storage system with copper metal foam for further solar applications. Silicon oil was utilized as heat transfer fluid. Hence, temperature uniformity improved and the reduction in time for melting the mixture by 37.6%. Xiao et al. [9] investigated thermal performance analysis of a solar energy storage using copper foam/nanosalt. The results show that the time duration of heat storage process at heating temperature of 160° is reduced by 58.5%. Jouybari et al. [10] experimentally investigated the use of metal foam using nanofluid to improve thermal performance. The performance evaluation criterion is used to reduce the pressure drop and increase the heat transfer. With the help of metal foam and nanofluid, the performance evaluation criteria increased more than 1% at a lower flow rate. The increase in nanofluid concentration increases the performance evaluation criteria. Rajarajeswari et al. [11] reported numerical and experimental results in porous and non-porous solar air heaters. Two types of screen wire mesh WSM-I and WSM-II having different porosities and characteristics are used. The increase in thermal efficiency for WSM-I and WSM-II is 5–17% and 5–20% respectively with mass flow rate from 0.01 to 0.05 kg/s. Jadhav et al. [12] accomplished the numerical study of horizontal pipe in the presence of metal foam. Darcy-extended Forchheimer (DEF) and local thermal non-equilibrium (LTNE) models were used. The novelty of the work is the selection of suitable flow and thermal models to find the heat transfer in metallic foams.

From the above literature, it is understood that metal foam is the best option to increase heat transfer rate. At the same time, the pressure drop increases due to the resistance offered by the metal foams. To overcome this issue, researchers have attempted several methods, but stepped-type arrangement is not studied till date in the literature. This type of arrangement not only increases the heat transfer but also decreases the pressure drop. Hence in this paper, four different stepped arrangements are considered. The objective of this work is to study the different stepped-type arrangement of metal foam to increase outlet temperature and reduce pressure drop.

3 Materials and Methods

A rectangular channel-type SAH experimental study of Rajarajeswari [11] is considered as a reference work for this numerical analysis of heat transfer through porous media like metal foam. The width is modified in this analysis. Width is considered to be 1 m because the industrial solar air heater absorber plate area is in general 2 m^2. The schematic diagram and numerical geometry are shown in Fig. 1.
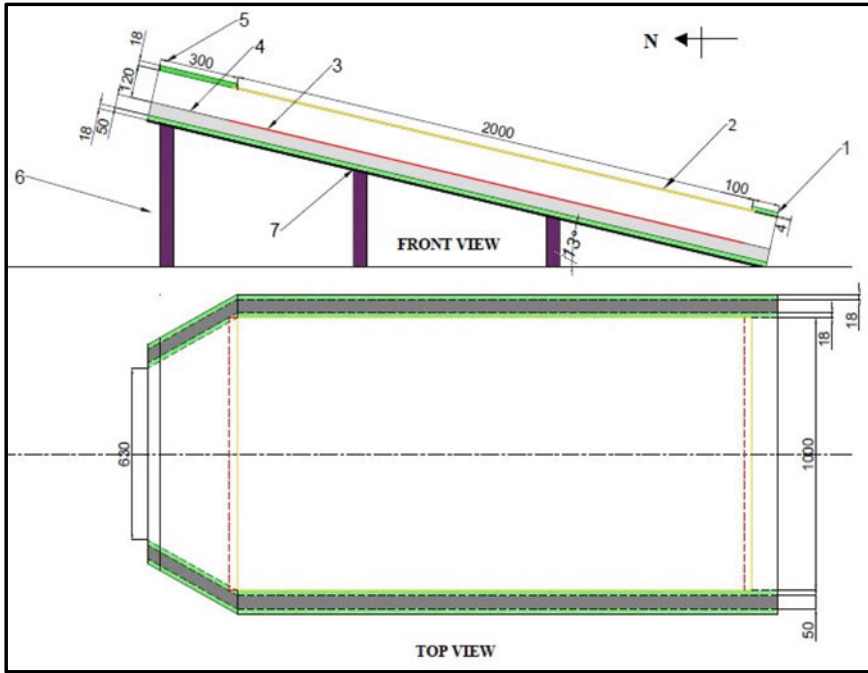
Fig. 1 Detailed schematic layout of SAH, 1 wooden material for entrance section, 2 toughened glass, 3 aluminum absorber plate, 4 insulation, 5 wooden material for exit section, 6 M S steel stand for support, and 7 wooden materials for the frame as an outer box of the solar air heater

It consists of $2 \times 1 \times 0.12$ (m) as a length, width, and height of solar air heater, respectively. The top plate is transparent toughened glass with 0.004 m thickness. The bottom absorber plate is considered as aluminum with 0.0005 m thickness. The wood material is considered as an insulation material to reduce heat losses from side wall and bottom wall of SAH. The location for the present study is the Department of Mechanical engineering, National Institute of Technology, Karnataka, India. The longitude and latitude for the location are 74.7951 ° and 12.9958 °, respectively. So, the SAH is tilted at 13 ° to facing south. The absorptivity of black painted aluminum plate is taken as 0.95 and wall is opaque. The transparent cover has 0.1 absorptivity and 0.9 transmissivity (Fig. 2).

3.1 Computational Details and Boundary Conditions

The 3D geometry is drawn with the help of Ansys Fluent 2019 R3 software. The solar air heater is divided into three parts, i.e., entrance zone, test zone, and exit zone. The fluid as air is taken for this analysis. The mesh for this domain is linear mesh.
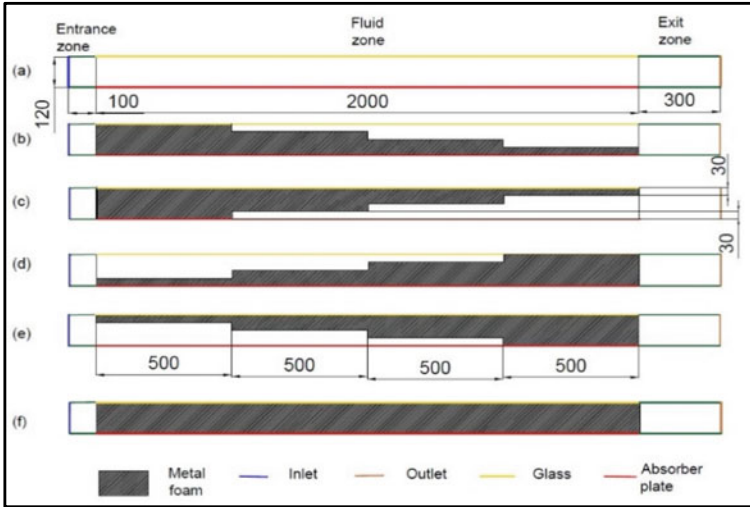
Fig. 2 Schematic diagram of stepped metal foam arrangement in solar air heater case **a** empty channel, case **b**, case **c**, case **d**, case **e**, and case **f** fully filled metal foam

The maximum skewness of the meshing is 0.3526. For the setup, pressure-based solver is taken with absolute velocity. The steady flow is considered for the present analysis. The RNG k-ε model with enhanced wall function is employed for the turbulent flow of air. The Reynolds number for the present study is from 4401 to 5868. The Rosseland radiation model is used with solar ray tracing method for complete analysis as mentioned in [11]. The sunshine factor is taken as 1. For direct beam radiation and diffuse radiation, the solar calculator is selected to get accuracy. All the simulations are done for the date 15 April. The maximum solar intensity for the day is 13:00 pm. Hence, 13:00 pm is considered for further analysis. The material properties are taken as mentioned in Table 1.

In the cell zone conditions, the porous zone is included to increase the heat transfer rate, i.e., to increase the outlet temperature of solar air heater by using metal foam. The porosity and pore diameter of metal foam are mentioned in [13]. The same configurations are used for comparing the heat transfer rate of solar air heater in the present study. The details are given in Table 2.

Table 1 Material properties used for CFD simulations

	Air	Aluminum	Glass	Wood
Density (ρ) kg/m^3	1.225	2719	2500	700
Specific heat capacity (Cp) kJ/kg K	1006.43	871	670	2310
Thermal conductivity (k) W/m K	0.0242	202.4	0.7443	0.173
Kinematic viscosity (μ) Ns/m^2	1.789 E-05	–	–	–

Table 2 Details of copper
metal foam

	Copper metal foam [13]
Pore diameter (mm)	0.216
Pitch (mm)	2.324
Porosity	0.92
Viscous resistance	6,082,725.061
Inertial resistance	148.97

Table 3 Boundary condition considered for CFD analysis

	Conditions
Inlet velocity	0.3, 0.35, and 0.4 m/s and its turbulent intensity 5.6063%, 5.4993%, and 5.4083% respectively
Outlet pressure	Zero
Absorber plate	No slip condition, stationary wall, heat flux = 850W/m^2, opaque wall
Glass	No slip condition, stationary wall, mixed heat transfer coefficient 9.5 W/m^2 K, free stream temperature and external radiation temperature are 300 K, emissivity = 0.88, and semi-transparent wall

The boundary conditions applied are given in Table 3. The hydraulic diameter is calculated for rectangular channel, and it turns out to be 0.2143 m. The inlet temperature for conventional SAH is 300 K. The local thermal equilibrium model (LTE) is used in the heat transfer from fluid zone to solid porous zone. Hence, the average temperature of glass and absorber plate is taken as inlet temperature for porous solar air heater.

The method used for solution is coupled wall scheme for pressure velocity coupling. The spatial discretization for pressure, momentum, turbulent kinetic energy, and turbulent dissipation rate and energy is second-order upwind scheme. The least square cell-based gradient is used to get more accuracy. The solution controls for pseudo-transient explicit relaxation factors are 0.5, 0.5, 1, 1, 0.75, 1, and 1 for pressure, momentum, density, body forces, turbulent kinetic energy, turbulent dissipation rate, and turbulent viscosity and energy, respectively. The residual for the energy is 10^{-6}. The other residual for continuity, momentum, and turbulent kinetic energy and dissipation are 10^{-4}.

3.2 Governing Equations

For fluid flow in solar air heater, continuity and Reynolds-averaged-Navier–Stokes (RANS) equations are used. In this study, the RNG k-ε turbulence model [5, 14] is used as it improves the performance for rotation and streamline curvature.

$$\text{Continuity equation, } \frac{\partial (\rho u_j)}{\partial x_i} = 0 \tag{1}$$

$$\text{Momentum equation } \quad \frac{\partial}{\partial x_j}(\rho u_i u_j) + \frac{\partial p}{\partial x_i}$$

$$= \frac{\partial}{\partial x_j}\left[\mu\left(\frac{\partial u_i}{\partial x_j} + \frac{\partial u_j}{\partial x_i}\right)\right] + \frac{\partial}{\partial x_j}\left[\mu_t\left(\frac{\partial u_i}{\partial x_j} + \frac{\partial u_j}{\partial x_i}\right)\right] \tag{2}$$

$$\text{Energy equation } \quad \frac{\partial}{\partial x_i}(\rho u_j T) - \frac{\partial}{\partial x_j}\left[(\Gamma + \Gamma_T)\frac{\partial T}{\partial x_J}\right] = 0 \tag{3}$$

where $\Gamma_T = \mu_t/\text{Pr}$ is the turbulent thermal diffusivity, $\Gamma = \mu/\text{Pr}$ is the molecular thermal diffusivity, Pr is the Prandtl number, μ and μ_t are the viscosity (Ns/m^2) and thermal viscosity, respectively, ρ is the density (kg/m^3), P is the pressure (Pascal), u is the velocity (m/s), and T is the temperature (K). To model flow through porous media, it is required to add an additional source term to governing flow equations by using the Forchheimer equation as given below as per [14]

$$\nabla p^* = \frac{\mu}{\alpha}u^* + \beta\rho u^{*2} \tag{4}$$

$$F_i = -\left(\frac{\mu}{\alpha}u_i + C_2\frac{1}{2}\rho|u|u_i\right) \tag{5}$$

where F_i is the source term for the i-th Navier–stokes equation and $C_2 = 2\beta$

For solar air heater with empty channel, hydraulic diameter and Reynolds number are considered.

Local thermal equilibrium model assumes that the solid and fluid phases of the porous medium are in thermal equilibrium, i.e., $Ts = Tf = T$. The net heat transfer between the phases of the porous medium is zero since the heat conduction in both the phases takes place simultaneously.

$$\text{For solid}(1 - \varepsilon)(\rho c)_s\frac{\partial T_s}{\partial t} = (1 - \varepsilon)\nabla \cdot (k_s\nabla T_s) + (1 - \varepsilon)q_s''' \tag{6}$$

$$\text{For fluid }\varepsilon\left(\rho c_p\right)_f\frac{\partial T_f}{\partial t} + \left(\rho c_p\right)_f U.\nabla T_f = \varepsilon\,\nabla.\left(k_f\nabla T_f\right) + \varepsilon\,q_f''' \tag{7}$$

Adding Eqs. (6) and (7)

$$(\rho c)_{eff}\frac{\partial T}{\partial t} + (\rho c)_f U.\nabla\text{T} = \nabla.\left(k_{eff}\nabla\text{T}\right) + q_{eff}''' \tag{8}$$

where

$$(\rho c)_{eff} = (1 - \varepsilon)(\rho c)_s + \varepsilon(\rho c_P)_f \tag{9}$$

$$k_{eff} = (1 - \varepsilon)k_s + \varepsilon k_f \tag{10}$$

$$q'''_{eff} = (1 - \varepsilon)q'''_s + \varepsilon q'''_f \tag{11}$$

3.3 Grid Independence Study

The grid study is important to know the minimum number of nodes for present simulation to get accurate outlet temperature and pressure drop. Case (a) is considered for grid study with Re = 5868. The heat flux on the absorber plate is 850 W/m^2. The deviation for outlet temperature and pressure drop of solar air heater is mentioned in Table 4. The baseline grid size is taken as 492,800 number of nodes. The deviation of outlet temperature and pressure drop is less than 1%. For further simulation and analysis purpose, 492,800 number of nodes are considered. Figure 3 shows the quadrilateral meshing of the empty channel of SAH.

Table 4 Grid independence study for empty channel solar air heater for Re = 5868 for case (a)

Number of grids	T_{out} (K)	ΔP (Pa)	Deviation (%)	
			T_{out} (K)	ΔP (Pa)
340,158	330.46	0.233	0.006	−0.427
408,900	330.45	0.234	0.003	0
492,800	330.44	0.234	Baseline data	
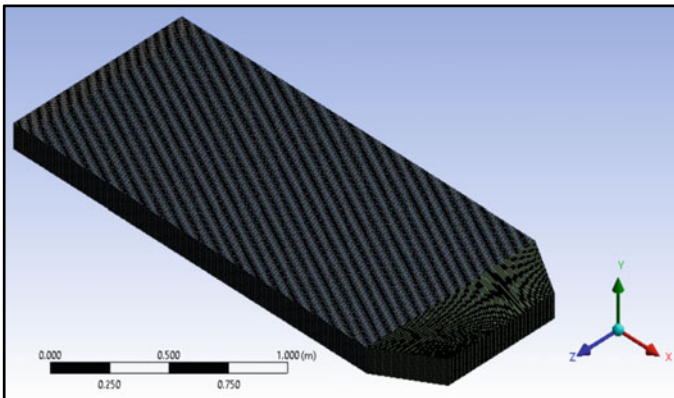
Fig. 3 Meshing of the solar air heater

Fig. 4 Validation of numerical present study with Rajarajeswari et al. experimental and numerical results [11]
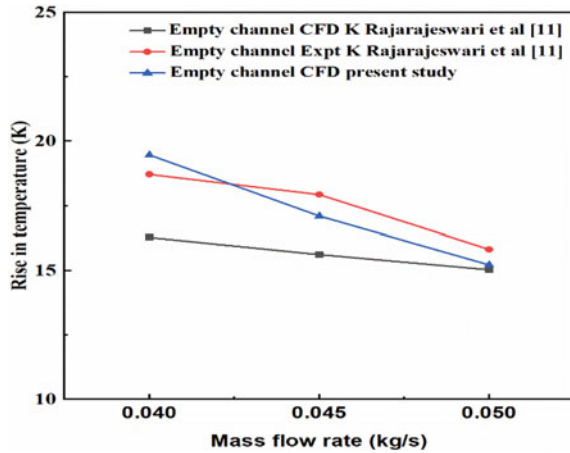
3.4 Validation

The empty channel SAH CFD analysis of present study is compared with the empty channel of Rajarajeswari et al. experimental results and CFD results. Figure 4 shows that the present study is following similar trend as per experimental and numerical analysis of [11]. The percentage deviation for experimental and numerical with the current study is 1.28% and 9.57%, respectively.

4 Results and Discussion

4.1 Velocity Distribution in Empty Channel and Porous Zone

Figure 5a and b show the velocity streamline of empty channel and porous zone of case d for 0.4 m/s velocity, respectively. From figure, it represents that the velocity near the outlet wall in porous media is higher due to pore structure of metal foam. The turbulence is created due to pores present in the metal foam. The air velocity near the absorber plate is low as shown in Fig. 5a.

4.2 Effect of Temperature for Different Arrangements of Metal Foam

Figure 6 shows the outlet temperature variation for different Reynolds for cases b to f. The temperature reduces as the velocity increases. From Fig. 6, it is observed that case (c) and case (f) have similar trend of outlet temperature. Case (f) is fully filled

Fig. 5 Effect of velocity in **a** empty channel **b** porous zone—case d for 0.4 m/s velocity

(a) velocity distribution of case a (empty channel)

(b) velocity distribution of case d (porous zone)
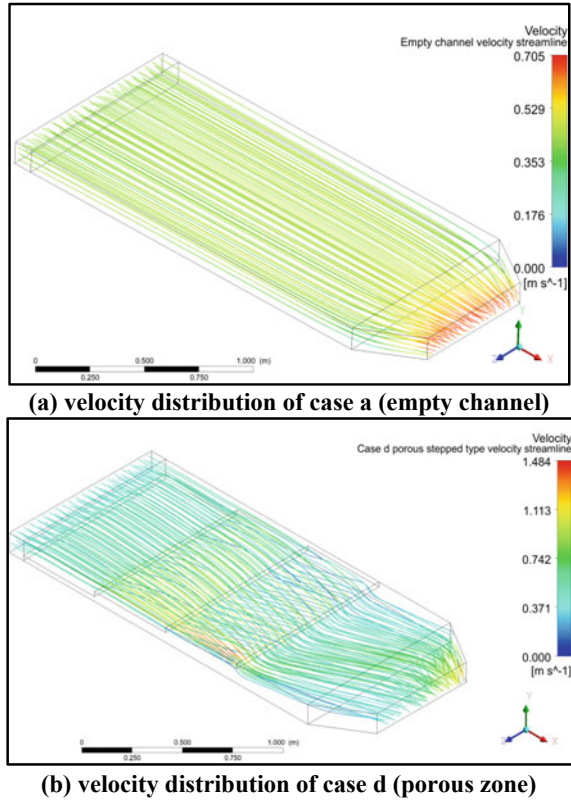
with metal foam which increases the cost of the solar air heater. Hence, to reduce the cost and to get maximum outlet temperature, case (c) is the best suitable configuration of metal foam instead of fully filled. Case (c) is giving 8.89% higher temperature than the empty channel. Case (c) and case (f) have nearly the same temperature rise.

4.3 Effect of Pressure Drop for Different Arrangements of Metal Foam

Figure 7 shows the variation in the pressure drop with respect to Reynolds number. As velocity increases, the pressure drop increases. The pressure drop is low for case c and higher for the case f. Higher the pressure drop, lower the performance of the solar air heater. Due to porous structure of metal foam, resistance increases which tends to increase pressure drop as well as pumping power. Hence, it is concluded that for higher Reynolds number, pumping power requirement of solar air heater is more.

Fig. 6 Effect of outlet
temperature for different
reynolds number
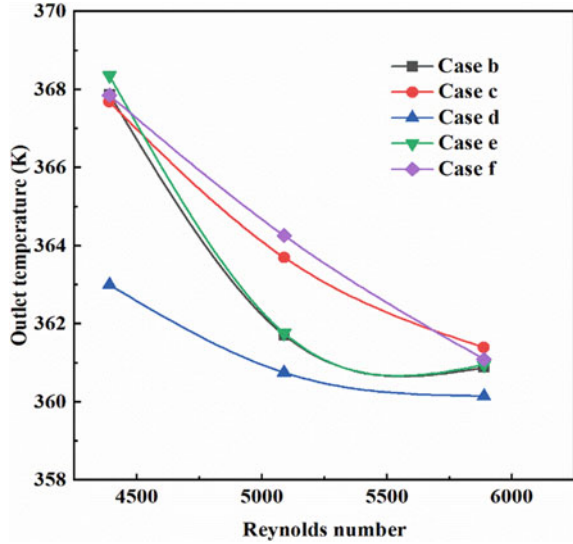
Fig. 7 Effect of pressure
drop for different reynolds
number
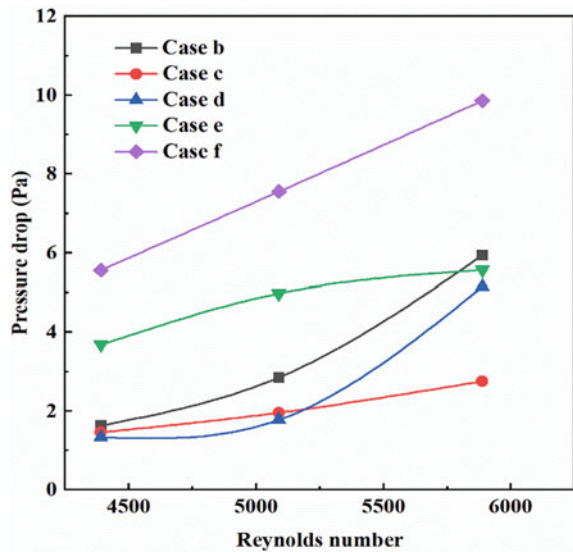
4.4 Effect of Performance Factor for Different Arrangements of Metal Foam

Figure 8 shows the performance factor versus Reynolds number. The performance
factor is important to know the overall performance of the solar air heater. Figure 8
shows that case (c) stepped-type metal foam is giving good results compared to cases

Fig. 8 Effect of
performance factor for
different Reynolds number
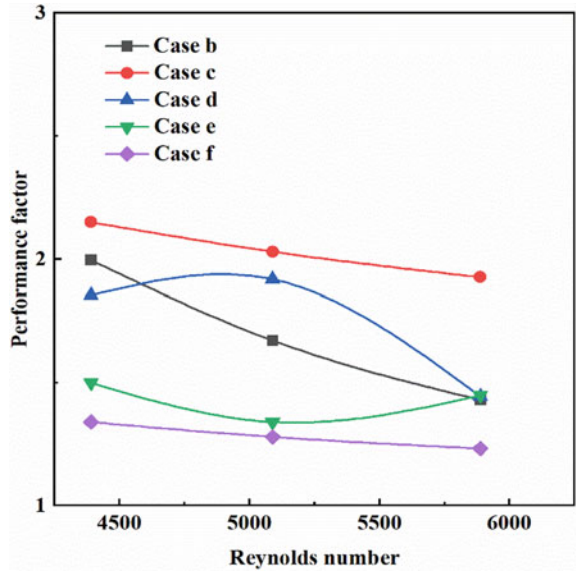
(a) to (f). For higher velocity, performance of solar air heater decreases in all type of
stepped-type arrangement of metal foam.

5 Conclusions

The solar air heater increases the heat transfer rate by using metal foam as porous
media. Numerical analysis is very important to save the time and development cost
of product. In this study, case (a)—empty channel, case (b) to case (e) stepped metal
foam, and case (f) fully filled metal foam are studied for metal foam properties of
92% porosity of copper.

- The analysis was carried out for the range of Reynold number 4401–5868.
- The porous metal foam has better rise in temperature compared to empty channel.
  The increase in temperature is 8.89% than empty channel.
- Among the six cases from (a) to (f), case (c) is the best suitable configuration for
  further experimental work. Case (c) is the best option which saves the material
  cost, and it reduces the pressure drop.
- The average temperature rise and the performance factor for case (c) are 364. 6 K
  and 2.035, respectively.

References

1. Saedodin S, Zamzamian SAH, Nimvari ME, Wongwises S, Jouybari HJ (2017) Performance evaluation of a flat-plate solar collector filled with porous metal foam: Experimental and numerical analysis. Energy Convers Manag 153:278–287. https://doi.org/10.1016/j.enconman.2017.09.072

2. Jadhav PH, Gnanasekaran N, Perumal DA, Mobedi M (2021) Performance evaluation of partially filled high porosity metal foam configurations in a pipe. Appl Therm Eng 194. https://doi.org/10.1016/J.APPLTHERMALENG.2021.117081

3. Kansara R, Pathak M, Patel VK (2021) Performance assessment of flat-plate solar collector with internal fins and porous media through an integrated approach of CFD and experimentation. Int J Therm Sci 165. https://doi.org/10.1016/j.ijthermalsci.2021.106932

4. Anirudh K, Dhinakaran S (2020) Performance improvement of a flat-plate solar collector by inserting intermittent porous blocks. Renew Energy 145:428–441. https://doi.org/10.1016/j.renene.2019.06.015

5. Singh S (2020) Experimental and numerical investigations of a single and double pass porous serpentine wavy wiremesh packed bed solar air heater. Renew Energy 145:1361–1387. https://doi.org/10.1016/j.renene.2019.06.137

6. Peng H, Li M, Liang X (2020) Thermal-hydraulic and thermodynamic performance of parabolic trough solar receiver partially filled with gradient metal foam. Energy 211:119046. https://doi.org/10.1016/J.ENERGY.2020.119046

7. Valizade M, Heyhat MM, Maerefat M (2020) Experimental study of the thermal behavior of direct absorption parabolic trough collector by applying copper metal foam as volumetric solar absorption. Renew Energy 145:261–269. https://doi.org/10.1016/J.RENENE.2019.05.112

8. Wang Z, Wu J, Lei D, Liu H, Li J, Wu Z (2020) Experimental study on latent thermal energy storage system with gradient porosity copper foam for mid-temperature solar energy application. Appl Energy 261:114472. https://doi.org/10.1016/J.APENERGY.2019.114472

9. Xiao X, Jia H, Wen D, Zhao X (2020) Thermal performance analysis of a solar energy storage unit encapsulated with HITEC salt/copper foam/nanoparticles composite. Energy 192:116593. https://doi.org/10.1016/J.ENERGY.2019.116593

10. Jouybari NF, Lundström TS (2020) Performance improvement of a solar air heater by covering the absorber plate with a thin porous material. Energy 190:116437. https://doi.org/10.1016/J.ENERGY.2019.116437

11. Rajarajeswari K, Alok P, Sreekumar A (2018) Simulation and experimental investigation of fluid flow in porous and non-porous solar air heaters. Sol Energy 171:258–270. https://doi.org/10.1016/j.solener.2018.06.079

12. Jadhav PH, Gnanasekaran N, Perumal DA (2021) Numerical consideration of LTNE and darcy extended forchheimer models for the analysis of forced convection in a horizontal pipe in the presence of metal foam. J Heat Transf 143(1). https://doi.org/10.1115/1.4048622

13. Kamath PM, Balaji C, Venkateshan SP (2013) Convection heat transfer from aluminium and copper foams in a vertical channel—an experimental study. Int J Therm Sci 64:1–10. https://doi.org/10.1016/j.ijthermalsci.2012.08.015

14. Ansys Fluent R2 Student version (2022)

Energetic and Exergetic Performance of an Evacuated Tube U-Type Solar Collector for Medium-Temperature Industrial Process Air Heating: An Experimental Study

Thota S. S. Bhaskara Rao and S. Murugan

Abstract In this research work, experiments are conducted in a U-type evacuated tube solar collector (ETSC), which can be used for producing medium-temperature industrial process hot air. The amount of heat gain, thermal performance, and efficiency of the U-type ETSC with air as the working fluid are studied experimentally. Solar radiation is found as the main important parameter for the efficiency and higher collector outlet temperatures. The values of the highest collector efficiencies are observed between 1:30 PM and 2 PM due to higher solar radiation at this time. The energetic and exergetic efficiencies of the collector are determined, and the results are presented in this paper. From the experimental results, it can be concluded that the developed U-type with ETSC can be useful for medium-temperature industrial process heating applications.

Nomenclature

Symbols

A_{ETSC}	Area of the collector [m^2]
C_{pa}	Specific heat of air [kJ/kg K]
I	Incident solar radiation [W/ m^2]
m_a	Mass flow rate of the air [kg/sec]
Q	Heat gain [W]

T. S. S. Bhaskara Rao (✉) · S. Murugan
Heat Power Laboratory, Department of Mechanical Engineering, National Institute of Technology Rourkela, Rourkela 769008, India
e-mail: bhaskar.mech328@gmail.com

T_a Temperature of the ambient air [°C]
T_{ao} Air temperature at collector inlet [°C]
T_{ai} Air temperature at collector outlet [°C]
T_s Temperature of the sun [°C

Subscripts

c Collector
c_i Collector inlet
c_o Collector outlet
Ex Exergy
in Inflow of exergy
out Outflow of exergy
rad Radiation

1   Introduction

Solar energy is considered to be one of the potential alternative sources to fossil fuels shortly [1]. The application of solar energy includes air heating, drying, space heating, power generation, etc. Generally, for these industrial applications, two types of non-concentrating solar thermal collectors are used: (i) flat-plate solar collectors (FPSC) and (ii) evacuated tube solar collectors (ETSC) [2]. Various experimental and simulation works have been carried out on both collectors, and among these, ETSC shows better efficiency compared to the FPSC. Among the evacuated tube configurations, U-type ETSC has two major advantages that are: (i) efficient working in cold climates and (ii) cost-effectiveness. Considering the lowest initial possible investment, U-pipe ETSC provides an extremely low-cost alternative to the heat pipe collectors [3].

In the U-type ETSC, U-shaped copper tubes are used on the inner side of the glass tubes. Generally, aluminum or copper fins are attached along and between the glass tubes and the U-tubes. The incident solar radiation on the collector aperture is absorbed by the glass tubes and then passes to the outer side of the inner glass tube through radiation. The gap between the outer and inner glass tube is created with a vacuum (<5*10^{-3} Pa) before the thermal sealing at the tube end. The outer surface of the inner glass tube is coated with the three target selective coatings of the absorption layer (aluminum nitride), bonding agent cum absorption layer (aluminum nitride and stainless steel), and anti-reflection layer of copper for the better absorption of the heat energy [4]. The working fluid in the U-tube is heated by the solar radiation collected by using the evacuated tube and passing through the metal fin. This creates the flow of the medium by convection. The evacuated tubes do not directly contact

the working fluid (air or water). Since the air is used as a working medium in the U-tube, clogging, scaling, and freezing issues will not happen. For forcing the air into the U-tubes, an air blower is used to continuously force the air. The exit temperature of the U-tubes can reach a high range between 80 and 120 °C during summer. The glass tubes are made of thin glass and are prone to breakage during transportation and shifting. The advantage is that if one of the glass tubes is broken, that tube itself can change instead of all the tubes. No corrosion takes place in the evacuated tubes as it is made up of glass, and lesser heat losses were found due to the vacuum space in between the two glass tubes [5]. The motivation of the current research study is to find the thermal performance of a U-type ETSC with air as the working fluid for medium-temperature industrial process applications.

2   Literature Review and Objective

Various researchers worked on the thermal performance of the ETSC and obtained similar results. Gao et al. [6] proposed mathematical modeling for the thermal performance of an ETSC U-type, and the results are validated by the experimental observations. The thermal performance of the collector is investigated with the corresponding meteorological conditions, and the various thermal performance characteristics, including mass flow rate, tube length and tube size, type of coating on the absorber, and heat loss coefficient of the collector, are assessed. Nie et al. [7] studied the thermal performance of a U-type ETSC whose working fluid temperature is lower than the ambient air. The thermal efficiency of the collector is estimated by various solar radiations that are changed by a solar simulator and at the different mass flow rates of the working fluid and found higher thermal efficiencies at the lowest inlet temperatures of the working. It is concluded that, at lower solar radiations during the experimentation, the thermal efficiency and its growth rate are higher at the lower input temperatures of the collector.

Wang et al. [8] experimentally assessed the performance of a U-type ETSC surrounded by a compound parabolic concentrator consisting of 10 tubes. All the U-tubes are made up of copper, and during the experimentation, the air is heated up when passing through the tubes, and the outlet air temperature of the collector reaches a maximum of 200 °C. A model for heat transfer is developed to assess solar radiation, mass flow rate, and temperature. The efficiency parameters are calculated, and the collector can be useful for engineering applications that require a temperature range of 150–200 °C, even during winter climatic conditions. Naik et al. [11] performed numerical and experimental investigations on a U-type ETSC with different working fluids, and the results of the performance are compared. A mathematical model is developed for the heat gain by the collector and the outlet temperatures of the working fluid, viz., water, air, and lithium chloride solution, and found that the performance of the collector highly depends upon the flow rate of the working fluid, length of the collector, and the amount of solar radiation incident on the collector. Water shows a higher amount of heat gain than the other working fluids with air and lithium chloride.

Tong et al. [9] experimentally investigated the thermal performance of a low-cost ETSC with a U-pipe and used copper fin as the intermediate material between the absorber tube and the U-type copper pipe. Performance results of the collector are compared with two working fluids, viz., water and multi-wall carbon nanotube (MWCNT) powder mixed with water by 0.24% vol. The results show that the performance increases by 4% with the use of MWCNT/water nanofluid and used water as the filler material between the copper fin and the absorber tube. The environmental analysis of the proposed system shows an annual decrement of 1600 and 5.3 kgs of CO_2 and SO_2 in the atmosphere.

Till now, no experimental studies have been found on the U-type ETSC with air as the working fluid, and no literature is available on its energy and exergy performances of it. Based on this research gap, an attempt is carried out on an in-house fabricated U-type ETSC, and the experimental study is proposed for air heating purposes. The objectives of the present research study are to perform the thermal performance, useful heat gain, efficiency, energy, and exergy analyses of the proposed ETSC with U-type. The novelty of the current research study is the heating of air to medium-temperature heating applications in the process industries, including paper, dairy, textile, pulp, pharma, leather, and automotive industries with the use of ETSC collector.

3 Materials and Methods

An experimental setup is fabricated for medium-temperature industrial process applications and installed at the National Institute of Technology in Rourkela, India. The fabricated copper U-pipe and insertion of the U-pipe in the evacuated glass tubes are shown in Fig. 1. The experimental setup consists of 10 evacuated tubes, and inside of that, U-tubes are connected in parallel. The photograph of the experimental setup is shown in Fig. 2. An air blower is used for supplying air in the U-tube ETSC. The air blower of 2.8HP (220 V, 50 Hz, 2800 RPM) is connected to the inlet manifold through a flow control valve. From the inlet manifold, the air blower transfers the air to each U-tube, and the heated air leaves the outlet manifold of the collector. The outlet manifold is insulated with a 25 mm thickness of glass wool to prevent heat loss. Two thermocouples are placed at the inlet and outlet of the collector to measure the temperature at the respective conditions. A pyranometer is also kept nearer to the collector to record the radiation data falling on the collector during the experimentation days. The orientation of the ETSC is set at an angle of 19° toward the south direction (22.26° N, 84.85° E). The overall design specifications of the ETSC with U-pipe are given in Table 1. The mass flow rate of the air through the U-tube ETSC is fixed at the mass flow rate of 0.03 kg/s. Three sets of experiments were conducted in the month of May 2021, and the mean values are taken for the calculation. The hourly variation of the ambient temperatures, solar radiation, and inlet and outlet temperatures from the collector during the day with time is given in Table 2.

Fig. 1 Fabricated images of the **a** copper U-pipe and **b** photograph of the U-pipe with the manifold fitted into the evacuated tube glass

| 1. U-Pipe | 2. Copper pipe | 3. Manifold Header |
| 4. Inserted Copper pipe | 5. Sealing plug | 6. Glass tube |
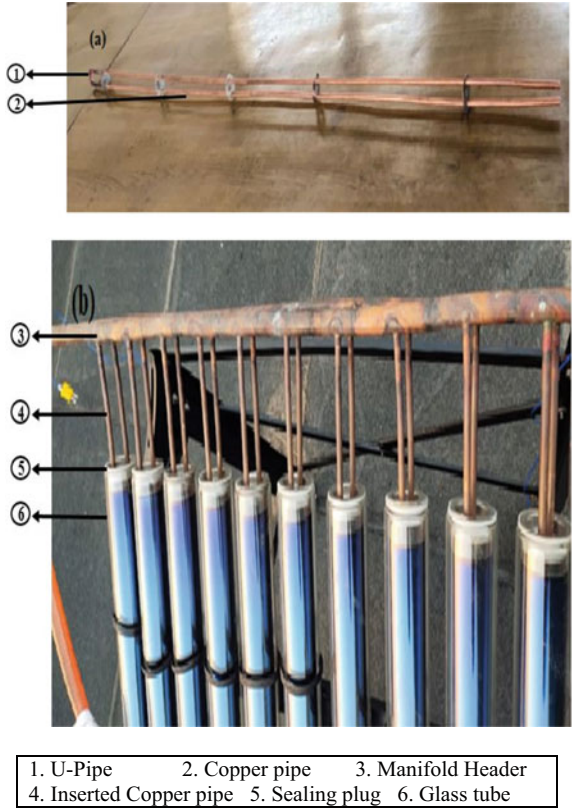
4 Thermal Performance

4.1 Useful Heat Gain

The useful heat gain of the ETSC is proportional to the rate of the mass flow of air. The rate of heat gain by the evacuated U-tube solar collectors depends on the density, ambient temperature, mass flow rate, and inlet and outlet temperatures of the air, and this can be calculated by Eqs. (1) and (2)

$$Q_u = m_a C_{pa}(\Delta T) \tag{1}$$

$$Q_u = m_a C_{pa}(T_{ao} - T_{ai}) \tag{2}$$

Fig. 2 Schematic diagram
of the experimental setup
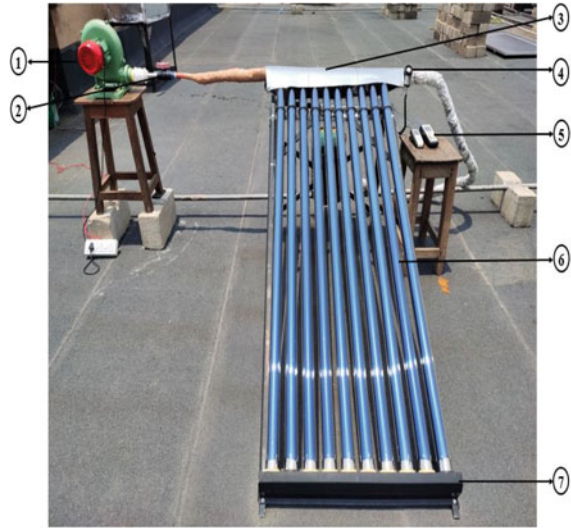
1. Blower 2. Flow control valve 3. Manifold header with insulation 4. Pyranometer 5. Digital temperature indicator 6. Evacuated glass tubes 7. Collector stand

4.2 Energy Analysis

The energy analysis of an ETSC is calculated based on the conservation of the mass and energy equations. The experimental data required for the analysis are: (i) temperatures of the inlet and outlet air of the collector, (ii) rate of mass flow of air, and (iii) inflow and outflows of the energy. The inflow energy of the ETSC is electrical energy supplied to the blower to force the air into the collector and incident solar radiation on the surface area of the collector. The energy outflow of the collector is the heat loss to the surroundings due to the reflection of the radiation, improper insulation at the collector outlet, and the useful heated air.

The general energy balance equation of a solar thermal collector is given in Eq. (3)

$$\sum E_{in} = \sum E_{out} \tag{3}$$

The amount of solar energy that falls on the collector is calculated by using Eq. (4)

$$E_{in} = A_{ETSC} I \tag{4}$$

The amount of useful energy attained by the air in the collector is expressed in Eq. (5)

$$E_{out} = m_a C_{pa} (T_{ao} - T_{ai}) \tag{5}$$

Table 1 Design specifications of the ETSC with U-type collector

Component/parameter	Material/dimension
Glass	Borosilicate glass
Number of tubes	10
Collector area (m^2)	1.44
Transmittance of the glass	0.91
Emissivity of glass	0.90
Outer glass tube length (m)	1.8
Outer diameter of glass tube (mm)	58
Inner diameter of glass tube (mm)	44
Tilt angle (°)	19°
Absorber coating	AI-N/AI (aluminum nitride)
U-pipe outer diameter (mm)	8
U-pipe thickness (mm)	0.5
Conductivity of copper pipe (W/mK)	397
Conductivity of aluminum fin (W/mK)	238
Emissivity of aluminum fin	0.1
Aluminum fin thickness (mm)	0.5
Manifold outer diameter (mm)	18
Manifold thickness (mm)	1
Working fluid	Air
Thermal conductivity of air (W/mK)	0.024
U-tube and manifold headers material	Copper
Insulation material	Glasswool
Thickness of the insulation material (mm)	25
Sealing plug	Silicon rubber with stainless steel cover

The energy efficiency of the solar thermal ETSC collector is calculated by using Eqs. (6) and (7)

$$\eta_{ETSC} = \frac{E_{out}}{E_{in}} \tag{6}$$

$$\eta_{ETSC} = \frac{m_a C_{pa}(T_{ao} - T_{ai})}{A_{ETSC} I} \tag{7}$$

Table 2 Experimental operating conditions for 10 number of ETSC connected in parallel (average values of the three sets of experiments conducted in May 2021)

Time (hours)	Solar radiation (W/m^2)	Ambient temp. (°C)	Collector inlet temp. (°C)	Collector outlet temp. (°C)
9:00	652	24	44.8	108.4
9:30	661	24.6	44.2	107.2
10:00	672	25	44.8	108.4
10:30	683	26	45.6	110.8
11:00	699	26	46.2	115.4
11:30	721	27.1	47.9	118
12:00	757	28	46.8	115
12:30	802	28.2	49.3	118.2
1:00	895	29	50.2	119.8
1:30	898	29	52.4	121.3
2:00	900	28	53.1	122.8
2:30	853	28	41.5	117.1
3:00	814	27	42.8	113
3:30	786	27	40	111.5
4:00	754	26	38.2	104.6
4:30	728	25	36.6	103.8
5:00	692	25	33.7	102.5

4.3 *Exergy Analysis*

The exergy analysis of the ETSC is performed based on the second law of thermodynamics. The exergy of the solar radiation falling on the ETSC is given in Eq. (8) [10]

$$Ex_{rad,c} = A_c I \left[1 - \frac{4}{3} \left(\frac{T_a}{T_s} \right) + \frac{1}{3} \left(\frac{T_a}{T_s} \right)^4 \right] \tag{8}$$

The exergy inflow of the solar collector is given as Eq. (9)

$$Ex_{in,c} = m_a c_{pa} \left[(T_{ci} - T_a) - T_a \ln \left(\frac{T_{ci}}{T_a} \right) \right] \tag{9}$$

The exergy outflow of the solar collector can be written as Eq. (10)

$$Ex_{out,c} = m_a c_{pa} \left[(T_{co} - T_a) - T_a \ln \left(\frac{T_{co}}{T_a} \right) \right] \tag{10}$$

Table 3 Uncertainties of the variables during experimentation

Parameter	Device	Range	Accuracy	Make/model
Digital temp. indicator	K-type thermocouple, RTD sensor	°C	± 2 °C	ACE Instruments RTD PT 100 Sensor
Air velocity	Anemometer	0–45 m/s	± 0.1 m/s	Metravi AVM-04 Digital Thermo-anemometer
Solar radiation	Pyranometer	0–1999 W/m^2	± 3 W/m^2	Metravi Solar Power Meter-207

The efficiency of the solar collector can be written as Eq. (11)

$$\eta_{Ex,c} = \frac{Ex_{out,c}}{Ex_{in,c}} \tag{11}$$

4.4 Uncertainty of the Experimentation

The uncertainty of the present experimental study depends on factors including temperatures and mass flow rate of the air. The uncertainty analysis is carried out for the accuracy and reliability of the dependent parameters [11]. The experimental uncertainty in the dependent value W_R and independent variables w_1, w_2, ...w_n calculated from the equation below is (12) [12]

$$W_R = [(\frac{\delta R}{\delta x_1} w_1)^2 + (\frac{\delta R}{\delta x_2} w_2)^2 + \ldots + (\frac{\delta R}{\delta x_n} w_n)^2 \tag{12}$$

where W_R is the uncertainty of the estimated value and w_1, w_2, ...w_n are the errors in the independent variables. The uncertainties of the variables during experimentation and the uncertainty calculation of the experiments used in this study are given in Tables 3 and 4, respectively. The overall uncertainty of the drying experiment is found as ± 1.4533%.

5 Results and Discussion

The proposed ETSC collector is installed on the roof terrace of the Department of Mechanical Engineering at the National Institute of Technology Rourkela, Odisha, India, and the experiments are conducted. The experiments begun at 9 AM and continued up to 5 PM. The ambient temperature and the incident solar radiation

Table 4 Detailed uncertainty calculation of the experiment

Parameter	Uncertainty calculation with the value
Temperature	$W_T = [(w_{RTD\,Sensor})^2 + (w_{digital\,thermometer})^2$ $+ (w_{connection\,points})^2 + (w_{readings})^2]^{\frac{1}{2}}$ $W_T = [(0.1)^2 + (0.1)^2 + (0.1)^2 + (0.25)^2]^{\frac{1}{2}}$ $= 0.3041$
Air velocity	$W_{AV} = [(w_{anemometer})^2 + (w_{readings})^2]^{\frac{1}{2}}$ $W_{AV} = [(0.1)^2 + (0.1)^2]^{\frac{1}{2}}$ $= 0.1414$
Solar radiation	$W_{SR} = [(w_{pyranometer})^2 + (w_{readings})^2]^{\frac{1}{2}}$ $W_{SR} = [(1)^2 + (1)^2]^{\frac{1}{2}}$ $= 1.4141$
Total uncertainty	$W_{Exp} = [(W_T)^2 + + (W_{AV})^2 + (W_{SR})^2]^{\frac{1}{2}}$ $W_{Exp} = [(0.3041)^2 + (0.1414)^2 + (1.4141)^2]^{\frac{1}{2}} = \pm 1.4533\%$

during the experimental day are shown in Fig. 3. The starting value of 1 on the X-axis indicates the time of 9 AM. During the experimental days, the ambient temperature is found to be 24 °C during the initial time of 9 AM and increases to 29 °C at 1 PM; after that, ambient temperatures follow a declining trend and are found to be about 25 °C at 5 PM during sunset. The value of incoming solar radiation is also observed to have the same trend with an initial radiation value of 652W/m^2 and increases to a maximum value of 900 W/m^2 at 2 PM, and after that, the radiation value falls to 692 W/m^2 at 5 PM.

The variation in the inlet and outlet temperatures of the heated air coming up from the U-pipe ETSC is shown in Fig. 4. A temperature difference of 70–80 °C is found at the outlet of the collector in comparison with ambient temperatures on a typical sunny day of experimentation. This high temperature from the collector may be due to the incident solar radiation and higher amount of heat collection in the ETSC collectors due to the vacuum insulation and effectiveness in the design configuration.

The amount of useful heat gain and the thermal efficiencies of the U-pipe ETSC is shown in Fig. 5. The heat gain during the initial time of the experimentation is 100 W/m^2 and then increases with the increase in the solar radiation up to a maximum of 550 W/m^2 and found to have a reduction in the value of heat gain till 5 PM to a minimum of 180 W/m^2. The thermal efficiency increases with the value increase in heat gain by the collector. The thermal efficiency value increases from 0.34% to 0.66% till 2 PM and then follows a declining trend to a minimum value of 0.38% at 5 PM.

The variation in the energy and exergy efficiencies of the U-pipe collector with time is shown in Fig. 6. It can be observed from the figure that the energy efficiency
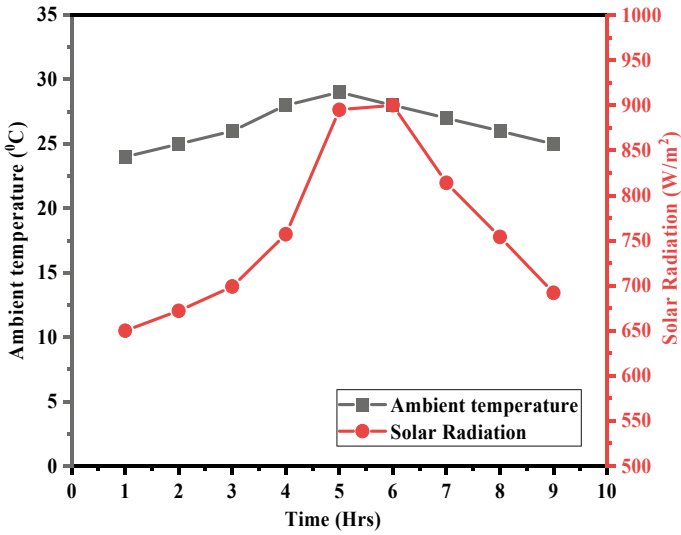
Fig. 3 Variation of the ambient temperature and solar radiation with the time
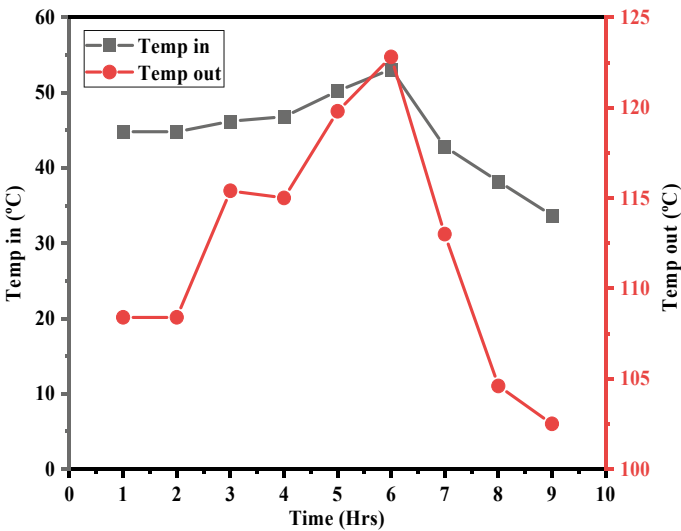
Fig. 4 Variation of the inlet and outlet temperatures coming out from the collector with the time

varies from 31 to 53%, with an average of 39%. The value of the highest collector efficiency lies between the experimentation time of 1:30 PM to 2 PM due to the higher solar radiation at this time, and the variations in the percentage of the efficiencies are also due to the continuous change in the solar radiation falling on the collector.
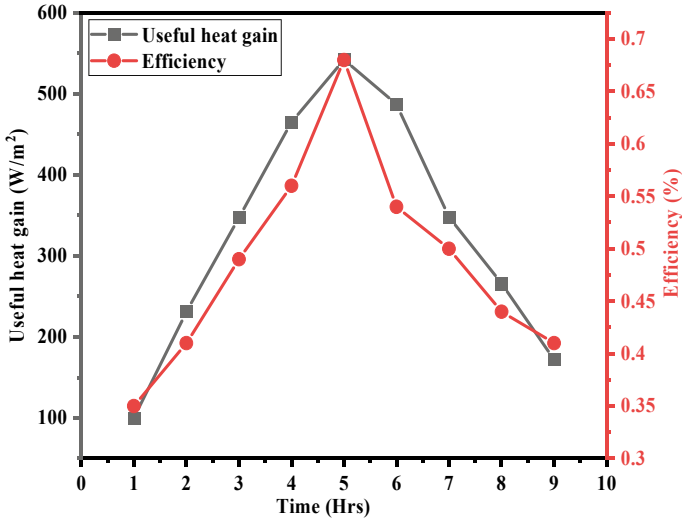
Fig. 5 Amount of useful heat gain and the thermal efficiency of the collector with the time

It can be inferred that the exergy efficiency of the setup varies from 25 to 60%, with an average exergy efficiency of 42% during the day.
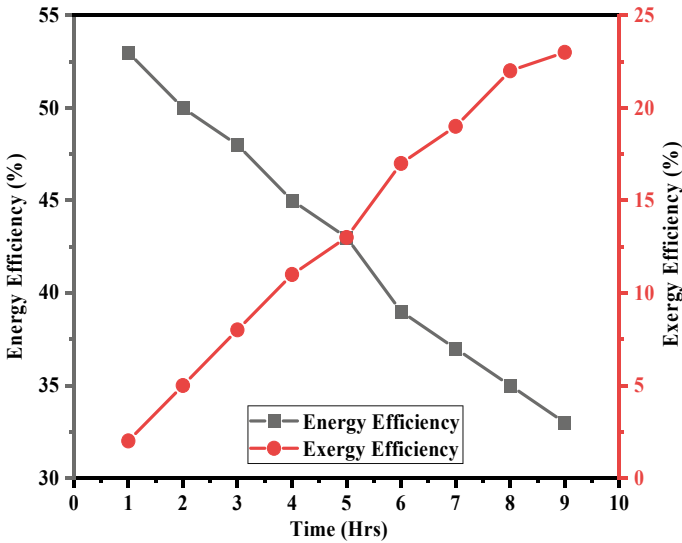
Fig. 6 Variation of the energy and exergy efficiency with the time

6 Conclusions

An in-house U-type ETSC is used to heat the air for industrial process medium-temperature applications. Experiments are carried out using air as the working medium, and thermal performance, useful heat gain, energy, and exergy efficiency analyses are performed. The following are the important conclusions of the study.

- Solar radiation and the number of U-type evacuated tubes are the main important parameters for the efficiency and higher collector outlet temperatures.
- A maximum of 70-80ºC higher temperature is found at the collector outlet of the ETSC. So, the developed U-type with ETSC can be useful for medium-temperature industrial process heating applications.
- The useful heat gain and the thermal efficiencies of the collector are found between 100 to 550W/m^2 and 0.34 to 0.66%, respectively.
- The energy efficiency varies from 31 to 53%, with an average of 39%. The value of the highest collector efficiency is observed between the experimentation time of 1:30 to 2 PM due to higher solar radiation at this time, and the variations in the percentage of the efficiencies are also due to the continuous change in the solar radiation falling on the collector.
- The exergy efficiency of the setup varies from 2 to 23%, with an average exergy efficiency of 11% during the day.

References

1. Farjana SH, Huda N, Mahmud MAP, Saidur R (2018) Solar process heat in industrial systems—a global review. Renew Sustain Energy Rev 82:2270–2286. https://doi.org/10.1016/j.rser.2017.08.065
2. Vendan SP, Shunmuganathan LPA, Manojkumar T, Thanu CS (2012) Study on design of an evacuated tube solar collector for high temperature steam generation. Int J Emerg Technol Adv Eng 2:539–541
3. Olfian H, Ajarostaghi SSM, Ebrahimnataj M (2020) Development on evacuated tube solar collectors: a review of the last decade results of using nanofluids. Sol Energy 211:265–282. https://doi.org/10.1016/j.solener.2020.09.056
4. Banthuek S, Suriwong T, Nunocha P, Andemeskel A (2018) Application of Ni-Al 2 O 3 cermet coating on aluminium fin as the solar absorber in evacuated tube collector (ETC). Mater Today Proc 5:14793–14798. https://doi.org/10.1016/j.matpr.2018.04.007
5. Feliński P, Sekret R (2016) Experimental study of evacuated tube collector/storage system containing paraffin as a PCM. Energy 114:1063–1072. https://doi.org/10.1016/j.energy.2016.08.057
6. Gao Y, Fan R, Zhang XY, An YJ, Wang MX, Gao YK YY (2014) Thermal performance and parameter analysis of a U-pipe evacuated solar tube collector 714–27
7. Nie X, Zhao L, Deng S LX (2017) Experimental study on thermal performance of U-type evacuated glass tubular solar collector with low inlet temperature 192–201
8. Wang PY, Guan HY, Liu ZH, Wang GS, Zhao F, Xiao HS (2014) High temperature collecting performance of a new all-glass evacuated tubular solar air heater with U-shaped tube heat exchanger. Energy Convers Manag 77:315–323. https://doi.org/10.1016/j.enconman.2013.08.019

9. Tong Y, Kim J, Cho H (2015) Effects of thermal performance of enclosed-type evacuated U-tube solar collector with multi-walled carbon nanotube/water nanofluid. Renew Energy 83:463–473. https://doi.org/10.1016/j.renene.2015.04.042
10. Ge Z, Wang H, Wang H, Zhang S, Guan X (2014) Exergy analysis of flat plate solar collectors. Entropy 16:2549–2567. https://doi.org/10.3390/e16052549
11. Naik BK, Bhowmik M, Muthukumar P (2019) Experimental investigation and numerical modelling on the performance assessments of evacuated U—Tube solar collector systems. Renew Energy 134:1344–1361. https://doi.org/10.1016/j.renene.2018.09.066
12. Lakshmi DVN, Muthukumar P, Layek A, Nayak PK (2019) Performance analyses of mixed mode forced convection solar dryer for drying of stevia leaves. Sol Energy 188:507–518. https://doi.org/10.1016/j.solener.2019.06.009

Comparison of Analytical Wake Models with CFD Study of Savonius Vertical Axis Wind Turbine

Sunil Kumar, Visakh Vaikuntanathan, Nishant Mishra, and Santanu Mitra

Abstract Wake characteristics of wind turbines such as wake width, velocity deficit, and turbulence intensity are important factors for optimal placement of wind turbine rotors in an array in a typical wind farm. Reduced-order analytical wake models are useful tools in wind-farm layout design due to their simplicity and low computational demand. However, the suitability of such reduced-order models has to be tested with more refined CFD studies before they can be deployed in the optimization of wind-farm layout. In this study, a detailed comparison of widely used analytical wake models with CFD studies on static and dynamic Savonius Vertical Axis Wind Turbine (S-VAWT) is done. The CFD studies involve solving the Reynolds-averaged Navier–Stokes (RANS) equations using finite volume method-based Ansys Fluent. The comparative investigation showed that the analytical wake models reported in the literature are capable of predicting wake characteristics such as the wake width; however, they fail to predict the wake velocity deficit. Moreover, the asymmetry in the wake velocity profile, which is a characteristic feature of S-VAWTs, is not captured by the models. This highlights the need for developing new analytical wake models that are better suited for S-VAWTs.

Keywords VAWT · Savonius · Wake models · CFD

Nomenclature

A_r Frontal area of rotor [m^2]
U Freestream velocity [m/s]
ρ Density of air [kg/m^3]
ω Rotor rotational speed [rad/s]

S. Kumar (✉) · V. Vaikuntanathan · S. Mitra
Department of Mechanical Engineering, Shiv Nadar Institution of Eminence (deemed to be University), Delhi NCR-201314, India
e-mail: sk300@snu.edu.in

N. Mishra
School of Engineering, UPES, Dehradun 248001, India

V	Wake velocity [m/s]
D	Rotor diameter [mm]
D_w	Wake width [mm]
a	Axial induction factor [–]
$\overline{V}$	Velocity vector [m/s]
V	Control volume [m^3]
TSR	Tip speed ratio ($\omega D/2U$) [–]
C_p	Coefficient of power [–]
C_t	Coefficient of torque [–]

1 Introduction

Wind energy is one of the most promising forms of renewable energy [1]. Based on the orientation of their axis of rotation, wind turbines are broadly classified into two: Horizontal Axis Wind Turbine (HAWT) and Vertical Axis Wind Turbine (VAWT). VAWTs are becoming popular in urban areas, as they are suitable for power generation in small areas. While designing the layout of a S-VAWT wind farm, comprising many such Savonius rotors, in constrained urban spaces, an understanding of the characteristics of the wake behind each rotor is important, since they affect the performance of the downstream rotors [2, 3].

2 Literature Review and Objective

Conventional Savonius rotor is a type of VAWT with two semicircular halves of a cylindrical surface, referred to as buckets, joined with an overlap ratio. At an overlap ratio of around 0.15, it was reported that the conventional two-bucket Savonius rotors perform at their best; moreover, two-bucket configuration was seen to perform better than three-bucket configuration [4, 5]. Numerous efforts have been made to analyze the wake characteristics, especially for HAWTs, by analytical, numerical, and experimental methods [6].

Analytical wake models are widely used in commercial sector because of their simplicity and low computational cost. These analytical wake models are mainly derived from the mass and momentum conservations. There are several key assumptions made to simplify the predictions in these models: fluid flow is assumed to be homogeneous, incompressible, and steady; the assumption of an infinite number of blades leads to a cylinder/disk-shaped rotor on which uniform force is exerted by the fluid flow; the wake is assumed to be symmetric and non-rotating; and the flow far upstream and far downstream of the rotor is assumed to be unperturbed [2]. A detailed comparison of the predictions from such wake models with CFD studies is

required to judge the suitability of these models for S-VAWTs. In the next section, a brief summary of the most prominent analytical wake models is given.

3 Wake Models

Jensen and Katic developed a simple wake model in their pioneering works [7]. This model assumes a top-hat-shaped velocity profile in the wake (see Fig. 1). Mathematically, the velocity in the wake, V (normalized with the freestream velocity U), can be written as follows:

$$\frac{V}{U} = 1 - \frac{2a}{\left(1 + \frac{2kx}{D}\right)^2} \tag{1}$$

Here, $a = 1 - \frac{U_r}{U} = \left(1 - \sqrt{1 - C_t}\right)/2$ is the axial induction factor, U_r is velocity near the rotor, C_t is torque coefficient of the rotor, D is rotor diameter, $D_w(x) = D + 2kx$ is the wake width at a distance x downstream of the rotor, and k is the rate of wake expansion (0.1 in Jensen-Katic model, and 0.075 for land applications) [8]. This model is used by various commercial software such as WasP, WindPRO, and WindSim [6].

Frandsen's wake model [9] uses momentum conservation over a control volume around the rotor. One of the differences between Katic and Frandsen wake models is in the definition of the wake width and the choice of wake decay constant. In addition, Frandsen uses momentum conservation, while Katic uses only mass conservation over the control volume. Frandsen proposed the velocity deficit in wake through Eq. (2), assuming a top-hat velocity profile in the wake.

$$\frac{V}{U} = \frac{1}{2} \pm \frac{1}{2}\sqrt{1 - 2\frac{A}{A_w(x)}C_t} \tag{2}$$

Fig. 1 Schematic of fluid flow over rotor and wake region
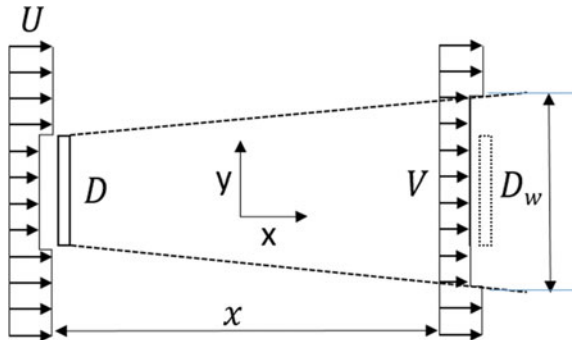
Here, A is the swept area of rotor, and $A_w(x) = \pi D_w^2/4$ is the circular wake area at a distance x downstream of the rotor, where the wake width is expressed as follows:

$$D_w(x) = D\left(\beta^{\frac{j}{2}} + \alpha\frac{x}{D}\right)^{\frac{1}{j}} \tag{3a}$$

$$\beta = \frac{\left(1 + \sqrt{1 - C_t}\right)}{2\left(\sqrt{1 - C_t}\right)} \tag{3b}$$

Here, decay factor $\alpha = 0.5$ and $j = 2.0$ for rectangular shape of wake velocity profile. The wake velocity profile for flow over cylindrical or bluff bodies is generally Gaussian [10]. Taking inspiration from the similarity in the rotational symmetry of a cylindrical body and Savonius rotor, a wake model was proposed by Bastankhah and Porte-Agel [10] as well as Ishihara et al. [11]. This model assumes a Gaussian velocity profile in the rotor wake given by Eq. (4)

$$\frac{V}{U} = 1 - C(x)e^{\frac{-y^2}{2\sigma^2}} \tag{4}$$

$$C(x) = 1 - \sqrt{1 - \frac{C_t}{8\left(\frac{k^*x}{D} + \varepsilon\right)^2}}, \sigma/D = \left(\frac{k^*x}{D} + \varepsilon\right) \tag{5a}$$

$$\varepsilon = 0.25\sqrt{\beta}, \quad k^* = \partial\sigma/\partial x \tag{5b}$$

4   Numerical Model and Methodology

In this study, the flow over a Savonius rotor is simulated by solving RANS equations using finite volume method in Ansys Fluent [12]. Conventional Savonius rotor has a plane of symmetry in the third dimension (here, along the Z-axis); hence, two-dimensional simulations are performed. In the following subsections, the details of the computational domain and methodology of the simulations are explained.

4.1   Computational Domain

The computational domain (Fig. 2) is prepared by Ansys "Design Modeler' package. Entrance and outlet lengths are kept sufficiently large so as to avoid any boundary effects on wake structure [13].

The upstream and downstream boundaries are set at a distance of 20D. The inlet and exit boundaries are imposed with a constant velocity of 6 m/s in the x-direction

Fig. 2 Geometry of computational domain
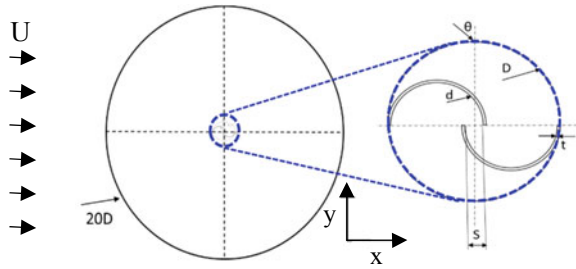
Table 1 Rotor geometry details

Number of buckets	2
Blade diameter, D	300 mm
Buckets diameter, d	164 mm
Blade thickness, t	2 mm
Overlap ratio, S/d	0.15

and pressure outlet condition, respectively. The details of the computational domain and rotor are given in Fig. 2 and Table 1.

4.2 Mesh Generation

Ansys meshing package is used to create a high-quality mesh. For discretization, quadrilateral and triangular mesh elements are utilized, and inflation layers of 10 layers of quadrilateral elements are used on solid walls of rotor to achieve $y^+ < 1.0$ [14]. The grid structure is shown in Fig. 3.
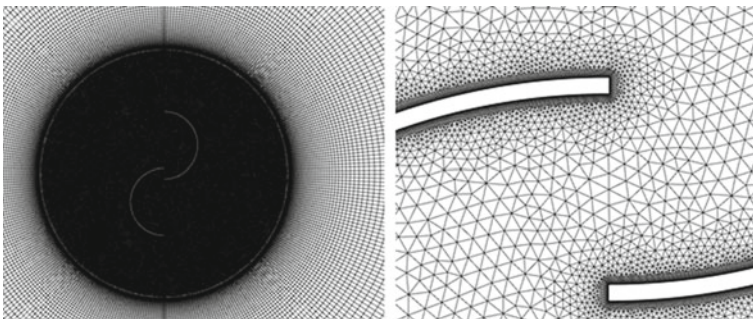
Fig. 3 Grid structure and near-wall inflation layers

4.3   Solver Details

Once geometry and meshing are done, the case files are put in Fluent setup where RANS equations are solved using Semi-Implicit Method for Pressure Linked Equation (SIMPLE) algorithm. Second-order scheme is used for pressure, momentum, and turbulence equations. k-ω shear stress transport (SST) model, which is a good choice for high Reynolds number flows [15–17], is used for turbulence modeling; note that some studies have also used the k-ε model [18]. The governing equations are given below. Equation (6) is the integral form of the continuity equation for a finite control volume fixed in space. In this study, the control volume is the computation domain.

$$\frac{\partial}{\partial t} \iint\limits_{V} \int \rho dV + \iint\limits_{S} \int \rho \bar{V} \cdot dS = 0 \tag{6}$$

Momentum equations for the two-dimensional flow analysis can be written as follows:

$$\frac{\partial(\rho u)}{\partial t} + \frac{\partial\left(\rho u^2\right)}{\partial x} + \frac{\partial(\rho uv)}{\partial y} = -\frac{\partial p}{\partial x} + \frac{\partial}{\partial x}\left(\lambda \nabla.\bar{V} + 2\mu\frac{\partial u}{\partial x}\right)$$
$$+ \frac{\partial}{\partial y}\left[\mu\left(\frac{\partial v}{\partial x} + \frac{\partial u}{\partial y}\right)\right] + \rho f_x \tag{7a}$$

$$\frac{\partial(\rho v)}{\partial t} + \frac{\partial(\rho uv)}{\partial x} + \frac{\partial\left(\rho v^2\right)}{\partial y} = -\frac{\partial p}{\partial y}$$
$$+ \frac{\partial}{\partial y}\left(\lambda \nabla.\bar{V} + 2\mu\frac{\partial v}{\partial y}\right) + \frac{\partial}{\partial x}\left[\mu\left(\frac{\partial v}{\partial x} + \frac{\partial u}{\partial y}\right)\right] + \rho f_y \tag{7b}$$

Flow around the rotor in static position is solved, and static torque coefficient is calculated at each angular position of the buckets. Six angular positions from 0° to 180°, with an interval of 30°, are considered. Turbulence intensity is set to be 3.17% at both inlet and outlet.

For dynamic rotor studies, sliding mesh model (SMM) is used. The computational domain is divided into two parts: one is fixed, and the other one is rotating at a tip speed ratio (TSR $= \frac{\omega D}{2U}$, ω is the angular speed of the rotor) varying from 0.2 to 1.2. Each time step corresponds to one-degree rotation of the rotor. In total, the rotor is subjected to ten full revolutions. Convergence criteria are set at a residual of 1×10^{-6} for continuity, velocity in x and y directions, turbulent kinetic energy, and dissipation rate. The static torque, T, is calculated at the rotor center and along the normal to the plane. The torque generated is mainly due to pressure force, with a negligible contribution from shear force. The coefficient of torque, C_t, and coefficient of power, C_p, are given as follows:

$$C_t = \frac{4T}{\rho A_r U^2 D}, \quad C_p = \frac{2T\omega}{\rho A_r U^3} = C_t \times TSR \tag{8}$$

Here, $A_r = D \times H$ is the projected frontal area of the rotor.

5   Results and Discussion

In this section, the CFD results are discussed. Grid sensitivity study of the generated mesh and validation against experimental results of Sheldahl et al. [5] are discussed first. Further, the wake characteristics from the CFD simulations of Savonius VAWT rotor at static and dynamic conditions are compared with the predictions from the analytical wake models discussed in Sect. 3.

5.1   Grid Sensitivity Test

Steady-state simulation of the single Savonius rotor at 90° is done to study the grid sensitivity. The value of C_t at each grid refinement level (number of grid elements) is shown in Fig. 4. Figure 4 also shows the percentage change in C_t with each refinement, as denoted by the numbers below black arrows.

Figure 4 also shows the grid sensitivity rate, which is defined as the rate of change of measured value (here, C_t) with respect to the change in the number of grid elements. In Fig. 4, grid sensitivity rate is plotted in multiples of 10^{-7}. It is found that after
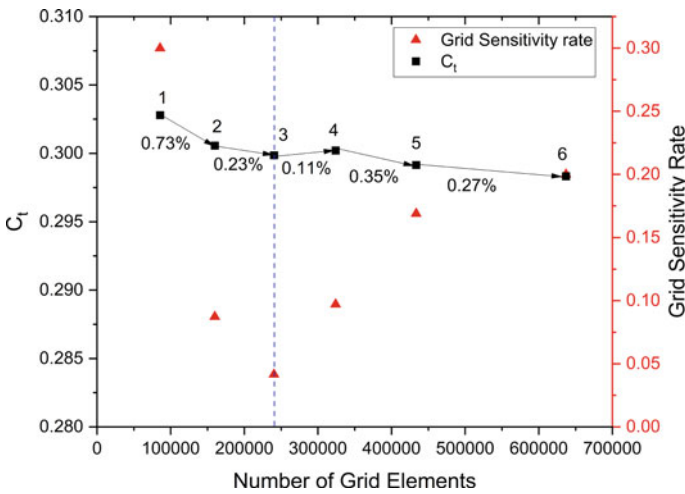
Fig. 4 Grid sensitivity analysis

refinement level corresponding to the vertical dashed line, the grid sensitivity rate is at its minimum. Hence, the number of grid elements at this refinement level (that is, 240,390) is seemed to be sufficient for further simulations.

5.2 Validation with Experimental Results

Simulation results of the Savonius rotor are compared with the experimental results of Sheldahl et al. [5]. As seen in Fig. 5, the coefficient of power C_p oscillates with the angular coordinate of the rotor. The average value of C_p, marked as a horizontal dashed line in Fig. 5, is calculated at each value of the TSR. These values are plotted in Fig. 6 at different values of TSR, showing a reasonable agreement with the experimental results [5]. The simulation results differ from the experimental data relatively by 6% on an average, with the minimum and maximum values of this relative difference being 1 and 14%. At low values of TSR, C_p increases with increase in TSR, reaching a maximum at around TSR $= 1.0$. Further increase in TSR beyond 1.0 leads to a decrease in C_p.
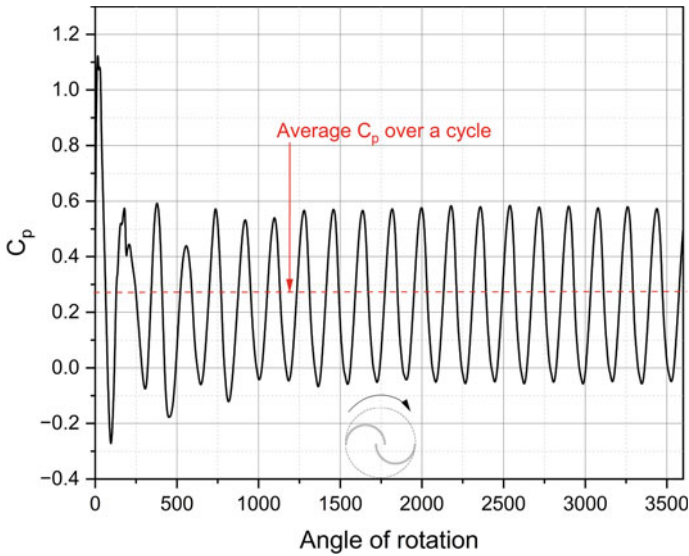
Fig. 5 C_p versus rotational angle; TSR $= 1$
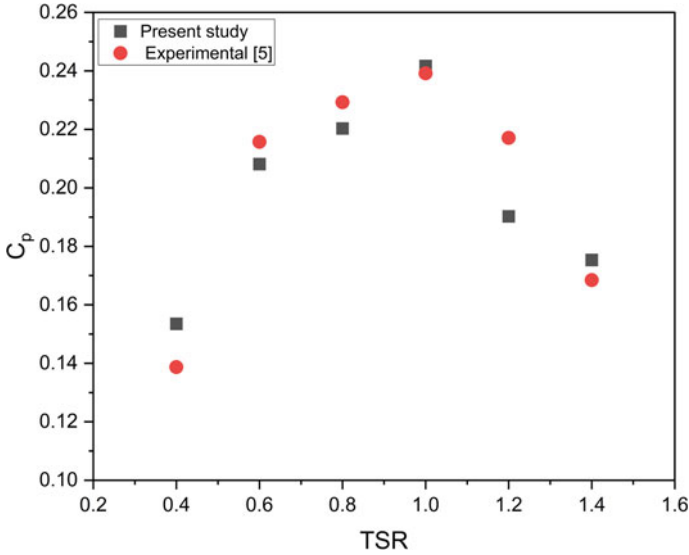
Fig. 6 Comparison of C_p at different values of TSR from the current CFD study with experiments [5]

5.3 Comparison with Wake Models: Static Rotor

First, the results corresponding to the rotor in a static configuration are discussed. A static configuration is specified using the corresponding angular position of buckets with respect to the fixed wind direction. At zero-degree position of the rotor, the velocity contours are shown in Fig. 7a. Savonius rotor has two buckets: one is an advancing bucket producing positive torque, and the other one is a returning bucket producing negative torque. The vertical lines at D, $2D$, $4D$, and $8D$, marked in Fig. 7a, correspond to typical locations along the x-direction downstream of the rotor. The velocity profiles along those lines, as well as the analytical wake model predictions of the same, are plotted in Fig. 7b. In each of the four panels in Fig. 7b, the horizontal axis represents the wake velocity and the vertical axis represents the distance from the center line of the rotor in Y-direction in terms of the rotor diameter. The above-mentioned details of the plots remain the same for all the subsequent velocity profile plots in this study. Wake width, shown by horizontal dashed lines in Fig. 7b, is taken as the wake diameter defined by Katic et al. [7]. At zero-degree static position, there is a very low velocity region just after the rotor up to $2D$ (see Fig. 7a). After this, the recovery of wake velocity starts, and at $4D$, the average wake velocity recovers by 80–85% of the freestream velocity. This wake recovery distance is less compared to that for HAWTs [19]. This enables a denser placement of the VAWTs as compared to the HAWTs. The wake width from both the CFD data and analytical wake models is in good agreement. However, the wake velocity deficit is more in CFD compared to the wake models. The flow patterns around advancing and returning buckets are

different, as shown in Fig. 8. Hence, the flow patterns at different static positions of the buckets (and, hence, the rotor) need to be investigated. The velocity vectors for different static angle positions are shown in Fig. 8. At 60° (Fig. 8a), the pattern of flow is dominated by dragging flow and overlap flow [20]. At 90° (Fig. 8b), vortex shedding from the advancing and returning blades occur, whereas in the static positions greater than 90°, the vortex separates from the tip of the advancing bucket.

In Fig. 9, the wake velocity profiles are shown for the rotor at the static position of 90°. Overall, similar trends, as seen in Fig. 7b, can be observed: (a) a higher velocity deficit in the wake in CFD compared with the predictions from the wake models and (b) regions with velocities higher than the freestream velocity are observed in CFD, whereas the wake models fail to capture these regions.

5.4   Comparison with Wake Models: Dynamic Rotor

The velocity contours are shown in Fig. 10a for the clockwise rotation of the rotor. The velocity contours highlight the wake region as well as a higher velocity region at the boundary of the near-wake. The time-averaged wake velocity profiles, over a complete rotor revolution, are plotted in Fig. 10b at the same downstream distances from the rotor as in Fig. 7a. Figure 10b clearly shows the asymmetry of the wake about the rotor axis; wake tends toward the returning bucket, and the higher velocity region tends toward the advancing bucket.

Near the rotor, the higher velocity region is at the edge of the wake and is more prominent on the advancing bucket side. On the returning bucket side, there is a region of less accelerated flow compared to that on the advancing bucket side, highlighted in blue. This shows a shift of the wake region toward the returning bucket side and accelerated flow on the advancing bucket side. A similar study done for the case of anticlockwise rotation showed that the wake shifts toward the upper returning bucket and the higher velocity region shifts toward the lower advancing bucket side. This reconfirms the existence of wake asymmetry as well as the location of high velocity regions outside the wake at rotating conditions. It can be concluded that the optimal placement of the downstream rotor should be on the advancing side of the upstream rotor and just outside the near-wake region, in order to extract energy from the high velocity regions. This leads to a possibility of the overall cluster performance enhancement.
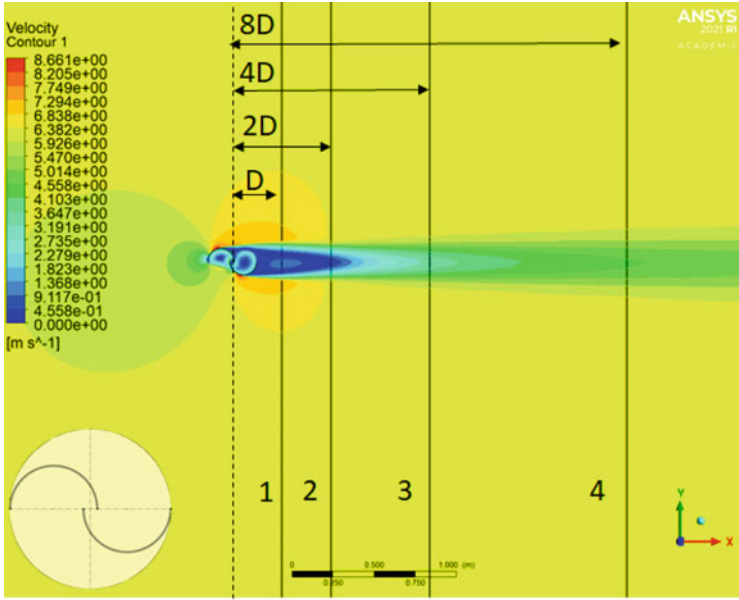
(a)
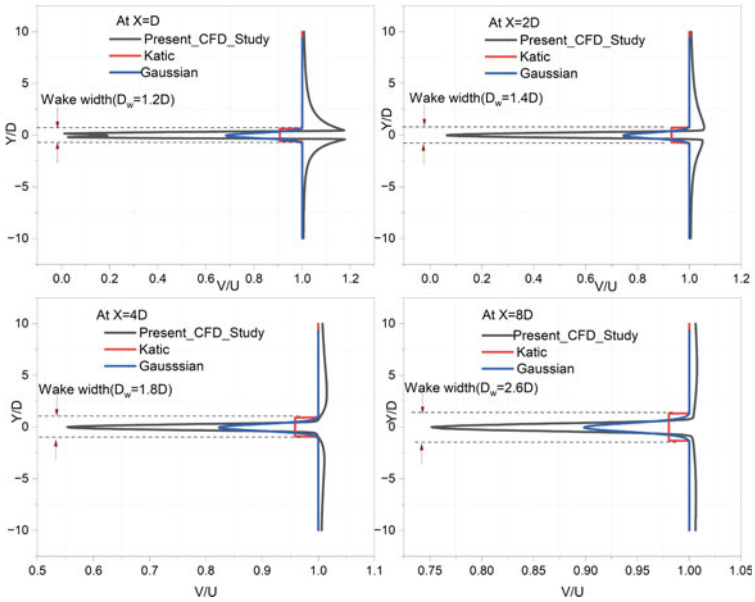
(b)

Fig. 7 Rotor at a static angle of 0°. **a** Velocity contours and **b** velocity profiles along the different positions in the wake region
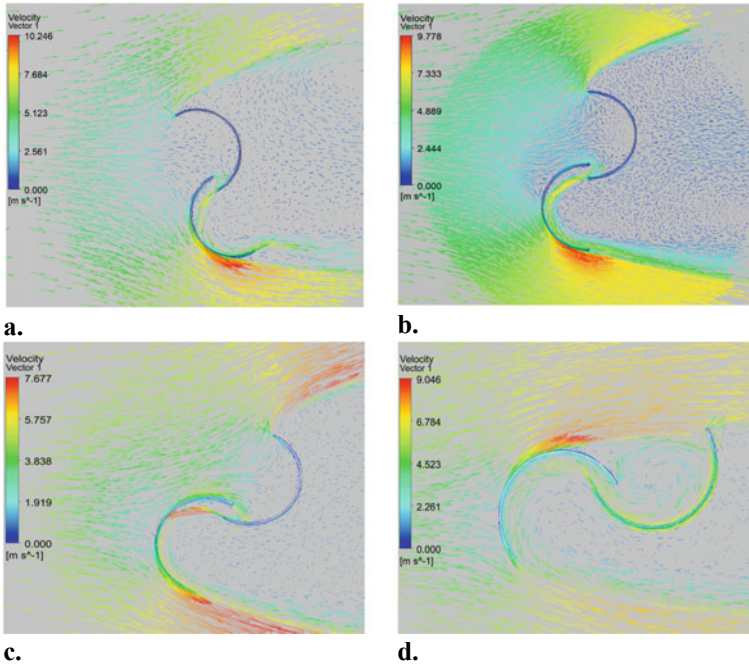
Fig. 8 Velocity vectors at different static angle positions of rotor: **a** 60° **b** 90° **c** 120° **d** 150°

6   Conclusions

A detailed CFD study of the static and dynamic Savonius rotor was done. The velocity profiles of the wake region were compared with the different analytical wake models. Following are the key findings from this study:

(1)   Wake models work well in predicting wake width but not good in predicting the wake velocity deficit.
(2)   The wake velocity deficit from the CFD studies is much higher than that predicted by the wake models.
(3)   When the VAWT is rotating, the wake region is asymmetric toward the returning bucket.
(4)   At the edge of wake, there is higher velocity region, which could be extracted by placing the downstream rotors.
(5)   A new wake model is needed for VAWTs with the following highlights: considers the wake asymmetry, is capable of predicting the higher wake velocity deficit, and can capture the high velocity regions outside the wake.
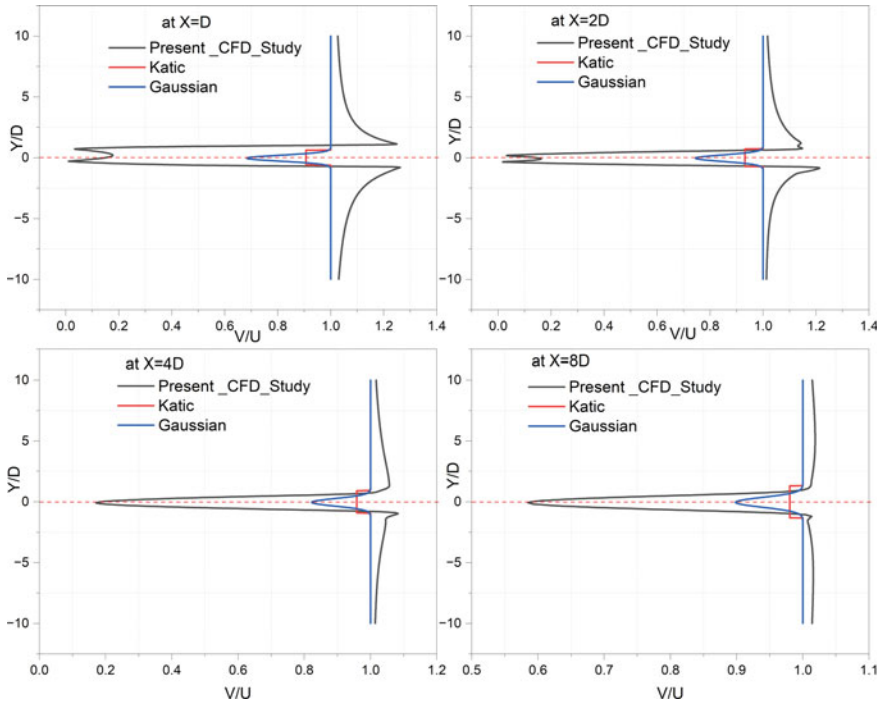
Fig. 9 Velocity profiles at 90° static position of rotor

These results will guide in the optimization of S-VAWT clusters through a reduced-order modeling approach. Savonius rotor has a low aerodynamic performance compared to Darrieus type VAWTs and HAWTs; but by employing Savonius rotors in a cluster, there is a potential to increase the average cluster performance.
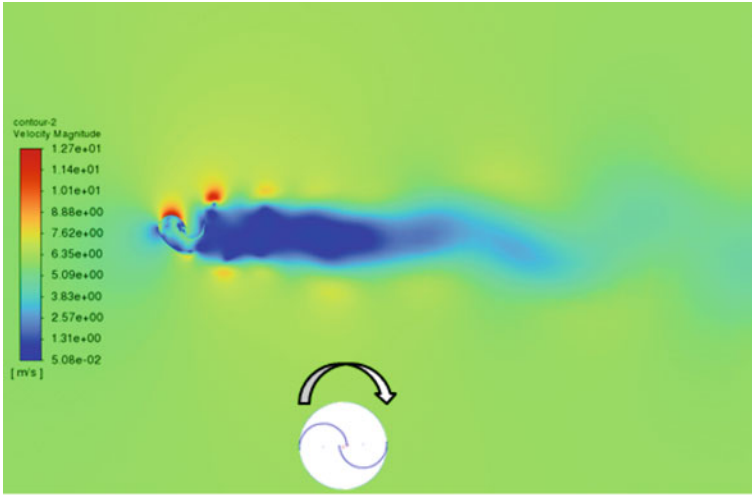
(a)
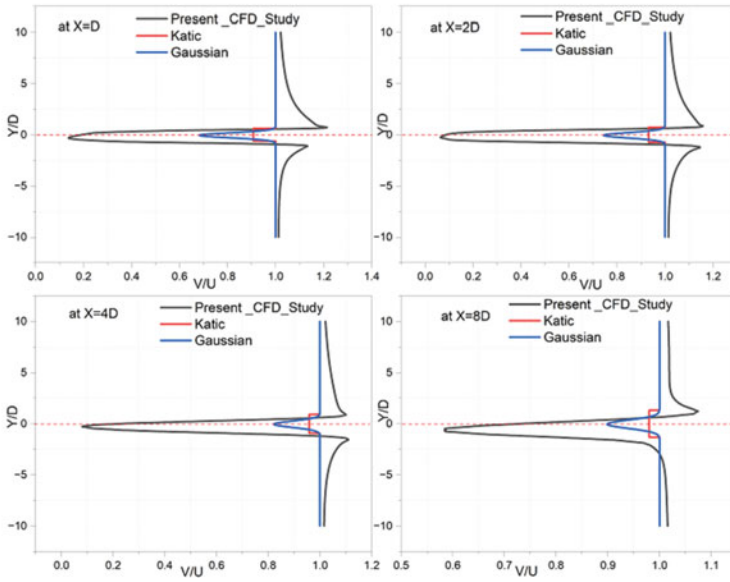
(b)

Fig. 10 **a** Velocity contours and **b** velocity profiles for the rotating Savonius rotor. TSR = 1.0, clockwise rotation

References

1. Cozzi L, Gould T (2021) World energy outlook 2021, pp 1–386. Available online: www.iea.org/weo
2. Mathew S (2006) Wind energy: Fundamentals, resource analysis and economics
3. Aliferis AD, Jessen MS, Bracchi T, Hearst RJ (2019) Performance and wake of a Savonius vertical-axis wind turbine under different incoming conditions. Wind Energy 22(9):1260–1273
4. Fujisawa N (1992) On the torque mechanism of Savonius rotors. J Wind Eng Ind Aerodyn 40(3):277–292
5. Sheldahl RE, Blackwell BF, Feltz LV (1978) Wind tunnel performance data for two- and three-bucket Savonius rotors. J Energy 2(3):160–164
6. Göçmen T, Van Der Laan P, Réthoré PE, Diaz AP, Larsen GC, Ott S (2016) Wind turbine wake models developed at the technical university of Denmark: a review. Renew Sustain Energy Rev 60:752–769
7. Katic I, Højstrup J, Jensen NO (1987) A simple model for cluster efficiency. In: Palz W, Sesto E (eds) EWEC'86 Proceedings, vol 1. pp 407–410
8. Barthelmie RJ et al (2006) Comparison of wake model simulations with offshore wind turbine wake profiles measured by sodar. J Atmos Ocean Technol 23(7):888–901
9. Frandsen S et al (2006) Analytical modelling of wind speed deficit in large offshore wind farms. Wind Energy 9(1–2):39–53
10. Bastankhah M, Porté-Agel F (2014) A new analytical model for wind-turbine wakes. Renew Energy 70:116123
11. Ishihara T, Qian GW (2018) A new Gaussian-based analytical wake model for wind turbines considering ambient turbulence intensities and thrust coefficient effects. J Wind Eng Ind Aerodyn 177:275–292
12. ANSYS Inc, ANSYS Fluent Tutorial Guide 17 (2017)
13. Barnes A, Hughes B (2019) Determining the impact of VAWT farm configurations on power output. Renew Energy 143:1111–1120
14. Zhou T, Rempfer D (2013) Numerical study of detailed flow field and performance of Savonius wind turbines. Renew Energy 51:373–381
15. Rezaeiha A, Montazeri H, Blocken B (2019) On the accuracy of turbulence models for CFD simulations of vertical axis wind turbines. Energy 180:838–857
16. Mishra N, Gupta AS, Dawar J, Kumar A, Mitra S (2018) Numerical and experimental study on performance enhancement of Darrieus vertical axis wind turbine with wingtip devices. J Energy Resour Technol 140(12):121201(1–7)
17. Laws P, Saini JS, Kumar A, Mitra S (2020) Improvement in Savonius wind turbines efficiency by modification of blade designs—a numerical study. J Energy Resour Technol 142(6):061303(1–12)
18. Bethi RV, Mitra S, Kumar P (2021) An OpenFOAM based study of Savonius turbine arrays in tunnels for power maximisation. Renew Energy 179:1345–1359
19. Kinzel M, Mulligan Q, Dabiri JO (2012) Energy exchange in an array of vertical-axis wind turbines. J Turbul 13(6):1–13
20. Nakajima M, IiO S, Ikeda T (2008) Performance of Savonius rotor for environmentally friendly hydraulic turbine. J Fluid Sci Technol 3(3):420–429

Floating Solar PV Systems—Global Research Reported in the Year 2022

C. J. Ramanan, Sukanta Roy, Ke San Yam, King Hann Lim, Bhaskor Jyoti Bora, and Bhaskar Jyoti Medhi

Abstract The world is witnessing the transformation of countries toward the adoption of renewable sources for power generation. Power generation through solar photovoltaic is at the top preference due to its proven advantages. Among the various technology in solar PV, floating solar photovoltaic is emerging in the past decade as it shows higher performance than ground-mounted PV system, reduces CO_2 emission, saves land, and saves water from evaporation. In this view, the research that has been conducted across the world in the year 2022 and reported in various publications has been discussed in this article. The review presents the reported software used for the geographical and meteorological data collection, performance analysis, thermal analysis, FSPV in hydro-reservoirs, environmental effects, and FSPV in marine condition are discussed. Based on the investigation, it is proved that the floating solar photovoltaic is a robust source of energy that has a huge demand in the global market as it can replace the non-renewable sources for power generation.

Keywords Floating solar photovoltaics · Renewable energy · 2022 review · Global analysis · Green energy

C. J. Ramanan (✉) · S. Roy · K. S. Yam · K. H. Lim
Faculty of Engineering and Science, Curtin University, 98009 Miri, Sarawak, Malaysia
e-mail: hseramanan@gmail.com

S. Roy
National Institute of Technology Mizoram, Chaltlang, Aizawl, Mizoram 796012, India

B. J. Bora
Energy Institute, Centre of Rajiv Gandhi Institute of Petroleum Technology, Bengaluru 562157, Karnataka, India

B. J. Medhi
Assam Energy Institute, Centre of Rajiv Gandhi Institute of Petroleum Technology, Sivasagar 785697, Assam, India

1   Introduction

In the growing trend for the utilization of the abundant solar energy, technological advancement of different solar energy conversion devices resulted in the invention of various methods and models [1]. One among them is the floating solar photovoltaics (FSPV) or floatovoltaics that is placing the PV panels over the surface of water for electricity generation. Generally, the pontoons/floats, mooring, water proofing, and the buoyance force are the important terms that make up an FSPV system [2]. The main advantages of a FSPV systems are performance increase due to cooling effect provided by the water beneath it, and it reduces the water evaporation, decreases the use of land thereby saves cost, less effort for installation, can be mobilized easily, and less shading/soiling compared to ground-mounted system [2–5]. The carbon emission is zero during power generation and emits in a negligible amount in its entire life cycle. In the below sub-sections, an introduction has been provided on the evolution and performance analysis of FSPV systems.

1.1   Evolution

"Jacona" powership was the first floating power generating plant with the water base [6, 7]. The origin of the floating solar PV systems takes us to the US patent filed in the year 1980 that uses the same concept of floating solar technique but for the generation of steam [8]. In the year 1982, the Japanese patent entitled "Floated on water surface solar-ray power generation apparatus" assigned by Mitsui Engineering and Shipbuilding Co. Ltd., Mitsui Zosen KK, is presumed to be the commencement of FSPV systems [9]. In the year 2007, the 20 kW solar plant installed at Aichi of Japan is the world's 1st floating solar PV system [10]. In 2008, USA installed a 175 kW FSPV in California, which is the 1st commercial-scale installed FSPV [11]. Following it, the performance analysis of the FSPV in water has been presented in the 2008 European Solar PV conference [12]. Eventually, an Italian patent filed in the same year stating the efficiency increase by immersing the solar panel is alleged to be the pioneer concept for the usage of solar panel in water [13]. South Korea and Japan installed FSPV in Mega Watt scale in the year 2013 [11]. Diplomatically, the emergence of the FSPV systems in the market of the following decade can be confirmed by the various patents filed across the globe [14, 15]. The growth of FSPV can be witnessed by its expansion from 100 MW in 2016 to more than 3 GW in 2021 [16]. To say more, the power generated by the fossil fuel plants can be satisfied by the installation of FSPV in a 10% of the world's hydropower reservoirs and will lead to electricity decarbonization by 2050 [17].

1.2 Performance Analysis

Approximately, FSPV shows 12% higher performance than a rooftop or a ground-mounted system [18]. For a summary about the performance of FSPV, the authors would like to present the research conducted by the Nisar et al. [19] in NUST, Pakistan. Two 80W solar PV panels in monocrystalline and polycrystalline each for a ground-mounted and floating system was used for the test condition [19]. Floating solar PV (FSPV) system was set up in an artificial pond. These 3-day experimental research completely used individual sensors to detect the performance and stored the real-time data in using specified components [19]. Optimal angle is 30 °C for the selected location. In tilted position, the temperature was observed to be low at the bottom and for flat position, and it is uniform distributed [19]. The reduction in evaporation is 17% for partially covered and 28% for full coverage [19]. The temperature reduction range at the front side of the FSPV was 2 to 4°C and at the back side was 5–11 °C. FSPV power production was 27% to 35% higher than a ground-mounted solar PV at flat position and 8% higher for a tilt of 30º [19]. Also a 32,600 kWp FSPV engineering project at Taiwan reported in the "Energy Reports" by Chiang and Young [20] gives the readers a complete installation and assessments in detail.

The world is covered with 70% of water bodies with a large area of ocean. It could be a vital source for the establishment of FSPV plants for electricity generation, and this attracts the countries across the world. The leading nations are already distributing electricity produced by FSPV, some are in the early stage and others in research stage. In this view, the objective of this study is to analyze and present the global status of FSPV reported in various articles in the year 2022.

2 Global Analysis

In this section, various research that have been conducted and published in research articles especially in the year 2022 are discussed on regional-wise. Following it, a discussion has been made based on the study of FSPV technology.

2.1 Asia

There has been many research conducted on the feasibility of FSPV in various Indian conditions. It is reported that using FSPV 280 GW of power can be generated in the 18,000 km^2 of available water reservoirs in India [21, 22]. The comparative analysis for the on-grid FSPV and on-grid PV systems based on the location Bhilai steel plant of Chhattisgarh, India, used HOMER Pro software for system architecture found that FSPV as the most feasible system [21]. Using HelioScope software, the electrical

performance of FSPV was investigated for 20 various hydroelectric reservoirs plants across different states of India [23]. It resulted that in common, a tilt angle of 10–20° is found to be the enhanced angle [23]. Also by covering the water surface of 0.9 km^2 with FSVP in these 20 reservoirs, it can save 1.40 cubic meter of water per day [23]. In a specific case for a Metur dam in Tamil Nadu, India, a tilt angle of 10° was found to be suitable and the cover with FSPV saved 1,84,589 cubic meters of water. It also calculated the efficient system to be flat-mounted FSVP owing to the high cost associated with the tracking integrated FSPV system [24]. The research for the possibilities of FSPV in Koyana dam of Maharashtra, India, using PVsyst and PVwatt calculator tool resulted in 4.08% more energy production than a ground-mounted PV system [25]. The research also said that dual-axis tracking FSPV yields higher, but the author did not analyze the cost comparison between the different FSPV models. Similar successful result has been simulated using PVsyst and MATLAB/Simulink for the potential analysis of FSPV in Rajghat dam in Uttar Pradesh India and Chilika lake in Odisha [26, 27]. After complete analysis, Mamatha and Kulkarni [28] state that less than a 4% coverage on the existing Indian reservoirs would double the power production. Bangladesh which is located to the northeastern border of India has set a target of achieving 6000 MW of solar PV electricity generation in Bangladesh by the year 2041 [29]. FSPV will play an important role in its achievement. There has been a report for the Chalan Beel wetland of Bangladesh [30]. The experimental analysis said that in overall the FSPV is cost-efficient compared to a ground-mounted PV system [30]. Sri Lanka too have already installed FSPV by the company named "Current Solar" at the Kilinochchi [31]. It was examined for a year, and the author appreciated the performance and reliability but stated the yield was only 0.6% higher than ground-mounted PV system [31]. Also it stated that the drought or dried lake does not affect the performance of the performance of the FSPV [31]. In an study in Indonesia, using Earth Observatory System (EOS) software the area covered by water hyacinth at Cirata reservoir was calculated and suggested to replace it with FSPV or any other water-based renewable energy systems [32]. The preliminary assessment in Philippines reported a massive potential for the supply of electricity to a fisherman community people by installing the FSPV in the Mainit lake [33]. Peters et al. [34] conducted experimental research to analyze the thermal performance of a FSPV compared to a roof top solar PV nearby in a remote location of Cambodia. It resulted in an inversion, where the temperature of FSPV was about 9 K higher at noon than the roof toped one [34]. This is because of the flow of wind for the FSPV was affected due to the obstacle like grass, rocks, tilted PV panel at the edges, and the low attitude of the water body than the land surface, whereas on the other hand the placement of solar PV in roof top is at high attitude in an open surrounding leading to high heat dissipation by the force of wind. Similar result exhibiting a high cooling for the ground-mounted system than a FSPV was also reported by Kjeldstad et al. [31] in an experimental research at Sri Lanka. The experimental results generated by a 2 MW FPV system in the Mudasarlova reservoir of Vishakhapatnam of India were compared with their simulation results generated by the PVsyst, HelioScope, and the System Advisory Model (SAM) [35]. The error metric approach revealed that these software are not capable of predicting the FSPV performance as they do not meet

the experimental results [35]. Similarly in another case, the results generated by of SAM were found to be with a mean absolute percentage error of 15% in the case of Hapcheon dam of South Korea [36]. Although many FSPV investigations reported in India, it is already producing and commenced to produce more than 1.7 GW of electricity using FSPV [11]. Similarly Singapore powers five of its water treatment with the aid of 60 MW FSPV [16]. In 2021, the world's largest 320 MW FSPV was installed in China [16]. Though European Union produces power using renewable energy higher than China, in the FSPV technology, China is the leader [37].

2.2 Europe

Tina et al. [38] conducted research on 2 places of Europe—Frankfurt, DE, and Catania, IT, considering high and intermediate latitudes, respectively. The author reported that bifacial panels perform 13.5% higher that monofacial panels for a FSPV owing to albedo on the back surface of the bifacial panel [38, 39]. Similar study for the effect of albedo on FSPV based on North Sea reported that a dynamic albedo due to sea wave performs more than a constant one [40]. Tina et al. [38] also suggested that on comparison PVsyst simulation software for solar PV is better than SAM software. With the positive results for the analysis of electricity production from renewable energies such as solar PV, biomass, and wind, Osorio-Aravena et al. [41] suggested that the implementation of FSPV and agrivoltaic will generate an additional income for the farmers of Jaén at Spain. Moreover, by laying FSPV over the 10% water surface of Spain, it can fulfill 31% of its electricity demand by eliminating 81% non-renewable electricity source [42]. FPV system for the regions Anapo dam, Italy, and Aar dam, Germany, has been analyzed using PVsyst software. Results indicated that for the combination of natural cooling, tracking, and bifaciality, the maximum gain is 47.4% and 42.5% in a dual-axis system [43]. Eyring and Kittner [44] developed an algorithm for FSPV site selection based on meteorological data for alpine regions. Demonstrating the potential of FSPV in the alpine region of Switzerland, the author also mapped the worldwide alpine regions capable of harvesting FSPV power generation [44]. Unlike the other European nations, it is found that FSPV does not suit for Poland condition assessed in the PVsyst owing to the use of the commercially available modules in the market having poor tilt angle [45]. Popa et al. [46] conducted research using the tool PVsyst software and Global Solar Atlas for potential of FSPV in the Lacul Morii reservoir of Bucharest, Romania, and then stated that this type of cleaner energy production in Romania is the 1st to be conducted, and it can be an example for all other European cities. The target set by the Portugal to install 500 MW FSPV plant by the year 2022 is in good progress, and it is the largest FSPV plant in the Europe [16, 47]. Similarly, FSPV occupies a space in the 150 MW solar PV project in Spain [16]. Also it could save a minimum of 450 mcm from 9380 mcm being evaporated every year [48]. Investigation revealed that by installing FSPV covering 2.3% area of the European Union's reservoirs can generate 42.31 TWh of energy where overall EU's net production is 2664 TWh (2020) [49].

Apart from the technical and economic feasibility of FSPV, the case study in Oost-voornse lake of Netherland highlighted the importance of the moral and humanitarian values [50]. The lake having installed with a pilot-scale FSPV plant in the year 2020 was analyzed in the view point of societal value, threats, opportunity, deficiencies, role players, socioeconomical, ecological, cultural, and landscape impact [50]. It is observed that recreationist welcomes the project, while the stakeholders and local community oppose it [50].

2.3   Middle East

Abu Dhabi installed the first 80 kW FSPV in the gulf countries [51]. The feasibility of FSPV for Iran in the Caspian Sea was studied using MATLAB/Simulink and RETScreen programs [52]. And on the optimistic results, the author suggested for the implementation of policy to promote solar PV in Iran [52]. In another study using PVsyst and RETScreen, the author found that by covering 0.3% of a reservoir by FSPV, it can save a minimum of 441 thousand cubic meter of water evaporated in the lake of Zabon, Iran [53]. Research from the Technical Engineering College of Iraq obtained an increase in the efficiency by integrating the FSPV with solar pond combined to produce heat and electricity [54]. The installation of FSPV for the location Aden of Ymen using PVsyst resulted in a high performance [55]. Based on the environmental, technical, and accessibility criteria using fuzzy AHP technique and GIS software, Koca et al. [56] suggest Beyşehir lake is highly suitable for FPV in Turkey. For Büyükçekmece lake of Turkey, it suggested for a strong wave resistance design for FSPV system to balance the unique harsh wave and wind environment in this type of lake [57]. There has been a report in finding the optimal location for FSPV in Demirköprü dam of Turkey. The author used satellite images and found that among the 3000 ha surface area of dam, 88.5% of the area has the high irradiation value at a particular location for long duration [58]. This gives the researchers an option to identify the proper region on the reservoir for FSVP. In Israel, Vaschetti et al. [59] replaced the floating cover of the Hefer reservoir with FSPV and generated 230 kW peak output with 616 panels tilted at 5° avoiding evaporation. For a farm irrigation reservoir located at the Mafraq governate in Jordan, the analysis for the FSPV using HOMER Pro software has been conducted [60]. In this case, a 300 kW power large footprint FSPV tilted at an angle of 15° with a 200 kW inverter is found to be the most suitable system than any other advanced FSPV systems owing to cost efficiency [60]. In another instance, on comparing FSPV and a ground-mounted system using SAM software, ground-mounted system performed well than FSPV in the Ma'an region of Jordan [61]. The author feels that it is due to the tilt angle where it was 30° for ground mounted and 10° for FSPV.

2.4 African Nations

The potential of FSPV in Africa is investigated accounting to its 146 hydropower reservoirs [62]. Just by laying FSPV in less than 1% area of the reservoirs, the energy generated by the hydropower can be doubled and can save 753 million cubic meter of water per year [62]. FSPV can preserve the water body and can control 80% of the water evaporation in Nqweba dam in South Africa [63]. FSPV is a potential source for electricity generation in Nigeria that avoids land acquisition and technically profits the Nigerian power grid [39]. Another study reveals high irradiance, ambient temperature, and the wind flow makes FSPV as a high potential for electricity generation in the Great Ethiopian Renaissance dam [64].

2.5 American Region

NREL reported that the growth of FSPV in USA is slow due to the availability of land and lack of incentives for the installation of FSPV systems. FSPV installed and planned in California and New Jersey is 6.4 MW and 4.4 MW capacity, and developers have targeted to cross more than 10 MW FSPV system by 2023 [65, 66]. There were several reports published on Brazil which is located in South America. Brazil can generate 12% of its electricity that is consumed by 16.5% of its population by installing FSPV in 1% of its total artificial water bodies (45,502 km^2) [67]. A high potential for the electricity generation through FSPV for the Tocantins-Araguaia basin of Brazil was calculated theoretically using SunData tool [68]. The installation of FSPV in the Passaúna river of Brazil can save 60% of evaporated water which is 2.69 cubic hectometer of water from 4.47 cubic hectometer of water evaporation per year [69]. Also, the author mentioned the effective method for the calculation of evaporation rate as FAO Penman–Monteith method and for evaporation reduction by FSPV as the Assouline, Narkis, and Or method [69]. In the post-COVID-19 pandemic situation, the new policies adopted by Brazil pave a robust growth for FSPV systems in the country [17].

2.6 Other Countries

The assessment for the potential of FSPV in the irrigation reservoirs of Albania suggested to consider the hydro-meteorological and geophysical parameters and also to encounter the shortcomings [70]. An experimental research for the novel partially submerged FSPV in Port Said, Egypt, stated that on a calm water, at an optimal submerge ratio of 12%, compared to the land-based PV system, the temperature difference was found to be 12 °C, and it showed 23.7% increased power generation [71]. Extending to it on the examination of thermal-electrical relationship of a

partially submerged FSPV, 10% submerge ratio for tilt angle of 15° was found to be suitable in case of Port Said, Egypt [72]. Also polycrystalline FSPV seems to be more suitable Egyptian location [73]. The size of the solar PV arrays installed in any area is directly related to the production capacity. In this view, Reges et al. [74] propose a methodology for optimizing size of a FSPV with respect to the area of the reservoir on the basis of reliability which is the flood existing over a period of time in the reservoir. The case study was analyzed in Brazil and Australia as the semi-arid places will not have hydroelectric plants [74]. Also, this methodology is easy and simple but requires historical data of dam especially the times gone by flood.

3 Thermal Analysis

Recent analysis in the Huainan City of China noticed that there was an increase in land surface temperature by 1.24 °C for a radius of 200 m of the floating solar park [75]. After the review on the thermal aspects of FSPV, Michile [76] revealed that though if the temperature of water is higher than the ambient temperature, cooling occurs due to the high U value of the water-cooled FSPV modules. In some case, the design parameter such as FSPV structure exposure, size, obstacles in the wind path, and the wind speed influences the thermal performance [76]. Cooling effect of the FSVP is effective only at high temperature where in a study, 37 °C showed increased performance followed by 24 °C and no performance effect for 6 and 16 °C [77]. Impact of thermal variation in the reservoir's water due to the overlaying of FSPV on the water surface had been explored in the hydropower station of Xiangjiaba, China [78]. Interestingly apart from increased power generation, CO_2 reduction, and water resource conservation, it states that the effect of FSPV on the water temperature is spatial, and for Xiangjiaba condition, it increases the rate of spawning of fish in winter and autumn weather conditions [78].

4 Environmental Effects

The water quality change due to the FSPV in aquaculture ponds of Taiwan Fisheries Research Institute was examined by experimentation [79]. FSPV creates shading in the water body, and this lowers the temperature, pH, planktons, biochemical oxygen demand, and the dissolved oxygen [79]. Though reduction, the aerator provided enough dissolved oxygen and nutrients [79]. Analogous investigation was also successful in increasing the dissolved oxygen from 3.2 to 4.4 mg/L with an aerator powered by FSPV [80]. The use of FSPV exhibited high oxidation–reduction potential that favors nitrification. This in overall favors the growth of the cultured species, and the production was 1.1 to 1.4 higher than an uncovered one [79]. These reports can be validated with the Andini et al. [81] which stated a decrease in the temperature, dissolved oxygen, pH, conductivity, chlorophyll, and total dissolved

solids in the Mahoni lake of Indonesia covered with FSPV and suggested for aeration to overcome the shortcomings to balance the marine ecosystem. Also the case study over the FSPV plant in Büyükçekmece lake, Turkey, stated no harm to the ecological balance in its surrounding [57].

5 FSPV in Ocean

There has been a discussion that FPV interrupts the ecosystems especially in the small water bodies and to advance the installation of FPV technology in ocean where China has already started its trials [82, 83]. The installation of FSPV in the marine region has to endure corrosion, extreme marine load (wave, wind, and current), strong mooring, mechanical degradation, microplastic pollution, and salt accumulation. Kiener et al. [84] used EnergyPLAN tool and estimated that Maldives can generate and meet 100% of its energy demand by 2030 with the aid of FSPV and wave power in ocean. Hong and Alano et al. [85] successfully developed an Energy Management System to sort out the challenges faced to interconnect the FSPV microgrid networks. Technically advanced integrated system was proposed by Temiz et al. [86] for the benefits of island regions with FSPV and CSP systems as base and states that FSPV will save land. This study was based on Northern Cyprus where he highlights the complexity involved in the system including economic aspect and addressed the corrosion problem in the ocean for technological development of FSPV in sea base [86]. In the emergence of FSPV for marine environment, Claus et al. [87] analyze and suggest the suitable structure to be a pontoon type available in the market. The author proposes the use of high-density polyethylene (HDPE), fiber reinforced plastic (FRP), antifouling coating, traditional anchoring systems, and overcoated and highly encapsulated rigid PV modules for successful installation. The same materials were suggested by Zhang et al. [88] for the ocean environment. Also the author adds that this type of a FSPV system can be more competent for an hybrid system with offshore wind turbines [87]. Twin hull double-circular cylinder FSPV platform was also analyzed as a platform for the FSPV [89]. The author performed the numerical model in FORTAN, and the validation with experimental results is successful but both indicated the platform to be a unstable model for FSPV [89]. The hydrodynamics analysis for pontoon-structured FSPV considering the nearshore regions of Singapore was analyzed based on empirical, two-step, and hydro-elastic or generalized mode methods with the support of offshore simulations software OrcaFlex and WAMIT [88]. All these three methods resulted nearly same values for long waves but exhibited a huge differences for short waves [88]. Moreover, due to non-availability of experimental data, the results are not validated [88]. Also the author stated the column stabilized type of FSPV to be the robust model to withstand the ocean waves [88]. In another study for Maldives using HelioScope software, the author used a thin-film PV module stating that it has good water resistance and avoids algal growth [90]. The author stated that at harsh condition, a pontoon-based structure is not recommended [90]. Here, the thin-film-based floating solar PV performance was higher than a conventional FSPV and a

ground-mounted system [90]. The simulation of wave interaction with floating array for a FSPV using Fluid Structure Interaction (FSI) method in COMSOL Multiphysics gave similar results with the experimental data [91]. This can be applicable in the future for the installation of FSPV in ocean region. Also in a conference at China, CFD analysis for the strength of the FSPV structure support was performed in another research [92].

6 Discussion

Based on the above analysis, the authors would like to put forward the following discussions.

- The role of wind in the performance of the FSPV has a greater impact [31, 34]. Peters et al. [34] point out the variation in the wind speed at surface level of the FSPV from a global whether report tool. Hence, it is preferred to measure the wind speed at the surface level of the FSPV using physical instrument.
- For high energy yield, FSPV with a tracking system performs well. But on economical aspect, a flat-mounted FSPV system with an appropriate fixed tilt angle for the particular location is better than it. In this regard, the technological development in the areas of tracking system needs to be developed for more economic feasibility.
- FSPV in the water bodies of urban area is not preferable as it is affected by high soiling which leads to additional cleaning cost. And the decrease in the solar irradiation due to high humidity increases DC loss [93].
- Installation of FSPV is not suggested for remote locations, very cold region, high wind and disaster facing region, natural/recreational water body, soft ground mud, and water body with protected species or dedicated for birds [4].
- Minor loss in the performance is observed due to the change in the water level of a FSPV installed reservoir [94].
- In addition to the elimination of CO_2 emission, it is also found that the emission of NOx, SOx and SPM was also reduced by the use of FSPV [53].
- The fluctuating water level will change the surface area of a reservoir. Therefore with the help of satellite images and adjusting the Hue-Saturation Value (HSV), the maximum surface area of water that remains for a long duration and appropriate location to float FSPV can be spotted [58]. Also, it is noted that tilt angle plays an important role.
- In addition to the global installation of FSPV, technological advancement like thin-film floating solar PV will have an global impact in upcoming years [5, 90].
- Though the negative effect of the FSPV are not identified, there are some predictions and detections which are change in the oxygen level, increase in the surrounding ground temperature, and change in water taste and odor [4]. Literatures reported that FSVP did not affect the aquatic living organisms and promotes the fisheries.

- Zahid et al. [95] analyzed the installation of FSPV in the Tarbela hydropower plant of Pakistan. Analogous research was conducted in Mazar dam of Ecuador [96]. In both the cases, the low power generation due to the seasonal and water flow variation of reservoir was successfully supplied by the FSPV. This system can be added to the existing hydropower reservoirs without interfering its operation [97]. In such a system, the hydropower reservoirs can act as a battery, where during deficiency in the production by FSPV, hydropower can be utilized to meet the demand [97]. Adaption of this hybrid system would be suitable to all the region of the world. Integrating solar PV, agrivoltaic and floatovoltaics can be more beneficial [98].
- FSPV technology involves the use of water body as platform which is a primary need of human being. The research of the kind investigated by Bax et al. [50] creates a harmony between the government and the people to avoid conflicts. In case of illiteracy, awareness can be created to the communities. And on the other hand, actions can be taken to the fair impacts put forward by the community.
- Literatures reported the use of Global Solar Atlas, Google Earth, Earth Observatory System (EOS), GIS Software, SunData and PVsyst, HOMER Pro, HelioScope, SAM software, PVwatt, FORTAN, MATLAB/Simulink, RETScreen, etc. for data collection and simulation where PVsyst and GIS are used by maximum researches. Though the simulation results were successfully executed, it lacks in validation with the experimental research.

7 Conclusion

Renewable energies such as bio-, wind, and solar energies are the promising alternative source to replace the fossil fuel power generation that has a lot benefits [99–102]. Especially floating solar PV has a wide range of applications with proven robust energy production that can satisfy the target of affordable and green energy, sustainability, and climate actions set by the UN [11, 103–128]. In this regard, this article has investigated and successfully reported the status of floating solar photovoltaic published in various article in the recent years of 2022. The various software used for the geographical and meteorological data collection, performance analysis, thermal analysis, FSPV in hydroreservoirs, environmental effects, and FSPV in marine condition are discussed. Based on the discussion, it can be concluded that floating solar PV has the potential to replace the fossil fuel for power generation. This will then lead to reduction in the import of fossil fuel to form a sustainable and self-sufficient nations.

References

1. Darwish AA, Abdelmohsen RS, Ahmed M, Megeed M (2022) Solar cells: types, modules, and applications–a review. Tanzania J Sci 48(1):124–133. https://doi.org/10.4314/tjs.v48i1.11
2. Essak L, Ghosh A (2022) Floating photovoltaics: a review. Clean Technol 4(3):752–769. https://doi.org/10.3390/cleantechnol4030046
3. Polo J (2022) Advances and challenges in solar PV system's performance. Energies 15(16):6080. https://doi.org/10.3390/en15166080
4. Cuce E, Cuce PM, Saboor S, Ghosh A, Sheikhnejad Y (2022) Floating PVs in terms of power generation, environmental aspects, market potential, and challenges. Sustain 14(5). https://doi.org/10.3390/su14052626
5. BelliniEmiliano (2022) Open-source method to build flexible floating PV systems. pv magaizne. https://www.pv-magazine.com/2020/11/09/open-source-method-to-build-flexible-floating-pv-systems/ (Accessed 27 Sep 2022)
6. Pamik M, Bayraktar M, Konur O, Nuran M (2022) A revelatory case study for the emergence of powerships: the floating power plant innovation for rural electrification. Trans Marit Sci 11(1):54–66. https://doi.org/10.7225/toms.v11.n01.w10
7. Button and Photograph Yourself Rubber—Tired Railroad Cars Power Ship "Jacona " Huge Floating Generating Station. Sci Invent 307
8. Testolini G (1982) Floating solar collector. United States Patent
9. Kikui K (1982) Floated on water surface solar-ray power generation apparatus. Japan Pat. JP57198990A Art no JP57198990A. Accessed 19 Sep 2022. [Online]. Available: https://patents.google.com/patent/JPS5989471A/en
10. Trace-software.com (2022) Floating PV plants: a promising future for solar energy. Trace Software, *Trace-software.com*, pp 1–8. Accessed: 19 Sep 2022. [Online]. Available: https://www.trace-software.com/blog/floating-pv-plants-a-promising-future-for-solar-energy/
11. Acharya M, Devraj M (2019) Floating solar photovoltaic (FSPV): a third pillar to solar PV sector ?. In: TERI Discussed Paper ETC India Project (New Delhi Energy Resour. Institute), pp 68. [Online]. Available: www.teriin.org
12. Ueda Y, Sakurai T, Tatebe S, Itoh A, Kurokawa K (2008) Performance analysis of PV systems on the water. In: 23rd European photovoltaic solar energy conference and exhibition, 2008, September, pp 2670–2673
13. Rosa-Clot M, Rosa-Clot P (2008) Support and method for increasing the efficiency of solar cells by immersion. Italy Pat. PI2008A000088 8
14. Mohanty JP (2016) Folating solar power plant. WIPO\PCT, vol. WO 2016/18
15. Chua C, Aditya S, Shen Z (2012) (12) Patent Application Publication (10) Pub . No .: US 2012 / 0286657 A1 Patent Application Publication. 1(19):10–13
16. Renewables 2022 Global Status Report (2022) REN21, vol. Paris. [Online]. Available: https://www.ren21.net/wp-content/uploads/2019/05/GSR2022_Fact_Sheet_Germany.pdf
17. Almeida RM et al (2022) Floating solar power could help fight climate change—let's get it right. Nature 606(7913):246–249. https://doi.org/10.1038/d41586-022-01525-1
18. Refaai MRA, Dhanesh L, Ganthia BP, Mohanty M, Subbiah R, Anbese EM (2022) Design and implementation of a floating PV model to analyse the power generation. Int J Photoenergy 2022. https://doi.org/10.1155/2022/3891881
19. Nisar H, Kashif Janjua A, Hafeez H, Shakir S, Shahzad N, Waqas A (2022) Thermal and electrical performance of solar floating PV system compared to on-ground PV system-an experimental investigation. Sol Energy 241:231–247. https://doi.org/10.1016/j.solener.2022.05.062
20. Chiang CH, Young CH (2022) An engineering project for a flood detention pond surface-type floating photovoltaic power generation system with an installed capacity of 32,600.88 kWp. Energy Rep 8:2219–2232. https://doi.org/10.1016/j.egyr.2022.01.156
21. Rizvi T, Dubey SP, Tripathi N, Makhija SP (2022) A comparative analysis of FSPV-grid and grid-only systems for an industrial subsection. In: 2022 2nd International conference advanced

electrical computing communication sustainable technology. ICAECT 2022. https://doi.org/10.1109/ICAECT54875.2022.9807931

22. Ravichandran N, Ravichandran N, Panneerselvam B (2022) Review on the structural components of floating photovoltaic covering systems. In: Smart innovation, systems and technologies, vol 265. Springer, Singapore, pp 125–133

23. Ravichandran N, Ravichandran N, Panneerselvam B (2022) Floating photovoltaic system for Indian artificial reservoirs—an effective approach to reduce evaporation and carbon emission. Int J Environ Sci Technol 19(8):7951–7968. https://doi.org/10.1007/s13762-021-03686-4

24. Ravichandran N, Ravichandran N, Panneerselvam B (2021) Performance analysis of a floating photovoltaic covering system in an Indian reservoir. Clean Energy 5(2):208–228. https://doi.org/10.1093/ce/zkab006

25. Patil A, Mamatha G, Kulkarni PS (2022) Techno-economic analysis of proposed 10 kWp floating solar plant at Koyana Dam, Maharashtra, India. In: 2022 2nd International conference power electronics IoT applications renewable energy its control. PARC 2022, pp 5–10. https://doi.org/10.1109/PARC52418.2022.9726247

26. Agrawal KK, Jha SK, Mittal RK, Vashishtha S (2022) Assessment of floating solar PV (FSPV) potential and water conservation: case study on Rajghat Dam in Uttar Pradesh, India. Energy Sustain Dev 66:287–295. https://doi.org/10.1016/j.esd.2021.12.007

27. Meena M, Sharma M, Singh M, Saha R (2022) Modeling of stand-alone Floatovoltaics to enhance energy security in Gurubai Village Near Chilika Lake in Odisha. In: 2022 International conference advanced technology, ICONAT 2022, pp 1–9. https://doi.org/10.1109/ICONAT53423.2022.9725955

28. Mamatha G, Kulkarni PS (2022) Assessment of floating solar photovoltaic potential in India's existing hydropower reservoirs. Energy Sustain Dev 69:64–76. https://doi.org/10.1016/j.esd.2022.05.011

29. Uddin MN, Biswas MM, Nuruddin S (2021) Techno-economic impacts of floating PV power generation for remote coastal regions. Sustain Energy Technol Assessments 51:101930. https://doi.org/10.1016/j.seta.2021.101930

30. Shatil AH, Saha S, Ahmed KF, Shahebul Hasan ANM, Imrat Rahman SM (2022) Design and comparison of floating solar panel for Chalan beel. In: 2022 International conference advanced electrical electronics engineering. ICAEEE 2022, pp 12–15. https://doi.org/10.1109/ICAEEE54957.2022.9836432

31. Kjeldstad T et al. (2022) The performance and amphibious operation potential of a new floating photovoltaic technology. Sol Energy 239:242–251. https://doi.org/10.1016/j.solener.2022.04.065

32. Sibuea RT, Pratna R, Hapsari A, Kristi YW (2022) Satellite remote sensing using earth observing system in environmental monitoring for hydropower and floating photovoltaic reservoir (Case Study: Algae Blooming on Cirata Reservoir, West Java-Indonesia). IOP Conf Ser Earth Environ Sci 1009(1):1–14. https://doi.org/10.1088/1755-1315/1009/1/012001

33. Dellosa J, Palconit EV (2022) Resource assessment of a floating solar photovoltaic (FSPV) system with artificial intelligence applications in Lake Mainit, Philippines. Eng Technol Appl Sci Res 12(2):8410–8415. https://doi.org/10.48084/etasr.4863

34. Peters IM, Nobre AM (2022) Deciphering the thermal behavior of floating photovoltaic installations. Sol Energy Adv 2:100007. https://doi.org/10.1016/j.seja.2021.100007

35. Manoj Kumar N, Chakraborty S, Kumar Yadav S, Singh J, Chopra SS (2022) Advancing simulation tools specific to floating solar photovoltaic systems—comparative analysis of field-measured and simulated energy performance. Sustain Energy Technol Assessments 52. https://doi.org/10.1016/j.seta.2022.102168

36. Choi K, Suh J, Choi Y, Jang Y (2022) Evaluation and validation of photovoltaic potential from fixed and tracking floating photovoltaic system in Hapcheon Dam. J Korean Soc Miner Energy Resour Eng 59(3):293–302. https://doi.org/10.32390/ksmer.2022.59.3.293

37. Crijns-Graus W, Wild P, Amineh MP, Hu J, Yue H (2022) International comparison of research and investments in new renewable electricity technologies: a focus on the European Union and China. Energies 15(17):6383. https://doi.org/10.3390/en15176383

38. Tina GM, Bontempo Scavo F, Merlo L, Bizzarri F (2020) Comparative analysis of monofacial and bifacial photovoltaic modules for floating power plants. Appl Energy 281:116084. https://doi.org/10.1016/j.apenergy.2020.116084

39. Odetoye OA, Ibikunle FA, Olulope PK, Onyemenam JO, Okeke UN (2022) Large-scale solar power in Nigeria: the case for floating photovoltaics. In: 2022 IEEE Nigeria 4th international conference on disruptive technologies for sustainable development (NIGERCON), April 2022, pp 1–5. https://doi.org/10.1109/NIGERCON54645.2022.9803156

40. Golroodbari S, van Sark W (2022) On the effect of dynamic albedo on performance modelling of offshore floating photovoltaic systems. Sol Energy Adv 2:100016. https://doi.org/10.1016/j.seja.2022.100016

41. Osorio-Aravena JC, Rodríguez-Segura FJ, Frolova M, Terrados-Cepeda J, Muñoz-Cerón E (2022) How much solar PV, wind and biomass energy could be implemented in short-term? A multi-criteria GIS-based approach applied to the province of Jaén, Spain. J Clean Prod 366. https://doi.org/10.1016/j.jclepro.2022.132920

42. López M, Soto F, Hernández ZA (2022) Assessment of the potential of floating solar photovoltaic panels in bodies of water in mainland Spain. J Clean Prod 340. https://doi.org/10.1016/j.jclepro.2022.130752

43. Tina GM, Bontempo Scavo F (2022) Energy performance analysis of tracking floating photovoltaic systems. Heliyon 8(8):e10088. https://doi.org/10.1016/j.heliyon.2022.e10088

44. Eyring N, Kittner N (2022) High-resolution electricity generation model demonstrates suitability of high-altitude floating solar power. iScience 25(6):104394. https://doi.org/10.1016/j.isci.2022.104394

45. Boduch A, Mik K, Castro R, Zawadzki P (2022) Technical and economic assessment of a 1 MWp floating photovoltaic system in Polish conditions. Renew Energy 196:983–994. https://doi.org/10.1016/j.renene.2022.07.032

46. Popa B, Vuta LI, Dumitran GE, Picioroaga I, Calin-arhip M, Porumb RF (2022) Fpv for sustainable electricity generation in a large European city. Sustain 14(1). https://doi.org/10.3390/su14010349

47. Loughran J (2022) Europe's largest floating solar panel facility built on top of hydro-electric dam. E&T Magazine 2022. https://eandt.theiet.org/content/articles/2022/07/europe-s-largest-floating-solar-panel-facility-built-on-top-of-hydro-electric-dam/ (Accessed 28 Sep 2022)

48. Kakoulaki G et al (2022) Benefits of pairing floating solar photovoltaic with hydropower reservoirs in Europe (National and Regional Level). SSRN Electron J. https://doi.org/10.2139/ssrn.4074448

49. Eurostat (2022) Electricity production, consumption and market overview, 2014. Accessed 25 Sep 2022. [Online]. Available: https://ec.europa.eu/eurostat/statistics-explained/index.php?title=Electricity_production,_consumption_and_market_overview

50. Bax V, van de Lageweg WI, van den Berg B, Hoosemans R, Terpstra T (2021) Will it float? Exploring the social feasibility of floating solar energy infrastructure in the Netherlands. Energy Res Soc Sci 89:102569. https://doi.org/10.1016/j.erss.2022.102569

51. Bellini E (2022) Floating PV in the Persian Gulf—pv magazine international. PV Magazine, 2020. https://www.pv-magazine.com/2020/02/17/floating-pv-in-the-persian-gulf/ (Accessed 28 Sep 2022)

52. Semeskandeh S, Hojjat M, Hosseini Abardeh M (2022) Techno–economic–environmental comparison of floating photovoltaic plant with conventional solar photovoltaic plant in northern Iran. Clean Energy 6(2):353–361. https://doi.org/10.1093/ce/zkac019

53. Omrani MM (2022) Techno-economic and environmental analysis of floating photovoltaic techno-economic and environmental analysis of floating photovoltaic power plants: a case study of Iran. Renew Energy Res Appl 1(5):1–14

54. Aweid RS, Ahmed OK, Algburi S (2022) Performance of floating photovoltaic/thermal system: experimental assessment. Int J Energy Res 1–14. https://doi.org/10.1002/er.8729

55. Ali A, Saleh N (2022) Designing and modeling of 300 Mw floating solar photovoltaic (Fspv) power system in Aden. IRJMETS 04(07):3878–3893. [Online]. Available: www.irjmets.com

56. Koca K, Karipoğlu F, İlbahar E (2022) Convenient site selection of a floating Pv power plants by using gis-fuzzy analytical hierarchy process in Turkey. SSRN Electron J. https://doi.org/10.2139/ssrn.4108876

57. Kaymak MK, Şahin AD (2022) The first design and application of floating photovoltaic (FPV) energy generation systems in Turkey with structural and electrical performance. Int J Precis Eng Manuf—Green Technol 9(3):827–839. https://doi.org/10.1007/s40684-021-00369-w

58. Yilmaz OS, Gülgen F, Ateş AM (2022) Determination of the appropriate zone on dam surface for floating photovoltaic system installation using RS and GISc technologies. Int J Eng Geosci 8(1):63–75. https://doi.org/10.26833/ijeg.1052556

59. Vaschetti G, Bacchelli M, Tronel F (2022) Using reservoirs for floating PV plants. In: E3S Web conference, vol 346. pp 02001. https://doi.org/10.1051/e3sconf/202234602001

60. Farrar LW, Bahaj ABS, James P, Anwar A, Amdar N (2022) Floating solar PV to reduce water evaporation in water stressed regions and powering water pumping: Case study Jordan. Energy Convers Manag 260:115598. https://doi.org/10.1016/j.enconman.2022.115598

61. Owhaib W, Borett A, Alkhalidi A, Al-Kouz W, Hader M (2022) Design of a solar PV plant for Ma'an, Jordan. In: IOP Conference series earth environment science, vol 1008(1). https://doi.org/10.1088/1755-1315/1008/1/012012

62. Gonzalez Sanchez R, Kougias I, Moner-Girona M, Fahl F, Jäger-Waldau A (2021) Assessment of floating solar photovoltaics potential in existing hydropower reservoirs in Africa. Renew Energy 169:687–699. https://doi.org/10.1016/j.renene.2021.01.041

63. Basson G, Bosman E, Vonkeman J (2022) Reservoir sedimentation mitigation measures to deal with a severe drought at Graaff-Reinet, South Africa. E3S Web Conference, vol 346. pp. 03012. https://doi.org/10.1051/e3sconf/202234603012

64. Getie EM, Jember YB (2022) Potential assessment and performance evaluation of a floating solar photovoltaic on the Great Ethiopian Renaissance Dam. Int J Photoenergy. https://doi.org/10.1155/2022/6964984

65. YSG Solar (2022) 5 largest floating solar farms in the World in 2022. YSG Solar. https://www.ysgsolar.com/blog/3-largest-floating-solar-farms-united-states-2022-ysg-solar (Accessed 28 Sep 2022)

66. Ramasamy V, Margolis R (2021) Floating photovoltaic system cost benchmark: Q1 2021 installations on artificial water bodies. Natl Renew Energy Lab 1(10):1–15

67. Padilha Campos Lopes M, Nogueira T, Santos AJL, Castelo Branco D, Pouran H (2022) Technical potential of floating photovoltaic systems on artificial water bodies in Brazil. Renew Energy 181:1023–1033. https://doi.org/10.1016/j.renene.2021.09.104

68. Moraes CA et al (2022) Floating photovoltaic plants as an electricity supply option in the Tocantins-Araguaia basin. Renew Energy 193:264–277. https://doi.org/10.1016/j.renene.2022.04.142

69. dos Santos FR, Wiecheteck GK, das Virgens Filho JS, Carranza GA, Chambers TL, Fekih A (2022) Effects of a floating photovoltaic system on the water evaporation rate in the Passaúna reservoir, Brazil. Energies 15(17):6274. https://doi.org/10.3390/en15176274

70. Kuriqi A, Hysa A, Finger DC, Jurasz JK (2022) Potential use of irrigation reservoirs for power generation via floating photovoltaic systems case of Albania. In: International conference on renewable energies and smart technologies (REST—22), 2022, August. https://doi.org/10.13140/RG.2.2.30455.09127

71. Elminshawy NAS, Mohamed AMI, Osama A, Amin I, Bassam AM, Oterkus E (2022) Performance and potential of a novel floating photovoltaic system in Egyptian winter climate on calm water surface. Int J Hydrogen Energy 47(25):12798–12814. https://doi.org/10.1016/j.ijhydene.2022.02.034

72. Elminshawy NAS, Osama A, Saif AM, Tina GM (2022) Thermo-electrical performance assessment of a partially submerged floating photovoltaic system. Energy 246:123444. https://doi.org/10.1016/j.energy.2022.123444

73. Ravichandran N, Fayek HH, Rusu E (2021) Emerging floating photovoltaic system—case studies high dam and aswan reservoir in Egypt. Processes 9(6). https://doi.org/10.3390/pr9061005

74. Reges JP, Carvalho PCM, De Arau.jo JC, Carneiro TC (2022) Sizing methodology of floating photovoltaic plants in dams of semi-arid areas. J Sol Energy Eng Trans ASME 144(4):1–13. https://doi.org/10.1115/1.4052959

75. Yingjie B, Guoqing L, Yelong Z, Zhe L (2022) Floating solar park impacts urban land surface temperature distribution pattern. Photogramm Eng Remote Sens 88(4):271–278. https://doi.org/10.14358/pers.21-00083r2

76. Micheli L (2022) The temperature of floating photovoltaics: case studies, models and recent findings. Sol Energy 242:234–245. https://doi.org/10.1016/j.solener.2022.06.039

77. Güllü E, Doğru Mert B, Nazligul H, Demirdelen T, Gurdal Y (2022) Experimental and theoretical study: design and implementation of a floating photovoltaic system for hydrogen production. Int J Energy Res 46(4):5083–5098. https://doi.org/10.1002/er.7502

78. Ji Q, Li K, Wang Y, Feng J, Li R, Liang R (2022) Effect of floating photovoltaic system on water temperature of deep reservoir and assessment of its potential benefits, a case on Xiangjiaba Reservoir with hydropower station. Renew Energy 195:946–956. https://doi.org/10.1016/j.renene.2022.06.096

79. Wang TW et al (2022) Effects of floating photovoltaic systems on water quality of aquaculture ponds. Aquac Res 53(4):1304–1315. https://doi.org/10.1111/are.15665

80. Muramulla SM, Rajeshwari R, Rejina Parvin J, Anand Chakaravarthi MC, Janardhana K, Bhattacharya S (2022) Study on induced aeration for fishery fields using floating SPV. J Phys Conf Ser 2272(1). https://doi.org/10.1088/1742-6596/2272/1/012007

81. Andini S, Suwartha N, Setiawan E, Ma'arif S (2022) Analysis of biological, chemical, and physical parameters to evaluate the effect of floating solar PV in Mahoni Lake, depok, Indonesia: Mesocosm experiment study. J Ecol Eng 23(4):201–207. https://doi.org/10.12911/22998993/146385

82. Nobre R, Boulêtreau S, Cucherousset J (2022) Small lakes at risk from extensive solar-panel coverage. Nature 607(7918):239. Nature Research. https://doi.org/10.1038/d41586-022-01891-w

83. Xiao X, Yang Y (2022) Could the oceans host floating solar power plants? Nature 607(7918):239–239. https://doi.org/10.1038/d41586-022-01893-8

84. Keiner D et al (2022) Powering an island energy system by offshore floating technologies towards 100% renewables: a case for the Maldives. Appl Energy 308:118360. https://doi.org/10.1016/j.apenergy.2021.118360

85. Hong YY, Alano FI (2022) Hierarchical energy management in islanded networked microgrids. IEEE Access 10:8121–8132. https://doi.org/10.1109/ACCESS.2022.3143307

86. Temiz M, Dincer I (2022) Development and analysis of a solar-based offshore energy system for sustainable island communities. Int J Energy Res 1–12. https://doi.org/10.1002/er.8017

87. Claus R, López R (2022) Key issues in the design of floating photovoltaic structures for the marine environment. Renew Sustain Energy Rev 164. https://doi.org/10.1016/j.rser.2022.112502

88. Zhang C, Santo H, Magee AR (2022) Review and comparative study of methodologies for hydrodynamic analysis of nearshore floating solar farms. https://doi.org/10.4043/31673-MS

89. Abbasnia A, Karimirad M, Friel D, Whittaker T (2022) Fully nonlinear dynamics of floating solar platform with twin hull by tubular floaters in ocean waves. Ocean Eng 257. https://doi.org/10.1016/j.oceaneng.2022.111320

90. Ravichandran N, Ravichandran N, Panneerselvam B (2022) Comparative assessment of offshore floating photovoltaic systems using thin film modules for Maldives islands. Sustain Energy Technol Assessments 53(PA):102490. https://doi.org/10.1016/j.seta.2022.102490

91. Sree DKK et al. (2022) Fluid-structural analysis of modular floating solar farms under wave motion. Sol Energy 233:161–181. https://doi.org/10.1016/j.solener.2022.01.017

92. Bei Y, Yuan B, Feng F, Deng X (2022) Simulation analysis of single solar floating photovoltaic panel structure based on wind direction change. MATEC Web Conf 358:01020. https://doi.org/10.1051/matecconf/202235801020

93. Hafeez H, Kashif Janjua A, Nisar H, Shakir S, Shahzad N, Waqas A (2022) Techno-economic perspective of a floating solar PV deployment over urban lakes: a case study of NUST lake Islamabad. Sol Energy 231:355–364. https://doi.org/10.1016/j.solener.2021.11.071

94. Kwon TH, Kim J, Kim E, Hong S-K (2022) Effect on power generation of floating photovoltaic power system power by water level change. J Korean Sol Energy Soc 42(2):13–21. https://doi.org/10.7836/kses.2022.42.2.013

95. Zahid H, Altamimi A, Kazmi SAA, Khan ZA, Almutairi A (2022) Floating solar photovoltaic as virtual battery for reservoir based hydroelectric dams: a solar-hydro nexus for technological transition. Energy Rep 8:610–621. https://doi.org/10.1016/j.egyr.2022.08.088

96. Salto A, Villacorta AR, Siguencia OM, Icaza D (2022) Feasibility analysis for the implementation of floating solar panels in reservoirs of hydroelectric dams. Case study mazar in ecuador. In: 2022 10th International conference on smart grid (icSmartGrid), June 2022, pp 448–453. https://doi.org/10.1109/icSmartGrid55722.2022.9848589

97. Loucks DP (2022) Meeting climate change challenges: searching for more adaptive and innovative decisions. Water Resour Manag. https://doi.org/10.1007/s11269-022-03227-9

98. Şevik S, Aktaş A (2022) Performance enhancing and improvement studies in a 600 kW solar photovoltaic (PV) power plant; manual and natural cleaning, rainwater harvesting and the snow load removal on the PV arrays. Renew Energy 181:490–503. https://doi.org/10.1016/j.renene.2021.09.064

99. Ramanan CJ et al (2022) Influence of pressure in RO filtration of crude biodiesel. IOP Conf Ser Earth Environ Sci 1074(1):012014. https://doi.org/10.1088/1755-1315/1074/1/012014

100. Ramanan CJ, Bora BJ, Alom N, Buradi A, Shukla S (2022) Investigation of dead-end filtration of crude biodiesel using reverse osmosis membrane through CFD simulation. Int J Energy a Clean Environ 23(6):49–66. https://doi.org/10.1615/INTERJENERCLEANENV.2022043253

101. Shukla S, Ramanan CJ, Jyoti Bora B, Deo A, Alom N (2022) Numerical analysis of vertical axis wind turbine blades in ANSYS fluent. Mater Today Proc 59:1781–1785. https://doi.org/10.1016/j.matpr.2022.04.377

102. Odoi-Yorke F, Woenagnon A (2021) Techno-economic assessment of solar PV/fuel cell hybrid power system for telecom base stations in Ghana. Cogent Eng 8(1). https://doi.org/10.1080/23311916.2021.1911285

103. Nation U (2015) THE 17 GOALS | Sustainable Development. Accessed 27 Sep 2022. [Online]. Available: https://sdgs.un.org/goals

104. McKuin B et al (2021) Energy and water co-benefits from covering canals with solar panels. Nat Sustain 4(7):609–617. https://doi.org/10.1038/s41893-021-00693-8

105. Cazzaniga R, Rosa-Clot M (2021) The booming of floating PV. Sol Energy 219:3–10. https://doi.org/10.1016/j.solener.2020.09.057

106. Banik A, Sengupta A (2021) Scope, challenges, opportunities and future goal assessment of floating solar park. In: 2021 Innovations in energy management and renewable resources (52042), Febrauary 2021, pp 1–5. https://doi.org/10.1109/IEMRE52042.2021.9386735

107. Ghose D, Pradhan S, Shabbiruddin (2021) Floating solar plants–exploring a new dimension of energy generation: a case study. Energy Sour Part A Recover Util Environ Eff 00(00):1–31. https://doi.org/10.1080/15567036.2021.1965266

108. Goswami A, Sadhu PK (2021) Degradation analysis and the impacts on feasibility study of floating solar photovoltaic systems. Sustain Energy, Grids Netw 26:100425. https://doi.org/10.1016/j.segan.2020.100425

109. Exley G et al. (2021) Scientific and stakeholder evidence-based assessment: Ecosystem response to floating solar photovoltaics and implications for sustainability. Renew Sustain Energy Rev 152:111639. https://doi.org/10.1016/j.rser.2021.111639

110. El Hammoumi A, Chalh A, Allouhi A, Motahhir S, El Ghzizal A, Derouich A (2021) Design and construction of a test bench to investigate the potential of floating PV systems. J Clean Prod 278:123917. https://doi.org/10.1016/j.jclepro.2020.123917

111. Gorjian S, Sharon H, Ebadi H, Kant K, Scavo FB, Tina GM (2021) Recent technical advancements, economics and environmental impacts of floating photovoltaic solar energy conversion systems. J Clean Prod 278:124285. https://doi.org/10.1016/j.jclepro.2020.124285

112. da Costa LCA, da Silva GDP (2021) Save water and energy: a techno-economic analysis of a floating solar photovoltaic system to power a water integration project in the Brazilian semiarid. Int J Energy Res 45(12):17924–17941. https://doi.org/10.1002/er.6932

113. Karimirad M, Rosa-Clot M, Armstrong A, Whittaker T (2021) Floating solar: beyond the state of the art technology. Sol Energy 219:1–2. https://doi.org/10.1016/j.solener.2021.02.034
114. Hooper T, Armstrong A, Vlaswinkel B (2021) Environmental impacts and benefits of marine floating solar. Sol Energy 219:11–14. https://doi.org/10.1016/j.solener.2020.10.010
115. Yousuf H et al (2020) A review on floating photovoltaic technology (FPVT). Curr Photovolt Res 8(3):67–78. https://doi.org/10.21218/CPR.2020.8.3.067
116. Padilha Campos Lopes M, de Andrade Neto S, Alves Castelo Branco D, Vasconcelos de Freitas MA, da Silva Fidelis N (2020) Water-energy nexus: floating photovoltaic systems promoting water security and energy generation in the semiarid region of Brazil. J Clean Prod 273. https://doi.org/10.1016/j.jclepro.2020.122010
117. International Finance Corporation (2020) Floating solar photovoltaic on the rise. May, pp 3. [Online]. Available: www.ifc.org/energy
118. Oliveira-Pinto S, Stokkermans J (2020) Assessment of the potential of different floating solar technologies—overview and analysis of different case studies. Energy Convers Manag 211:112747. https://doi.org/10.1016/j.enconman.2020.112747
119. Oliveira-Pinto S, Stokkermans J (2020) Marine floating solar plants: an overview of potential, challenges and feasibility. Proc Inst Civ Eng Marit Eng 173(4):120–135. https://doi.org/10.1680/jmaen.2020.10
120. Ranjbaran P, Yousefi H, Gharehpetian GB, Astaraei FR (2019) A review on floating photovoltaic (FPV) power generation units. Renew Sustain Energy Rev 110:332–347. https://doi.org/10.1016/j.rser.2019.05.015
121. Aznar AY, Lee N, Booth SS (2019) International applications for floating solar photovoltaics (Technical Report). Natl Lab U.S. Dep Energy 2014:1–4
122. Abid M, Abid Z, Sagin J, Murtaza R, Sarbassov D, Shabbir M (2019) Prospects of floating photovoltaic technology and its implementation in Central and South Asian Countries. Int J Environ Sci Technol 16(3):1755–1762. https://doi.org/10.1007/s13762-018-2080-5
123. Goswami A, Sadhu P, Goswami U, Sadhu PK (2019) Floating solar power plant for sustainable development: a techno-economic analysis. Environ Prog Sustain Energy 38(6). https://doi.org/10.1002/ep.13268
124. Barbuscia M (2018) Economic viability assessment of floating photovoltaic energy. Work Pap 1(1):1–11
125. Sujay PS, Wagh MM, Shinde NN (2017) A review on floating solar photovoltaic power plants. Int J Sci Eng Res 8(6):789–794. [Online]. Available: http://www.ijser.org
126. Sahu A, Yadav N, Sudhakar K (2016) Floating photovoltaic power plant: a review. Renew Sustain Energy Rev 66:815–824. https://doi.org/10.1016/j.rser.2016.08.051
127. Yasmeena S, Das GTR (2015) A review on new era of solar power systems: floatovoltaic systems or floating solar power plants. Ji-manager's J Instrum Control Eng 3(1):1–8. https://doi.org/10.26634/jic.3.1.3419
128. Hernandez RR, Hoffacker MK, Field CB (2015) Efficient use of land to meet sustainable energy needs. Nat Clim Chang 5(4):353–358. https://doi.org/10.1038/nclimate2556

Topology Optimization for Maximum Daily Solar Radiation for a Large-Scale Non-tracking Heliostat Solar Reflector Using CFD Analysis

Check for updates

Sunny J. Shiyal, Bamaniya Jayesh Pravinbhai, Guru Bachan Satsangi, and Amit R. Patel

Abstract The present research work proposes a method to optimize the geometrical parameters of a large-scale heliostat reflector using CFD analysis. The use of heliostat reflectors in solar cookers is well established because of its low-cost production. Determining the best configuration of a fixed shape of inverted frustum of a square pyramid reflector is very helpful as it can avoid the tracking of reflector. The reflector height and dimensions of sides of the top surface are kept constant which are 1.75 and 5×5 m^2, respectively. Results are obtained by varying the dimensions of the bottom sides of the reflector by 5%. All 32 combinations are tested for a time interval of 15 min considering daily radiation data for the time period starting from 0900 to 1700 h. To analyze the effect of these varying parameters, total daily radiation heat flux at the top and base is calculated, and a dimensionless concentration factor is calculated to get the topology optimization. Two dimensionless parameters are identified, viz., height-to-base ratio and area ratio of top to bottom surface, the values of which are 0.7 and 2. These dimensionless geometrical parameters can be utilized to manufacture heliostat solar reflectors.

Keywords Radiation · Heliostat reflector · CFD · Ansys · Fluent

Nomenclature

T	Thickness of the reflector [m]
A_b	Area of the base [m^2]
A_t	Area of the top [m^2]
BS	Bottom side of the reflector [m]
C_p	Heat capacity at constant pressure [J/mK]

S. J. Shiyal · B. J. Pravinbhai · G. B. Satsangi · A. R. Patel (✉)
Department of Mechanical Engineering, Faculty of Technology and Engineering, The Maharaja Sayajirao University of Baroda, Vadodara, Gujarat, India
e-mail: a.r.patel-med@msubaroda.ac.in

H	Height of the configuration [m]
H	Height of the reflector [m]
K	Thermal conductivity [W/m^{2}K]
p_{atm}	Atmospheric pressure [bar]
T_{atm}	Atmospheric temperature [K]
t_b	Thickness of the base [m]
TS	Top side of the reflector [m]
W_b	Width at the base/bottom [m]
ε	Emissivity of the reflector [–]
W_t	Width at the top [m]
P	Density [kg/m^3]

1 Introduction

India is the world's third largest renewable energy producer with 38% of energy capacity installed in year 2020 coming from renewable sources [1]. In November 2021, India had an installed renewable energy capacity of 150 GW in which 48.55 GW (32.36%) was from solar itself [2]. For achieving sustainable development, the use of renewable energy is necessary. Specific technologies have been intensively used and invented in recent times in the area of solar energy utilization. These methods are not as effective as conventional energy sources due to its efficiency issues. For that reason, industries related to solar energy tries to invent the cost-effective manufacturing, installation, and maintenance methods. Solar thermal energy has been utilized in different applications varying from cooking, drying to electricity generation. The basic principle used for solar energy utilization is to capture the maximum solar radiation emitted by the sun. For this, many researchers have proposed various techniques. In one of such applications, the use of heliostat reflector is used. The concentration of solar radiation by means of a number of heliostats distributed in the horizontal plane onto a receiver mounted on a tower is known as a central receiver system or tower system. The concentration system of this kind is considered to be the most useful for large-scale solar thermal processes such as electric power generation [3].

The efficiency of the heliostat reflector largely depends on the geometrical parameters or its configuration. Several attempts are made by researchers to optimize the dimensions of heliostat reflectors. Riaz stated in his research that a major feature of the ideal solar plant characteristics is their unique dependency on just two parameters: the sun Zenith angle θs (i.e., the time of the day) and the size of concentrator [4]. This is because the reflectors are already aligned to the path traced by the sun for a particular day. Takemaro calculated solar concentrations theoretically by central receiver systems for various values of obliquity of the incident radiation for plane heliostat mirrors [3]. He concluded that the central receiver system provides a useful concentrator for solar thermal power generation, since a large amount of solar energy

can be concentrated and a temperature sufficient for Brayton as well as Rankine cycle operation is obtained very easily for such systems. Christian et al. presented a novel concept for a track-mounted heliostat intended to be manufacturable at low cost for central receiver CSP plants [5]. The cost can be reduced up to $60/m2 when implemented in high volume. An efficient autonomous solar energy system was implemented by Ali et al. which concentrates the solar heat to turn water into steam [6]. The prototype utilizes two heliostat reflectors which tracks the sun throughout the day and reflects the solar radiation constantly. The final system produced a concentration efficiency of 86% to 92%. Belaid et al. tried to optimize the solar tower power plant heliostat field by considering different heliostat shapes [7]. The results showed 69.65% increase in yearly efficiency for the case of the rectangular heliostat shape. Noone et al. introduced a biometric pattern for heliostat field layout and have done a detailed calculation of the annual average optical efficiency accounting various losses [8]. The calculations showed the improvement in PS10 field by 0.36% in efficiency while simultaneously reducing the land area by 15.8%. Kiwan et al. introduced and investigated a novel idea of using two receivers on the same tower in a solar tower system [9]. It was concluded that the annual weighted optical efficiency for the 50 MW plant for a single receiver is 67.14%, while it reaches 67.64% using the two-receiver system.

2   Objective

Several researchers have tried to optimize large-scale heliostat field by assuming the dimensions of heliostat reflectors. In several cases, the width of the heliostat reflector is assumed as 12.84 m while the height as 9.45 m [7–9] to get the field optimization of the heliostat solar reflector plant, but the physics behind the selection of that particular parameters was not available. Besides this, several techniques have been carried out to track the solar radiation by using different mechanisms in case of heliostat reflectors. Some researchers have even tried to optimize the geometrical parameters of heliostat numerically and experimentally by considering the concentration factors. But there are very few studies carried out which specifies the ideal geometrical configuration that maximizes the solar radiation. Information of such optimized topology may help in designing corresponding furnace which can cater commercial applications like baking, etc. the present work helps in arriving out such dimensionless geometrical configuration that ensures maximum solar radiation at the base collector.

3   Methodology

In the present work, a number of heliostat reflectors are arranged in a geometry which is made in the form of an inverted frustum of a square pyramid which accepts the radiation from the top and diverts it to a bottom collector by way of multiple reflections

on the different slanting side reflectors (refer Figs. 1 and 2). A dimensionless ratio of top and bottom side and ratio of bottom side to the height can be a representative ratio for optimization. This can be obtained by testing various sizes of reactor design and obtaining efficiency of the reflector in each case. Different configurations were considered for the present study, and for each design, the change in the reflector angle and base dimensions is systematically varied, and 32 such combinations of design are considered for testing. Each design is further tested for a span of operation starting from 9:00 to 17:00 h of the day, and collector efficiency is determined at a regular interval of 15 min; this makes 33 instances of operation for each design configuration in a day of operation. Use of CFD technique is chosen to carry out this large number of numerical experiments as a means of testing is carried out. In doing so, solar database of Ansys Fluent is considered as an input to the analysis.

To understand the working of the reflector, two extreme cases of the collectors are considered. One is with the base area of 4.76 × 4.76 m, while another is with the base area of 1 × 1 m. The area of the top reflector in each case is kept constant, i.e., 5 × 5 m and the height of the reflector is kept constant, i.e., 1.75 m. As shown in Fig. 1, a typical reflector can have three basic types of rays. Type A rays, which reach the base collectors via multiple reflections. Type B rays, which never reach the base, and Type C rays, which reach the base directly. Figure 2 shows the basic configuration of the reflectors, and here TS, BS, and H are three key dimensions which are top side, bottom side, and height of the reflector, respectively (refer Fig. 2). For a reflector design having a fixed value of TS and H when BS is very small, the ray type B will be in a large number compared to ray types A and B. This type of reflector design will have poor reflector efficiency. On the other hand, when difference between TS and BS will be small for a fixed value of H, ray type C will be in the large number compared to A and B.
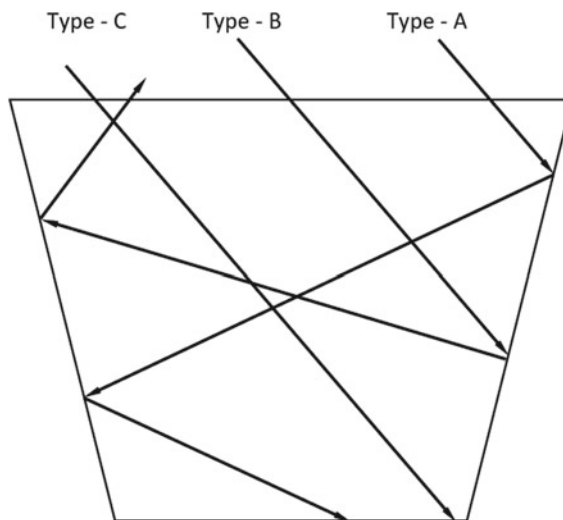
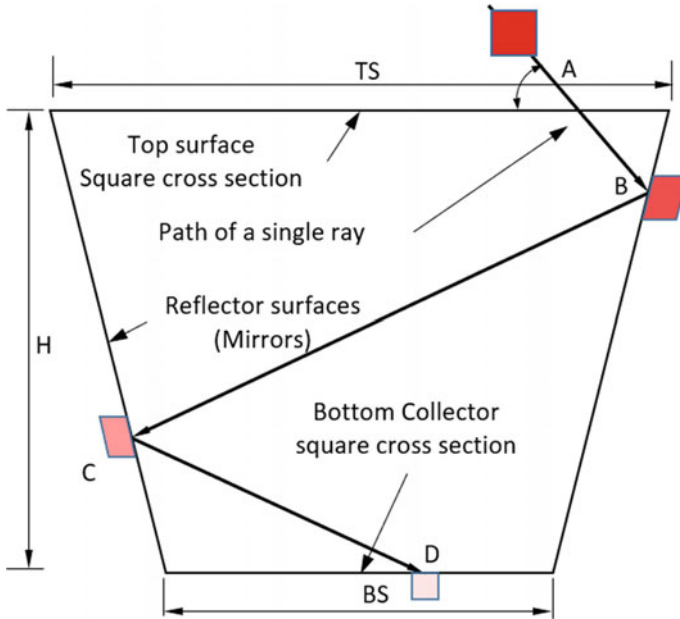**Fig. 1** Different types of rays encountered by reflector

Fig. 2 Heliostat reflector configuration

4 Geometrical Modeling and Meshing

4.1 Geometrical Modeling

In order to find out an optimum ratio of BS/TS, when H is constant that will give maximum value of reflector efficiency, 33 different combinations of the geometric configuration of the reflector design are considered which is as shown in Fig. 4.

To carry out the CFD analysis of each configuration, geometry was created using ANSYS Space Claim as shown in Fig. 3. The geometry is created by keeping four reflectors side by side making a shape of an inverted frustum of a square pyramid. The thickness (t) of the reflector is considered as 0.03 m. The thickness (t_b) of the base collector is also kept 0.03 m. The height (h) of the reflector is kept constant as 1.75 m for all design. The area of the top reflector is also kept constant and that is (A_t) 5 × 5 m. For the analysis, the area of the base (A_b) is increased 5% in each step as shown in Fig. 4 to get the variation in the base length as well as reflector angle. This is done to find the best configuration for topology optimization. Totally, 33 geometric shapes were created which are as shown in Fig. 3 and meshed in Ansys Meshing module.
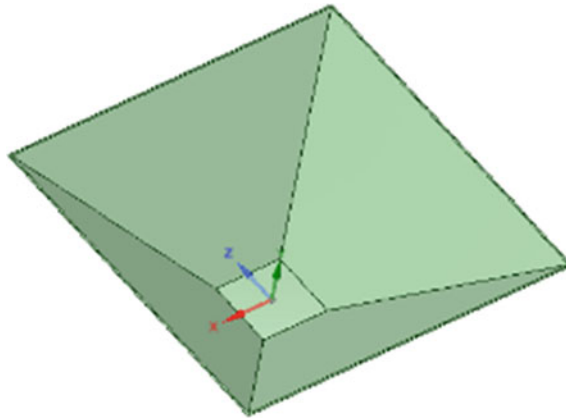
Fig. 3 Geometrical model for the analysis
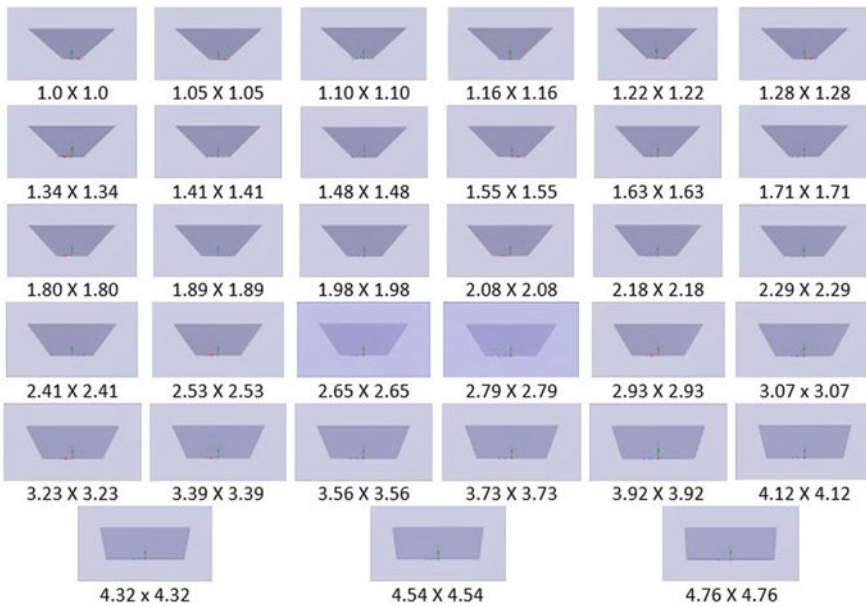
Fig. 4 Front view of geometry with variation at base

4.2 Meshing

In the present work, geometry was first split into different subvolumes to create meshing having uniform grid [10]. Meshing was carried out by edge sizing and face meshing operations. The mesh size near the reflectors and base plate is kept dense which was facilitated by giving biased edge sizing. This gives sufficient amount

of mesh elements near important geometrical features along with uniform mesh elements throughout the domain. The number of elements for the domain is 2,23,400. Figure 5 shows the meshing of the whole computational domain which was done using Ansys Meshing module. Figure 6 shows the cross-sectional view of the meshing at the center plane of the computational domain. As shown in Fig. 6, the meshing is denser at the base plate as well as the reflectors.

Fig. 5: 3D view of meshing for analysis
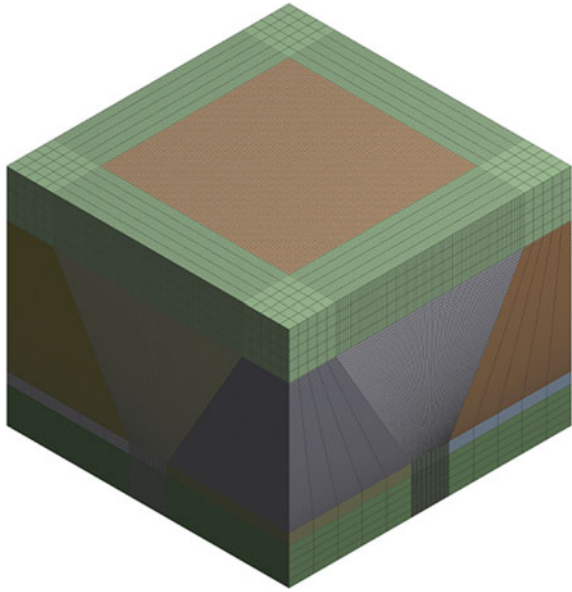
Fig. 6 Front view of the meshing
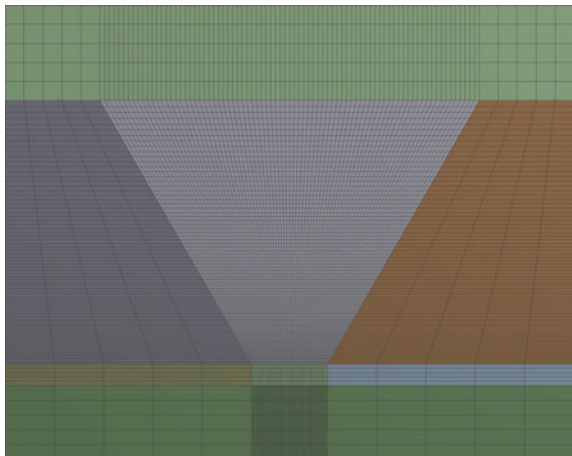
Table 1 Properties of materials used

Material	ρ (kg/m^3)	k (W/m^{2}K)	C_p (J/mK)
Mirror	2800	1.6	830
Glass	2500	1.15	830
Steel	8030	16.27	502.48

4.3   Boundary Conditions and Models Applied

Rossland with solar load model was selected as radiation model. As the intensity of the radiation changes with respect to time, transient solver with double precision is used. Also, radiation model supports only the pressure-based solver. For turbulence, standard $k - \epsilon$ model is selected. Location of Pokhran situated in Rajasthan, India, with latitude of 26.92050 and longitude of 71.91650 is selected for the present study. For the analysis, the day of 21 May is selected. The results are generated from 9:00 h in the morning to 17:00 h in the evening with the interval of 15 min. Standard operating conditions of atmospheric pressure (p_{atm}) as 1.01325 bar and atmospheric temperature (T_{atm}) as 300 K are considered.

Mirror is used as the reflector material. The base was considered as steel. The material of the top surface is glass. The standard properties of the air are considered. The emissivity of mirror is taken as 0.03 which is opaque wall. The emissivity of steel is taken as 0.8 for opaque wall. The thickness of all the mirrors, glass, and base plate is taken as 0.003 m. The properties of all the materials used are shown in Table 1.

5   Results and Discussions

CFD analysis is carried out for a selected particular day, time, and place. In the present case, the day considered is 21 May. This day is considered since it is the hottest day in the year compared to other days in summer season. The period of operation considered for analysis is from 0900 to 1700 h. The analysis is carried out for the interval of 15 min. The purpose of considering this time zone for the analysis is that beyond this time zone, the radiation intensity is found to be negligible. Since Rajasthan is having very high intensity of radiation density and clear weather, one of the locations of Rajasthan, i.e., Pokhran is considered for the analysis. The analysis considers the convection heat loss from the bottom reflector and the heat absorbed at the reflector surfaces which are two important factors for the analysis. Additionally, the emissivity of the reflector is considered as 0.03, which is in line with the reflectivity of a high-quality mirror available in the market.

In the present analysis, the time for the solar calculator available in the Ansys Fluent database is changed manually for each increment. This will help consider the direct irradiation and diffuse irradiation values into the calculations directly by using

an inbuilt solar calculator provided in the Ansys Fluent application. Both the direct and diffuse irradiation may be changed by just changing the time of the day. Also, this value changes by changing the place and date. Result of analysis is generated in terms of temperature contours taken at interval of 1 h each, taking radiation heat flux value at top and base of the reflector from Fluent (average value) and plotting graph of radiation heat flux at base (W/m^2-day) vs. radiation heat flux at top (W/m^2-day).

As shown in graph above in Fig. 7, the first point considered on the extreme right of the graph has coordinates as 3877.08 and 8742.28 W/m^2-day. In order to vary the angle, the base length of reflector is increased in step. It is observed from Fig. 7 that with each increase in the base length, the net radiation heat flux received at the top surface decreases while the net radiation heat flux received at the base increases. This trend is continued until a point where net radiation at the bottom of reflector is maximum. The 20th design combination gives this condition (refer Fig. 4). Beyond this point, all further design consideration that will reduce the net total radiation received at the base collector shows that the concentration of rays is increasing up to optimum point, 20th design point in this case, and then the concentration of rays decreases. On further increasing the base area from optimum point, the rate of decreasing of heat flux at base increases which shows that the role of reflector, i.e., reflection by reflector decreases. And at one point, the value of heat flux at top is almost equal to heat flux at base. To get the maximum solar radiation of the bottom, a concentration factor is defined which will give the improvement made by varying the geometrical parameters of the reflectors. In Sect. 3, it was discussed that there is a direct effect of the geometry which causes the concentration of the maximum solar radiation at the bottom. As we move toward the optimum point in the graph, the concentration at the bottom increases due to the dominant effect of type A and type C rays.

$$\text{Concentration Factor} = \frac{\text{Radiative Heat Flux at bottom}}{\text{Radiative Heat Flux at top}} \tag{1}$$

It is obvious that the relative ratio of types A, B or C of rays will vary throughout the operation of the day for a given location of site on the earth. Additionally, this distribution will also depend on the physical location of the operation of the site of the solar system, i.e., its latitude and longitude. As the combination of types A, B and C at a given instance of time will be different at different latitude of the earth. For instance, contribution of ray type C will be more for a given design of reflector operating at equator; however, if the same reflector design is made to operate at say 45° latitude, some of the ray type C will be converted to ray types A and B. The corresponding reflector efficiency will also be different in both the cases. Although, the effect of the location will be a factor on the operation and optimum design of the solar reflector.

Figure 8 represents the temperature distribution over the reflectors and base plate in case of an optimum angle geometry design. In this it can clearly be seen that with change in the sun's position, the left vertical slanting reflector surface is gradually showing higher and higher temperature. The trend is continued until 1300 h after this
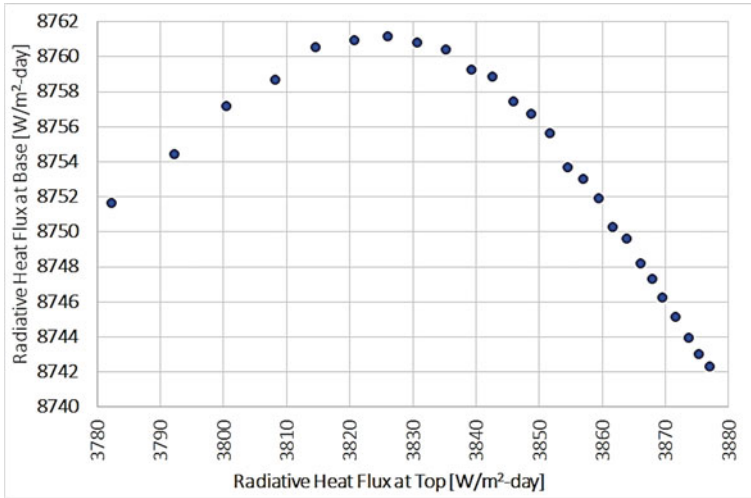
Fig. 7 Radiation heat flux at base versus top

gradual decrease in the temperature is observed. One can see clear transition in the temperature with passage of time. It is important to note that a little in-depth analysis of the reflector temperature with time will reveal clearly that the site selected for the analysis is not located at the equator but has certain angle of latitude, and the path of the sun is not exactly above the reflector.

Other observation made is that the maximum heat flux at the base was achieved in a day at 1545 h in case of the Rajasthan, Pokhran. However, carrying out similar analysis in case of Chennai, the maximum heat flux condition is observed at 1530 h

Fig. 8 Temperature contour for reflector at different time of the day

only. Above observation confirms the influence of the location of operation of the reflector on the efficiency of the reflector. In the present case, it was observed that the value of heat flux depends upon the position with reference to Tropic of Cancer, Equator, and Tropic of Capricorn. As the present study is carried out in India, one can say, based on the two extreme locations, that all over Ind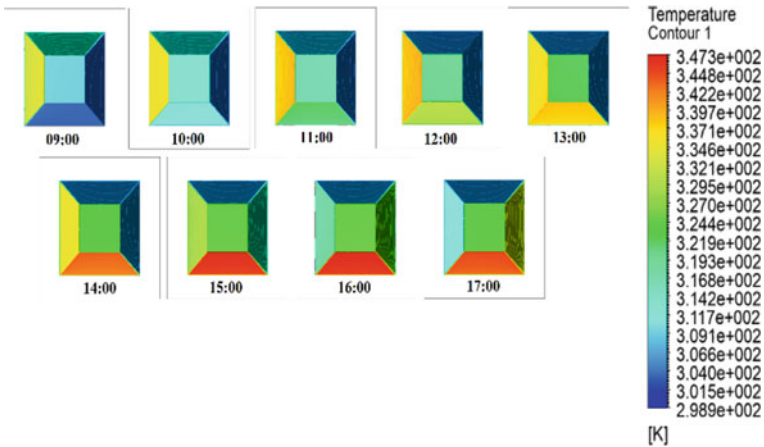ia the maximum radiation heat flux may occur between 1530 (for South India) and 1545 (for North India). The influence of finding the optimum angle for a particular type of reflector by changing the position is matter of further investigation.

This fact can be observed based on the Fig. 9. Figure shows the variation in the concentration factor between bottom reflector heat flux density and the top reflector heat flux density when size of bottom side of the reflector considered is 1×1 m. The three cities across the latitude of the India are considered, and they are Chennai in state of Tamil Nadu, Pokhran in the state of Rajasthan, and Meerut in the state of Uttar Pradesh. Based on the day chosen in the analysis which is 21 May, one can say that the tilting of northern hemisphere will be toward the sun as shown in the inset figure in Fig. 9. It is observed that due to the tilting, Pokhran will be the nearest city to the sun followed by Chennai and lastly Meerut. This is obvious from the concentration ratio also. It is observed that there is not only variation in the concentration factor but also the timing in which the peak of the concentration factor occurs. In case of Pokhran, the peak is achieved almost at the same time, i.e., at 15:30 h, compared to Chennai. It is important to note that due to the variation in latitudes of the respective locations, the variation in the combination of the rays (A, B or C) is observed. This variation is reflected in the concentration factor also. The variation may explain the existence of variation in distribution of types A, B, or C rays and their relative distribution due to the position of the reflector on the earth.

6 Conclusions

The study proposes the best configuration of reflector design. The analysis is carried out for time interval of 15 min each through the active time span of the day (from 9 AM to 5 PM) of the solar path. The radiation data considered for Pokhran, Rajasthan, India (latitude 26.92050 and longitude 71.91650). The temperature contours discussed can be helpful in the future works to identify and improve the reflector design. The design optimization can be further improved by varying the reflectivity of the mirrors as we know that as we move from bottom to top, the role of a reflector to concentrate the solar radiation decreases.

Based on the optimum condition, the study proposes two dimensionless numbers: (a) reduction ratio and (b) height to base width, the value of both is 2 and 0.7, respectively. The description of these number is as follows. The results derived in the present studies matches the dimensions considered by the researcher in the previous studies [7–9].
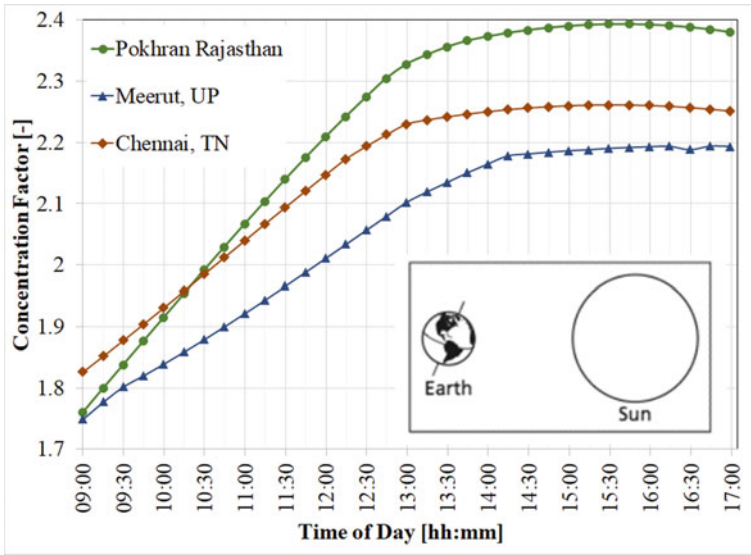
Fig. 9 Variation in concentration factor with time for different cities of India

$$\text{Height to base width} = \frac{\text{Height of the reflector } (H)}{\text{Width of the base (BS)}}$$
$$= 0.7 \tag{2}$$

$$\text{Reduction Ratio} = \frac{\text{Width at the top}(TS)}{\text{Width at the bottom}(BS)}$$
$$\approx 2 \tag{3}$$

The result is useful for large applications, for which the tracking of solar reflectors is not a practical option, and this is due to a large inertia of the reflectors. Under this, a particular design of the reflectors is standardized and tested to obtain the maximum radiation at the bottom plate that will help bypass the need of tracking. It appears that there is very small variation in the concentration factor values for different cities in India. Therefore, one can use a standard design of reflector for all the cities of India with very less variation.

References

1. Ernst, Young (2021) "2021 Renewable energy country attractiveness index (RECAI)". (https://www.ey.com/en_sg/recai)
2. "Brighter days await renewable energy space; investments likely to cross $15 billion in 2022", The Hindu. PTI, ISSN 00971–751X (https://www.worldcat.or/issn/0971-751X) December 24, (2021)
3. Sakurai T, Shibata Y (1982) Theoretical concentration of solar radiation by central receiver systems. Solar Energy 31(3):261–270
4. Riaz MR (1976) A theory of concentrators of solar energy on a central receiver for electric power generation. ASME J Eng Power
5. Davila-Peralta C, Rademacher M, Emerson N, Lopez GC, Sosa P, Cabanillas R, Peon-Anaya R, Montijo NF, Didato N, Angel R (2020) Progress in track-mounted heliostat, AIP Publishing, AIP Conference Proceedings 2303, 030011, December 11
6. Ali NT, Mezher KA, Qayed AA, McEwan N, AlTimimi AMM (2012) Efficient autonomous heliostat system. In: 2012 16th IEEE Mediterranean electrotechnical conference, IEEE, pp 573–576
7. Belaid A, Filai A, Gama A, Bezza B, Arrif T, Bouakba M (2022) Design optimization of a solar tower power plant heliostat field by considering different heliostat shapes. Int J Energy Res 1–18
8. Noone CJ, Torrilhon M, Mitos A (2012) Heliostat fields optimization: a new computationally efficient model and biomimetic layout. Solar Energy 86:792–803
9. Kiwan S, Khammash AL (2020) Optical performance of a novel two-receiver solar central tower system. J Solar Energy Eng 142:011005-1
10. Jayesh B, Kevat MD, Patel AR (2022) CFD analysis of air inside a circular duct around a series of vertically heated circular baffled discs at a different angles. In: 20th ISME conference on advances in mechanical engineering, May 2022, Ropar, Punjab

CFD Investigations on a Pitch Type Wave Energy Converter for a Potential Site Along the Indian Coast

Achanta V. V. D. Pavan, Anup P. Kamath, Dhanush Binu, Siddharthkumar B. Zadafiya, and Jyotirmay Banerjee

Abstract The objective of the present work is to assess the performance of a pitch type WEC suited for a potential location along the Indian coastline through CFD simulations of multiphase flows. A numerical wave tank (NWT) is modelled and validated with and without the presence of the WEC-rotor, with the waves being generated by the inlet velocity using Stokes second-order wave theory. Based on the hydrodynamic performance assessment carried out, the power absorption capacity and hydrodynamic efficacy of the WEC- rotor are estimated for a range of sea-states.

Keywords Renewable energy · Ocean wave energy harnessing · Pitch type WEC · CFD simulations · Stokes second-order wave theory

1 Introduction

India is estimated to have a wave potential of 60,000 MW, out of which around 6000 MW is exploitable by means of wave energy harnessing devices, having considered the site constraints and energy losses [1]. Unlike other renewable energy resources, ocean wave energy is highly predictable, owing to its propagation throughout. Ocean waves are found to have much higher energy densities compared to other alternative energy resources. With regard to the Indian scenario, energy from waves can be well tapped from coasts of Gujarat, Maharashtra, Karnataka, Kerala, Tamil Nadu, and Andhra Pradesh. It is important to consider the variability of wave power while selecting a site.

Wave resource in India is found to be richer in the western coast when compared to the eastern coast. Due to the strong winds from the east African mountains, the annual wave activity in the western coast is more enhanced. These winds help in strengthening the harsh oceanic circulation hence the heat received at the surface is transported southward and into the deeper ocean. The wave activity in the western

A. V. V. D. Pavan · A. P. Kamath · D. Binu · S. B. Zadafiya · J. Banerjee (✉)
Department of Mechanical Engineering, Sardar Vallabhbhai National Institute of Technology, Surat 395007, India
e-mail: jbaner@med.svnit.ac.in

93

coast is determined by the monsoon winds which occur during June to September and Shamal winds, which are the seasonal winds that occur during November to March and from June to August. On the contrary, the eastern coast experiences high cyclone frequency which describes the majority wave climate in this region. Extreme waves occur frequently in the eastern coast of India during the northeast monsoon season that impacts the life span of WECs. The uncertainties involved with such unprecedented natural occurrences require a critical analysis to account for the WEC safety.

The present study is divided as follows: Sect. 2 discusses bases for the wave resource assessment, which forms an integral part of site selection. Section 3 involves a quantitative approach towards site selection. Section 4 covers modelling and simulation of a NWT with and without a single degree of freedom pitch type WEC-rotor. The response of rotor is validated against the results of Poguluri et al. [2], which is further used for the performance assessment. Subsequently, Sect. 5 is focussed on the hydrodynamic performance study of the pitch type WEC-rotor for the selected site. A comparison has been carried out for a range of sea-states, with key parameters such as power absorption capacity and hydrodynamic efficiency. determined. Sections 6 and 7 enunciate key results and conclusions drawn from the study respectively.

2 Selection of Site

The selection of site suited for an optimal wave energy harnessing mechanism is a prime step towards ensuring an efficient exploitation of the available wave energy resource. Various methodologies have been studied to uniformly contrast operation sites based on the wave information acquired. Three such methods have been described, highlighting the pre-requisite input data and the computation of indices which denote the suitability of the site under consideration. The Geographic Information System (GIS) holds worthy to compare potential sites for WEC deployment. It involves gathering of site specific details such as wave energy resource, availability of grid, proximity to energy consumers, pre-installed infrastructure and interference with biological activities. Having weighted these factors, the GIS tool is integrated to determine the ideal site with minimal constraints. Lavidas George [3] proposed the Selection index for wave energy deployment (SIWED) that takes parameters pertaining to harnessing device as well as the location of interest into consideration. The SIWED approach requires wave data over a thirty-year period for an analysis of extreme events. The index is expressed as follows:

$$SIWED = \frac{e^{-CoV.CF}}{\left(\frac{H_{EVA}}{H_{\max}}\right)} \tag{1}$$

Kamranzad et al. [4] suggested adoption of Optimum hotspot identifier (OHI) to select a suitable site. This simplistic approach considers three factors for comparison

namely, local mean wave power flux, temporal variability in waves and frequency of exploitable power occurrence. Temporal variability indicates the variation of wave power over a specified time period. Trivially, a location with a higher variability index shall not be reliable for deployment.

$$OHI = \frac{P_{\text{mean}} \cdot F_{\text{mean}}}{MVI} \tag{2}$$

A few prospective locations along the western coastline of India have been analyzed based on oceanic information from ESSO-INCOIS so as to determine an optimal site for which a WEC can be deployed. The sites of interest (stations) analyzed are namely, Veraval, Ratnagiri, Karwar and Kollam. Through the OHI approach, the respective indices have been compared for each of these stations to take into account the trends in the local wave behaviour. Primarily, the wave power (P_w), which is a function of significant wave height and wave energy period, is computed as mentioned below [4].

$$P_w = \frac{\rho g^2 H_s^2 T_e}{64\pi} \tag{3}$$

It is stated that absorbed wave power greater than 2 kW/m improves capacity factor and the power produced, and hence is termed to be the exploitable wave power [5]. F_{mean} is thus determined by making use of an appropriate distribution to fit the wave power data so as to calculate the probability of exploitable wave power occurrence.

$$F_{\text{mean}} = P(P_w > 2\,\text{kW/m}) \tag{4}$$

Temporal variability index on a seasonal or annual basis is essential to take into account, the fluctuations in wave power levels over the specified period of time. Monthly variability index (MVI) is calculated for the stations to obtain the variability on an intra-annual basis for one year period, i.e., April 2020 to March 2021 based on the oceanic data retrieved. The MVI is computed using the equation below [4].

$$MVI = \frac{P_{m,max} - P_{m,min}}{P_{mean}} \tag{5}$$

Using Eq. 2, the OHI for the station can be solved, and the results are summarized in Table 1. It can be well observed that Karwar possessing a relatively higher OHI shall be considered as a potential site for WEC deployment.

Table 1 Comparison of OHI for the selected locations

Station	$P_{m,max}$	$P_{m,min}$	P_{mean}	MVI	F_{mean}	OHI
Veraval	24.807	1.486	6.538	3.567	57.97	1.0626
Ratnagiri	24.675	1.320	6.462	3.614	62.81	1.1230
Karwar	27.502	1.531	8.927	2.909	58.27	1.7881
Kollam	13.811	0.957	5.037	2.552	63.02	1.2439

3   Theoretical Aspects

The CFD simulations for ocean waves employ the numerical solutions of the Navier–Stokes equations and other accompanying equations. Some of the key theoretical aspects supporting the study are discussed herewith.

3.1   Navier–Stokes Equations

The Navier–Stokes equations for an incompressible, inviscid fluid flow are the fundamental equations required to be solved for momentum and pressure fields. These are represented in Cartesian coordinates as depicted below,

$$\rho\left(\frac{\partial u}{\partial t} + u\frac{\partial u}{\partial x} + v\frac{\partial u}{\partial y} + w\frac{\partial u}{\partial z}\right) = -\frac{\partial p}{\partial x} + \mu\left(\frac{\partial^2 u}{\partial x^2} + \frac{\partial^2 u}{\partial y^2} + \frac{\partial^2 u}{\partial z^2}\right) + \rho g_x$$

$$\rho\left(\frac{\partial v}{\partial t} + u\frac{\partial v}{\partial x} + v\frac{\partial v}{\partial y} + w\frac{\partial v}{\partial z}\right) = -\frac{\partial p}{\partial y} + \mu\left(\frac{\partial^2 v}{\partial x^2} + \frac{\partial^2 v}{\partial y^2} + \frac{\partial^2 v}{\partial z^2}\right) + \rho g_y$$

$$\rho\left(\frac{\partial w}{\partial t} + u\frac{\partial w}{\partial x} + v\frac{\partial w}{\partial y} + w\frac{\partial w}{\partial z}\right) = -\frac{\partial p}{\partial z} + \mu\left(\frac{\partial^2 w}{\partial x^2} + \frac{\partial^2 w}{\partial y^2} + \frac{\partial^2 w}{\partial z^2}\right) + \rho g_z \quad (6)$$

where, ρ is the density of the fluid mixture in kg/m^3, p is the pressure in Pa, g is the acceleration due to gravity in m/s^2, μ is the dynamic viscosity of fluid in Pa.s, t represents the time and u, v, w denote the velocity components in x, y and z directions respectively.

With the flow being considered incompressible, the continuity equation must be obeyed as follows:

$$\frac{\partial u}{\partial x} + \frac{\partial v}{\partial y} + \frac{\partial w}{\partial z} = 0 \quad (7)$$

3.2 Volume of Fluids (VOF) Model

Tracking the movement of the air–water interface requires the Volume of fluid (VOF) technique to solve the multiphase flow. The fluid proportions in a computational mesh cell (volume fractions) are defined using this technique. The volume fraction is computed using the given equation,

$$\frac{\partial \alpha_w}{\partial t} + \nabla \cdot (\alpha_w U) = 0 \tag{8}$$

where, U is the velocity field composed of u, v, and w components and α_w is the volume fraction of water, ranging from 0 to 1, with a null value depicting an air filled cell and value of unity representing water filled cell.

The density of the mixture within a mesh cell, required to solve the N-S equations is determined by the volume fraction as follows,

$$\rho = \alpha_w \rho_w + (1 - \alpha_w) \rho_a \tag{9}$$

where, ρ_w and ρ_a are the densities of water and air respectively.

3.3 Stokes Second-Order Wave Theory

The degree of accuracy in modelling the generation of ocean waves at the inlet wave and across the domain length is critical to be ensued. With the Ursell number being less than 100 as is the case in the present study, Stokes second-order wave theory is apt and the waves modelled are proved to be sufficiently realistic. The theoretical free surface elevation (η) of waves as per Stokes second-order wave theory is given by,

$$\eta(x, t) = a \left\{ \cos\theta + ka \frac{3 - \sigma^2}{4\sigma^3} \cos 2\theta \right\}$$
$$\sigma = \tanh(kh)$$
$$\theta(x, t) = kx - \omega t \tag{10}$$

where, a is first order wave amplitude, k is the wave number $\left(\frac{2\pi}{\lambda}\right)$, x is the horizontal co-ordinate, ω is the angular frequency $\left(\frac{2\pi}{T}\right)$, T is the time period and h is the mean water depth.

# 4 Wave Generation and WEC-Rotor Response Validation

The model WEC-rotor is to be analysed with the intent of assessing its hydrody-
namic performance and to estimate its power absorption capabilities. Initially, a
NWT is modelled and simulated without the WEC rotor to validate the behaviour
and propagation of ocean waves. The waves are generated using the inlet velocity
method, governed by Stokes second-order wave theory for shallow, intermediate
waves. There lies a close agreement in the theoretical and simulated surface eleva-
tion profiles. Further, the WEC-rotor is incorporated into the NWT for primarily
validating its response to the incoming waves. The results are found to qualitatively
match with those of Poguluri et al. [2]. The pitch type rotor may then hold suitable for
its performance evaluation. The simulations and analyses discussed are performed
using the commercial CFD software, Ansys Fluent 2020 R2. The NWT is primarily
simulated without the WEC rotor so as to accurately model the wave propagation.
The set-up and details pertaining to the NWT simulation are discussed herewith.

4.1 NWT Without WEC-Rotor

For the wave tank modelled, the mean free surface level is set at a height of 3.636 m.
The NWT has a domain length of 18.5 m, with coarser grid near the outlet to mitigate
reflection from the boundary and interference with upstream waves.

   The computational mesh is created using the Ansys meshing tool. A face meshing
has been adopted to create a uniformly structured mesh, with edge sizing specified to
divide the domain and specify the mesh parameters. A mesh with a higher resolution
(0.067×0.083 m) is created at the free surface and the beach to capture the waves
effectively. The computational uniform mesh for the NWT geometry is shown in
Fig. 1.

   At the inlet of the wave tank, inlet velocity method is adopted using Stokes second-
order wave theory, with wave conditions specified as following (Table 2). At the top,
an atmospheric outlet is specified allowing air to flow across the boundary. The
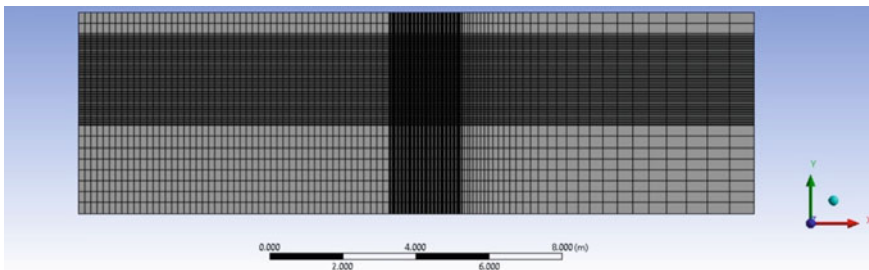
Fig. 1 Computational mesh for the NWT geometry

bottom is specified to be a wall with a no slip shear condition. Lastly, the outlet is to have a free surface level of 3.636 m subjected to pressure outlet.

The VOF formulation is explicitly marched. A piecewise-linear technique is used to depict the interface between fluids in the geometric reconstruction scheme. Comparative studies on the effects of turbulence on the wave behaviour reveal the results to be invariable in comparison with laminar flow. Thus, a laminar viscous model is used for this study. Second order upwind and body force weighted schemes are used for momentum and pressure discretization respectively. To enhance computation, the pressure-implicit with splitting of operators (PISO) scheme is considered in order to perform neighbour and skewness corrections.

The accuracy in results achieved is based on the comparison between the theoretical and simulated profiles of surface elevation. The water volume fraction contour at a sample time of $t = 30$ s. is shown in Fig. 2. This offers an insight on the propagation of waves from the inlet specified across the length of the domain, till the beach. The surface elevation profiles across the length of the NWT for different time intervals are depicted in Figs. 3, 4 and 5. The theoretical and simulated profiles are found to lie in close agreement. However, mismatches in the profiles at the wave crests and troughs are mainly attributed to the interference of a part of the reflected waves with the waves generated. It can be seen as an indication of the coarser grid near the outlet being ineffective in dampening the waves upstream. Techniques for enhancing the prevention of wave reflection include control over simulation time, creating a porous damping zone or increasing the domain length further.

The inlet velocity approach specified using higher order Stokes wave theories could be explored, with the prospects of improved results over those depicted. This however comes at the expense of greater computation times. Moreover, an alternative

Table 2 Wave parameters specified at inlet of NWT

Wave height	Wavelength	Wave period	Water depth
0.136 m	4.78 m	1.75 s	3.636 m

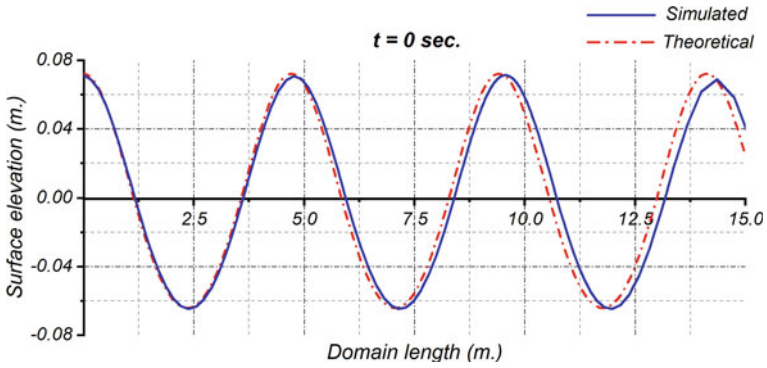**Fig. 2** Water volume fraction contour at a sample time of t = 30 s

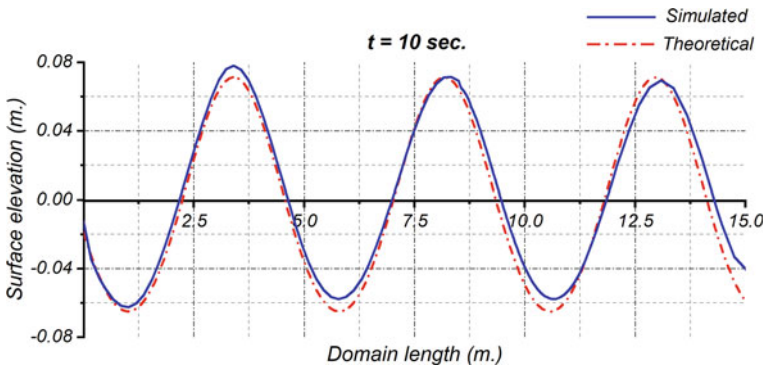**Fig. 3** Theoretical and simulated surface elevation at t = 0 s

Fig. 4 Theoretical and simulated surface elevation at t = 10 s
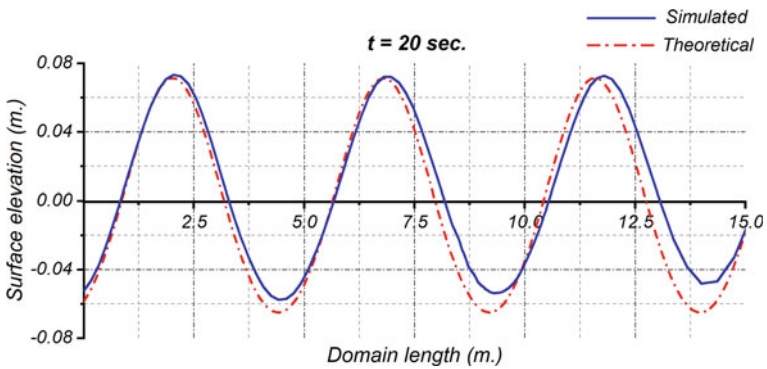

**Fig. 5** Theoretical and simulated surface elevation at t = 20 s

to generate the waves using the piston-type wave maker may allow control over simulation time to prevent reflection of waves at the boundary. This would aid to establishing simulated results having a better agreement with the theoretical profiles (Figs. 3, 4, and 5).

4.2 NWT with WEC- Rotor

A Salter's duck rotor has been considered for the present study. The paunch of the rotor replicates the fluid particle displacement. The wave dynamic pressure forces the rotor to pitch about its axis. The stern of the rotor is almost circular and does not reflect waves on the leeward side. The WEC-rotor is constrained to have a single degree of freedom rotary motion and the various parameters viz angular velocity, pitch response and power absorption are to be evaluated over time for a set of sea states. The system response has been studied without considering the effects of power take-off. The schematic of WEC-rotor with some of its features labelled is shown in Fig. 6. The WEC-rotor geometry is scaled with a Froude's factor of 11 (scale factor limits to 50 for short wave conditions as per Hughes [6]), the model data recorded in Table 3. The dimensional figures are adopted from the works of Poguluri et al. [2] for the validation of WEC-rotor response and further simulations for performance assessment. The set-up and details pertaining to the simulation of NWT in the presence of WEC-rotor are discussed in the subsequent sub-sections.

The set-up geometry is shown in Fig. 7. The geometry and meshing details for the background are as discussed. As for the WEC-rotor, a radial overset component mesh zone of 1.6 m diameter is created encircling it (refer Fig. 8).

The overset mesh superimposed on the background mesh ensures the needed data interpolation across these zones. A bias specified along the radial direction of the
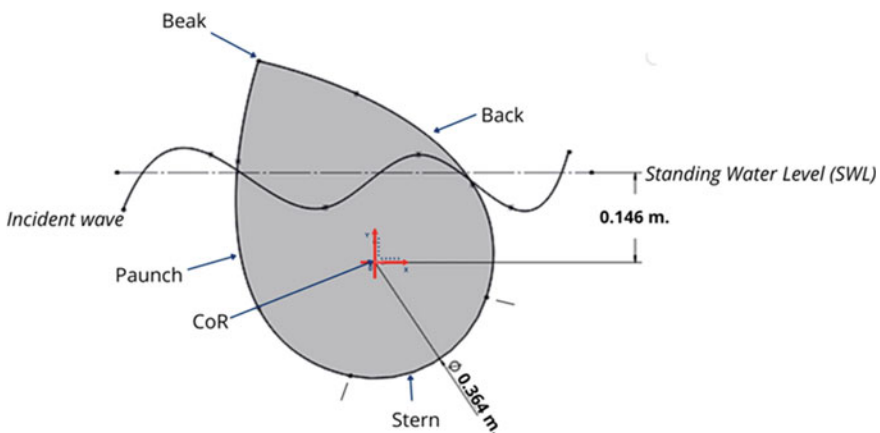

Fig. 6 Schematic of model WEC-rotor

Table 3 Full-scale and model data of wave and WEC-rotor parameters

	Full scale data	Model data (1:11)
Wave parameter		
Wave height (m)	1.5	0.1364
Wave period (s)	5.764	1.738
Wavelength (m)	51.741	4.704
Water depth (m)	40	3.636
WEC-rotor parameter		
Stern diameter (m)	4	0.364
Depth of submergence (m)	3.6	0.327
Beak angle (^{o})	60	60
Total mass (kg)	18,168.15	13.65
Pitch moment of inertia about CoR (kg.m^2)	120,450.04	0.7479
Horizontal CG w.r.t CoR (m)	−1.0241	−0.0931
Vertical CG w.r.t CoR (m)	1.0978	0.0998
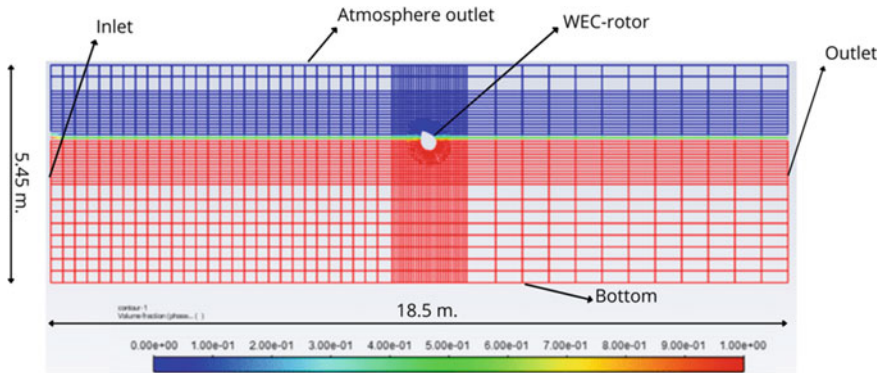
**Fig. 7** Geometry of numerical wave tank (NWT) with WEC-rotor
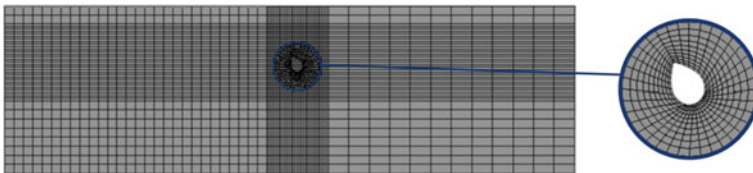
Fig. 8 Computational mesh for the NWT geometry with WEC-rotor—a magnified view of the overset mesh depicted

component mesh zone offers greater refinement at the rotor boundaries. Along the circumferential direction the grid is equispaced. The overset mesh has an orthogonal quality tending to unity (0.99).

Additionally, the component mesh zone boundary is specified as an overset, while the WEC-rotor boundary is considered to be a wall with no slip shear condition. The solution methods and controls adopted for the NWT simulations in the presence of WEC-rotor are modified to an extent in comparison with those in its absence. The VOF formulation is implicitly marched with the transport equation not to be solved iteratively for every time step. With regard to spatial discretization, the compressive volume fraction discretization scheme proves to depict improvised results over modified HRIC. The free surface is considered flat initially.

Based on the simulations performed, the pitch type motion of the WEC-rotor can be identified from the snap views shown in Fig. 9 at different time stamps. The motion of the rotor is found to be synchronizing with that of the incident waves, i.e., the rotor attains its mean position as the wave peak to its maximum height. As the waves strike the rotor boundary the amplitude of the wave is diminished aft of the rotor.

The angular velocity variation and pitch response of the WEC-rotor have been plotted (refer Figs. 10 and 11). The patterns are found to closely resemble those of isolated WEC-rotors without considering PTO in the works of Poguluri et al. [2]. The angular velocity gradually builds up over time and attains a nearly constant value. The plots could be verified by observing the complementary nature of angular
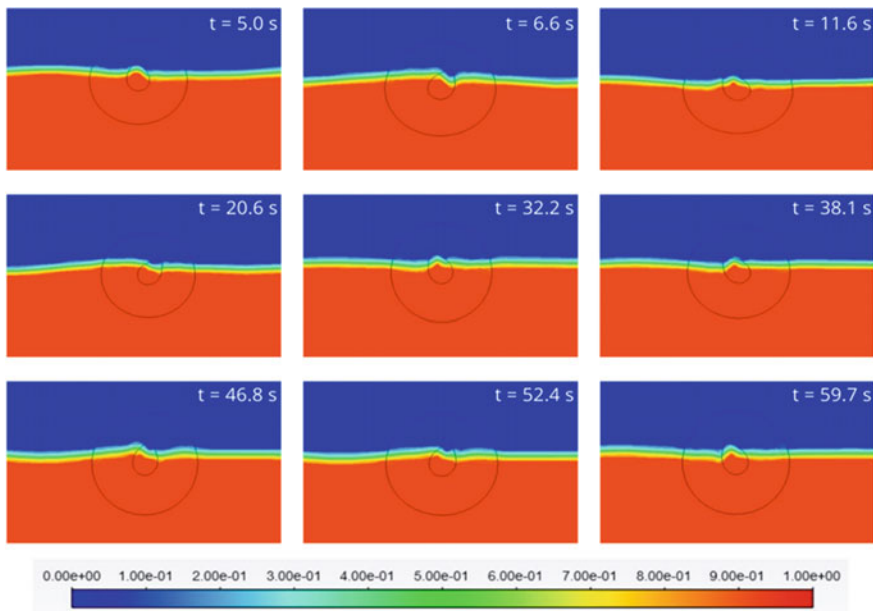
Fig. 9 WEC-rotor response to waves of $H_s = 1.5$ m and $T_e = 5.76$ s at different time stamps
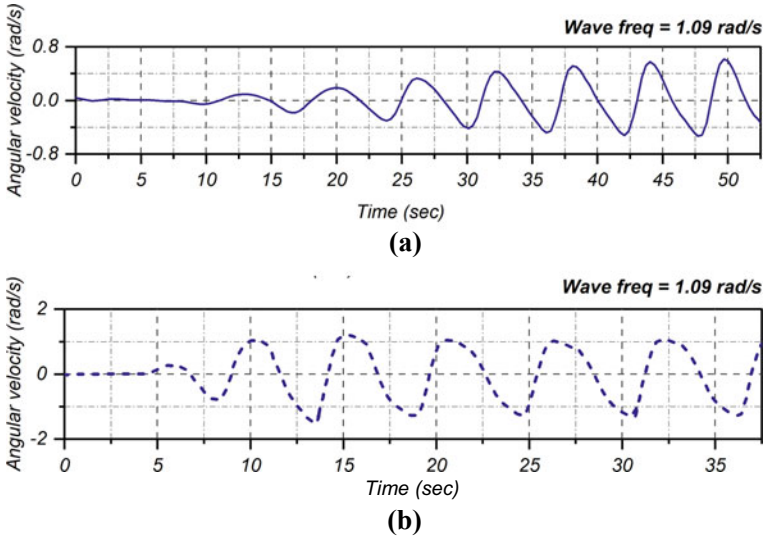
Fig. 10 Angular velocity variation of WEC-rotor over time for wave frequency of 1.09 rad/s **a** Fluent simulation **b** Poguluri et al.

velocity and pitch response. The peak angular displacement lags by nearly 1.44 s with respect to peak angular velocity of corresponding cycle. It is worthwhile to note that though the patterns are similar, the amplitude of angular velocity and pitch response seem under predicted. This could be attributed to restricting the simulations to a 2D domain, which fails to consider diffusion of waves across the rotor faces along the third dimension. This can cause further amplification or attenuation of profiles (see Figs. 10b and 11b).

5 Study of WEC-Rotor Behaviour in Selected Sea-States

The WEC-rotor performance is assessed for different sea- states (i.e., for different wave frequencies) of relatively higher probabilities of occurrence at the selected site, Karwar. This assessment is necessary in order to determine the feasibility of the rotor. The rotor power absorption capability followed by the efficiency of the rotor for each sea state is calculated and compared. The following sea-states are taken from the scatter diagram for the study (refer Table 4).

Two sample sets of resultant plots for angular velocity and pitch response of the WEC-rotor for each of the sea-states analysed are shown herewith (refer Figs. 12 and 13).

It may be observed that as wave height increases there is a surge in the angular acceleration of the rotor, as a result of which the power absorption trivially increases. At certain time periods of the waves, minor distortions in the angular displacement

(a)

(b)
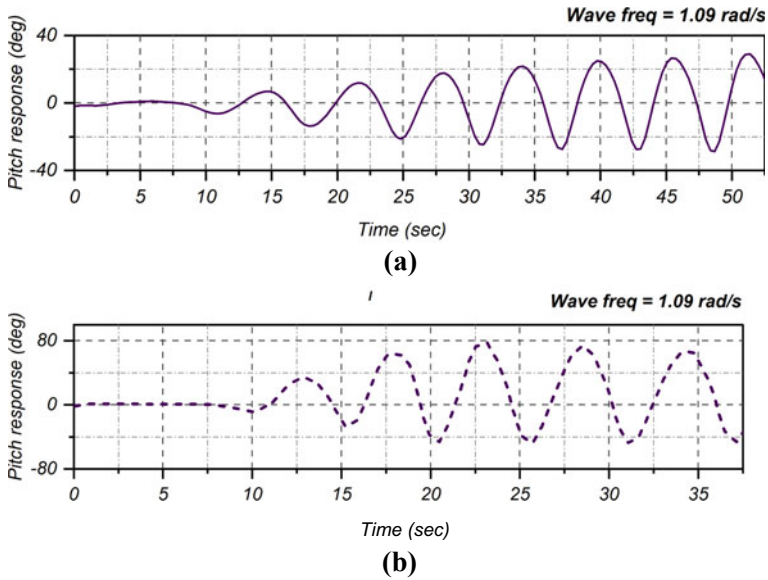
Fig. 11 Pitch response of WEC-rotor for wave frequency of 1.09 rad/s **a** Fluent simulation **b** Poguluri et al.

Table 4 Sea States considered for study of rotor assessment

Sea-state	Wave height (m)	Time period (s)
I	1.0	5.0
II	1.0	6.0
III	1.5	6.0
IV	2.0	6.0
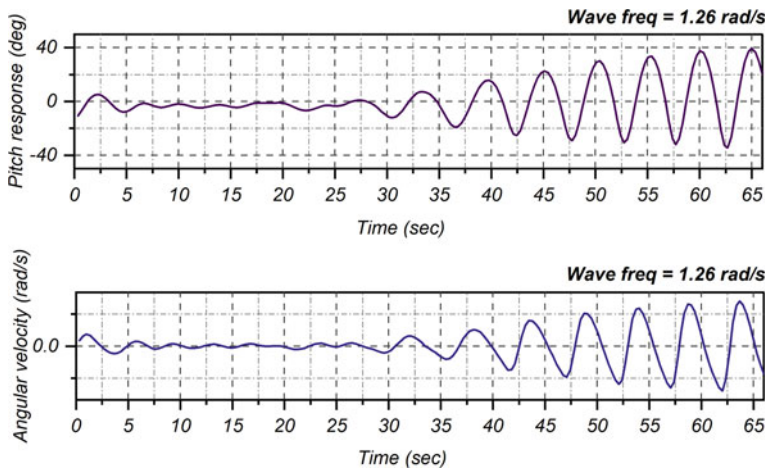
Fig. 12 Angular velocity and pitch response variation of WEC-rotor for $H_s = 1.0$ m and $T_e = 5$ s
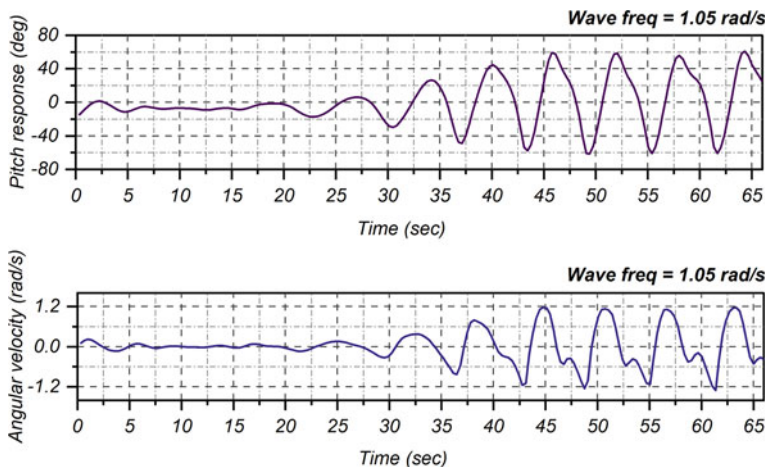
Fig. 13 Angular velocity and pitch response variation of WEC-rotor for $H_s = 1.5$ m and $T_e = 6$ s

profiles are notable. This is majorly due to the wave frequency being far from the natural frequency of the rotor. From the angular velocity data, the angular acceleration is obtained over time, considering minor increments of flow time. The power absorbed results in the acceleration of the WEC-rotor, while a part of it is dissipated due to viscous and PTO damping. Considering the power component causing acceleration to dominate, the average power absorption over the time stretch is computed and is given by. The results obtained by this are recorded below in Table 5.

$$\langle P_a \rangle = \frac{\int (I w_R \alpha_R) dt}{T} \tag{11}$$

The hydrodynamic efficiency of WEC-rotor would then be given as,

$$\dot{\eta}_H = \frac{\langle P_a \rangle}{P_w} * 100\% \tag{12}$$

Table 5 Power absorption and hydrodynamic efficiency at different sea-states

Sea-state	Power absorption (kW)	Incident power (kW)	Hydrodynamic efficiency (%)
I	9.916	12.371	80.15
II	13.282	14.846	89.47
III	23.652	33.403	70.81
IV	30.601	59.383	51.53

While there is an increase in the power absorption as the waves get stronger, there is a decrease in hydrodynamic efficiency of the WEC-rotor identified. This is owed to a failure in attaining the resonance condition.

6 Summary of Results

The present work discusses approaches involved in selection of optimal site for ocean wave energy harnessing based on comparison of indices. Based on an ideal mechanism chosen for the selected site, the Salter's duck WEC-rotor is considered for CFD investigations. For analysis, a numerical wave tank is first developed, with wave generation is specified using the Stokes second-order wave theory. The results show a close agreement between the theoretical and simulation surface elevation profiles. Subsequently, while the WEC-rotor is incorporated into the NWT, Froude's scaling is used to ensure dynamic parallels amid actual and simulation results.

The response of the pitch type WEC-rotor has been qualitatively validated against the results of Poguluri et al. [2]. The scatter diagram for the wave energy resource at the selected site, Karwar is used to for the selection of sea-states in the vicinity of the ones of suitable occurrence. Based on the simulations carried out, the average power absorption capacity and hydrodynamic efficiency of the WEC-rotor are computed. Although the power absorption increases as the waves strengthen, a decrease in hydrodynamic efficiency of the WEC-rotor occurs due to the wave frequency being much deviated from the natural frequency of the rotor.

7 Conclusions

With most of the wave energy harnessing mechanisms remaining far from their deployment for commercial use, efforts to make them techno-economically feasible are ongoing and vastly challenging.

- Based on the four sea-states considered with increasing incident power for the analysis, the power absorbed by the WEC-rotor is found to proportionally increase. However, the hydrodynamic efficiencies are roughly 80%, 89%, 70% and 51% for the respective sea-states.
- The present study incorporates a two-dimensional NWT for the assessment, but a CFD based three-dimensional NWT may be preferable to study the hydrodynamics of a pitching type WEC-rotor with incident regular waves.
- Moreover, a more realistic approach would be to consider irregular waves as those incident on the device are not always linear. The study also reveals the importance in dealing with PTO damping and its effects on the energy harnessing device.

- Besides, the WEC-rotor must be suitably designed such that it resonates with the wave field using control systems. Some of the recent technological developments include control strategies that bring variation in PTO damping through continuous monitoring of the incident waves to optimize the power absorption.

References

1. Raju VS, Ravindran M (1997) Wave energy: potential and programme in India. Renew Energy 1:10
2. Poguluri SK, Kim D, Bae YH (2021) Hydrodynamic analysis of a multibody wave energy converter in regular waves. Processes 9(7):1233
3. Lavidas G (2020) Selection index for wave energy deployments (SIWED): a near-deterministic index for wave energy converters. Energy 1(196):117131
4. Kamranzad B, Etemad-Shahidi A, Chegini V (2017) Developing an optimum hotspot identifier for wave energy extracting in the northern Persian Gulf. Renew Energy 1(114):59–71
5. Zubiate L, Villate JL, Torre-Enciso Y, Soerensen HC, Holmes B, Panagiotopoulos M, Neumann F, Rousseau N, Langston D (2009) Methodology for site selection for wave energy projects. In: 8th European wave and tidal energy conference, Uppsala, Sweden, Sep 2009
6. Hughes SA (1993) Physical models and laboratory techniques in coastal engineering. World Scientific

Thermohydraulic Performance of a Photovoltaic Thermal System Using CuO/EG Nanofluid

Amir Yousuf Bhat and Adnan Qayoum

Abstract Global energy demand has increased due to population expansion and improved living conditions. PV/T systems have lately gained popularity as a means of fulfilling this energy demand. The current study examines the effect of CuO/EG nanofluid on the performance of a flat-plate solar collector. An experimental investigation of the thermal rheological properties of CuO/EG nanofluid is carried out. TEM and XRD are used to determine the size and crystallinity of the particles. Stable nanofluids with a volume percentage of 1% are synthesised without the use of any surfactant. Experimental results show an increase of about 20% in thermal conductivity with a subsequent increase of 42% in viscosity. Furthermore, a numerical simulation is carried out for a flat-plate hybrid PV/T solar collector in a laminar flow regime with Re values ranging from 100 to 500. The effect of nanoparticle concentration on heat transfer is established by calculating the increase in heat transfer coefficient. Consequently, the effect of nanoparticle concentration on pressure drop is calculated to estimate the increase in pumping power. A comprehensive analysis is done by calculating the thermohydraulic efficiency of the fluid. As concentration increases from 0 to 1 vol%, the overall Nusselt number increases by 21% at Re = 100 and by 200% at Re = 500. Furthermore, as concentration increases from 0% to 1 vol%, the overall pressure drop increases by 75% at Re = 100 and by 210% at Re = 500. A maximum increase of 41.2% in thermohydraulic efficiency is achieved at Re = 500 and 1 vol%.

Keywords Experimental methods · Numerical · Nanofluid · Laminar flow · Heat transfer coefficient · Pressure drop

A. Y. Bhat · A. Qayoum (✉)
National Institute of Technology, Srinagar, India
e-mail: adnan@nitsri.ac.in

1   Introduction

Energy consumption in the building sector has been rising, primarily due to the increase in the population and comfort levels. The major energy consumers in the building sector are attributed to space heating, air-conditioning, and water heating. With the increasing demand for energy, researchers are continuously exploring the use of renewable energy sources as an alternative to fossil fuels. Solar energy is one of the most viable options on account of its desirable environmental and safety aspects. Solar energy can be better harnessed with the incorporation of nanofluid in solar heat collectors. Nanoparticles are nano-metric (100 nm)-sized metallic, non-metallic, or composite particles with a high thermal conductivity. These particles, mixed with base fluids using suitable methods, give rise to nanofluids. The term "nanofluids" was coined by Choi [1] at Argonne National Laboratory, USA. Lee et al. [2] determined the thermal conductivity of metal or metal oxide-based nanofluids using the hot wire method. Thermal conductivity improvement is dependent on nanoparticle size, dispersion, loading, temperature, and shape [3–5]. Moreover, viscosity is critical in the application of nanofluids in a variety of heat transfer systems [6–8]. Viscosity increases as the volume fraction of nanoparticles increases, resulting in an increase in the pumping power of the nanofluid. The improvement in heat transfer efficiency achieved by a nanofluid must be justified in terms of increased pumping power. Thus, estimating the viscosity of nanofluids becomes critical for determining their viability and fully harnessing their potential in a wide variety of applications [9]. Furthermore, nanofluid's stability is a significant barrier to its widespread application. With time, the instability of nanofluid causes a decline in system performance. Nanofluid's long-term stability and reusability are essential requirements for its successful industrial application [10]. Furthermore, the application of fluid must also be justifiable on account of it environmental implications [19].

2   Literature Review and Objective

Nanofluids, in general, are a feasible alternative to traditional heat transfer fluids. The literature demonstrates that nanofluids can enhance heat transfer in hybrid PV/T systems. An overview of investigations of solar photovoltaic thermal (PV/T) hybrid systems utilising nanofluids is presented briefly in Table 1. According to published research, the use of nanofluids results in an increase in thermal and electrical efficiency. It has been observed that the application of nanofluids in hybrid PV/Ts can result in more efficient heat removal from a system, resulting in a lower operating cell temperature. Furthermore, this results in improving the total efficiency of a PV/T hybrid power systems. It is reported that for every degree decrease in temperature, efficiency increases by 0.5% [20]. However, when nanoparticles are added, the viscosity increases, increasing the amount of energy required to circulate fluid around the PV/T systems. The studies cited in Table 1 make no mention of the

effect of nanoparticle inclusion on circulation-related energy consumption. Based on author's review of literature, no studies have been conducted to explore the effect of nanoparticles on the energy consumption in pumping for photovoltaic thermal systems. Exploring this aspect is critical in order to gain a better understanding of the practicality of nanofluids.

The current study tries to investigate the overall effect of nanoparticles on the performance of hybrid photovoltaic/thermal systems. This is done by studying the effect of nanoparticle concentration on the heat transfer enhancement. Subsequently, the effect of nanoparticle concentration is studied on the pressure drop in the system. Furthermore, the overall effect is quantified by determining the effect of nanoparticle concentration on the thermohydraulic performance of the hybrid PV/T system.

Table 1 Studies on PV/T hybrid collectors using nanofluids

Author	Collector type	Heat transfer fluid	Nanoparticles	Major findings
Sadarabadi et al. [11]	Flat plate/ cylindrical tube	Water	Al_2O_3 TiO_2 ZnO	• TiO_2/water and ZnO/water nanofluids present a better performance in terms of electrical efficiency compared to Al_2O_3/water nanofluid and deionised water • ZnO/water nanofluid is found to have the highest thermal efficiency
Lari et al. [12]	Flat plate/ serpentine tube	Water	Ag	• 8% increase in electrical output of water-cooled PVT system as compared to PV system • 13% increase in electrical output of a nanofluid cooled PVT system over a water-cooled system
Hasan et al. [13]	Flat plate/jet array	Water	SiC TiO_2 SiO_2	• SiC/water nanofluid system reported the highest electrical and thermal efficiency • The electrical, thermal, and combined PVT efficiencies were 12.75, 85%, and 97.95% • Increase in pressure with SiC nanofluid was 62.5%
Shohreh et al. [14]	Flat plate/ TEM*	Air (natural and forced) Water	SiO_2 Fe_3O_4	• SiO_2/water showed an efficiency improvement of 3.35% compared to Fe_3O_4 that showed 3.13% improvement • Power production of 54.29% and 52.40% for SiO_2/water and Fe_3O_4, respectively

(continued)

Table 1 (continued)

Author	Collector type	Heat transfer fluid	Nanoparticles	Major findings
Al-Waeli et al. [15]	Flat plate/ nano-PCM	Paraffin wax	SiC	• Increase in electrical efficiency from 7.1% to 13.7% • Thermal efficiency reached 72%
Nasrin et al. [16]	Flat plate/ serpentine tube	Water	MWCNT	• 9.2% performance enhancement using water cooling system • 3.67% by using nanofluid as compared to water
Lari et al. [17]	Flat plate/ PCM	Water	Ag	• 11.7% improvement in its electrical performance over an uncooled PV system • Thermal storage covers up to 27.3% of residential thermal load

3 Materials and Methods

Copper oxide nanoparticles with a size of 10 nm were acquired from Amnium Technologies, India. Table 2 lists the CuO nanoparticle specifications as provided by the manufacturer. Ethylene glycol is a colourless, viscous liquid. It dissolves entirely in water and some organics. It is a heat transfer fluid used in chillers and ice rinks. It is antifreeze and coolant. It has a boiling point of 197.1 °C and a freezing point of −13 °C. So it is widely employed in heat transmission. Table 2 summarises the properties of ethylene glycol [21]. Five samples were prepared with volume percentages of 0.125, 0.250, 0.500, 0.750 and 1.00%. The masses were weighed on an electronic scale with a precision of 0.0001 g. Magnetic stirring and ultrasonication are used to homogenise the samples. A magnetic bead coated with plastic is used for mixing. Magnetic stirring is followed by ultrasonication. Ultrasonication provides homogenisation of the constituents by breaking down the aggregates into finer particulates with the help of vibrational energy. The mixture is sonicated using a high-power ultrasonicator (Phoenix Instruments PHUC-300, India) for four hours.

Figure 1 illustrates the thermal conductivity measurement using KD2-Pro (Decagon Devices, Inc.). Thermal conductivity is measured at 22 °C. To reduce

Table 2 Material properties

CuO specifications		Ethylene glycol properties	
Form	Dry powder	Specific gravity	1.153
Colour	Dark brown/black	Boiling point	197.1 °C
Purity	99.9%	Freezing point	−13 °C
Bulk density	1–2 g/cc	Surface tension	48mN/m

Fig. 1 Thermal conductivity measurement setup

errors, 5 readings are taken. The read time is measured in minutes (typically more than 2) to allow the probe to equilibrate. The nanofluid sample is placed in a vial with a 20 mm diameter and a 150 mm height. The KS-1 probe is used to measure. Insert and turn on the probe. KD2-Pro uses the transient hot wire principle to measure thermal conductivity, which is given by Eq. (1):

$$k = \frac{q}{4\pi(\Delta T_2 - \Delta T_1)} \ln\frac{t_2}{t_1} \tag{1}$$

where

k = thermal conductivity
q = heat transfer rate.
t_1 = initial time, t_2 = final time.
ΔT_1 = temperature difference between two points at time t_1.
ΔT_2 = temperature difference between two points at time t_2.

As illustrated in Fig. 2, the viscosity is determined using an Anton Paar Modular Compact Rheometer (MCR 102). The plate is then filled with nanofluid, and the cone shaft is lowered until it comes into contact with the plate. Excess fluid is pushed out and then removed with microfibre. Following that, the cone is started (rotation). The data is acquired using a low-friction air bearing, an integrated normal force sensor, and a high-resolution optical encoder [18].
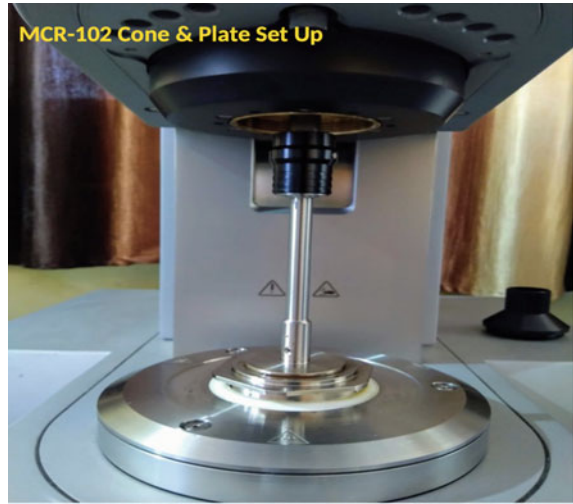
4 Mathematical Modelling

4.1 Modelling

A simplified hybrid photovoltaic thermal collector is modelled using COMSOL
Multiphysics 5.3.1.180. Conjugate heat transfer module coupled with laminar flow is
employed for the numerical study. Continuity, momentum, and energy equations for
single phase homogenous model are solved with constant heat flux of 2500 W/m^2
(125 Watts) applied at the top of the plate as shown in Fig. 3a. The flow is considered
in X-direction. Width (W) and height (H) of the flat channel are in Z and Y directions,
respectively. Steady state, single phase, laminar incompressible flow is considered.
The thermophysical properties (thermal conductivity and viscosity) found by experi-
mentation are used in the model to calculate overall heat transfer coefficient (h_{nf}) and
pressure drop (δ_p). Dimensions of the model are given in Table 3. Numerical simula-
tion is carried out for one symmetric section of the flat-plate solar collector as shown
in Fig. 3b. This is done to reduce the computational time and power consumption.
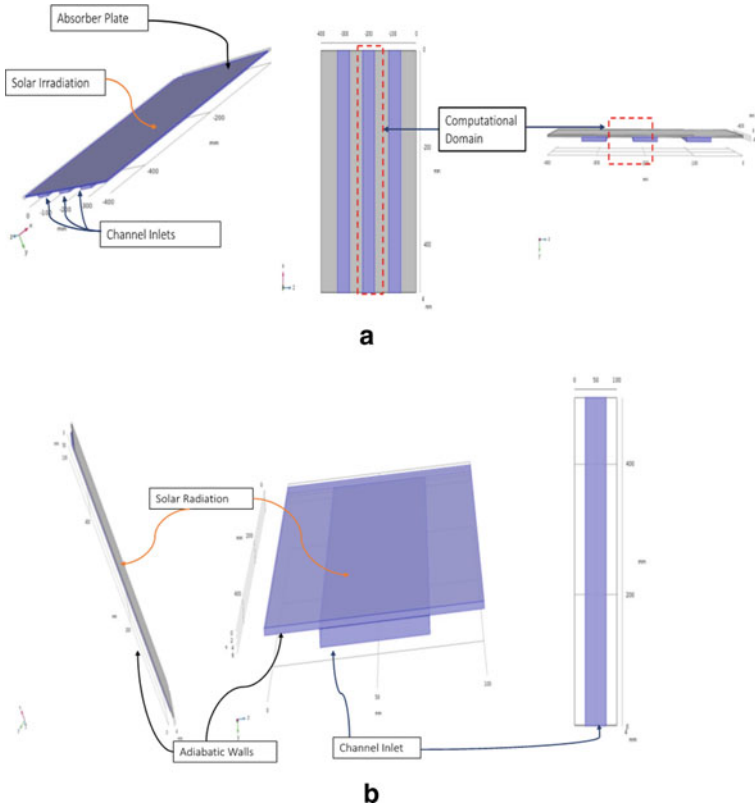
Governing Equations and Boundary Conditions

Equation of Continuity,

$$\nabla(\rho_{nf}.u) = 0 \tag{2}$$

Momentum Equation,

$$\rho_{nf}(V.\nabla)V = -\nabla p + \nabla.\left[\mu_{nf}\left(\nabla V + \nabla V^T\right)\right] + F \tag{3}$$

Fig. 3 **a** PV/T geometry. **b** Physical domain

Table 3 Model definitions

Length of micro-channel (X-axis)	500 mm
Width of micro-channel (Z-axis)	50 mm
Height of micro-channel (Y-axis)	5 mm
Thickness of absorber plate (Y-axis)	2 mm
Width of absorber plate (Z-axis)	100 mm
Length of absorber plate (X-axis)	500 mm
Heat flux	2500 W/m^2 (125 W)
Ambient temperature	300 K

Energy Equation,

$$\nabla . \left(\rho_{nf} C_{pnf} V T \right) = \nabla . \left(k_{nf} \nabla T \right) + \varepsilon.　\tag{4}$$

Following boundary conditions are applied:

1. No slip condition ($V_{\text{Walls}} = 0$)
2. Inlet conditions ($R_e = 100\text{-}500$)
3. Outlet pressure condition ($P_o = 0$)
4. Heat transfer occurs via top side of plate ($Q = 2500$) and to the fluid in the channel. All other surfaces are assumed to be perfectly insulated. Convective and radiative heat losses are neglected.

where k_{nf} and μ_{nf} are found experimentally.
F denotes the external body forces. For this case, $F = \rho g_j$.
ϵ denotes the viscous dissipation. For this case, $\epsilon = 0$.
Density,

$$\rho_{nf} = \rho_f(1 - \psi) + \rho_p \psi \tag{5}$$

Specific heat,

$$Cp_{nf} = \frac{\rho_f Cp_f(1 - \psi) + \rho_p Cp_p \psi}{\rho_{nf}} \tag{6}$$

Heat Transfer

The thermal performance of nanofluid is evaluated by calculating the heat transfer coefficient (h_{nf}). Nusselt number (Nu_{nf}) is calculated to evaluate heat transfer given by Eq. (8).

$$Nu_{nf} = \frac{h_{nf} D_h}{k_{nf}} \tag{7}$$

where

$$h_{nf} = \frac{\dot{Q}}{A \Delta T} \tag{8}$$

$$D_h = \frac{2wh}{(w + h)} \tag{9}$$

Pressure Drop

Pressure drop relation for micro-channels suggested by Upadhye et al. [23] is given in Eq. (10).

$$\Delta P = \frac{2P_0 \rho v_{in}^2 L}{Re D_H} \tag{10}$$

And friction factor,

$$f = \frac{D_H 2 \Delta P}{L_c \rho v_{in}^2} \tag{11}$$

where

$P_0 = 24(1 - 1.1355\alpha_{ch} + 1.9467\alpha_{ch}^2 - 1.7012\alpha_{ch}^3 + 0.9564\alpha_{ch}^4 - 0.2537\alpha_{ch}^5)$

α_{ch} is the aspect ratio of the micro-channel.

4.2 Grid Independence and Data Validation

When comparing to analytical investigations, the grid independence study allows us to set the system for an optimum element size where the findings are stable and exhibit minimal variance. The disparity in outcomes for both parameters is significant for element sizes ranging from 1.56E-04 (extra coarse mesh) to 5.4E-05 (normal mesh). After element size selection of 4.2E-05, both values are steady and show minimal change (fine mesh). At an element size of 4.2E-05, the heat transfer coefficient value stabilises around 875 W/m^{2}K and the pressure drop at 55 kPa (fine mesh). Hence, a fine mesh is chosen for the investigation because reducing element size further increases power and time consumption.

Equations 10 and 11 are used to validate the pressure drop and friction factor. Both these relations provide analytical relations for straight channel configurations. The calculated results are in agreement with the analytical results. At lower Reynolds numbers (100–200), the variation is about 1–1.5%, but at higher Reynolds number (500), it increases to up to a max of 9%. The variation increases with the increasing volume percentage of CuO. Nusselt number values are validated by comparing them with those obtained from correlation (Eq. 12) given by Jung et al. [22]. With a little modification of the Dittus-Boelter correlation for turbulent flow in macro-channels, Eq. 12 can be used to correlate the measured Nusselt number for various nanofluids in laminar flow regimes in micro-channels. The calculated values are strongly in agreement with the correlation. The minimum and maximum variation between calculated and analytic results is 0.5% for Re = 100 and 0.125% vol and 8.2% at Re = 500 and 1% vol, respectively.

$$Nu = 0.0095\phi^{0.01} \, \text{Re}^{0.42} \, \text{Pr}^{0.55} \tag{12}$$

where ϕ is the volume fraction.

Re and Pr are the Reynolds number and Prandtl number, respectively.

5 Results and Discussion

The nanofluid samples are transported to vertical glass tubes with a diameter of 20 mm and a height of 150 mm for thermal conductivity testing. A single needle probe is used to conduct the measurement (KS-1). Ethylene glycol has a thermal conductivity of 0.257 W/mK, while copper oxide has a thermal conductivity of 33 W/mK. Each test is repeated five times to ensure that error inconsistencies are minimised. Figure 4 illustrates thermal conductivity as a function of volume percentages. For 0.125 vol%, 0.25 vol%, 0.5 vol%, 0.75 vol%, and 1 vol% the enhancement is 4.28%, 8.9%, 12.0%, 16.3%, and 19%, respectively.

The samples were sonicated for 30 min before being evaluated for viscosity with an Anton Paar Modular Compact Rheometer [18]. Figure 5 illustrates that as the volume fraction increases, so does the viscosity. At 0.125 vol%, 0.250 vol%, 0.500 vol%, 0.750 vol%, and 1 vol%, the viscosity increases by 14.8%, 21.3%, 26.7%, 34.4%, and 42%, respectively. The tests are carried out 20 at a temperature of 20 °C with shear rate up to 1000 s^{-1}. All samples show consistent viscosity with varying shear rate.

The addition of nanoparticles enhances the heat transfer characteristics of fluids. However, it also leads to an increase in viscosity. Figure 6 shows the effect of Reynolds number and particle concentration on Nusselt number. At Re = 100, with an increase in particle concentration, the Nusselt number increases by 21%. Also, at Re = 500, the Nusselt number increases by more than 200% as the particle concentration is increased to 1 vol%. Furthermore, the Nusselt number is largely dependent on the Reynolds number. The synergistic effect of nanoparticle addition and Reynolds
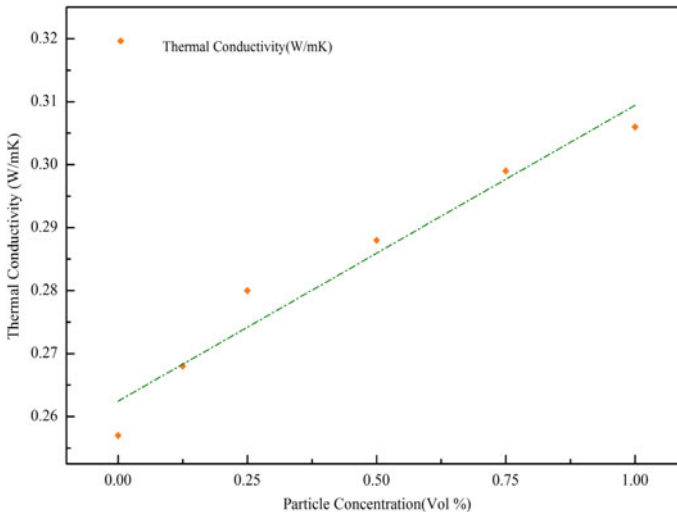
Fig. 4 Thermal conductivity
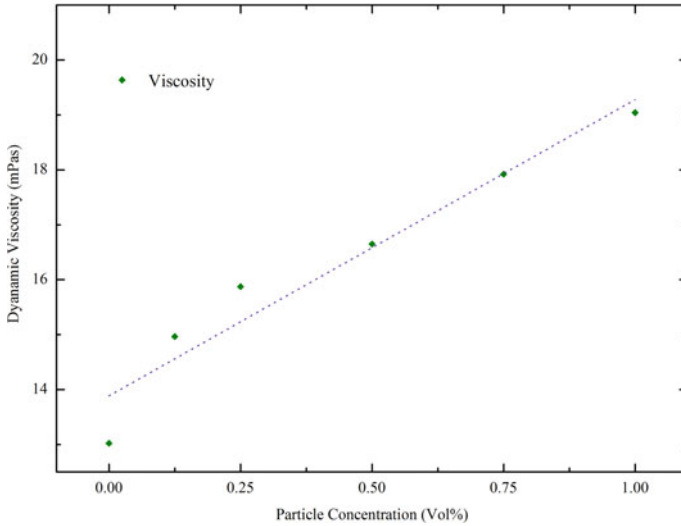
Fig. 5 Viscosity

number results in an overall increase in Nusselt number. At low particle concentration (<0.5 vol%), a marginal increase in Nusselt number is observed. However, at particle concentration greater than 0.5 vol%, the Nusselt number increases rapidly. The surge in Nusselt number may be attributed to greater interparticle interactions with increasing concentration and better mixing at higher Reynolds number. Figure 7 shows the effect of nanoparticle concentration and Reynolds number on pressure drop. With increasing concentration and Reynolds number, the pressure drop increases. At Re = 100, an overall increase of 75% in pressure drop is observed. Also, as particle concentration is increased to 1 vol% at Re = 500, pressure drop increases by approximately 210%. This is due increase in viscosity at higher particle concentrations.

The overall effect of nanofluid on the heat transfer enhancement and pressure drop is evaluated in terms of thermohydraulic performance given by Eq. 13. The thermohydraulic performance parameter expresses the net usable thermal energy gain by taking into account both the equivalent thermal energy required to overcome the increased friction or hydraulic losses.

$$\eta_{th} = \frac{Nu/Nu_0}{(\Delta P/\Delta P_0)^{1/3}} \tag{13}$$

where Nu is the Nusselt number of nanofluid

Nu_0 is the nusselt number of ethylene glycol at Re = 100

ΔP is the pressure drop of nanofluid

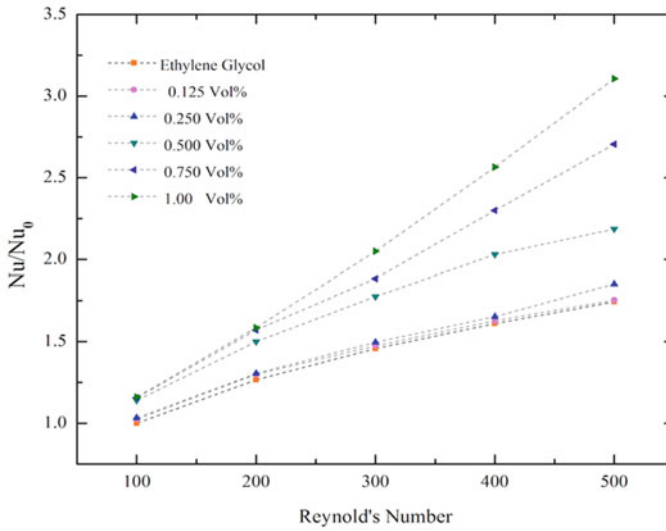ΔP_0 is the pressure drop of ethylene glycol at Re = 100

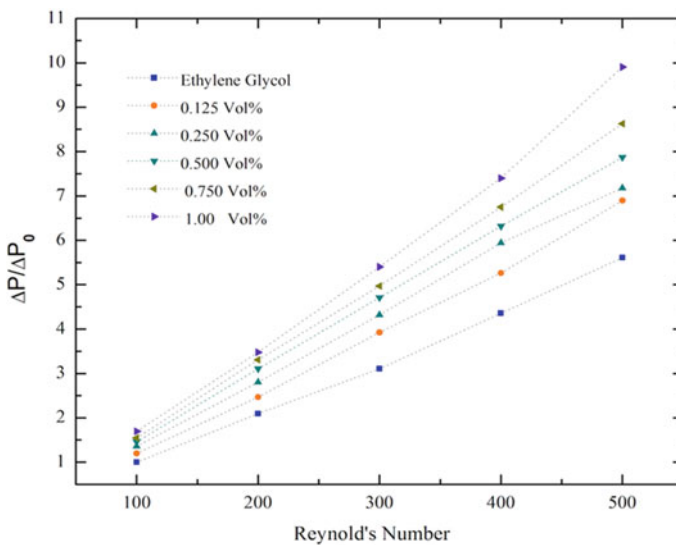**Fig. 6** Effective Nusselt number

Fig. 7 Effective pressure drop

As illustrated in Fig. 8, at particle concentrations up to 0.250 vol%, the pressure drop increases significantly with increasing Reynolds number. The corresponding increase in Nusselt number is marginal. Hence, the overall thermohydraulic efficiency of nanofluids with particle concentrations up to 0.250 vol% is lower than the
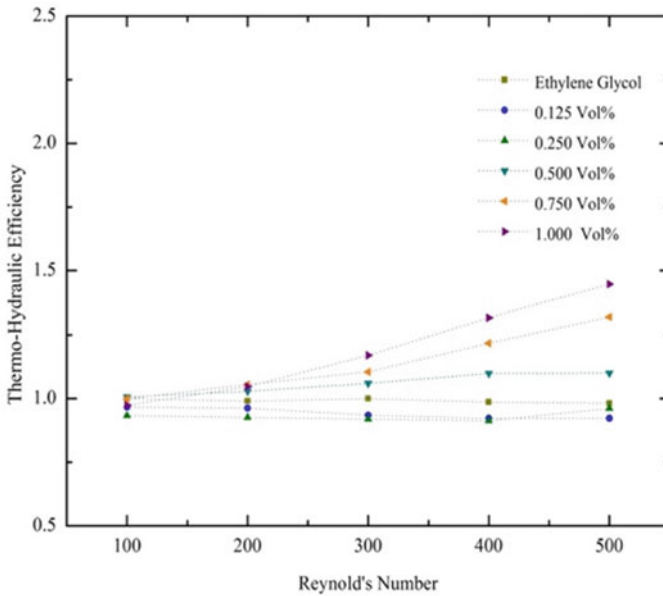
Fig. 8 Thermohydraulic efficiency

base fluid. Furthermore, higher particle concentrations of above 0.250 vol% result in greater interparticle interaction and better mixing with an increasing Reynolds number. This corresponds to a surge in Nusselt number. This leads to an increase in thermohydraulic performance. A maximum increase of 41.2% is observed at 1 vol%. The influence of nanoparticles on thermohydraulic performance is minimal at low concentrations and increases with volume % increase. Additionally, it is noted that the effect is more pronounced for Re values greater than 300. Increased Re values result in improved fluid mixing, which results in improved heat removal.

Taking into consideration the above discussion, it is possible to conclude that nanofluids prove to be an acceptable alternative to conventional heat transfer fluids at higher nanoparticle concentrations and Reynolds numbers. With such performance characteristics, nanofluids definitely justify their usage in hybrid photovoltaic/thermal systems. However, at lower concentrations and Reynolds numbers, the heat transfer enhancement achieved is not justified on account of the corresponding increase in pressure drop.
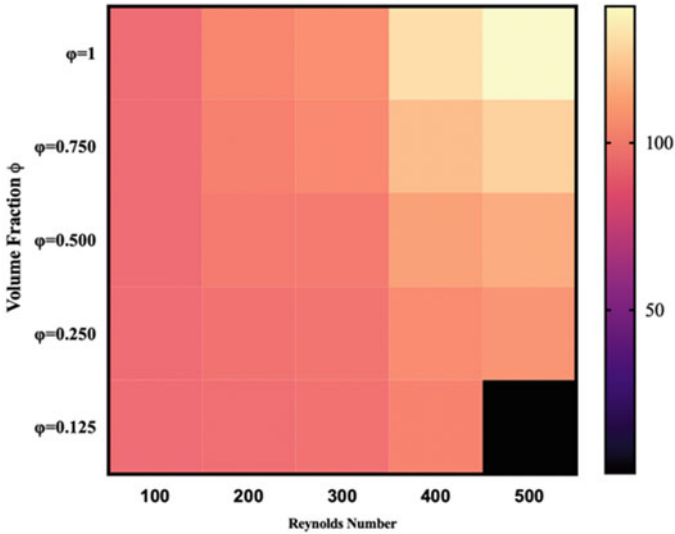
Fig. 9 Heat map for feasible parameters

6 Conclusions

In this study, the effect of CuO/EG nanofluid was investigated on the thermohydraulic performance of a photovoltaic thermal system at different Reynolds numbers. It was found that the overall Nusselt number increases by 21% at Re $= 100$ and by 200% at Re $= 500$. Subsequently, the overall pressure drop increases by 75% at Re $= 100$ and by 210% at Re $= 500$. The results show that at lower particle concentrations (up to 0.250 vol%), the Nusselt number increases marginally with a significant rise in pressure drop. However, at higher particle concentrations (> 0.250 vol%), Nusselt number values increase drastically. Furthermore, evaluation of thermohydraulic efficiency is carried out to evaluate the feasibility of proposed nanofluids for application in hybrid PV/T systems. It was found that nanofluids containing particle concentrations of up to 0.250 vol% exhibited lower thermohydraulic performance as compared to ethylene glycol. However, nanofluids containing higher particle concentrations exhibited higher thermohydraulic performance. Maximum increase of 41.2% in thermohydraulic efficiency was achieved at 1 vol% and Re $= 500$. Thus, at higher particle concentrations and Reynolds numbers, nanofluids prove to be a desirable alternative to conventional heat transfer fluids. The conclusion can be summarised with the help of a heat map in Fig. 9. The cells pertaining to values greater than 100 show feasible design parameters.

References

1. Choi SUS, Eastman JA (1995) Enhancing thermal conductivity of fluids with nanoparticles. UNT Digital Library. https://digital.library.unt.edu/ark:/67531/metadc671104/
2. Lee S, Choi SU, Li S, Eastman JA (1999) Measuring thermal conductivity of fluids containing oxide nanoparticles. J Heat Transf. ASME Digital Collection
3. Das SK, Putra N, Thiesen P, Roetzel W (2003) Temperature dependence of thermal conductivity enhancement for nanofluids. J Heat Transf.ASME Digital Collection
4. Vadasz P (2006) Heat conduction in nanofluid suspensions. J Heat Transf, ASME Digital Collection
5. Lotfizadeh S, Matsoukas T (2015) Effect of nanostructure on thermal conductivity of nanofluids. https://www.hindawi.com/journals/jnm/2015/697596/
6. Prasher R, Phelan P, Bhattacharya P (2006) Effect of aggregation kinetics on the thermal conductivity of nanoscale colloidal solutions (Nanofluid). https://pubs.acs.org/doi/10.1021/nl060992s
7. Evans W, Fish J, Keblinski P (2006) Role of brownian motion hydrodynamics on nanofluid thermal conductivity. Appl Phys Lett 88(9). AIP Publishing. https://aip.scitation.org/doi/10.1063/1.2179118
8. Koo J, Kleinstreuer C (2005) A new thermal conductivity model for nanofluids. J Nanoparticle Res. SpringerLink. https://link.springer.com/article/10.1007/s11051-004-3170-5
9. Ben-Abdallah P (2006) Heat transfer through near-field interactions. In: Nanofluids: applied physics letters.: vol 89(11). AIP Publishing. https://aip.scitation.org/doi/abs/10.1063/1.2349857
10. Bhat AY, Qayoum A (2022) Viscosity of CuO nanofluids: experimental investigation and modelling with FFBP-ANN. Thermochimica Acta 714:179267. ISSN: 0040–6031. https://doi.org/10.1016/j.tca.2022.179267
11. Sardarabadi M, Passandideh-Fard M (2016) Experimental and numerical study of metal-oxides/water nanofluids as coolant in photovoltaic thermal systems (PVT). Solar Energy Mater Solar Energy
12. Lari MO, Sahin AZ (2017) Design, performance and economic analysis of a nanofluid-based photovoltaic/thermal system for residential applications. Energy Convers Managem 149:467–484. ISSN 0196–8904
13. Hasan HA, Sopian K, Jaaz AH, Al-Shamani AN (2017) Experimental investigation of jet array nanofluids impingement in photovoltaic/thermal collector. Solar Energy 144:321–334. ISSN 0038–092X
14. Soltani S, Kasaeian A, Sarrafha H, Wen D (2017) An experimental investigation of a hybrid photovoltaic/thermoelectric system with nanofluid application. Solar Energy 155:1033–1043. ISSN 0038–092X
15. Al-Waeli AHA, Chaichan MT, Sopian K, Kazem HA, Mahood HB, Khadom AA (2019) Modeling and experimental validation of a PVT system using nanofluid coolant and nano-PCM. Sol Energy 177:178–191. https://doi.org/10.1016/j.solener.2018.11.016
16. Nasrin R, Parvin S, Alim MA (2014) Heat transfer by nanofluids through a flat plate solar collector. Proc Eng 90:364–370. ISSN 1877–7058
17. Kamran M, Qayoum A (2022) Effect of ZnO nanofluids on thermo-hydraulic characteristic of flow in a heated duct. Energy Sour Part A: Recovery Utilization Environm Effects 44(4):10681–10693. https://doi.org/10.1080/15567036.2022.2154871
18. Paar A (2019) Rheometer MCR 102. The modular compact Rheometer series
19. Nittaya Tamaekong CLSP (2014) Synthesis of thermally spherical CuO nanoparticles. J Nanomater
20. Breeze P (2016) Chapter 8, Solar photovoltaic technologies. In: Breeze P (ed) Solar power generation, Academic Press, pp 51e55
21. https://www.meglobal.biz/products/monoethylene-glycol/physicalproperties

22. Kamran M, Qayoum A (2023) Experimental investigation of natural convection of Fe_3O_4-water nanofluid in a cubic cavity. J Dispers Sci Technol. https://doi.org/10.1080/01932691.2023.2173607

23. Upadhye HR, Kandlikar SG (2004) Optimization of microchannel geometry for direct chip cooling using single phase heat transfer. In: Proceedings of the international conference on nanochannels, microchannels, and minichannels. Rochester, NY, USA, 17–19 June 2004

Performance Analysis of Solar Air Heater with Circular Finned Absorber Plate

Avnish Kumar, Bireswar Paul, and Swastik Acharya

Abstract In this report, we perform a numerical analysis of a three-dimensional solar air heater (SAH) having a finned absorber plate. The number of fins of circular cross-section (h = 5 mm to h = 25 mm) has been varied from 10 to 25. Finite volume method is adopted to solve the problem numerically. Fluid flow considered in the turbulence regime where Reynolds varies from 4000 to 16,000. Continuity, momentum, and energy equations with k-ε RNG turbulence model are solved to obtain the velocity and temperature field. Brief results of heat transfer are explained with the aid of graphical plots and contours. A uniform heat flux of 1000 W/m² is applied over the absorber plate. It is observed that the performance of the solar air heater mainly depends on Reynolds number, fin height, and relative coarseness of fins. It is found that the average absorber surface temperature at ten fins is 339.92 K and at 335.5944 K at 15 fins, which is the least among all cases. When the number of fins increases beyond 15, the absorber temperature starts rising and becomes 337.737 K at 25 fins. Thus, 15 fins on the absorber plate are the optimum configuration for maximum heat transfer.

Keywords Solar air heater · Circular fins · Absorber plate · Nusselt number · Pressure drop

Nomenclature

D	Duct equivalent diameter [mm]
E	Height of rib [mm]
H	Depth of duct [mm]
h	Coefficient of heat transfer [W/m²K]
K	Air thermal conductivity [W/m K]
L	Length of duct [mm]

A. Kumar (✉) · B. Paul · S. Acharya
Department of Mechanical Engineering, Motilal Nehru National Institute of Technology Allahabad, Prayagraj 211002, India
e-mail: avnish951729@gmail.com

P	Distance between two adjacent rib [mm]
q''	Heat flux [W/m^2]
u	Air flow velocity in x-directionm/s
w	Width of duct [mm]
n	Number of fins in a row (along flow direction)
d	Diameter of rib [mm]

Dimensionless Parameter

E/H	Rib-to-channel height ratio
L/D	Length of duct-to-hydraulic diameter ratio
P/E	Relative roughness pitch

1 Introduction

A variety of ever-evolving technologies have harnessed solar energy. Before 1970, a few studies and improvements turned into accomplished in some nations to take advantage of sun strength efficiently; however, the maximum of these paintings remained especially theoretical. After the considerable upward push in oil expenses in 1971s, numerous nations started to draw up enormous studies and improvement applications to take advantage of sun strength. They developed some powerful devices to utilize sun strength for space heating, timber seasoning, drying crops, etc. An easy sun air heater includes a collector surface to seize sun radiation and, through conduction heat transfer, transfers this sun (thermal) strength to air. This heated air is then transferred to the constructing area.

2 Literature Review

Yadav and Bhagoria [1] performed numerical study on solar air heater with triangular ribs (Fig. 1) and found a significant increment in convective heat transfer rate compared to solar air heater without triangular rib.

Chaube et al. [2] studied a two-dimensional numerical analysis of a solar air heater with artificial roughness of eight different shapes of fins (Fig. 2). Absorbents include rectangles, squares, chamfers, and triangles. Standard k-ε turbulence was used for the simulation. The best performance was seen in the size of the rectangular ribs. The results of the CFD simulations were compared with the existing results of the experiment.
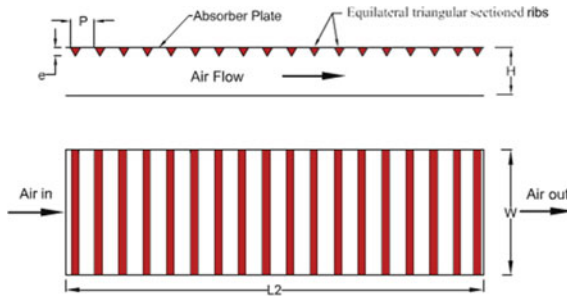
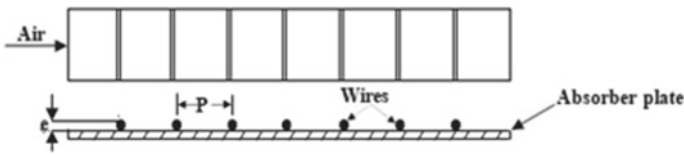**Fig. 1** Roughened absorber plate schematic [1]

Fig. 2 Transverse wire ribs [2]

Karmare and Tikekar [3] conducted a numerical study of a coarse solar air heater using grit ribs of metal as the coarseness factor of the collector. Standard k-ε turbulence was used for the simulation. The authors reported that a collector with a cross-section rib of square shape and an incidence angle of 58° was hydraulically more effective. Prasad and Malik [4] investigated transverse wire rib coarseness at (E/D: 0.017, P/E:11.9, Re: 10,000–40,000), and they reported a 13% improvement in the efficiency of heat transfer at a Re value of 40,000 over duct without wired rib. Choi and Choi [5] experimentally determined the electrical and thermal efficiency of a photovoltaic/thermal solar air collector by using non-uniform transverse rib at the back of the photovoltaic module. A significant improvement in the thermal efficiency from 35.2 to 56.72% was noticed when mass flow rate of air was increased from 0.0198 to 0.0769 kg/s. Square wave profile transverse ribs were used as roughness elements to improve the Nu of a solar air heater [6]. Nu increased 2.14 times that of the smooth duct at the cost of friction factor enhancement of 3.55 times of a smooth duct. A solar air heater with an arched absorber plate using turbulators was proposed by Singh [7]. A significant improvement in Nu is observed at a high Reynolds number (above 1000). Hans et al. [8] experimentally studied the effect of the discrete V-down ribs on the thermos-hydraulic performance of a solar air heater by varying roughness pitch, angle of attack, and relative roughness height. They determined the optimum parameters for the maximum Nu and f, which were noted as 3.04 and 3.11, respectively.

To the best of the author's knowledge, it is believed that the impact of the circular fins on the performance of the SAH with varying heights in the turbulence regime has yet to be studied. Thus, the objective of the present work is to obtain the heat

transfer rate and frictional head loss in terms of the absorber surface temperature and friction factor in a SAH by incorporating the fins over the absorber surface with varying fin height. The main aim is to minimize the temperature difference between the absorber surface temperature and the outlet temperature of air to get a maximum Nu. Employing fins on the absorber surface would result in decreasing the temperature which motivates the authors to conduct the present work to obtain the optimum geometric configuration. Since the temperature variation of the outlet air is negligible to the absorber surface temperature variation for various cases (because the boundary layer thickness is negligible with respect to the outlet area), we would focus mainly on the absorber surface temperature in the results and discussions section in order to predict the performance of SAH.

3   Problem Defination and Numerical Method

3.1   Problem Definition

Figure 3 shows the schematic diagram of a solar air heater (SAH) in front and top views. The SAH consists of a channel of 1 m in length, 0.025 m in height, and 0.25 m in width which is covered by an absorber plate. The absorber plate acts as a solar collector. The air blown through SAH gets heated by taking the heat from the absorber plate through convective heat transfer. In the present work, the main objective is to improve the heat transfer from the absorber plate which is achieved by using circular fins underneath the absorber plate. The fins are placed in a rectangular fashion. There are five fins in a row, and the number of rows is varied from 2 to 5. Thus, there are five cases with a total number of fins as 10 (2 row), 15 (three rows), 20 (four rows), and 25 (five rows) with uniform inter-fin spacing. The fin height h is varied from 5 to 15 mm, and the margin **m** is kept the same at 0.25 m on both the sides of first and last row of fins for all types of fin arrangements. The absorber plate is exposed to uniform solar heat flux which convects heat to the fluid.

3.2   Governing Equations

Continuity, momentum, and energy equations are solved to obtain the temperature and velocity field inside the SAH. Two additional equations are solved to capture turbulence in the flow. Following assumptions are made before solving the equations:
   Assumptions

1. Steady flow.
2. Three-dimensional incompressible flow.
3. Constant thermophysical properties of air and aluminium fins.
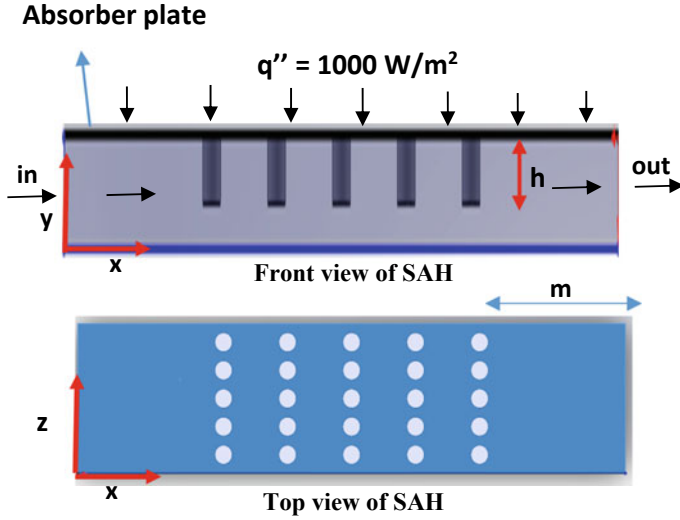
Absorber plate

Fig. 3 Schematic diagram of solar air heater (SAH)

Continuity equation:

$$\frac{\partial}{\partial X_i}(\rho u_i) = 0 \tag{1}$$

omentum equation:

$$\frac{\partial}{\partial X_i}(\rho u_i u_j) = -\frac{\partial P}{\partial X_i} + \frac{\partial}{\partial X_j}[\mu\left(\frac{\partial u_i}{\partial X_j} + \frac{\partial u_j}{\partial X_i}\right) + \frac{\partial}{\partial X_j}(-\rho u'_i u'_j) \tag{2}$$

Energy equation:

$$\frac{\partial}{\partial X_i}(\rho u_i T) = \frac{\partial}{\partial X_j}[(\tau + \tau^{\cdot})\frac{\partial T}{\partial X_j} \tag{3}$$

Here, $\tau = \frac{\mu}{P_r}$ and $\tau_t = \frac{\mu_t}{P_{rt}}$
k-ε RNG equations:

$$\frac{\partial}{\partial X_i}(\rho k u_i) = \frac{\partial}{\partial X_j}\left[\left(\mu + \frac{\mu_t}{\sigma_k}\right)\left(\frac{\partial k}{\partial X_j}\right)\right] + P_k - \rho\epsilon \tag{4}$$

$$\frac{\partial}{\partial X_i}(\rho\epsilon u_i) = \frac{\partial}{\partial X_j}\left[\left(\mu + \frac{\mu_t}{\sigma_\epsilon}\right)\left(\frac{\partial\varepsilon}{\partial X_j}\right)\right] + C_{1\varepsilon}\frac{\varepsilon}{k}P_k - C_{2\varepsilon}{}^*\frac{\varepsilon^2}{k}\rho \tag{5}$$

where $\mu_t = \rho C_\mu \frac{k^2}{\varepsilon}$, $C_{2\varepsilon}{}^* = C_{2\varepsilon} + \frac{C_\mu \eta^3 \left(1 - \frac{\eta}{\eta_0}\right)}{1 + \beta \eta^3}$, and $\eta = S\frac{k}{\varepsilon}$, and $S = \left(2S_{ij}S_{ij}\right)^{\frac{1}{2}}$.

The model constants are $C_\mu = 0.0845$, $C_{1\varepsilon} = 1.42$, $C_{2\varepsilon} = 1.68$, $\eta_0 = 4.38$, $\eta_0 = 0.012$, $\sigma_k = \sigma_\epsilon = 0.7194$

k-ε RNG turbulence model [9] is used to capture the turbulence in a flow.

Diffusion equation has been solved within the aluminium fins employing the heat flux and temperature continuity at the fin surface.

3.3 Boundary Conditions

The rectangular solution domain is enclosed by the wall boundaries such as the absorber plate and bottom insulated plate along with the inlet and outlet. No-slip condition is applied on wall surface. Both tangential and normal components of fluid velocity are set to zero at the wall because of no-slip condition. A uniform intensity of a solar radiation (1000 W/m^2) is incident on the absorber plate (top surface of SAH), and the bottom surface is adiabatic. The inlet temperature of air is fixed at 300 K with a uniform velocity. By using the value of Re, the average velocity of flow at inlet is determined, and the range of average flow velocity falls between 1.67 and 5.142 m/s. The outlet of the computational domain is set to zero-gauge pressure.

3.4 Output Parameters

After solving the governing equations with appropriate boundary conditions, the results are plotted in terms of the absorber surface temperature, outlet temperature of air, Nusselt number, and friction factor. The average surface and outlet temperature are measured by taking surface integrals over the local temperature of the surface of interest. Then Nu is computed using the absorber surface temperature (T_s) and the mean fluid temperature ($T_m = \frac{T_{in} + T_{out}}{2}$) as:

$$Nu = \left(\frac{q''}{T_s - T_m}\right)\frac{D_h}{k_f}. \tag{6}$$

where D_h and k_f are the hydraulic diameter of the SAH and thermal conductivity of air.

The friction factor is calculated as

$$f = \frac{\Delta p \times 2 \times D_h}{\rho L v^2} \tag{7}$$

Table 1 Test of validation

Re	Nu (present work)	Nu [10]	% error
12,500	83.61	90	7.64
52,500	190.08	197	3.5
86,000	264.66	270	2.01

3.5 Numerical Solver

Ansys Fluent [5] is used to simulate the problem. The computational domain is divided into a number of cells over which the discretized governing equations are integrated to for a set of nonlinear algebraic equations. The equations are solved in the solver of Ansys Fluent with the appropriate boundary conditions to obtain the pressure, velocity, and temperature within the computational domain. The convergence criteria for continuity, momentum, and energy equations are set to 10^{-4}, 10^{-5}, and 10^{-6}.

3.6 Validation

Before starting the simulation, the present solver is validated with the experimental results of Alfarawi et al. [10] for the solar air heater with p/e $= 26.6$. The comparison is presented in Table 1. The difference between the present solution and experimental results lies within an acceptable limit which affirms the present solver.

4 Results and Discussion

The performance of the SAH mainly depends on the average temperature of the absorber plate since the variation in the outlet temperature of the air is very marginal. Thus, the present section mainly focusses on the variation of the absorber surface temperature against the pertinent input parameters. In addition, the friction factor variation within the channel is also discussed.
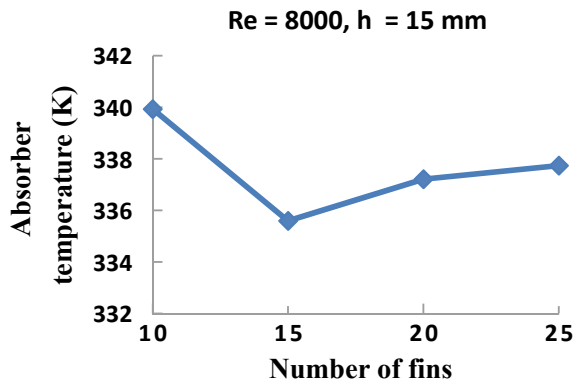
4.1 Absorber Surface Temperature Variation with Number of Fins

Figure 4 shows the variation of the absorber surface temperature with number of fins installed on the absorber surface. It can be observed that the absorber surface temperature reduces when number of fins increases from 10 to 15. It is to be marked

that those 10 fins represent two rows of fins and each row has 5 fins. Likewise, 25 fins represent five rows, and each row is having five fins (Fig. 3). Thus, when number of fin increases, the air has an increased contact surface area which removes more heat from the absorber plate via fins. Thus, the temperature reduces to 335 K from 340 K when the number of fins is increased from 10 to 15. However, when number of fins is increased further, the flow obstruction becomes significant which leads to a lower heat transfer. Thus, the temperature starts rising with number of fins and reaches a 338 at number of fins of 25.

Figure 5 shows the variation of the absorber surface temperature with number of fins at Re = 16,000. Figure 4 shows the same for a lower Re of 8000. The trend of the variation is exactly same for both Re; however, the temperature is less for the higher Reynolds number. The minimum temperature achieved for Re = 8000 is 336 K where as it 323 for Re of 16,000. For both cases, the minimum temperature is achieved at 15 fins. The high Reynolds number signifies in a stringer convective current to extract a significant heat away from the absorber plate which results in a lower absorber temperature.

Fig. 4 Variation of absorber surface temperature with number of fins at Re = 8000, h = 15 mm

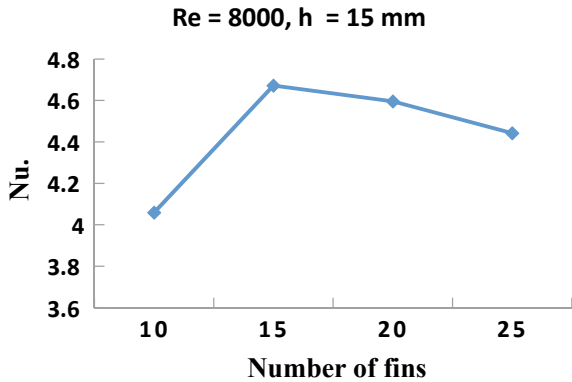**Fig. 5** Variation of absorber surface temperature with number of fins at Re = 16,000, h = 15 mm
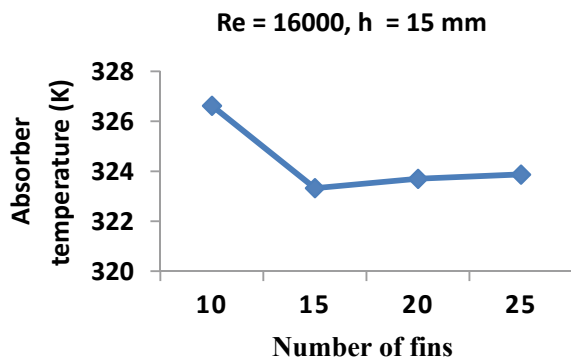
## 4.2 Variation of Nusselt Number with Number of Fins

Figure 6 shows the variation of the average surface Nusselt number with number of fins. Nu depends on the relative difference between the absorber surface temperature and the fluid temperature. Since the absorber surface temperature is minimum at 15 fins, Nu becomes maximum. It is to be marked that, the air temperature at outlet varies minutely for all the cases; however, the absorber surface temperature varies drastically. Thus, the discussions of the present work mainly focus on the absorber surface temperature which is the primary factor for evaluation of the performance of the SAH.

Figure 7 shows the friction factor variation with the number of fins. The friction factor increases monotonously with number of fins owing to the increase in flow resistance. Thus, by combining Figs. 6 and 7, it is concluded that SAH with 15 number of fins is more effective in enhancing the heat transfer and reducing the frictional resistance.
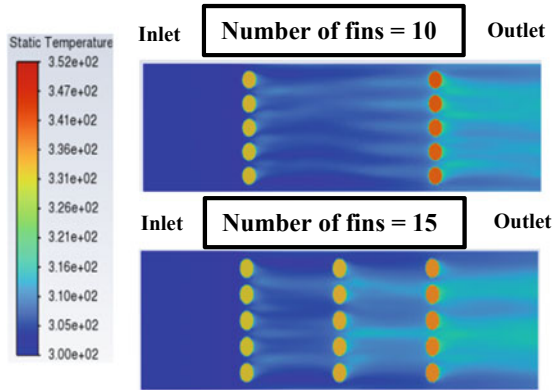

Fig. 6 Variation of absorber surface temperature with number of fins at Re = 16,000, h = 15 mm

Fig. 7 Variation of friction factor with number of fins
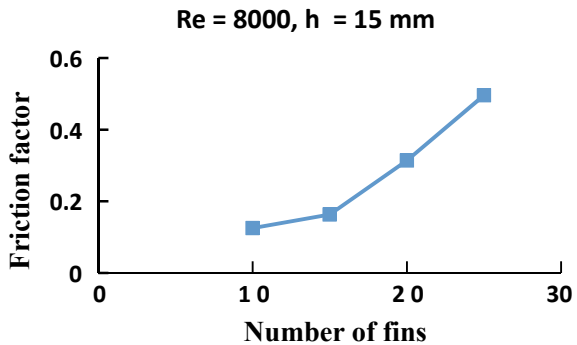
Fig. 8 Temperature contour on absorber surface with various number of fins

4.3 Temperature Contour on Absorber Plate at Various Numbers of Fins

Figure 8 shows the temperature distribution over the absorber surface with 10 and 15 fins. The fins on the third row for 3×5 case are at a lower temperature than the fins at second row of 2×5 fins. It means that there is more heat transfer for 15 number of fins which results in a lower absorber surface temperature. When number of fins increases, air gets obstructed causing a lower convective heat transfer with an outcome of higher temperature.

4.4 Absorber Surface Variation with Height of Fins

Fig. 9 shows the variation of the absorber surface temperature with fin height. With increasing in fin height, the contact surface area with air increases which improves the heat transfer rate resulting in a lower absorber surface temperature. The same phenomenon is observed for both Re of 8000 and 16,000. When fin height increases to 23 mm, the absorber temperature reaches minimum at 330 K and 320 K for Re of 8000 and 16,000.

5 Conclusions

Based on the results and discussions, the following conclusions have been drawn:

- The rate of heat transfer in case of finned solar air heater is more compared to the conventional solar air heater.

Fig. 9 Variation of absorber surface temperature with fin height for **a** Re = 8000, **b** Re = 16,000

Re = 8000, number of fins = 15

(a)

Re = 16000, number of fins = 15

(b)
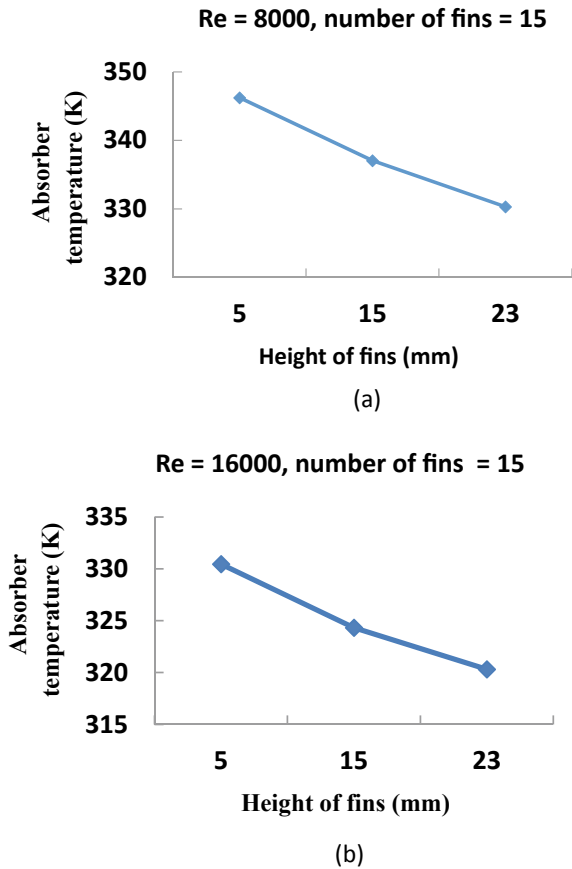
- As Reynolds number increases, the heat transfer rate between collector surfaces and flowing fluid increases.
- With increasing in number of fins from 10 to 15, Nu increases; however, a decrease in Nu is observed when the number of fins increases from 15 to 25.
- Absorber surface temperature decreases linearly with fin height.

References

1. Yadav AS, Bhagoria JL (2014) A numerical investigation of square sectioned transverse rib roughened solar air heater. Int J Therm Sci 79:111–131
2. Kumar S, Saini RP (2009) CFD based performance analysis of a solar air heater duct provided with artificial roughness. Renew Energy 34:1285–1291
3. Yadav AS, Bhagoria JL (2013) A CFD based heat transfer and fluid flow analysis of a solar air heater provided with circular transverse wire rib roughness on the absorber plate. Energy 55:1127–1142
4. Prasad BN, Saini JS (1988) Effect of artificial roughness on heat transfer and friction factor in a solar air heater. Sol Energy 41(6):555–560
5. Choi HU, Choi KH (2020) Performance evaluation of PV/T air collector having a single-pass double-flow air channel and non-uniform cross-section transverse rib. Energies 13(9):2203
6. Singh I, Singh S (2018) CFD analysis of solar air heater duct having square wave profiled transverse ribs as roughness elements. Sol Energy 162:442–453
7. Singh S (2017) Performance evaluation of a novel solar air heater with arched absorber plate. Renew Energy 114:879–886
8. Hans VS, Saini RP, Saini JS (2010) Heat transfer and friction factor correlations for a solar air heater duct roughened artificially with multiple v-ribs. Sol Energy 84(6):898–911
9. ANSYS, INC. Release 14.0, Canonsburg, Pennsylvania, USA
10. Alfarawi S, Abdel-Moneim SA, Bodalal A (2017) Experimental investigations of heat transfer enhancement from rectangular duct roughened by hybrid ribs 118:123–138

Effect of Concentration Ratio on Flow Pattern in Solar CPC Cavity

Aditi Garg, Bahni Ray, and Sanjeev Jain

Abstract A two-dimensional numerical model of the compound parabolic collector (CPC) with a tubular receiver has been developed to study the effect of the concentration ratio of the collector on the flow profile in a horizontally held cavity and heat losses by the collector. Six concentration ratio (CR) values have been analyzed for three diameters. As per the literature, very few studies have investigated this effect for a horizontal CPC cavity. The convective and radiative heat losses have been modeled using the k-epsilon turbulence and surface-to-surface (S2S) radiation models. The heat conduction in walls is considered by giving suitable wall thickness. Different cases have been simulated to obtain total heat losses, Rayleigh number, velocity vectors, and temperature contours. The results showed total heat losses, and the Rayleigh number increased with the concentration ratio. A symmetric bicellular flow pattern was obtained in the CPC cavity for four CR values (1.1, 1.4, 2.9, and 3.9). However, CR values of 2.0 and 2.5 showed a deviation from this behavior by showing an asymmetric behavior for the flow pattern for the same boundary conditions.

Keywords Solar collector · Cavity · Computational fluid dynamics · Aspect ratio · Inclination

Nomenclature

AR	Ratio of height to aperture width –
C_p	Specific heat capacity [J kg^{-1}.K^{-1}]
$C_{1\varepsilon}, C_{2\varepsilon}, C_\mu$	Turbulence model constants –
D_r	Receiver diameter [mm]
G_b	Generation of turbulence kinetic energy due to buoyancy [kg m^{-1} s^{-3}]
G_k	Generation of turbulence kinetic energy due to mean velocity gradients [kg m^{-1} s^{-3}]

A. Garg · B. Ray (✉) · S. Jain
Department of Mechanical Engineering, IIT Delhi, New Delhi 10016, India
e-mail: bray@mech.iitd.ac.in

g	Gravitational acceleration [m s^{-2}]
H	Height of CPC [m]
h_w	Wind heat transfer coefficient [W m^{-2} K^{-1}]
k	Turbulent kinetic energy [m^2 s^{-2}]
Q_T	Total heat loss from receiver [W]
Ra_H	Rayleigh number based on height of CPC –
T	Temperature [K]
T_r	Receiver temperature [K]
T_a	Ambient temperature [K]
t_{ap}	Aperture cover thickness [mm]
u	Velocity [m s^{-1}]
TR	Ratio of reduced height to full height of CPC –
W_{ap}	Aperture width [mm]

Greek Symbols

ε_{ap}	Aperture cover emissivity –
ρ	Density [kg m^{-3}]
ε	Turbulent dissipation rate of k [m^2 s^{-3}]
μ	Dynamic viscosity [kg m^{-1} s^{-1}]
θ_A	Half acceptance angle of CPC [°]
λ	Thermal conductivity [W m^{-1} K^{-1}]
ε_r	Receiver tube emissivity –
ε_{ref}	Reflector wall emissivity –
ΔT	Temperature difference [K]
β	Thermal expansion coefficient [K^{-1}]
φ	Transverse tilt angle [°]
μ_t	Turbulent viscosity [kg m^{-1} s^{-1}]
σ_k	Turbulent Prandtl numbers for k –
σ_T	Effective Prandtl number for T –
σ_ε	Turbulent Prandtl numbers for ε –

Abbreviations

AR	Aspect ratio –
CPC	Compound parabolic collector –
CR	Concentration ratio –
$S2S$	Surface-to-surface radiation –
TR	Truncation ratio

1   Introduction

Solar compound parabolic collectors, also known as CPCs, have been gaining popularity worldwide due to their applications in sorption cooling and heating, domestic water heating, and industrial processes for low to medium temperature ranges (60–240 °C) [1, 2]. CPCs can receive solar energy over a large range without a tracking system since they have a low concentration and a wide acceptance angle. These concentrating collectors can also collect direct and diffuse solar radiation. The current generation of CPCs is the product of years of research and development work conducted by various research groups worldwide.

Many changes have been made to the geometry of both the receiver and the CPC to improve its thermal, optical, and electrical performances. Receivers used for CPCs have different geometries: cylindrical, flat plate, inverted-V, and vertical fin. The tubular receiver is the most commonly used receiver due to its simplicity and convenience, and it outperforms the flat plate receiver above 340 K [3, 4].

The CPC consists of a receiver tube, an aperture cover, and two reflector walls with involute parabolic shapes. The reflector walls and the aperture cover form a closed space or cavity that is mostly air-filled or evacuated. The solar radiation passes through the aperture cover and is absorbed by the receiver tube directly or after reflection from the reflector walls. The hot receiver transfers heat by convection and radiation to the surrounding air and cold surfaces of the cavity (aperture cover and reflector walls). The hot air near the receiver surface rises, collides with cold surfaces, and flows down the reflector walls. This creates natural convection airflow in the receiver's cavity, causing heat loss. This airflow within the cavity is influenced by various factors such as geometry, orientation, environmental conditions, optical properties, fluid properties, and boundary conditions. Numerous studies have been conducted to investigate the impact of these variables on the airflow pattern in the cavity of the CPC, which will be discussed in the next section.

2   Literature Review and Objective

Winston [5] introduced the CPC as an optical concentrator for photovoltaic and thermal applications. After that, Winston and Hinterberger [6] and Rabl and Winston [7] provided further explanations on the working of CPC. The natural convective flow in the cavity was studied by Abdel-Khalik et al. [8] using finite element methods for a horizontal CPC cavity with a planar receiver for CR ranging from 2 to 10 and truncation ratios (TR) of 1/3, 2/3, and 1. They found that at high CR values, convections get suppressed, and a stable unicellular convection pattern cannot be maintained at very high Rayleigh numbers. Prapas et al. [9] analyzed the steady-state temperature distributions inside the CPC cavity with a tubular receiver using a Mach Zender interferometer. The effect of CR (1.56, 2.67, and 4.13), transverse

tilt angles (0°, 10°, 20°, 30°), and receiver temperatures were investigated on the average Nusselt number.

The numerical study conducted by Chew et al. [3] for a two-dimensional CPC cavity for transversely tilted (0°, 15°, 30°, 60°, 90°) collector for a CR = 2 and truncation ratios (TR) of 1/3, 2/3, and 1 found that the convective flow patterns in the cavity are dependent on the tilt angles, Grashof number, and height of collector (H). After initialization from pure conduction mode for all TR and tilt angles, it was found that the flow patterns were bicellular, with two cells lying symmetrically to the axis of the collector. However, at low Grashof number (100–5000), for all 3 TR, the flow was found to be bicellular for 0° and 15°, and as the tilt angle was increased, the flow became unicellular. For a high Grashof number (higher than 5000), the flow was bicellular for a TR of 1/3 for 0° and 15° and one cell plus a weak counter-rotating cell for all angles till 60°. The flow was not bicellular for tall cavities (TR = 2/3, 1); instead, it was one cell plus a weak counter-rotating cell for all angles till 60°. The flow was unicellular at 90° for a Grashof number greater than 100. Eames and Norton [10] reported the effect of adiabatic side walls and realistic side walls with a back loss on natural convective airflow in the CPC cavity for CR = 1.15, 1.41, and 2.0 for four values of tilt angles (0°, 15°, 30°, 45°). It was found to have bicellular flow for 0° for all CR for both wall boundary conditions. For CR = 1.15, for tilt angle less than or equal to 30°, a bicellular flow was reported for realistic side walls and a unicellular flow for adiabatic conditions, while for CR = 1.41, a similar behavior was observed for tilt angle less than or equal to 15°. For CR = 2, however, the transition from bicellular to unicellular occurred at a smaller tilt angle for both wall conditions. They also concluded that the tilt angle associated with the transition from bicellular to unicellular flow is affected by boundary conditions and concentration ratios (CR). The transverse aspect ratio and height had a significant impact on the convective flow pattern in the cavity.

Previous studies have assumed the convective heat transfer to be independent of radiative exchange between the surfaces. The study conducted by Diaz and Winston [11] studied the effect of surface radiation on the convective airflow in the CPC cavity for CR = 2 and 4 and surface emissivity of 0, 0.1, 0.5, and 1. It was found that the onset of the fluid motion was delayed by the level of concentration when radiation was neglected. However, when radiation was considered, it significantly affected the cavity's temperature distribution. Singh and Eames [12] have experimentally studied the natural convective heat transfer occurring in the CPC cavity for CR = 2 and TR of 1/2, 3/4, and 1 with a planar receiver for longitudinal (0°-10°) and transverse tilt angles (0–40°). They observed three-dimensional temperature gradients in the cavity. A bicellular flow was seen for a horizontally held collector (0°). However, it became unicellular at a transverse tilt angle of 20° for TR = 3/4 and 1 and 30° for TR = ½. Antonelli et al. [4] analyzed the CPC with planar and tubular receivers for tilt angle values of 35°, 40°, 45°, and 50° for a CR = 2. They observed a unicellular flow pattern for these inclinations. Reddy et al. [13] conducted a parametric study to analyze their effect on heat losses for a CPC with a planar receiver for a CR = 2. The airflow in the cavity was bicellular for the horizontally aligned cavity and unicellular flow for all other angles.

As per the literature review, very few studies have analyzed the flow pattern for a horizontally inclined CPC cavity for a tubular receiver considering the effect of both natural convection and surface radiation on the airflow in the cavity for different concentration ratios (CR). In the present work, the 2D CPC numerical model developed in the previous study of Garg et al. [14] was modified and extended to study the fluid flow pattern in the horizontally inclined cavity at various concentration ratios and receiver diameters.

3 Materials and Methods

3.1 Numerical Model

A two-dimensional numerical model of CPC with a tubular receiver was developed in Ansys 19.2. Figure 1a depicts a full-height CPC with a half acceptance angle θ_A for CR = 2.0. Now CR = 1/ sin (θ_A) for a full-height CPC. For $\theta_A = 30°$, angle θ was taken from 0° to 120° for the involute section and 120°-240°for the parabolic section of the curve, as depicted in Fig. 1b. The receiver radius (R) was taken as 7.5 mm with a half acceptance angle (θ_A) of 30°, and height from the center of the receiver tube (H) was 96.62 mm. A 1 mm gap was maintained between the contact points on the reflector wall and the receiver to prevent conduction loss from the receiver to the reflector. Equations (1) and (2) were used to calculate the $\rho(\theta)$, which represented the distance from the receiver tube to the curve along the tangent line, and Eqs. (3) and (4) were used to determine the coordinates X and Y.

$$\rho(\theta) = R\theta, \, |\theta| \leq \theta_A + \pi/2 \tag{1}$$

$$\rho(\theta) = R\left\{\frac{\theta + \theta_{A+}(\pi/2) - \cos(\theta - \theta_A)}{1 + \sin(\theta - \theta_A)}\right\}, \, \theta_A + \pi/2 \leq \theta \leq \frac{3\pi}{2} - \theta_A \tag{2}$$

$$X = R \sin\theta - \rho(\theta) \cos\theta \tag{3}$$

$$Y = -R \cos\theta - \rho(\theta) \sin\theta \tag{4}$$

The 2D model was validated with the computational results reported in the literature [4, 14]. The mesh sensitivity study was conducted with element sizes varying from 0.5 to 0.9 mm to obtain total thermal losses from the receiver, including both convective and radiative heat loss. The element size of 0.6 mm was considered for meshing. The mesh was refined to capture velocity and temperature gradients and resolve the viscous sub-layer of air near boundary walls. The maximum value of y + was ensured to be less than one. The orthogonal quality ranged between 0.9

Fig. 1 a Geometric
dimensions of CPC,
b elements used to generate
curve coordinates of CPC

(a)

(b)
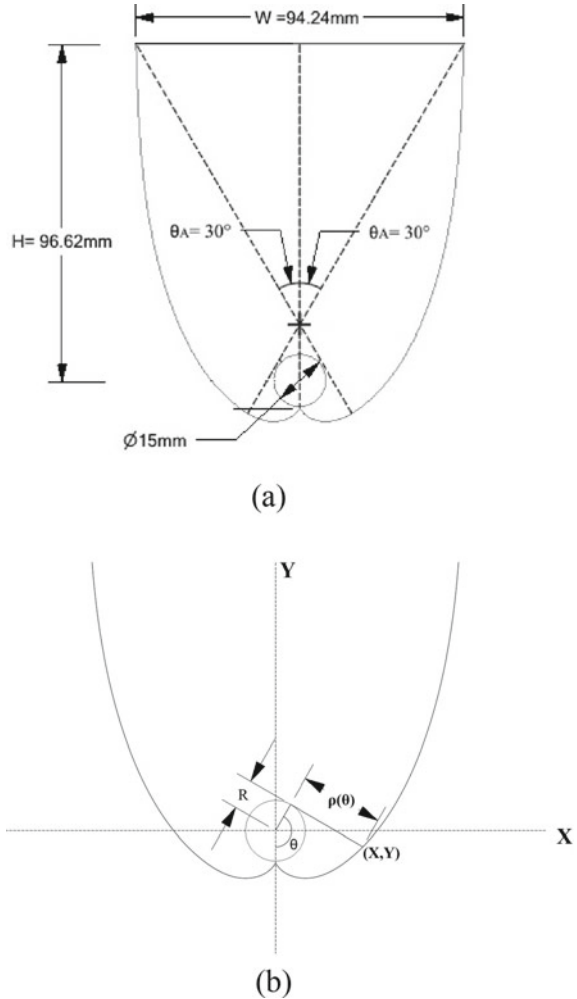
and 1, indicating a high-quality mesh. Air in the cavity was taken at atmospheric
pressure of 101,325 Pa and modeled as an incompressible ideal gas. The air density
was considered temperature-dependent for the buoyancy effects generation and the
study of free convection in the cavity. The thermophysical properties of solids were
considered constant, while air properties were calculated at a temperature average
of the receiver and ambient temperature. The material properties are tabulated in
Table 1 and were taken from the previous study [14].

Table 1 Thermophysical properties of materials

Material	λ (W/m.K)	ρ (kg/m^3)	C_p (J/kg.K)
Aluminum (reflector walls)	202.4	2719	871
Glass (aperture cover)	1	2530	840
Copper (receiver)	387.6	8978	381

3.2 Governing Equations

The steady-state simulation for the developed model was performed with a Navier–Stokes solver employing a pressure-based solver with double precision. For buoyancy forces, gravity was applied in the negative y-direction. The Rayleigh number (Ra_H), which describes the buoyancy-driven fluid flow within the CPC cavity, was calculated using Eqs. (5, 6, and 7). It considered characteristic length as height (H) of CPC and the temperature difference between the receiver temperature (T_r) and ambient temperature (T_a).

$$\Delta T = T_r - T_a \tag{5}$$

$$\beta = \frac{2}{T_r + T_a} \tag{6}$$

$$Ra_H = \frac{g * \beta * \cos\varphi * \Delta T * H^3 * Pr * \rho^2}{\mu^2} \tag{7}$$

The continuity equation, RANS equation for momentum, and energy equation were used to solve the fluid flow and heat transfer problems in the model. Turbulence flow was modeled using the conventional k-epsilon model with enhanced wall treatment, which resolves the transport equations for turbulent kinetic energy and dissipation rate [13–15]. The governing equations are mentioned as Eq. (8, 9, 10, 11, 12, 13). Surface-to-surface (S2S) radiation model with a convergence criterion of 10^{-7} was used to solve the radiation heat transfer. It assumed all surfaces to be opaque, diffuse, and gray and medium to be non-participating.

Continuity equation

$$\frac{\partial}{\partial x_j}(\rho u_j) = 0 \tag{8}$$

Momentum equation

$$\frac{\partial(\rho u_i u_j)}{\partial x_j} = -\frac{\partial P}{\partial x_i} + \frac{\partial}{\partial x_j}\left[(\mu + \mu_t)\left(\frac{\partial u_i}{\partial x_j} + \frac{\partial u_j}{\partial x_i}\right) + \rho g_i\right] \tag{9}$$

Energy equation

$$\frac{\partial\left(\rho u_j C_p T\right)}{\partial x_j} = \frac{\partial}{\partial x_j}\left[\left(\lambda + \frac{\mu_t C_p}{\sigma_T}\right)\frac{\partial T}{\partial x_j}\right] + \frac{\partial u_i}{\partial x_j}\left[(\mu + \mu_t)\left(\frac{\partial u_i}{\partial x_j} + \frac{\partial u_j}{\partial x_i}\right)_i\right] + u_j\frac{\partial P}{\partial x_j}$$
(10)

Transport equation for turbulent kinetic energy

$$\frac{\partial(\rho k u_i)}{\partial x_i} = \frac{\partial}{\partial x_j}\left[\left(\mu + \frac{\mu_t}{\sigma_k}\right)\frac{\partial k}{\partial x_j}\right] + G_k + G_b - \rho\varepsilon$$
(11)

Transport equation for turbulent dissipation rate

$$\frac{\partial(\rho\varepsilon u_i)}{\partial x_i} = \frac{\partial}{\partial x_j}\left[\left(\mu + \frac{\mu_t}{\sigma_\varepsilon}\right)\frac{\partial \varepsilon}{\partial x_j}\right] + C_{1\varepsilon}\frac{\varepsilon}{k}G_k - \rho C_{2\varepsilon}\frac{\varepsilon^2}{k}$$
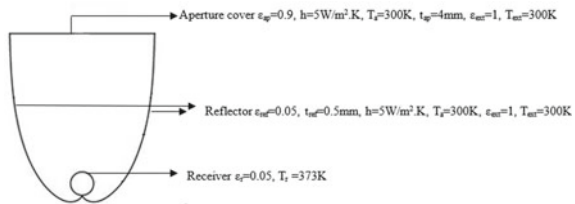(12)

Turbulent viscosity

$$\mu_t = \rho C_\mu \frac{k^2}{\varepsilon}$$
(13)

3.3   Boundary Conditions

The receiver tube was considered at a constant temperature of 373 K, assuming that the receiver completely absorbs the solar radiation. The receiver emissivity was considered to be 0.05. The aperture cover and reflector walls were given a mixed boundary condition to account for convective and radiative heat transfer to the surroundings, with a wind heat transfer coefficient of 5 W/m^2.K, ambient temperature of 300 K, and internal emissivity of 0.9 and 0.05 for aperture cover and reflector walls. The thicknesses for the reflector wall and aperture cover were set to 0.5 and 4 mm to account for wall conduction. The external emissivity and temperature were set to 1 and 300 K. All the walls were given no-slip conditions. The boundary conditions were considered from the previous study [4, 14]. The transverse tilt angle is taken to be 0°. Figure 2 depicts the boundary conditions considered for the model.

Fig. 2 Boundary conditions for the numerical model

Aperture cover ε_{ap}=0.9, h=5W/m^2.K, T$_a$=300K, t$_{ap}$=4mm, ε_{ext}=1, T$_{ext}$=300K

Reflector ε_{ref}=0.05, t$_{ref}$=0.5mm, h=5W/m^2.K, T$_a$=300K, ε_{ext}=1, T$_{ext}$=300K

Receiver ε_r=0.05, T$_r$=373K

3.4 Solution Methods

Calculations were performed with pressure-based steady formulations using a coupled scheme with body force-weighted discretization for pressure and a second-order upwind approach for momentum, energy, turbulent kinetic energy, and turbulent dissipation rate. Pseudo-transient formulation, hybrid initialization, and convergence criteria of 10^{-6} for energy and 10^{-3} for all other variables were taken into consideration.

4   Results and discussion

In the present work, CPCs with different concentration ratios were analyzed to study their effect on the flow profile in the cavity. The isotherms and velocity vectors obtained for the various cases were studied to understand the effect of CR. Now CR = $1/\sin(\theta_A)$ for a full-height CPC. The concentration ratios considered are 1.15, 1.41, 2, 2.5, 2.92, and 3.86 for half acceptance angle (θ_A) values of 60°, 45°, 30°, 23.5°, 20°, and 15°.

## *4.1 Effect of Concentration Ratios on the Flow Profile*

The flow profiles obtained for a horizontal cavity are mostly symmetric and bicellular for the various cases in the literature. However, for specific concentration ratios, a deviation was found from this behavior. However, it became symmetric as the height was reduced.

In this case, a receiver tube of diameter 15 mm was considered for different CR for full height. The boundary conditions were kept the same as mentioned in the above section of boundary conditions. The velocity vector and isotherms obtained for the analyzed concentration ratios are shown in Figs. 3 and 4. Table 2 summarizes the values for total heat loss, Rayleigh number, aspect ratio, and trends for flow profile for the analyzed concentration ratios. The aspect ratios, total heat losses, and Rayleigh number increased with increasing CR. The flow profiles obtained were symmetric for all CR except 2.0 and 2.5. They show a kind of imbalance in the flow profile leading to one large, strong cell at the center and one weak cell pushed to the side of the cavity, as shown in Fig. 3c, d. Another analysis was carried out by varying the diameter of the receiver tube to 10 and 30 mm for CR = 2 and 2.5. It was found to show similar asymmetric behavior for these two diameters, as shown in Figs. 5 and 6.
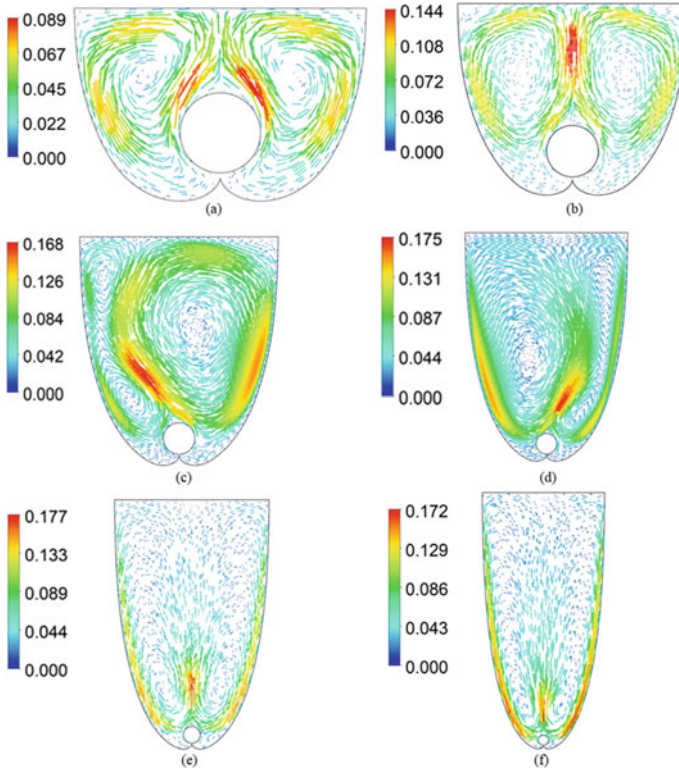
Fig. 3 Velocity vectors (m/s) for receiver diameter of 15 mm with CR values **a** 1.15, **b** 1.41, **c** 2.0, **d** 2.5, **e** 2.9, **f** 3.86

It was observed that as CR increases, the aspect ratio (AR), which is the ratio of height (H) to aperture cover width (W_{ap}), also increases. This leads to decreased air temperature in the cavity, as shown in Fig. 4. It is further noticed that with increased CR, the regions in the cavity with either stagnant air or very low airflow velocity increase in size. It can be concluded that the airflow patterns undergo a transition when CR moves from 1.41 to 2.9, as depicted in Fig. 3.
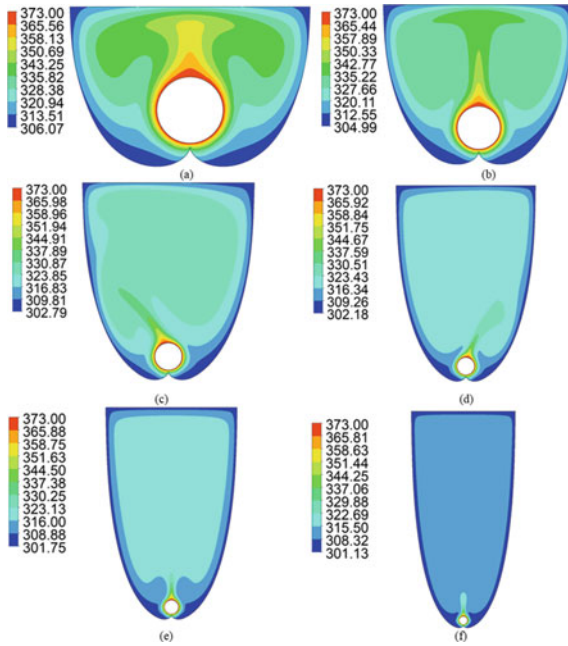
Fig. 4 Temperature contours for receiver diameter of 15 mm with CR values **a** 1.15, **b** 1.41, **c** 2.0, **d** 2.5, **e** 2.9, **f** 3.86

Table 2 Summary of flow pattern and thermal performance at various CR values ($D_r = 15$ mm)

CR (−)	θ_A (°)	AR (−)	Q_T (W)	Ra_H (−)	Flow behavior
1.15	60	0.43	25.3	5.16E + 04	Symmetric
1.41	45	0.64	27.9	3.20E + 05	Symmetric
2.0	30	1.01	30.5	3.65E + 06	Asymmetric
2.5	23.5	1.30	31.0	1.47E + 07	Asymmetric
2.9	20	1.52	31.3	3.76E + 07	Symmetric
3.86	15	2.01	32.0	2.01E + 08	Symmetric
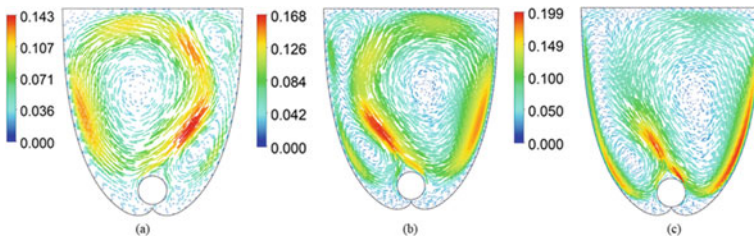
Fig. 5 Velocity vectors for CR $= 2$ for different receiver diameters **a** 10 mm, **b** 15 mm, **c** 30 mm
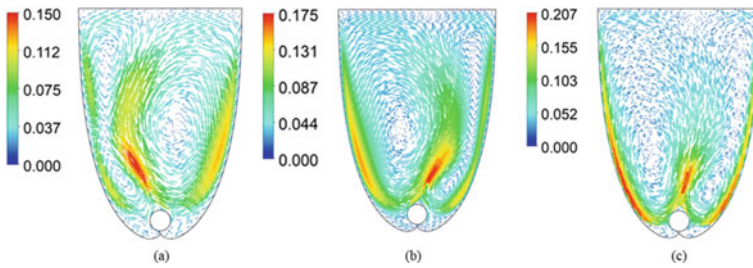
Fig. 6 Velocity vectors for CR = 2.5 for different receiver diameters **a** 10 mm, **b** 15 mm, **c** 30 mm

5 Conclusions

This work analyzes the effect of various geometric configurations of CPC on the flow pattern in a horizontal cavity.

1. The CR = 1.15, 1.41, 2.9, and 3.86 gives a symmetric and bicellular flow in the cavity of the collector.
2. The CR = 2 and 2.5 shows a deviation from the symmetric flow pattern, resulting in one central cell and one small weak cell in the cavity.
3. The aspect ratio increases with the concentration ratio and significantly influences the flow pattern in the cavity.

References

1. Kalogirou S (2003) The potential of solar industrial process heat applications. Appl Energy 76(4):337–361
2. Pranesh V, Velraj R, Christopher S, Kumaresan V (2019) A 50-year review of basic and applied research in compound parabolic concentrating solar thermal collector for domestic and industrial applications. Sol Energy 187:293–340
3. Chew TC, Tay AO, Wijeysundera NE (1989) A numerical study of the natural convection in CPC solar collector cavities with tubular absorbers. ASME J Sol Energy Eng 111:16–23
4. Antonelli M, Francesconi M, Di Marco P, Desideri U (2016) Analysis of heat transfer in different CPC solar collectors: a CFD approach. Appl Therm Eng 101:479–489
5. Winston R (1974) Principles of solar concentrators of a novel design. Sol Energy 16:89–95
6. Winston R, Hinterberger H (1975) Principles of cylindrical concentrators for solar energy. Sol Energy 17:255–258
7. Rabl A, Winston R (1976) Ideal concentrators for finite sources and restricted exit angles. Appl Opt 15:2880–2883
8. Abdel-Khalik SI, Li HW, Randall KR (1978) Natural convection in compound parabolic concentrators – a final element solution. ASME J Heat Transfer 100:199–204
9. Prapas E, Norton B, Melidis PE, Probert SD (1987) Convective heat transfer within air spaces of compound parabolic concentrating solar-energy collectors. Appl Energy 28:123–135
10. Eames PC, Norton B (1993) Detailed parametric analyses of heat transfer in CPC solar energy collectors. Sol Energy 50(4):321–328

11. Diaz G, Winston A (2008) Effect of surface radiation on natural convection in parabolic enclosures. Numeric Heat Transfer Part A Applicat 53(9):891–906
12. Singh H, Eames PC (2012) Correlations for natural convective heat exchange in CPC solar collector cavities determined from experimental measurements. Sol Energy 86:2443–2457
13. Reddy KS, Parthiban A, Mallick TK (2020) Numerical modeling of heat losses in a line focusing solar compound parabolic concentrator with planar absorber. Appl Therm Eng 181:1–20
14. Garg A, Ray B, Jain S (2023) Development of Nusselt number correlation for solar CPC with a tubular receiver. Therm Sci Eng Prog 37:101553, ISSN 2451–9049
15. ANSYS Inc (2013) ANSYS Fluent Theory Guide, Release 15.0. Canonsburg, PA 15317

Vortex Bladeless Turbines with Wings

Gosu Satish Kumar Reddy and Debopam Das

Abstract Vortex bladeless turbine is a non-conventional turbine that does not use any rotor blades to capture energy from flowing fluid. The device captures the energy of periodic vortices shed downstream of a bluff body, an aero- hydrodynamic effect that has plagued structural engineers and architects for ages in different engineering designs. As the wind passes a fixed structure, the Von Karman vortex sheet-type vortices generate alternate lift forces on the mast (movable structure) and make it start oscillating. Research has shown that such bladeless turbines have an excellent ability to harvest low-speed wind or hydro-energy. Innovative modifications of the mast's outer surface open the possibility of extracting energy from a flowing stream. In this paper, a new mast system is designed, developed, and experimented with in an open airflow system, which results in a nearly fivefold increase in the amplitude of the vibrations due to vortices. Wake-Induced Vibration (WIV) is also tested in another set of experiments which does not show the same possibilities.

Keywords Bladeless wind turbines · Vortex-induced vibration (VIV) · Vortex shedding · Wake-induced vibration (WIV) · Mast with wings

1 Introduction

Due to the decrease in non-renewable resources and the increase in demand for energy consumption in the present day-to-day life, renewable resources promise to play an important role in all the needs in the future. Extensive research is being carried out to develop new models for effectively using renewable resources. In today's scenario, wind energy is one of the important resources to harvest as it is available the whole day in many areas. Extensive research is being carried out to extract the energy from

G. S. K. Reddy (✉)
Department of Sustainable Energy Engineering, IIT Kanpur, Kanpur-208016, India
e-mail: skreddy21@iitk.ac.in

D. Das
Department Sustainable Energy Engineering and Aerospace Engineering IIT Kanpur, Kanpur-208016, India

the wind flow. At high altitudes, velocity is high, and available energy is more. To extract that energy with high efficiency, mainly two types of wind turbines have been developed, namely horizontal axis wind turbines (HAWT) and vertical axis wind turbines (VAWT). They require a minimum wind speed to run and generate power. So, at low wind speeds, they are inefficient. There is a third type of wind turbine called Vortex bladeless wind turbine, which is an alternative to HAWT and VAWT at low speeds.

Harvesting energy from low-speed wind has many applications where grid connectivity is complex. The present work aims at developing a novel bladeless turbine that can harvest the vortex energy of fluid flow at low velocities using a new and simple design. The turbine consists of a cylinder mounted on four springs and is subjected to a uniform and steady fluid flow. As the fluid passes the bluff body, it starts generating alternative vortices behind the bluff body periodically creating pressure differences, alternative lift forces act on the body and make the body oscillate with a certain frequency and amplitude. As the fluid's velocity increases, the vibration amplitude increases at a specific range of Reynolds numbers. The vibration frequency approaches the body's natural frequency, which results in a near resonance-like condition. The movable cylinder (mast) vibrates at higher amplitudes which indirectly helps in higher power generation at resonance. The oscillating motion is converted to rotary motion, which is connected to the actuator via gears and a transmission mechanism to generate power.

The vibration due to vortex shedding frequency (fvs) is determined by a dimensionless number called Strouhal number, $St = fvsD/v$, where v and D are the free flow fluid speed and the cylinder diameter, respectively. In Wake-Induced Vibration (WIV), a circular bluff body is placed just behind the fixed cylinder so that the periodic vortices generated by the fixed cylinder interact with the movable mast periodically and vibrate. WIV is tested by varying the distance of the obstacle cylinder from the mast to increase the vibration amplitude. Different ways have been tried to improve the amplitude by changing the structure. Wing structures made of plastic are added on both sides of the mast and conducted the experiment. In the future, the experiment is to be conducted with different wing orientations, connecting the conversion mechanism and generator to extract energy.

2   Literature Review and Objective

A substantial amount of research is being carried out on the shedding of vortices downstream of bluff bodies. Yoshitake et al. [1] generated a small amount of energy as a by-product of suppressing the VIV of towering structures in.

airflow. A model named Vortex-Induced Vibration Aquatic Clean Energy (VIVACE) is fabricated and tested in water by Bernitsas et al. [2]. Another model, VIV Resonant Wind Generators, is being developed by the company named vortex bladeless. It uses wind and bluff body interaction to vibrate. The vibrational energy is converted to electrical energy using piezoelectric materials. Experiments are carried

out on Wake-Induced Vibration (WIV) by placing a movable mast at different locations in the wake generated by a fixed cylinder which claims to have a good rise in the amplitude of the vibration [3].

In the present study, two models for energy harvesting using VIV are considered. In the first model, a mast similar to Farsi et al. [3] is considered, and experiments are conducted by varying the distance between the mast and the obstacle. The design of the mast is chosen in such a way that the amplitude of the vibration increases substantially and the turbine harvest more energy at low speeds. In the second model, a novel design of VIV based turbine is conceived where only one cylinder is used with some attachment of a wing with the cylinder surface. Here in this paper, we concentrated only on maximizing the amplitude of the vibration in both models for a given wind speed.

3   Experimental Setup and Methodology

The experiments are conducted in the Unsteady Aerodynamics Laboratory of IIT Kanpur in open wind flow conditions. The airflow velocity is limited to an average wind speed of 3 m/sec. The setup is mounted on an iron stand with a width of 90 cm and a height of 70 cm. A hollow cylinder with an outer diameter (d) of 8.5 cm is used as the oscillating device (mast). The length of the movable mast used is 80 cm with an aspect ratio is 9.4. It is made of cardboard material. The mast is balanced by four springs at a distance of 15 cm from the edges, and no external motor or damping element is attached. As no external damping is added, only fluid interaction damping is present. A pointer is fixed at the center of the hollow mast as a reference indicator.

Experiments are performed for four different configurations: (i) vortex-induced vibrations with only a freely oscillating mast, (ii) wake-induced-vibration where the oscillating mast is placed in the wake of a fixed cylinder, (iii) modified cylinder surface with an attached wing over it, and (iv) an obstacle cylinder is placed in front of the modified cylinder.

4   Freely Oscillating Mast

The Von Karman vortex sheet-type shedding generates alternative lift forces on the mast and makes it oscillate freely. Experiments are performed at a wind speed of 3 m/s which corresponds to Reynolds number 17000. This case is considered as the base case, and the performances of the other two models are compared with the base case. The amplitude variation is visually observed and noted down.

5 Mast and Wake Interaction

5.1 Cylinder of 9 cm Diameter as an Obstacle

Here, the cylinder is allowed to interact with the wakes generated by the obstacle cylinder. As the fluid interacts with the obstacle cylinder, it alternatively creates a pair of vortices on both ends [3].

As shown in Fig. 1a, b, the mast is placed just behind the obstacle cylinder to study the behavior of the mast with wake interaction. The distance between the obstacle cylinder is varied, and the behavior of the mast is observed. At the wake, a pair of vortices generate and interact with the mast alternatively, resulting in the movement of the mast up and down. The obstacle is placed at a distance of 16.5cm (1.94d), 20cm (2.35d), 25cm (2.94d), 30cm (3.53d), 35cm (4.12d), and 45cm (5.3d) from the mast. The amplitude of oscillation changes with time and hence the vibration's average amplitude and peak amplitude are noted for all cases.

6 Cylinder of 6 cm Diameter as an Obstacle

Here, the obstacle cylinder is replaced by a cylinder of diameter 6 cm. The same flow conditions have been maintained throughout the experimentation. Similarly, the distance between the obstacle cylinder varied from 16.5 cm (1.94d) to 45 cm (5.3d), and amplitude variation was observed. This is done to understand at what distance the mast has a maximum amplitude at this Reynolds number.

## 7 Mast with Wing Protrusion

In this case, an airfoil-shaped protrusion made from a Mylar sheet of thickness 100 mm is added on both sides symmetrically as shown in Fig. 2. The same flow conditions are maintained as in previous cases. Here also, we experimented in three cases. The first one was without any obstacles. The second and third are masts with wing in the wake of cylinders with 9 and 6 cm diameters. We did not vary the distance of the obstacle cylinder. We fixed the distance between the obstacle and the wing mast to 25 cm since maximum amplitude is obtained at this distance in previous cases.

The amplitude variations and peak amplitude are noted. Since the motive is to increase vibration amplitude, we did not add the generator and conversion mechanism to the system. Care is taken to minimize errors in measurements while performing experiments.
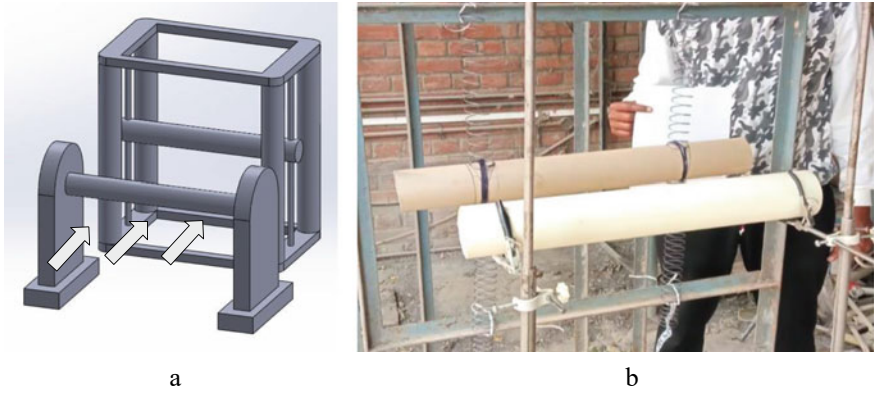
Fig. 1. **a** Schematic of the experimental setup. **b** Photograph of the experimental setup; a cylinder of 9 cm diameter is shown as an obstacle

Fig. 2. 3D model of the cylinder with protruded wings
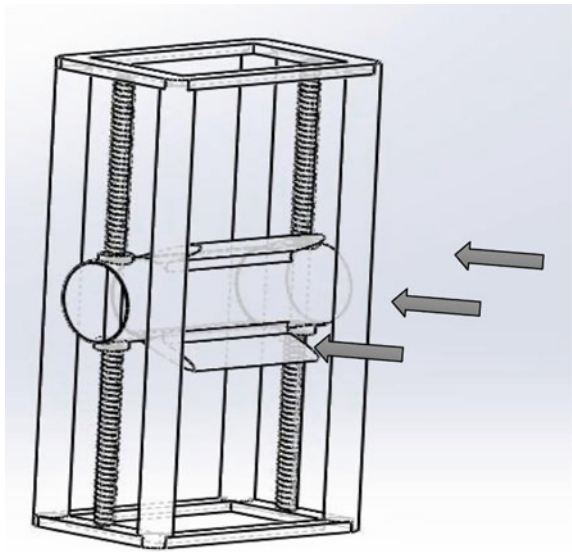
8   Results and Discussion

The experiment is carried out in all the cases mentioned previously with the aim of achieving large amplitude oscillations. Two parameters, namely the shape of the mast and the distance between the obstacle cylinder and the oscillating mast, significantly impact the amplitude. We conducted experiments for all the cases mentioned in

Tables 1, 2, and 3. The peak and average amplitude of all the instances are calculated from the images captured at 240 frames per second.

From the observation, the average half-amplitudes and peak half-amplitudes are calculated for all the cases as shown in Table 1. The average half-amplitude is calculated as the cylinder does not reach always the same top and bottom positions in a cycle as shown in Fig. 3a,b. In the base case where the cylindrical mast is free to oscillate the average half-amplitude and peak amplitude are 1.5 and 1.8 cm, respectively.

Table 1 Cylinder with a diameter of 9 cm is used as an obstacle

Obstacle distance from mast (cm)	Peak half-amplitude (cm)	Avg. half-amplitude (cm)
16.5	2	1.8
20	1.2	1.0
25	2.7	2.6
30	3.2	3.1
35	1.2	1.1
40	2.2	2.1

Table 2 Cylinder with a diameter of 6 cm is used as an obstacle

Obstacle distance from mast (cm)	Peak half-amplitude (cm)	Avg. half-amplitude (cm)
16.5	2.2	2.1
20	1.4	1.2
25	3	2.8
30	1.8	1.7
35	2.5	2.4
40	2	1.9

Table 3 Wing-protruded mast

Case	Peak half-amplitude (cm)	Avg. half-amplitude (cm)	
Reverse wind flow with no obstacle	1.1	0.9	
No obstacle	9.5	8.7	
Obstacle cylinder of diameter 9 cm at a distance of 25 cm	8.2	8.0	
Obstacle cylinder of diameter 6 cm at a distance of 25 cm	10.2	8.6	
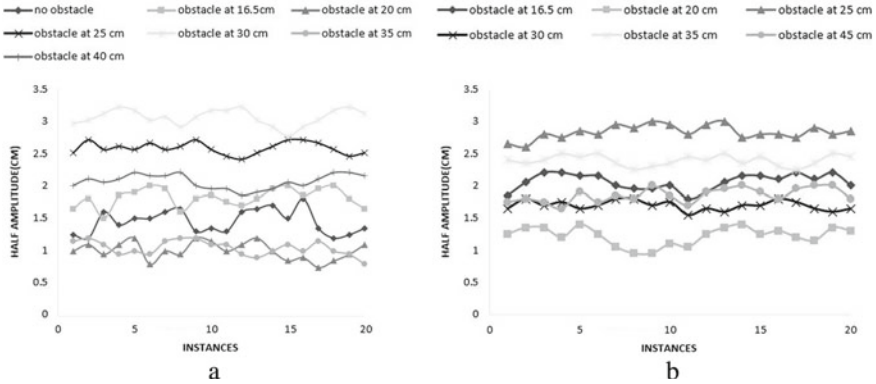
Fig. 3. **a** Half-amplitude for the obstacle of 9 cm diameter placed at different distances. **b** Half-amplitude for the obstacle of 6 cm diameter placed at different distances

9 Discussion

The curves in Fig. 3a. show that the mast with no obstacle has a half-amplitude range of 1.2 cm-1.8 cm, which is quite small to convert the oscillatory motion into rotary motion and extract energy. The frequency was observed to be 4.1 Hz. We observed that amplitude is raised when an obstacle cylinder of diameter 9 cm is placed at a distance of 25 and 30 cm. A peak half-amplitude of 3.2 cm and an average half-amplitude of 3.1 cm are observed for an obstacle cylinder of a diameter of 9 cm at a distance of 30 cm from the mast. And in a few cases (obstacle at 16.5 and 20 cm), the amplitude is mitigated.

Figure 3b shows the results for the second case where the obstacle cylinder is replaced with a cylinder of diameter 6 cm. Here also the amplitude is increased for a few cases and mitigated for a few other cases. An increase in amplitudes is observed for obstacles between 25 and 35 cm. A peak half-amplitude of 3 cm and average half-amplitude of 2.8 cm is obtained for an obstacle cylinder of a diameter of 6 cm at a distance of 25 cm from the mast.

A = No obstacle B = Obstacle cylinder of diameter 9 cm C = Obstacle cylinder of diameter 6 cm

10 Wing-Protruded Mast

D = Reverse wind flow with no obstacle, E = No obstacle F = Obstacle cylinder of diameter 9 cm

G = Obstacle cylinder of diameter 6 cm
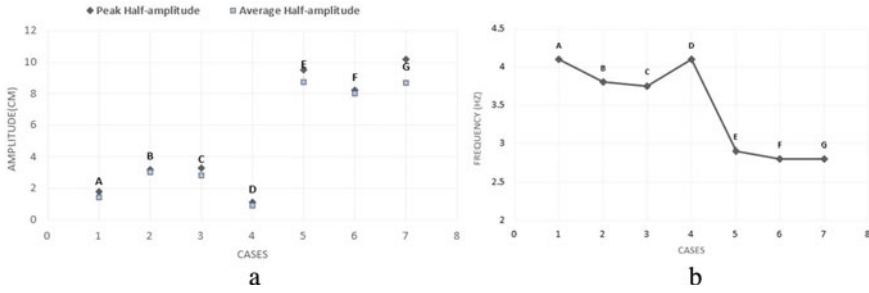
Fig. 4. a Variation of peak half-amplitude and average half-amplitude for different cases. **b** Variation of frequency for different cases

In a novel design of mast for energy harvesting, a wing protrusion is added on both sides symmetrically. It is observed that the vibration is mitigated when fluid is flown from the direction opposite to the direction shown in Fig. 2.

However, when the flow is directed from the front side of the wing-protruded mast (the direction shown in Fig. 2), the amplitude increased drastically from the range of 1 to 3 to 7.5 to 9.5 cm (see Fig. 4a). The frequency of vortex shedding dropped from 4.1 Hz to 2.9 Hz, and the variation can be seen in Fig. 4b. Figure 4a shows the variations of peak amplitude and average amplitude in all the cases. The highest average half-amplitude of 8.7 cm is observed in the case of no obstacle, and the highest peak half-amplitude of 10.2 cm is found in the case of an obstacle cylinder of a diameter of 6 cm.

11   Conclusions

The idea of increasing the amplitude of oscillations from the flow-induced vibration (vortex shedding phenomenon) has been experimentally investigated so that such devices can be used for energy harvesting from a flowing stream. The effects of mounting a fixed cylinder as an obstacle at different distances upstream of an oscillating mast are studied. In a new design of a mast, the impact of adding a wing to the oscillating mast is also investigated. The results can be summarized as follows:

1. Adding an obstacle cylinder and varying its distance from the mast increase the amplitude up to a certain distance and then decrease in both cases considered.
2. Amplitude rise is maximum when the obstacle cylinder is placed at a distance range of 25–35 cm.
3. Results show that the change in the shape of the mast has a good impact on increasing the amplitude of operations.
4. Wing-protruded mast mitigates the vibration when the flow direction is reversed. It is observed that a peak half-amplitude of 1.1 cm and an average half-amplitude of 0.9 cm are less than the no-wing case.

5. Wing-protruded mast gave promising results of increasing amplitude. The maximum half-amplitude of 10.2 cm is observed when an obstacle cylinder of diameter 6 cm is placed at a distance of 25 cm from the wing-protruded mast.

6. Highest average half-amplitude of 8.7 cm is observed without any obstacle placed for the wing-protruded mast.

Thus the present study shows the possibility of extracting energy from an oscillating mast with an airfoil-shaped wing attached to it. In the future, we will investigate possible other shaped masts and find their performances at different wind speeds. We plan to investigate the performance in a flowing water stream too. Based on the detailed study, we will design an energy harvesting device from the flowing air and water stream.

References

1. Yoshitake Y, Sueoka A, Yamasaki M, Sugimura Y, Ohishi T (2004) Quenching of vortex- induced vibrations of towering structure and generation of electricity using hula-hoops. J Sound Vib 272:21–38

2. Bernitsas MM, Raghavan K, Ben-Simon Y, Garcia EMH (2008) VIVACE (vortex induced vibration aquatic clean energy): a new concept in generation of clean and renewable energy from fluid flow. J Offshore Mechan Arctic Eng 130(4)

3. Farsi M, Shariatzadeh MJ, Bijarchi MA, Pournasiri Masouleh E, Shafii MB (2022) Low- speed wind energy harvesting from a vibrating cylinder and an obstacle cylinder by flow-induced vibration effect. Int J Environ Sci Technol 19(3):1261–1272

A Numerical Analysis of Baffled Solar Air Heater

Vishal Kumar and Swastik Acharya

Abstract Solar energy is one of the most important renewable energies utilized in numerous applications. The present work focuses on numerical analysis of a solar air heater (SAH). The main challenge in SAH is to improve the temperature of the air keeping the absorber plate temperature within the limiting range. It can be achieved with the addition of fins or baffles at the cost of pressure loss. In the present work, the effect of conducting baffles on the thermos-hydraulic performance of SAH is studied. A constant heat flux (1110 W/m^2) is applied on the absorber plate. Average Nu and the frictional pressure drop across the solar air heater are comprehensively investigated using the commercial software of Ansys Fluent. The baffle height and number of baffles are varied in the range of 0 to 0.03 m and 0 to 33. The air flow in SAH is considered in turbulence range with Reynolds number varying from 4000 to 16,000. It is observed that Nu becomes maximum at nine baffles at a baffle width and height of 0.06 and 0.02 m for both Re of 8000 and 16,000. The pressure drop follows the same trend of Nu and becomes maximum at nine baffles.

Keywords Solar air heater · Conducting baffles · Nusselt number · Pressure drop · Renewable energy

1 Introduction

Solar energy, one of the renewable energies, is vastly used nowadays for several applications such as solar air heater (SAH), organic Rankine cycle (ORC), solar dryer, solar photovoltaic panel, and solar water heaters. Before 1970, a few studies and improvements were made to take advantage of sun strength greater efficiently. However, the maximum of this remained theoretical. After a considerable upward push in oil expenses in the year 1971, numerous nations started to draw up enormous studies and developed some powerful devices to utilize sun strength for warming applications, i.e., space heating, seasoning of timber, drying of crops, etc. An easy

V. Kumar (✉) · S. Acharya

Department of Mechanical Engineering, MNNIT Allahabad, Prayagraj 211004, India
e-mail: umarvishal117@gmail.com

sun air heater includes a collector surface to seize sun radiation through conduction heat transfer. The heat is transferred to the air by convection to increase the air temperature. Nowadays, a continuous effort is being made by researchers to improve the efficiency of the solar air heater.

2   Literature Review and Objective

Many researchers have improved SAH performance. Air has low heat transfer coefficient, which results in a lower heat transfer in SAH. So, to improve the performance and efficiency of SAH, many researchers adopted various techniques and ideas that are discussed below.

Yadav and Bhagoria [1] performed a numerical study on solar air heater with triangular ribs and found a significant increment in convective heat transfer rate as compared to solar air heater without triangular ribs. Kumar and Saini [2] studied a 3D artificial roughened solar air heater with an arch-shaped collector surface. K-ε turbulence model was used to simulate fluid flow and heat transfer. A general gain up to 1.6 was achieved, and the simulation result was approved with experimental data successfully. Karmare and Tikekar [3] conducted a numerical study of a coarse solar air heater using grit ribs of metal. Standard k-ε turbulence model was used for the simulation. The authors reported that a collector with a cross-section rib of square shape, and an incidence angle of 58° was hydraulically more effective. Yadav and Bhagoria [4] conducted a numerical study of a solar air heater with artificial roughness of a circular cross-wire rib on the collector surface. A 2D standard k-ε turbulence was used for the simulation. The highest heat increment factor was found to be 1.61. Yadav and Bhagoria [5] conducted CFD-based research on traditional solar air heaters. The nature of the flow was analyzed using the Ansys Fluent and RNG k-ε models of turbulence. He observed that the result obtained by numerical analysis was in accord with the existing results. Choi and Choi [6] experimentally determined the electrical and thermal efficiency of a photovoltaic/thermal solar air collector by using non-uniform transverse rib at the back of the photovoltaic module. A significant improvement in the thermal efficiency from 35.2 to 56.72% was noticed when mass flow rate of air was increased from 0.0198 to 0.0769 kg/s. Square wave profile transverse ribs were used as roughness elements to improve the Nu of a solar air heater [7]. Nu increased 2.14 times that of the smooth duct at the cost of friction factor enhancement of 3.55 times of a smooth duct. A solar air heater with arch absorber plate using turbulators was proposed by Singh [8]. A significant improvement in Nu is observed at a high Reynolds number (above 1000). Hans et al. [9] experimentally studied the effect of the discrete V-down ribs on the thermo-hydraulic performance of a solar air heater by varying roughness pitch, angle of attack, and relative roughness height. They determined the optimum parameters for the maximum Nu and f, which were noted as 3.04 and 3.11, respectively.

Based on the literature review, it is concluded that significant studies have been conducted on the effect of artificial roughness over solar air collectors to enhance heat

transfer. However, the use of conducting baffles on the absorber surface in improving the performance of the SAH has yet to be studied. The fluid in a baffled solar air heater follows a serpentine path, providing more surface area for heat exchange and improving thermal efficiency. Thus, the present study aims at evaluating the Nu and pressure drop of the SAH with aluminum baffles attached beneath the collector in a staggered manner. To analyze heat transfer performance, the baffle height and number of baffles have been varied from 0.01 to 0.03 m and 5 to 33, and the results have been compared with the SAH without baffles. Air is blown through the SAH varying Re in the turbulence range from 4000 to 16,000.

3 Problem Description and Numerical Methods

3.1 Problem Description

A schematic diagram of SAH is shown in Fig. 1. The dimensions of the test section are provided in compliance with the ASHRAE standard [10]. All the geometrical details with thermo-physical properties are listed in Table 1. Baffles are provided beneath the absorber plate. In this design, baffles act like conducting fins and turbulators, which improves heat transfer. The height of baffles (h) is taken as in the range of 10 mm to 30 mm, and the width of baffles (w) is fixed at 60 mm. The number of baffles (n) in SAH varies from 0 to 33. The baffles are attached staggered along the longitudinal direction which can be visible in top view (Fig. 1). Reynolds number (Re) lies in the turbulence range of 4000 to 16,000, which is the operating range used for most SAHs. The solar heat flux at the absorber plate is fixed at 1110 W/m^2 which is transferred to the air by convection process. The presence of conducting baffles enhances the convective heat transfer rate by increasing the convective area. The absorber surface and mean fluid temperature have been measured to evaluate Nusselt number. Nu and pressure drop have been plotted for various cases in order to find the optimum baffle configurations.

3.2 Governing Equations

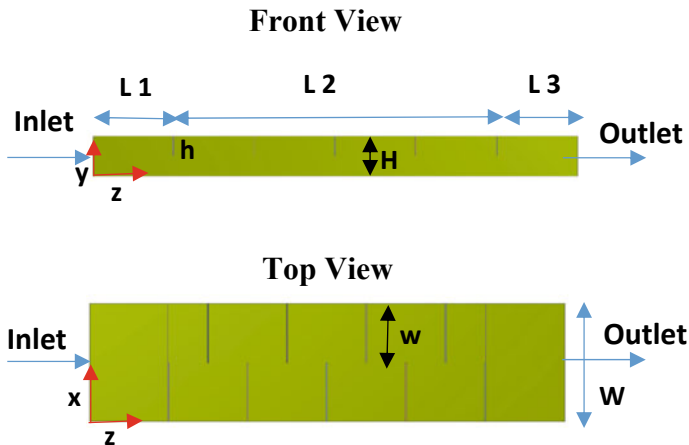To solve the governing equations, following assumptions are made.

Flow is steady.
Thermo-physical properties of absorber plate are constant; however, it is variable for air inside the duct and constant at inlet.
Radiation heat transfer is neglected.

Following equations are solved:
Continuity equation:

Front View

Top View

Fig. 1 Schematic diagram of a solar air heater with baffles

Table 1 Geometrical dimensions of SAH

Geometrical parameters	Value
Inlet length of duct (L1)	80 mm
Absorber plate (L2)	320 mm
Outlet length of duct (L3)	80 mm
Width of duct (W)	120 mm
Height of duct (H)	20 mm
Width of baffles (w)	60 mm
Height of baffles (h)	0–30 mm
Number of baffles (N)	0–33

$$\frac{\partial}{\partial X_i}(\rho u_i) = 0 \tag{1}$$

Momentum equation:

$$\frac{\partial}{\partial X_i}(\rho u_i u_j) = -\frac{\partial p}{\partial X_i} + \frac{\partial}{\partial X_j}\left[\mu\left(\frac{\partial u_i}{\partial X_j} + \frac{\partial u_j}{\partial X_i}\right)\right] + \frac{\partial}{\partial X_j}\left(-\rho \overline{u_i' u_j'}\right) \tag{2}$$

Energy equations

$$\frac{\partial}{\partial X_i}(\rho u_i T) = \frac{\partial}{\partial X_j}\left((\tau + \tau_t)\frac{\partial T}{\partial X_j}\right) \tag{3}$$

Here, τ is the molecular thermal diffusivity, while τ_t is the turbulent thermal diffusivity, and they are evaluated as:

$$\tau = \frac{\mu}{p_r} \text{ and } \tau_t = \frac{\mu_t}{p_{r_t}} \tag{4}$$

k-ε RNG equations:

$$\frac{\partial}{\partial X_i}(\rho k u_i) = \frac{\partial}{\partial X_j}\left[\left(\mu + \frac{\mu_t}{\sigma_k}\right)\left(\frac{\partial k}{\partial X_j}\right)\right] + P_k - \rho \in \tag{5}$$

$$\frac{\partial}{\partial X_i}(\rho \in u_i) = \frac{\partial}{\partial X_j}\left[\left(\mu + \frac{\mu_t}{\sigma_\in}\right)\left(\frac{\partial \varepsilon}{\partial X_j}\right)\right] + C_{1\varepsilon}\frac{\varepsilon}{k}P_k - C_{2\varepsilon}^*\frac{\varepsilon^2}{k}\rho \tag{6}$$

where $\mu_t = \rho C_\mu \frac{k^2}{\varepsilon}$, $C_{2\varepsilon}^* = C_{2\varepsilon} + \frac{C_\mu \eta^3\left(1-\frac{\eta}{\eta_0}\right)}{1+\beta\eta^3}$, and $\eta = S\frac{k}{\varepsilon}$, and $S = \left(2S_{ij}S_{ij}\right)^{\frac{1}{2}}$.

The model constants are $C_\mu = 0.0845$, $C_{1\varepsilon} = 1.42$, $C_{2\varepsilon} = 1.68$, $\eta_0 = 4.38$, $\eta_0 = 0.012$, $\sigma_k = \sigma_\epsilon = 0.7194$

k-ε RNG turbulence model is used to capture the turbulence in a flow.

The Reynolds number (Re) is kept between 4000 and 16,000 and calculated as:

$$\text{Re} = \frac{\rho v D}{\mu} \tag{7}$$

After solving the equations, average absorber surface temperature (T_s) and mean fluid temperature ($T_m = \frac{T_{in}+T_{out}}{2}$) are computed. Then Nu can be evaluated as:

$$Nu = \left(\frac{q''}{T_s - T_m}\right)\frac{D_h}{k_f}. \tag{8}$$

where D_h and k_f are the hydraulic diameter of the SAH and thermal conductivity of air.

3.3 Boundary Conditions

Air is used as a working fluid in SAH, and the baffles are made of aluminum. The thermo-physical properties of air are constant at the inlet but vary with temperature inside the duct of SAH. The thermo-physical properties of the aluminum baffles are kept constant. Heat flux from solar insolation on absorber plate is kept constant at 1110 W/m^2. Back pressure and temperature at the outlet are set to the atmospheric conditions. Velocity at the inlet is kept constant and calculated from Reynolds number using Eq. 7. No-slip boundary condition is applied at all walls of duct.

3.4 Mesh Generation

To solve the governing equations the computational domain is divided into number of cells using Ansys mesh generator. Very fine mesh was generated near the boundary wall. The mesh elements of 3,472,831 with an interior grid size of 0.00025 m were seemed to be the best number since the results did not change beyond it. Grids adjacent to the wall was made sufficiently finer to capture the turbulence generated due to the presence of the wall.

3.5 Numerical Methods

A CFD solver of Ansys Fluent [11] is used to simulate the problem. The computational domain is divided into a number of cells over which the discretized governing equations are integrated to for a set of nonlinear algebraic equations. The equations are solved in the solver of Ansys Fluent with the appropriate boundary conditions to obtain the pressure, velocity, and temperature within the computational domain. The convergence criteria for continuity, momentum, and energy equations are set to 10^{-4}, 10^{-5}, and 10^{-6}.

3.6 Validation

Before starting the simulation, the present solver is validated with the experimental results of Alfarawi et al. [12] for the solar air heater with p/e = 26.6. The comparison is presented in Table 2. The difference between the present solution and experimental results lies within an acceptable limit which affirms the present solver.

Table 2 Test of validation

| Re	Nu (present work)	Nu [12]	% error
12,500	83.61	90	7.64
52,500	190.08	197	3.5
86,000	264.66	270	2.01

4 Results and Discussion

After solving the governing equations with appropriate boundary conditions, the average absorber surface temperature and the mean fluid temperature are measured. Using those two parameters, Nu is calculated and plotted against various input parameters. Pressure drop is another important parameter in a forced convection which has also been plotted. The physical phenomena have been well explained.

4.1 Effects of Number of Baffles

Figure 2 shows variation of Nu with number of baffles attached to the absorber plate. Nu mainly depends on the difference between the absorber surface temperature and mean temperature of air. For an effective SAH, a high Nu is expected. When the baffles are attached to the absorber plate, the contact surface area with air increases and the air takes more heat away from the plate which reduces the absorber surface temperature. However, the air temperature at the outlet of the SAH does not vary significantly since the boundary layer thickness under the absorber surface at the outlet is very small compared to the height of the channel. Thus, Nu increases with increase in number of baffles. However, when N increases beyond 9, the flow obstruction becomes dominant which reduces the convective heat transfer. Thus, the temperature of the absorber surface temperature becomes more and Nu reduces. Nu increases from 80 to 190 when number of baffles increases from 0 to 9 and then reduces to 100 when number of baffles increases to 33 for a Re of 16,000. For a Re reduces to 8000, the variation in Nu follows the same trend but with a lesser magnitude. It means that high Re flow carries a more heat form the absorber plate due to a stringer convective heat transfer.

Figure 3 shows the variation of the pressure loss in a SAH with number of baffles at baffle height h = 0.02 m and width w = 0.06 m. Pressure loss is minimum when there are no baffles attached over the absorber plate. The plane channel (without any

Fig. 2 Variation of nusselt number (Nu) with number of baffles (N)
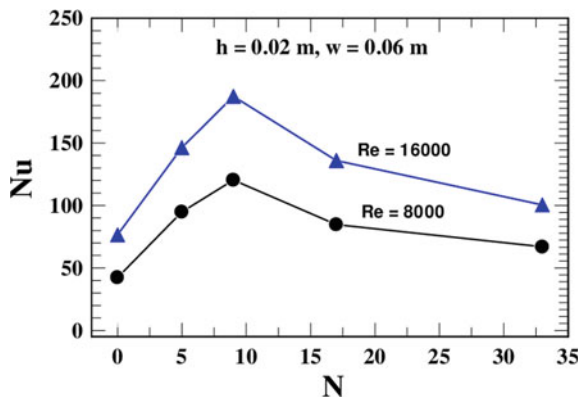
Fig. 3 Variation of pressure
loss with number of baffles
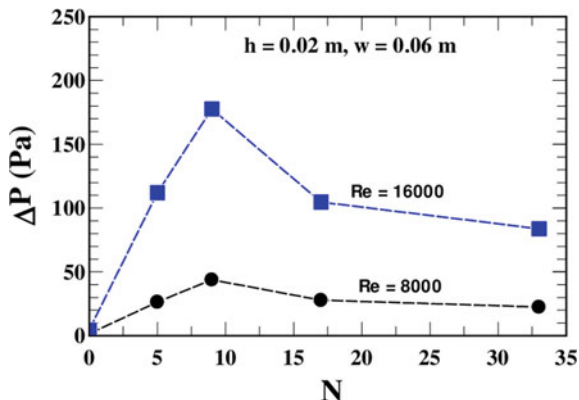
baffles) provides very less frictional resistance to the upcoming air which results in a
minimum pressure loss. When the baffles are attached, flow resistance significantly
increases owing to the flow obstruction and the wall friction which results in a
substantial pressure loss.

The pressure loss increases linearly with baffles up $N = 9$, then it starts decreasing
with further increase in the baffles. When number of baffles becomes more than 9, the
gap between the baffles becomes significantly less which does not allow air to enter
the inter baffle spacing. Thus, air moves underneath the baffles. When N becomes
33, the presence of baffles acts like a solid body attached under the absorber plate,
and the air moves in the path between the baffles and the bottom plate with lesser
obstruction. Therefore, for such case, the pressure loss reduces. It can be seen that
the pressure loss is maximum at $N = 9$ with 180 and 50 Pa for Re = 16,000 and
8000 and then reduces to 80 and 25 Pa at $N = 33$. The pressure drop becomes more
for a higher Re. For a plane SAH, the pressure drop for a higher Re is marginally
more; however, the pressure drop variation widens with introduction of the baffles.

Figure 4 shows the temperature and pressure contour in the mid-longitudinal plane
of a SAH. Left side of Fig. 4 is the inlet, and right side is the outlet of the channel.
When $N = 0$ (without baffles), the absorber plate temperature is higher than the
channels with baffles. Thus, Nu is lower for the SAH without baffles. When $N =
9$, the absorber plate becomes lower. When N increases to 33, air cannot penetrate
the inter baffle spacing and the temperature becomes high due to lower convective
heat transfer. Thus, the absorber surface temperature increases. The pressure drop
is minimum for $N = 0$. When the number of baffles is increased to 9, the pressure
drop increases drastically. When the number of baffles is increased to 33, the baffles
become so close that they behave like a solid wall and air moves below the baffles.
In such cases, the participation of baffles is reduced in flow obstruction.

Figure 5 shows the variation of Nu with baffle height for $Re = 8000$ and 16,000. Nu
increases with an increase in baffle height for $N = 9$. With the increase in height, air
takes more heat away from the absorber plate, owing to an increase in the surface area.
Thus, the absorber surface temperature reduces with an increase in height resulting
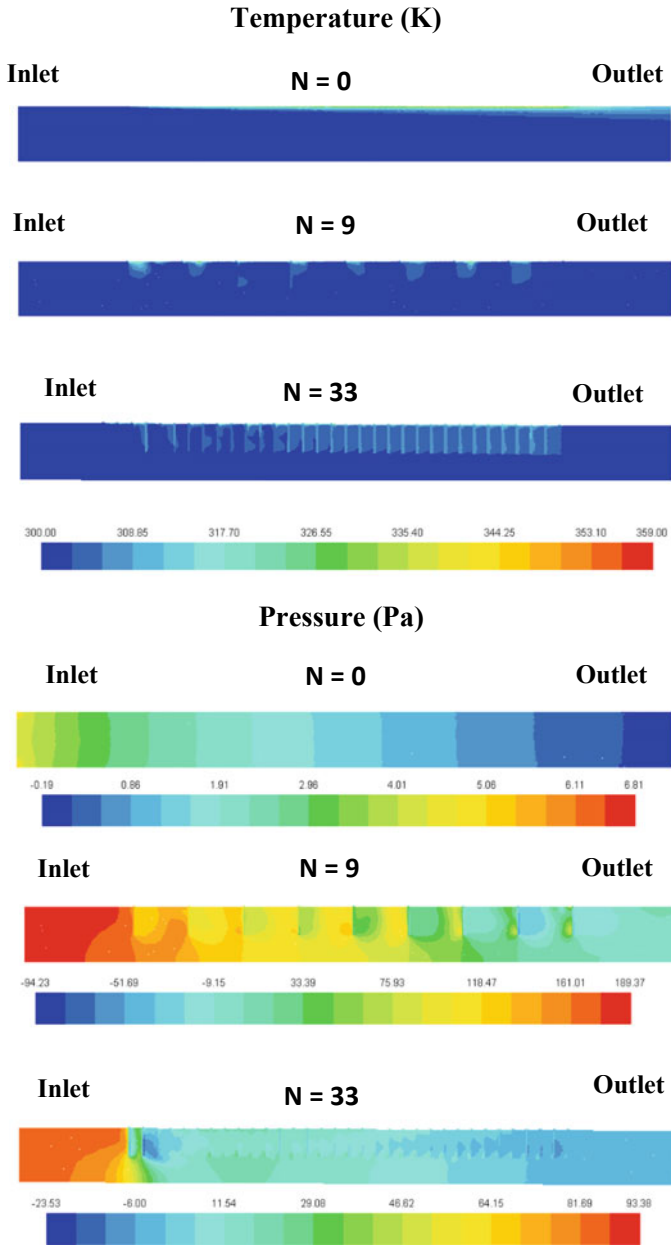
Fig. 4 Temperature and pressure contour in the mid-longitudinal plane of a SAH for $N = 0$, $N = 9$, and $N = 33$

Fig. 5 Nu variation with
respect to the height of the
baffles at $N = 9$ and $w =$
0.06 m
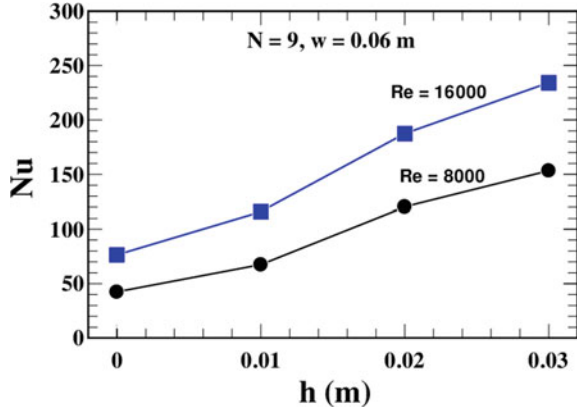
in a higher Nu. Here, with an increase in height though flow resistance increases, the
enhancement in surface area improves the heat transfer rate. Nu increases almost 2.5
times the plane SAH (without baffles) when baffle height becomes 0.03 m.

4.2 Effects of Height of Baffles

Pressure drop increases with baffle height (Fig. 6). When fin height increases beyond
0.02 m, the pressure drop rises sharply. Pressure drop almost increases four times
when baffle height increases from 0.02 to 0.03 m.

Fig. 6 Pressure drop with
respect to the height of the
baffles at $N = 9$ and $w =$
0.06 m
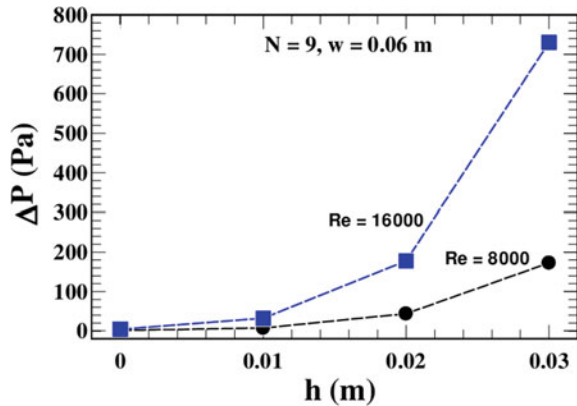
5 Conclusions

Based on the results and discussions, the following conclusions have been drawn:

- When number of baffles is increased to 9, Nu enhances 2.3 times of the plane duct. When number of baffles increases beyond 9, Nu starts decreasing.
- The maximum Nu for Re of 16,000 is nearly 200, whereas the maximum Nu for Re of 8000 reduces to 120.
- Pressure drop sharply increases with the introduction of baffles up to 9 baffles and then starts reducing with a further increase in the baffles.
- The maximum pressure drop becomes almost three times when Re changes from 8000 to 16,000.
- Nu increases linearly with baffle height; however, pressure drop increases with a higher slope at the greater baffle height.
- The increase in Nu becomes maximum at 250% when nine baffles of height h = 0.03 m are attached over the plane SAH (without baffles).
- When baffle height increases beyond 0.02 m, pressure drop increases sharply and becomes almost four times when baffle height increases to 0.03 m.

Abbreviations

NOMENCLATURE

D_h	Duct equivalent diameter[mm]
h	Height of baffle[mm]
H	Depth of duct[mm]
k_f	Air thermal conductivity [W/mK]
L	Length of duct [mm]
μ	Dynamic viscosity[Pa.s]
Nu	Nusselt number
N	Number of baffles in SAH
q"	Heat flux [W/m^2]
ρ	Density of air[kg/m^3]
T	Temperature[K]
v	Inlet velocity of air[m/s]
u	Air flow velocity in x-directionm/s
w	Width of baffle[mm]
W	Width of duct[mm]
x	Cartesian coordinate[m

Abbreviation:

SAH   Solar air heater
CFD   Computational fluid dynamics

References

1. Karima MA, Hawladerb MNA (2006) Performance investigation of flat plate, v-corrugated and finned air collectors. Energy 31:452–470
2. Prasad BN, Saini JS (1988) Effect of artificial roughness on heat transfer and friction factor in a solar air heater. Solar Energy 41(6):555–560
3. Karwa R, Solanki SC, Saini JS (1999) Heat transfer coefficient and friction factor correlations for the transitional flow regime in rib roughened rectangular ducts. Int J Heat Mass Transfer 42:1597–1615
4. Kumar A, Saini RP, Saini JS (2012) Experimental investigation on heat transfer and fluid flow characteristics of air flow in a rectangular duct with Multi v-shaped Rib with gap roughness on the heated plate. Sol Energy 86:1733–1749
5. Singh S, Chander S, Saini JS (2011) Heat transfer and friction factor correlations of solar air heater ducts artificially roughened with discrete V-down ribs. Energy 36:5053–5064
6. Choi HU, Choi KH (2020) Performance evaluation of PV/T air collector having a single-pass double-flow air channel and non-uniform cross-section transverse rib. Energies 13(9):2203
7. Singh I, Singh S (2018) CFD analysis of solar air heater duct having square wave profiled transverse ribs as roughness elements. Sol Energy 162:442–453
8. Singh S (2017) Performance evaluation of a novel solar air heater with arched absorber plate. Renew Energy 114:879–886
9. Hans VS, Saini RP, Saini JS (2010) Heat transfer and friction factor correlations for a solar air heater duct roughened artificially with multiple v-ribs. Sol Energy 84(6):898–911
10. ASHRAE handbook (2009) Fundamentals. Atlanta, GA, American Society of Heating, Refrigeration and Air-Conditioning Engineers. Retrieved from http://app.knovel.com/hotlink/toc/id:kpASHRAE37/2009-ashrae-handbook
11. ANSYS, INC. Release 14.0, Canonsburg, Pennsylvania, USA
12. Alfarawi S, Abdel-Moneim SA, Bodalal A (2017) Experimental investigations of heat transfer enhancement from rectangular duct roughened by hybrid ribs 118:123–138

Influence of Number of Turbine Rotations on Numerical Prediction Accuracy of a Three-Bladed NACA0021 VAWT

V. Vishnu Namboodiri and Rahul Goyal

Abstract Performance improvements on wind turbines are emerging due to increased renewable energy demand. The researchers are focusing on improvements in turbine efficiencies. The advancements in numerical simulations immensely support the new design developments and deployment of wind turbines. However, the fidelity and shortcomings of various numerical models are highly challenging to predict accurate results. One of the challenges in numerical simulations is the stopping criteria for the simulations after specific turbine rotations for highly accurate predictions. This paper investigates the influence of turbine rotations on the numerical prediction accuracy for a standalone three-bladed NACA0021 vertical axis wind turbine. The SST k-ω turbulence model is used in 2D turbine configurations. A comprehensive turbine revolution study is carried out for an extensive range of tip speed ratio (TSR) values. The simulation result shows that the operating TSR highly influences prediction accuracy. For lower TSR, a minimal number of turbine rotations are required as compared to higher TSR.

Nomenclature

D	Diameter of the rotor [mm]
C_P	Coefficient of power [–]
C_T	Coefficient of torque [–]
c	Chord length [mm]
ρ	Density of air [kg/m^3]
N	Number of blades [–]

V. Vishnu Namboodiri · R. Goyal (✉)
Department of Energy Science and Engineering, IIT Delhi, New Delhi 110016, India
e-mail: rahulgoyal@dese.iitd.ac.in

V   Freestream wind velocity [m/s]

A   Swept area [m^2]

1 Introduction

The performance enhancement of wind turbines is of greater interest to the researchers. Over the years, the implementation of medium and small-scale vertical axis wind turbines (VAWTs) has become more challenging as a result of operational instabilities and poor cost-effectiveness. Simultaneously, the wake dynamics and performance in turbulent environments are challenging for horizontal axis wind turbines in larger wind farms. Further, to overcome those shortcomings, various numerical models are proposed by researchers. However, the fidelity of the models is quite reliant on the design problem and the operating environment. The complex design problems are resolved by adopting numerical simulations and subsequent experimentations. Reynolds-averaged Navier–Stokes (RANS) equations are the fundamental basis of numerical methods, and various models are developed based on RANS. However, the prediction accuracies of models are highly influenced by certain numerical, design, and operating parameters. The numerical problems are usually resolved in 2D or 3D domains. However, both environments have their advantages and disadvantages. Many challenges can be identified in the different CFD simulations [1]. One of such challenges is to determine the stopping criteria for the numerical simulations after specific turbine rotations for high accuracy predictions.

## 2 Literature Review and Objective

The numerical techniques have significantly improved their fidelity. The performances of various models are compared and presented in this section. Chowdhury et al. [2] performed various numerical simulations with multiple turbulence models (i.e., shear stress transport (SST) k-ω, Re-normalization group (RNG) k-ε, and Spalart–Allmaras (SA)) and compared with experimental results in a tilted and upright configuration. The NACA0018 blade profiles were considered for the studies, and the result shows that the SST k-ω turbulence model provides the closest value in comparison with the experimental results. Rogowski et al. [3] also reported similar observations about the superior performance of SST k-ω. One of the prominent advantages of the SST k-ω turbulent model is the improved prediction in the near-wall region, which helps to understand the flow separation behaviors [4]. Rezaeiha et al. [5] performed a comparison of various turbulence models. The models such as the inviscid model, SA, RNG k-ε, realizable k-ε, and SST-based models were considered for 2D numerical simulations. Various turbine configurations, such as NACA 0015 ($N = 1$), NACA 00,118 ($N = 2$), and NACA 0021 ($N = 3$), were

also simulated. SST-based models were observed to predict better than other models. Furthermore, the inviscid model over-predicts for high tip speed ratio (TSR) values. RNG model over-predicts at lower TSR and underpredicts at higher TSR. Rezaeiha et al. [6] performed a study on improving numerical models' accuracy. Their study concludes that the torque value attains convergence after the 20th turbine of rotation. However, this study does not include the variation of numerical prediction accuracy with respect to progress in the TSR values. The literature analysis shows the limited research on the influence of the number of turbine rotations required for convergence for specific ranges of TSR values. This motivated to investigate the effect of a number of turbine rotations on the numerical prediction accuracy in a wide range of TSR.

3 Materials and Methods

This section deals with the methodology for investigating the influence of a number of turbine rotations on torque in a wide range of TSR. The methodology consists of the selection of airfoil, geometry modeling, meshing, numerical settings, analysis, and post-processing. The detailed methodology can be seen in Fig. 1.

Fig. 1 Methodology
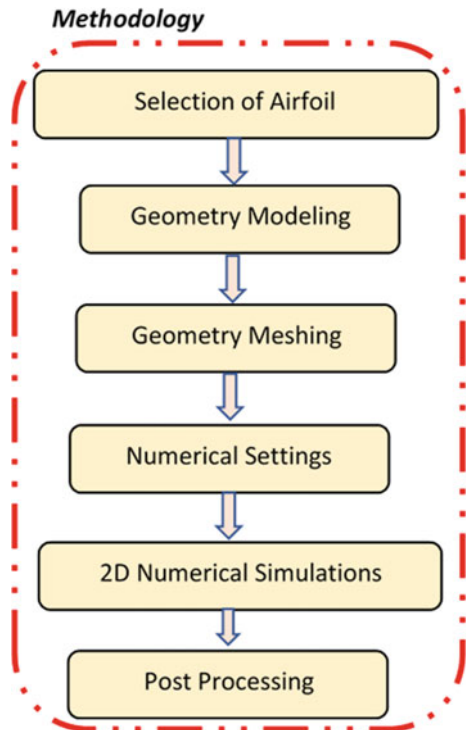
Table 1 Turbine specifications

| Parameters	Details/values
Airfoil (–)	NACA0021
Rotor diameter (mm)	1030
Number of blades (–)	3
Chord length (mm)	85.8

3.1 Turbine Specifications

The present study utilizes the NACA0021 as the airfoil profile. The NACA0021 is a thicker symmetric airfoil and can perform well at lower TSR ranges. As the number of blades progresses, the *Cp* value decreases, which is influenced by the airfoil profile. In this context, the number of blades has been fixed as three. The 2D numerical analyses were considered for the present studies due to the availability of validation data from reference literature [7]. Table 1 shows the details of the turbine selected for the present study.

3.2 Geometry Modeling and Meshing

Ansys design modeler has been chosen as the geometrical modeling platform. The turbine specifications are adopted and integrated into a domain to mimic real-life scenarios (see Fig. 2).

Ansys mesh module was considered for the present study. The imported geometry from the design modeler was used for creating an unstructured mesh. Further, the domain is differentiated as inner rotating body, outer rotating body, airfoils, and
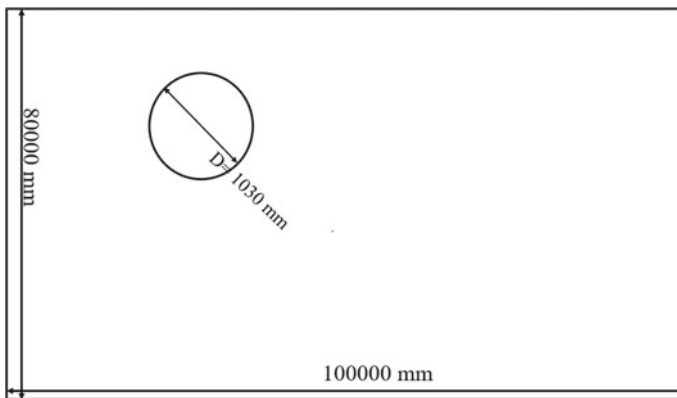
Fig. 2 Fluid domain
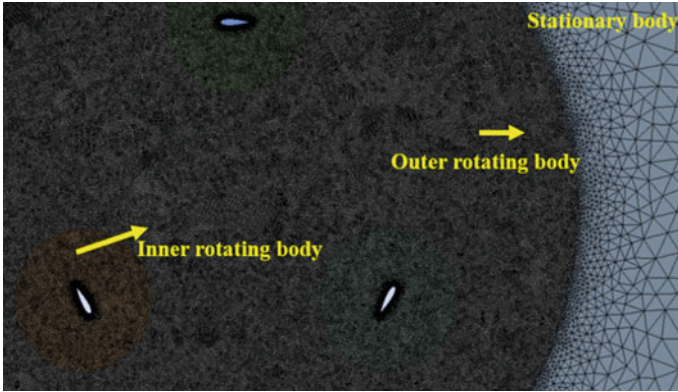
Fig. 3 Domain details

Table 2 Mesh information

Mesh information	Values
No. of elements (–)	15,42,525
Mesh element (–)	All triangle
Inflation layer number (–)	20
Inflation layer growth (–)	1.2
Skewness (–)	$5.64e^{-2}$
Orthogonality (–)	0.9654
Aspect ratio (–)	2.3817
Element size (mm)	Stationary body-115 mm Rotating body-6 mm
Airfoil body (division) (–)	1000

stationary body (see Fig. 3). Table 2 shows the details of the mesh metrics used for the present studies.

3.3 Numerical Settings

The various literatures indicate the reliability of SST-based turbulence models. The present work utilizes SST k-ω for the numerical analysis. The detailed numerical settings adopted for the present study are depicted in Table 3.

Table 3 Numerical settings

Numerical settings	Details
Analysis environment	2D unsteady simulation
Solver	Ansys fluent
Solver type	Pressure based
Fluid	Air
Turbulence model	SST k-ω
Inlet velocity (m/s)	9
Size of the domain (mm^2)	80,000 × 100,000
Inlet boundary condition	Velocity inlet
Outlet boundary condition	Pressure outlet
Blade wall	Moving wall with no-slip boundary condition
Far-field domain	Symmetry
Rotating body	Moving mesh with rotational velocity according to the tip speed ratio
Inlet turbulent viscosity ratio (TVR) (–) and turbulent intensity (TI) (%)	10 and 0.1
Pressure velocity coupling	SIMPLE
Spatial discretization	
Gradient	Least square cell-based
Pressure	Second order
Turbulent kinetic energy	Second order
Specific dissipation rate	Second order
Transient formulation	Second order implicit
Residual	$10^{-3}/10^{-4}$
Degree of rotation (º)	1
TSR range (–)	1.44–3.296
Turbine output parameter (nm)	Average torque (T_{avg})
Number of turbine rotations	25

3.4 Post-processing

The results from 2D CFD simulation are presented for average torque (T_{avg}) and average coefficient of torque (C_T). These variables were calculated using Eqs. (1 and 2) for *Cp* values with respect to TSR. The torque value was calculated for each rotation with respect to the TSR values for studying the influence of the number of turbine rotations,

$$C_T = \frac{T_{avg}}{T_{available}} = \frac{T_{avg}}{0.5 \rho A V^2 R} \tag{1}$$

$$C_P = C_T \times TSR \tag{2}$$

4 Results and Discussion

At TSR 1.67, the evolution of torque values exhibits a steady-state nature after an initial unsteady state.

This shows faster convergence of the torque value and can be observed in Fig. 4. Further, the variation of torque value at TSR 1.67 shows a uniform nature of positive and negative torque generations during the upstream and downstream travel of airfoils. This positive and negative torque combines the overall average torque values at specific TSR and turbine rotations. This trend can be clearly seen in Fig. 5.

The variation of torque value across the turbine rotations is evaluated, and the result shows that at TSR 1.67 no significant change in torque value between the 5th and 25th turbine rotations. This shows the convergence and steadiness of the torque value and is clearly observed in Fig. 6.

At TSR 2.513, as the number of turbine rotations increases, slight changes in the torque value are observed. However, as compared to TSR 1.67, there is a gradual decrease in the torque value. It is observed that after 15th rotation, the torque value starts converging to a steady-state condition with minimal change till 25th rotation of turbine blade and is clearly observed in Fig. 7.
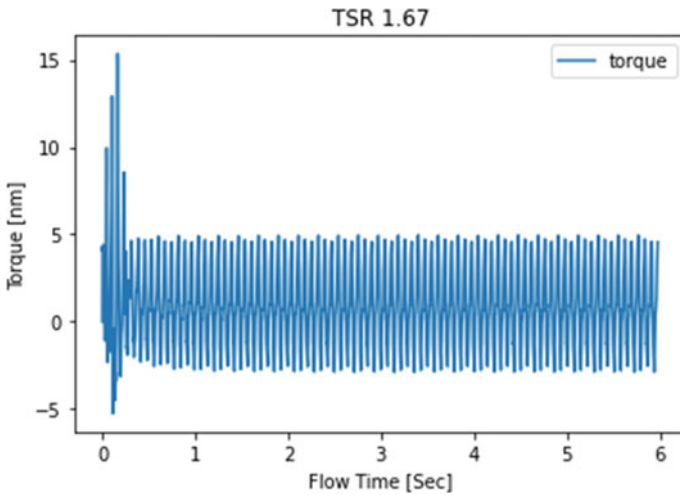
Fig. 4 Evolution of torque
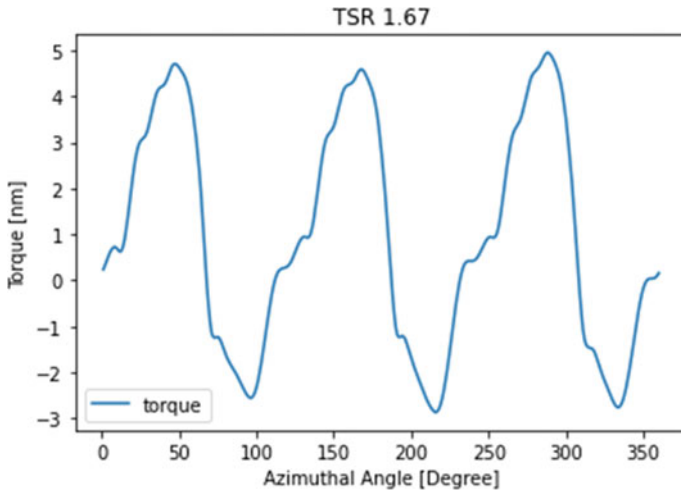
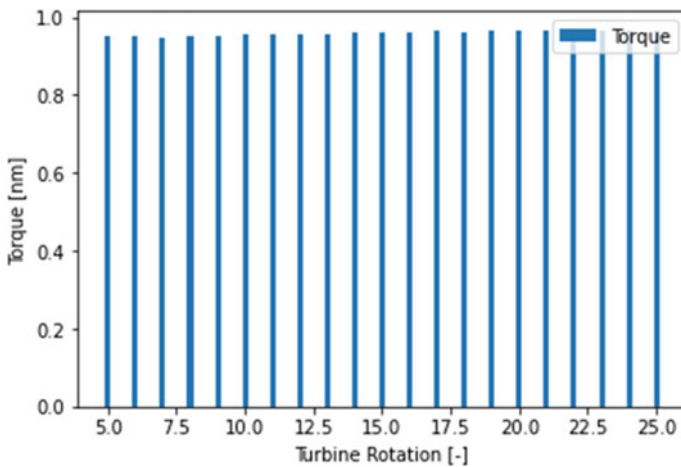**Fig. 5** Torque trend with respect to the azimuthal angle

Fig. 6 Variation of torque with number of turbine rotations at TSR 1.67

As the turbine rotations progress at 3.296 TSR, a significant change in torque value is observed between 5 and 10th rotations. This gradual decrease in trend is observed to extend till the 20th rotation. After the 20th rotation, there is no significant variation in the torque value. This infers that the torque value achieved a steady-state value. Thus, numerical simulations for higher TSR turbines require a higher number of turbine rotations to obtain steady-state torque. Figure 8 shows the variation of torque value for turbines operating at higher TSR.
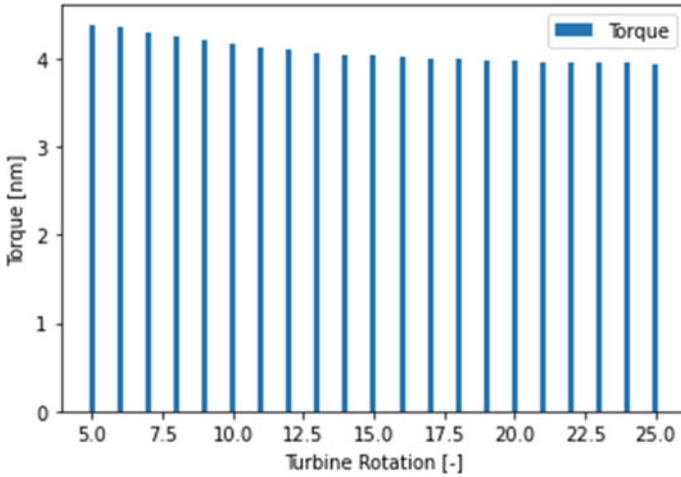
Fig. 7 Variation of torque with the number of turbine rotations at TSR 2.513
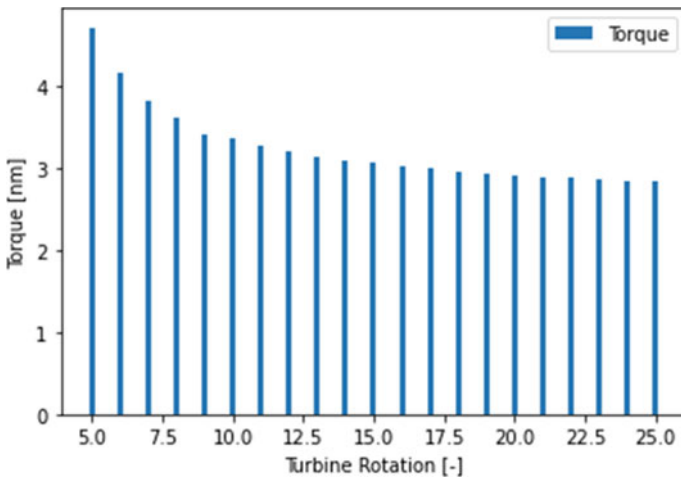
Fig. 8 Variation of torque with the number of turbine rotations at TSR 3.296

The *Cp* at each turbine rotation is computed from torque values for wide ranges of TSR to establish numerical prediction accuracy. Since torque and *Cp* are directly related, the *Cp* values are compared with numerical and experimental results from reference literature [7]. The results infer that at lower TSR, the convergence of the *Cp* value is obtained at a lesser number of turbine rotations. After 2.327 TSR, the influence of the number of turbine rotations is significant and affects results. This trend is observed till 3.296 TSR (see Fig. 9). Further, the analysis revealed that the *Cp* values predicted by the current numerical study outperformed the numerical analysis
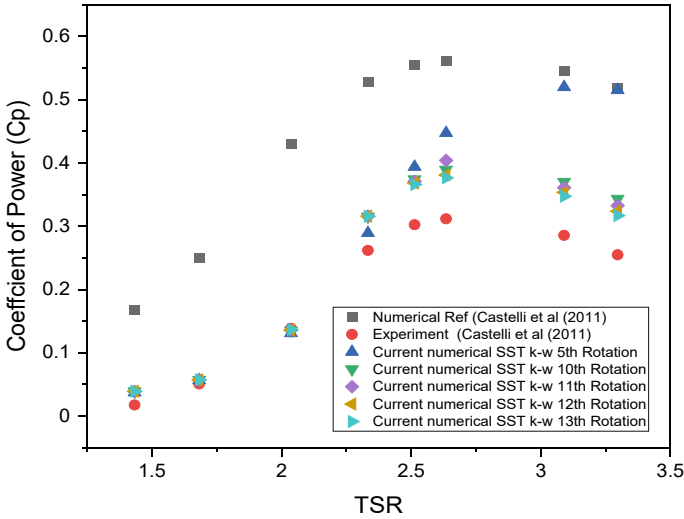
Fig. 9 Variation of C_P with a wide range of TSR

data from the reference literature. Accuracy comparisons with reference literature were carried out and observed that minimal turbine revolutions satisfy the good accuracy at 1.67 TSR. Medium TSR (i.e., 2.513) requires more than ten revolution cycles for good accuracy. Furthermore, higher TSR (i.e., 3.089) requires more than twenty revolution cycles for good accuracy, and similar observations were reported by Rezaeiha et al. [6] (see Fig. 10).

A comparison study with the *Cp* value at the 20th rotation of the turbine is compared with reference literature. The present study agrees well with the experimental reference studies (see Fig. 11).

5 Conclusions

The influence of turbine rotations on numerical prediction accuracy is carried out for a wide range of TSR and compared with the reference literature. The following conclusions can be drawn from the above results.

1. Operating TSR of turbines highly influences the numerical prediction accuracy.
2. At lower TSR, the small number of turbine rotations yield good accuracy. However, at greater TSR, significant changes in the torque value were observed at a low number of turbine rotations.
3. Turbines operating at higher TSR may require more turbine rotations to reach convergence.
4. The number of turbine rotations shall be decided based on the operating TSR range for better numerical prediction accuracy.
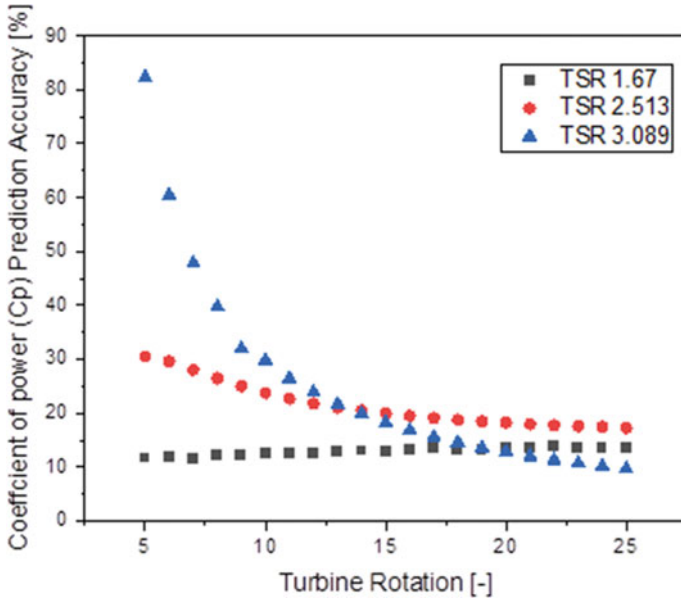
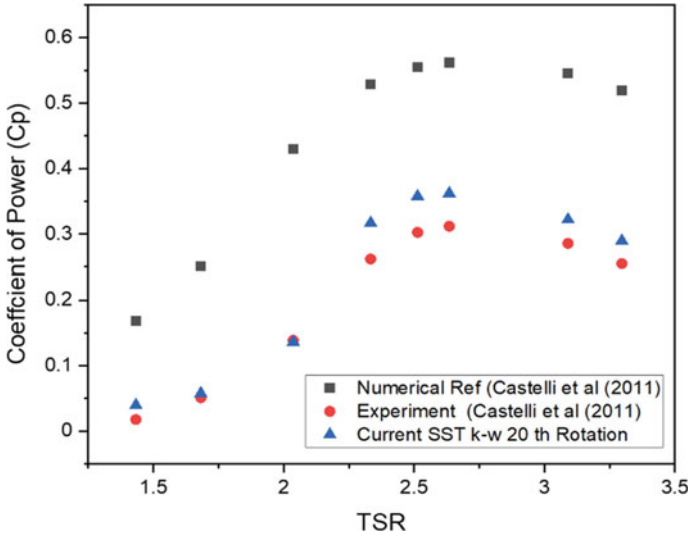**Fig. 10** Variation of accuracy with turbine rotations at various TSR

Fig. 11 Performance comparison of reference and current study

References

1. Balduzzi F, Bianchini A, Maleci R, Ferrara G, Ferrari L (2016) Critical issues in the CFD simulation of Darrieus wind turbines. Renew Energy 85:419–435. https://doi.org/10.1016/j.renene.2015.06.048
2. Chowdhury AM, Akimoto H, Hara Y (2016) Comparative CFD analysis of vertical axis wind turbine in upright and tilted configuration. Renew Energy 85:327–337. https://doi.org/10.1016/j.renene.2015.06.037
3. Krzysztof R, Martin Otto Laver H, Ryszard M (2018) Steady and unsteady analysis of NACA 0018 airfoil in vertical-axis wind turbine. J Theoretic App Mech 56(1):203–212. https://doi.org/10.15632/jtam-pl.56.1.203
4. Eltayesh A, Castellani F, Burlando M, Bassily Hanna M, Huzayyin AS, El-Batsh HM, Becchetti M (2021) Experimental and numerical investigation of the effect of blade number on the aerodynamic performance of a small-scale horizontal axis wind turbine. Alex Eng J 60(4):3931–3944. https://doi.org/10.1016/j.aej.2021.02.048
5. Rezaeiha A, Montazeri H, Blocken B (2019) CFD analysis of dynamic stall on vertical axis wind turbines using Scale-Adaptive Simulations (SAS): Comparison against URANS and hybrid RANS/LES. Energy Convers Manage 196:1282–1298. https://doi.org/10.1016/j.enconman.2019.06.081
6. Rezaeiha A, Montazeri H, Blocken B (2019) On the accuracy of turbulence models for CFD simulations of vertical axis wind turbines. Energy 180(838):857. https://doi.org/10.1016/j.energy.2019.05.053
7. Raciti Castelli M, Englaro A, Benini E (2011) The Darrieus wind turbine: proposal for a new performance prediction model based on CFD. Energy 36:4919–4934. https://doi.org/10.1016/J.ENERGY.2011.05.036

A Feasibility Analysis of Using Savonius VAWT on a Vehicle for Energy Capture

Punit Prakash, Chittanuri Sucheth, Santanu Mitra, and Nishant Mishra

Abstract Savonius vertical axis wind turbines (VAWT) are very common off-grid power producing devices. The ideal environment for its operation is undisturbed freestream wind which is rarely available in urban surroundings. Operational environment has a significant effect on the performance of VAWT related to power production. The last decade has served as a transition period in the transport industry, from fossil fuel-based to electric-based vehicles. Regenerative braking and other methods are already in place to produce electricity onboard. This work aims to produce power onboard using a VAWT in the air vents of cars by utilizing the air intake space. A 2D computational study was conducted on an open-source tool OpenFOAM to showcase the potential of power production, when the turbine is kept between the blocks representing the car body and when the turbine is in the free stream velocity. A wind velocity of 5, 7, and 9 m/s was adopted to compare both the models with Re. no. 12804, 17,925, and 23,047. The performance for the turbine between blocks performs better in terms of coefficient of torque and C_P values.

Keywords Savonius · VAWT · OpenFOAM · Wind energy · Fluid structure interaction

Nomenclature

D	Rotor diameter [m]
d	Blade diameter [m]
C_m/C_t	Coefficient of moment
C_p	Coefficient of performance
FSI	Fluid structure interaction

P. Prakash · C. Sucheth · S. Mitra
Department of Mechanical Engineering, Shiv Nadar Institute of Eminence, Delhi 201314, India

N. Mishra (✉)
School of Engineering, UPES, Dehradun 248007, India
e-mail: nishant.mishra@ddn.upes.ac.in

1 Introduction

Wind energy is one of the most abundant forms of energy on earth and one of the major contributors of green renewable energy. According to IRENA [1], wind turbine installed capacity has increased from 200 to 1600 TW during the last decade. Savonius VAWT are drag-based energy harvesting devices which transform kinetic energy of wind into electrical energy. They are simple to construct and have low cut-in wind speed. Bethi et al. [2] (2019) presented a computational work on Savonius turbine producing power by train inside a tunnel and reported a distance of 0.5 m to be the best suited for power production. Mao et al. [3] study an aerodynamic performance study for building integrated power performance and reported a significant increase in power production than in uniform wind flow conditions. Putri et al. [4] studied the turbine with an obstacle on the inlet and stated that the angle of an obstacle has a major effect on torque produce and changing Reynolds number has less effect on the static torque produced. Sugiharto [5] studied characteristics for Savonius turbine with addition of guide vanes and shows 58% increment in the C_p values. A similar study was performed by Kalluvila and Sreejith [6] and observed a similar increment and reported maximum 28% C_p at TSR 0.85 in their computational work at 10 m/s with guide blades. Tantia et al. [7] have worked on design modifications of Savonius blades for increasing the performance of turbine. Mishra et al. [8, 9] have added bio-inspired design for increasing the performance for VAWT including the ducted arrangements with ducted Savonius with end plates showing a 30% increment in C_p value. Shouman et al. [10] stated that the performance can be greatly increased with proper selection of curtain arrangement on the blade surface along with no. of fins added to the blade surface. Mishra et al. [11] have worked on placement on dimples on Savonius VAWT to increase the performance by changing the shape of the blade. The coefficient of torque C_t and coefficient of power C_p equation are stated in Eqs. (1) and (2)

$$C_t = \frac{T_{turbine}}{T_{available}} = \frac{T_{turbine}}{0.5 \times \rho \times A \times V^2 \times R} \tag{1}$$

$$C_p = C_t \times TSR \tag{2}$$

The present work has been divided into further sections, where Sect. 2 represents problem statement followed by Sect. 3 for governing physics and labeled as materials and methods, Sect. 4 for results and discussion, and Sect. 5 for conclusions.

2 Problem Statement

A simplified study for Savonius VAWT has been conducted for a freestream wind velocity and rotor placed in between the intake of a car. Firstly, a 3D study static study is performed on a basic modified car model with turbine placed at air intake space as shown in Fig. 1.

To determine the effect of drag generated by the Savonius rotor on the car model. Three static cases were tested (a) without turbine, (b) turbine facing min surface area, and (c) turbine facing maximum surface area. Later, a 2D study has been performed with a freestream condition of wind and to represent the air intake space of two block areas placed at top and bottom indicating the car body. The aim of the work is to observe the effect these blocks will have on the performance of the turbine, i.e., the torque produced and the coefficient of performance C_P. The two models that are being studied are labeled as Model A as freestream condition of Savonius turbine and Model B is the turbine in between block as shown in Fig. 1. The domain is set as 10 D at the inlet and 20 D toward the outlet, and other specifications are listed in Table 1 and Fig. 2.
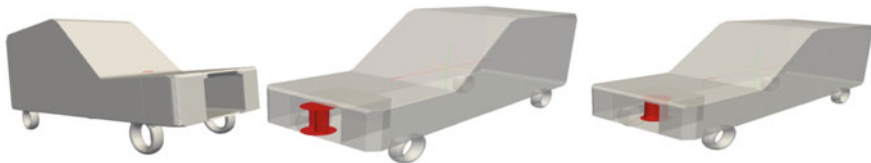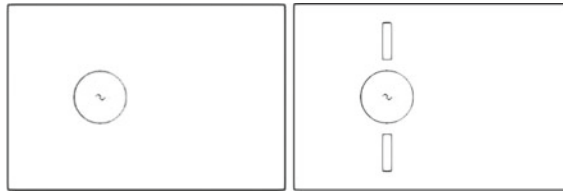

Fig. 1 Model of a modified car with turbine placed at max and min surface area

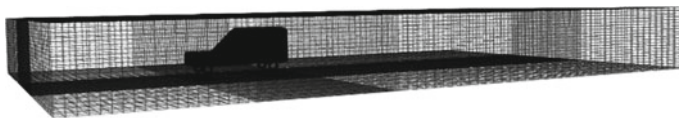| **Table 1** Specifications for rotor	Specification	
	Rotor diameter (D)	0.5 m
	Overlap gap	0.1 D
	Blade diameter	0.27 m
	Thickness	0.003 m
	Distance between blocks and turbine	4D

Fig. 2 Schematic for models A and B

3   Materials and Methods

The computational work has been performed using OpenFOAM, an open-source toolbox for solving Navier–Stokes equations using dual intel Xeon silver 4216 CPU @ 64 processors with 64 GB 2666 MHz DDR4 RAM. The meshing tool used is Gmsh to create hexahedral cell mesh for rotor and stator as shown in Figs. 3, 4a,b. This study uses overset/chimera mesh technique to solve the NS equation. In this method, the cell data is transmitted from the background cell to the moving cell using at the outer boundary of the rotor. The cell sizing needed to be similar for better cell data transmission. In this paper, a mergeMeshes tool has been implemented to combine two mesh together to perform CFD analysis. The static analysis uses overSimpleFoam solver for analysis of drag for car body and turbines.

A meshing tool snappyHexMesh [12] is used to cut out cells and formulate the car and blade shape and refine meshing around the blades shaped in the rotor mesh as shown in Fig. 4b. The study focuses on fluid flow analysis for prescribed rotation of rotor as well as flow induced rotation to get a consolidated comparison of performance during each case. The rotor body is treated as a wall for prescribed rotation, and only fluid equations are needed to be solved; the solver used for solving dynamic mesh is dynamicOversetFvMesh. For flow-induced analysis, the rotor inertial parameters have been updated and a sixDoFDynamicMotion [13] solver for solving the dynamic mesh with solidbodyMotion function having crankNikolsan solver. To solve Reynolds-averaged Navier–Stokes equation, $k - \omega$ SST model is used. The fluid-induced motion required the inertial description for the blades. The various simulation parameters are listed in Table 2. The cell information transfer takes place by transfer of information form background domain cells to the rotor cell with the outer cells of rotor boundary as shown in Fig. 5. In this region, no computation takes place in domain cells, and only rotor cells are being solved. The first cell height was targeted to 10^{-4} to achieve greater accuracy.
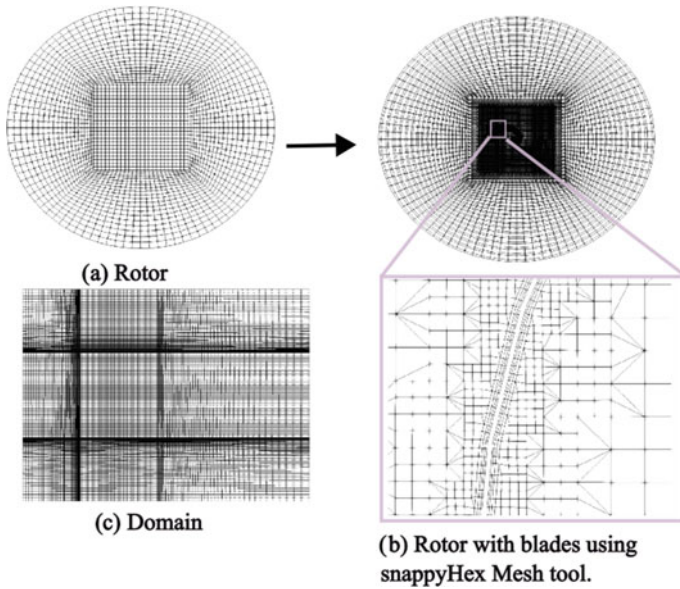

Fig. 3 Meshed car body

(a) Rotor

(c) Domain

(b) Rotor with blades using snappyHex Mesh tool.

Fig. 4 Meshing scheme for **a** rotor mesh, **b** rotor with blades and refinement, and **c** domain mesh

Table 2 Specifications for simulation

Boundary conditions	
Inlet	X = 5,7, and 9; Y = 0, Z = 0
Outlet	Pr. = 0 Bar
Blades	Walls with no-slip boundary condition
FvScheme	
Ddt scheme	Euler
gradScheme	Gauss linear
DivScheme	Limited linear
Laplacian scheme	Gauss linear corrected
Interpolation scheme	Linear
Constant	
Transport model	Newtonian
Dynamic mesh solver	DynamicOversetFvmesh
solidBodyMotionFunction	rotatingMotion and sixDoFDynamicMotion

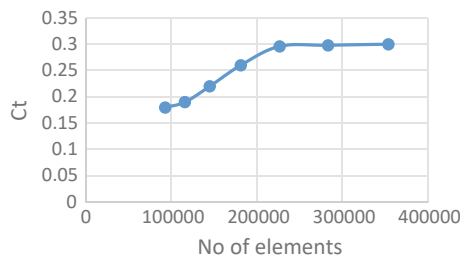The meshed scheme for Model A and Model B is shown in Fig. 6.
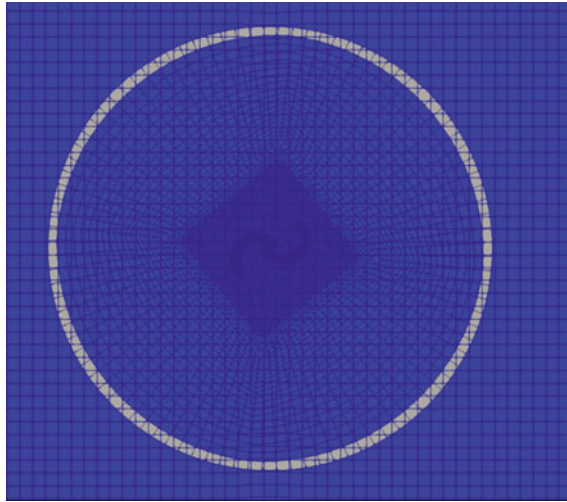
Fig. 5 Region of cell information transfer from domain to rotor
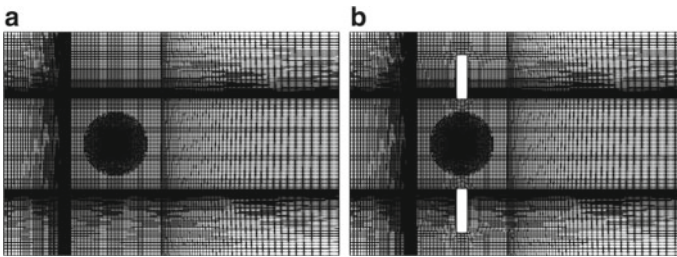
Fig. 6 Meshing scheme for **a** Model A, **b** Model B

A mesh independent study was conducted for TSR 0.4 as shown in Fig. 3, and the mesh with 354,351 cells is used to run all other TSR cases as shown in Figs. 5 and 7.

Fig. 7 Mesh independent study

4 Results and Discussion

The steady-state analysis for car was performed, and velocity contour has been shown for comparison in Fig. 8. All three car models showed a similar drag coefficient value c_d of 0.65 as shown in Fig. 9. The 2D study for Savonius was performed for three different wind velocities 5, 7, and 9 m/s for the prescribed rotation case, and respected averaged coefficient of torque with TSR has been shown in Fig. 10. The C_p obtained is presented in Fig. 11. An incremental increase in C_p was observed for increasing the wind velocity. The addition of blocks shows an increment in the C_p values from 8 to 18% with prescribed rotation scheme as shown in Fig. 12, and this increment can be linked to the wake effect caused due to the blocks and be stated as a tunneling effect caused due to the blocks.

A similar trend of increase in C_p was observed for flow-induced rotation case. A comparative plot for pressure at time 2 s has been shown in Fig. 13. We observe a higher pressure on the blade side facing the wind, and a low pressure region is created on the outlet side. A clear pressure variation from high pressure to low pressure can be seen in model at the offset that indicates the flow through the offset region. As flow passes the blade, Model A has a slight decrease in pressure. Model B which has a greater decrease in pressure compared to Model A could have been caused due to the turbulence created and is shown in Fig. 14 using arrow diagram for pressure for each cells. A recirculation can be seen on both Models A and B which indicated that a lower pressure region could have been created due to flow recirculation. To have a flow pattern at this time step, a streamline plot has also been shown in Fig. 15, and recirculation and difference in wind speed due to addition of the blocks can be clearly observed. The velocity contour of both the model at same time step has been shown
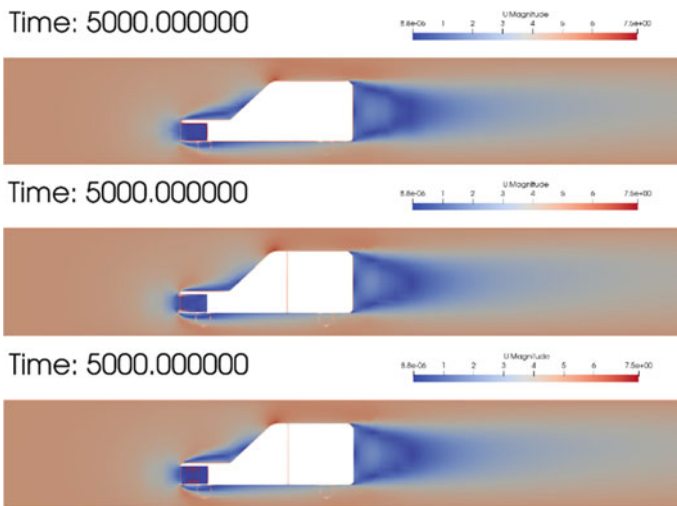

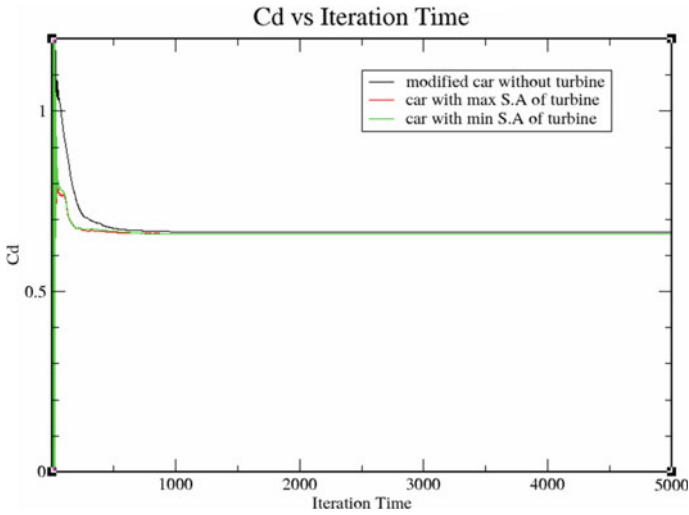**Fig. 8** Velocity contour for modified model, min surface area, and maximum surface area

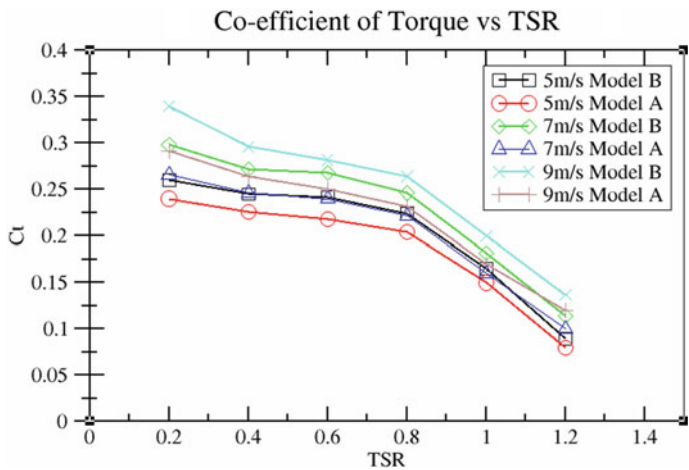**Fig. 9** Coefficient of drag versus iteration time

Fig. 10 Coefficient of moment versus time, Models A and B

in Fig. 16. The block case shows high velocity region near the turbine. Figure 17 shows a comparative plot for coefficient of moment for both models with their mean coefficients for label Model A which is 0.21 for freestream condition and Model B
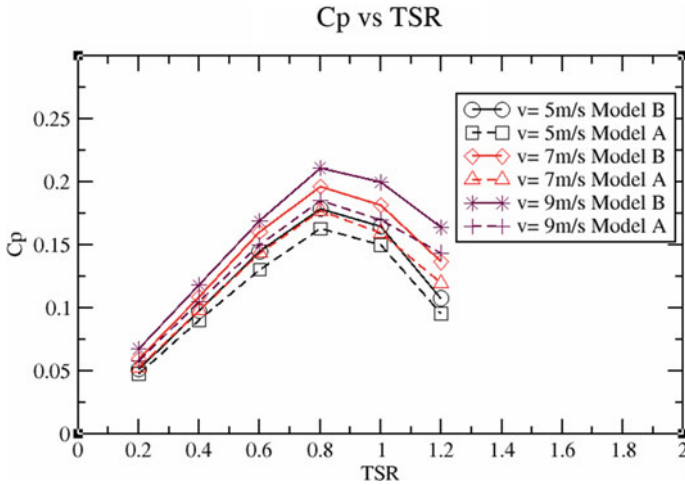
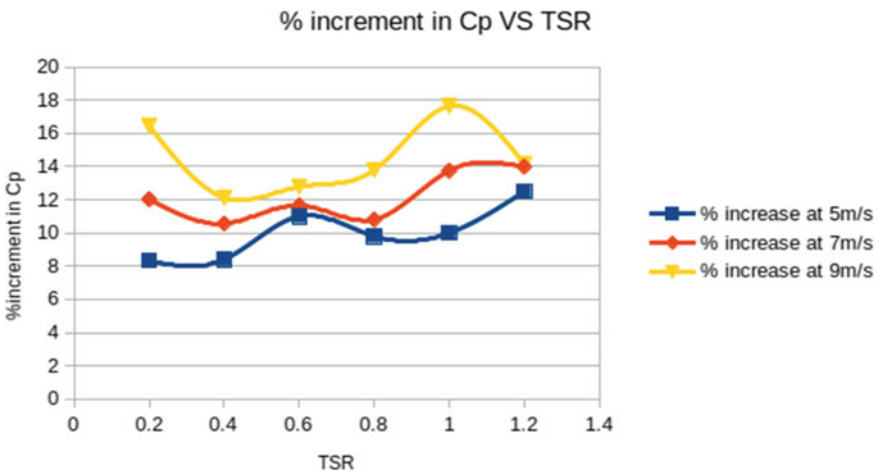**Fig. 11** Coefficient of performance C_p versus time

Fig. 12 Increment in C_p values for comparing the Models A and B at different TSR values

with blocks which has a mean value of 0.32. It can be clearly observed that Model B with block is having a greater coefficient of moment values; we observe a 52% increment in C_m with the addition of blocks in Model B. The C_m is an indicative of self-starting characteristics of the turbine; it can be clearly observed from the Figure that Model B which is having block performs better along with the improvement in the self-starting time with addition of blocks. The comparative drag coefficient has been shown in Fig. 18, and Model B outperforms Model A and has a peak at time step 1.5 s as 3. Figure 19 shows a comparative angular velocity plot, and both
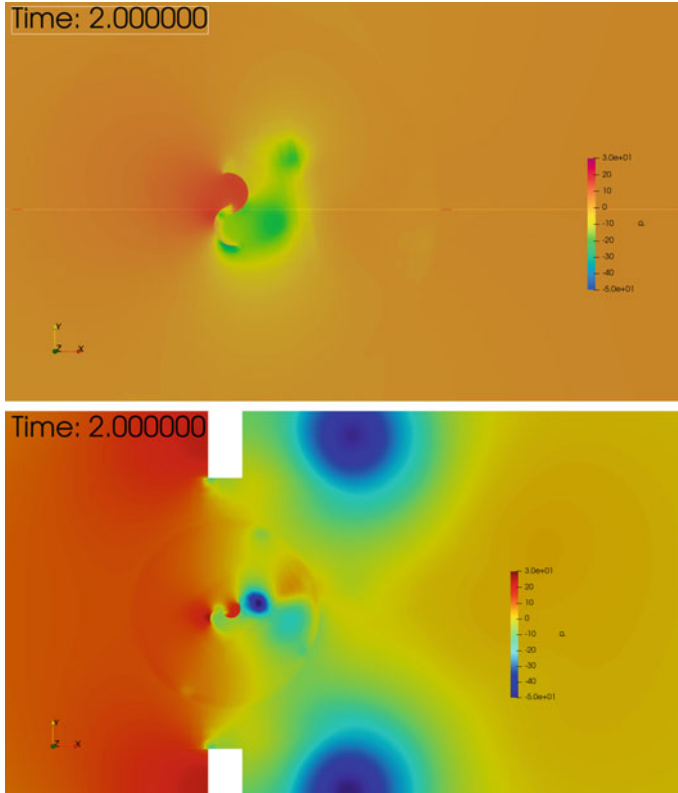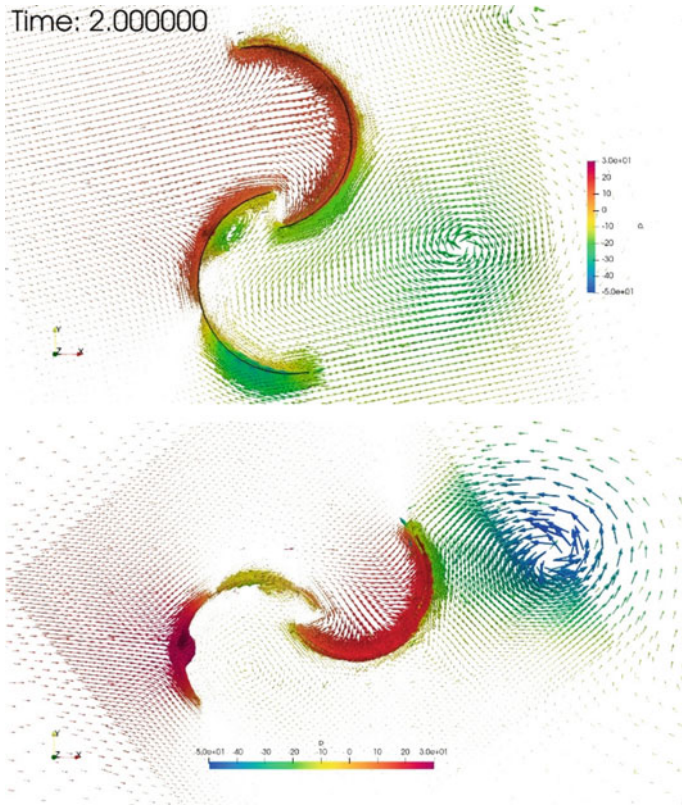
Fig. 13 Pressure contour for models A and B

models do start to rotate at 0.5 s, Model A lags behind the Model B, and at 3 s 24% increment in angular velocity was observed for Model B. This increment in angular velocity can contribute toward better self-starting characteristics for Model B.

## 5 Conclusions

The present work performs a steady-state analysis of a 3D modified car models with different placement orientation to formulate the losses associated with addition of the turbine on board the vehicle. The analysis showed no appreciable losses associated with the addition of the turbine onboard and showed a c_d as 0.65 in a steady-state analysis performed at 5 m/s wind speed.

Fig. 14 Pressure contour for models A and B

Furthermore, a 2D CFD study is done by creating dynamic similarity that VAWT placed in the front of the car. The study shows an increment in the performance compared to isolated and Savonius turbine by placing a block at top and bottom of the turbine. The placement has been considered as 4D for each block in the present paper. Two different schemes have been utilized for the simulation. Firstly, the prescribed rotation case which showed 8 to 18% increment as shown in Fig. 12 and the other case uses a fluid structure interaction where the fluid interacts with the solid to rotate the turbine . The analysis was limited to only calculation of fluid
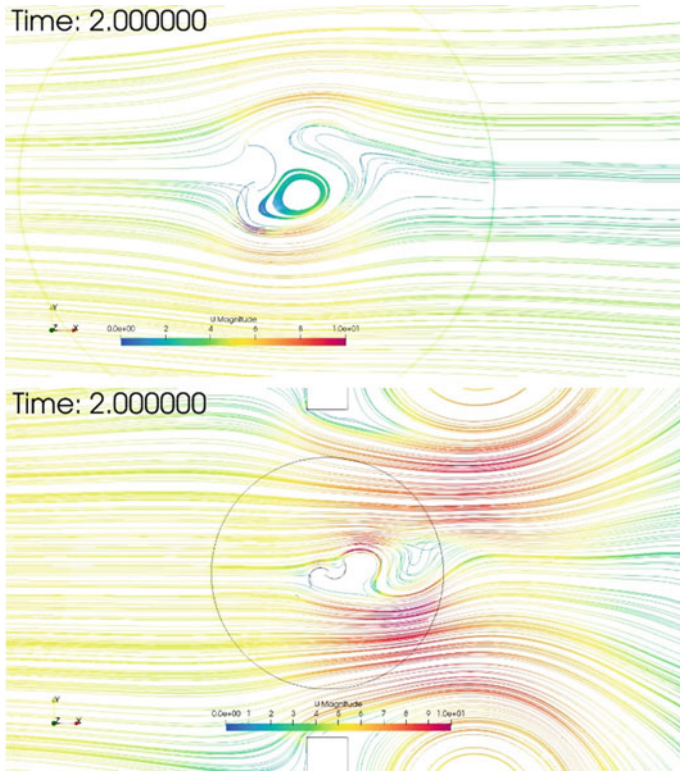
Fig. 15 Streamlines for velocity in models A and B

forces on solid. An increment was observed as 50% for coefficient of moment/torque values and 24% for the angular velocity. The fluid structure interaction scheme is more realistic to the actual nature of wind induced rotation and can be helpful in having a greater understanding of the energy extraction from wind wakes [14] and freestream conditions.

For more accurate results, 3D simulation or an experimental study can be performed for exploring the area of harvesting energy onboard the vehicle.
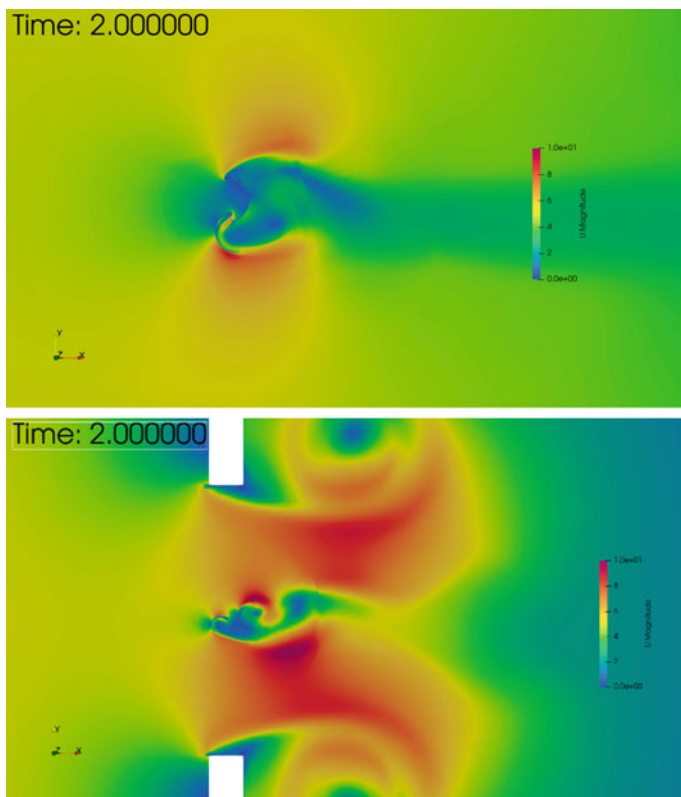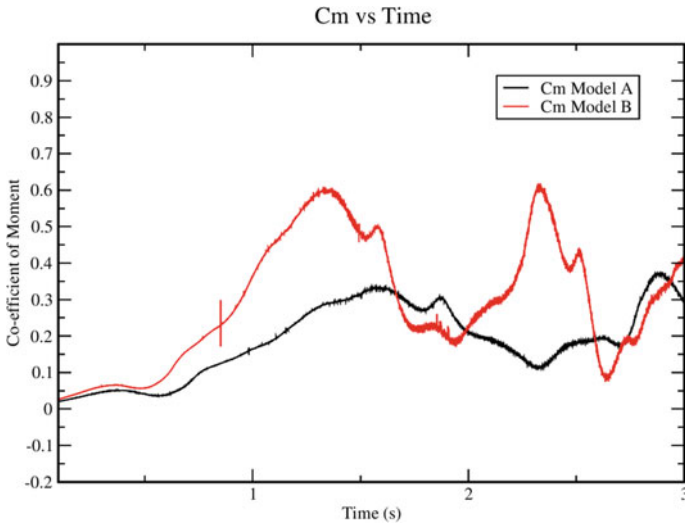
Fig. 16 Velocity contour for model A and model B

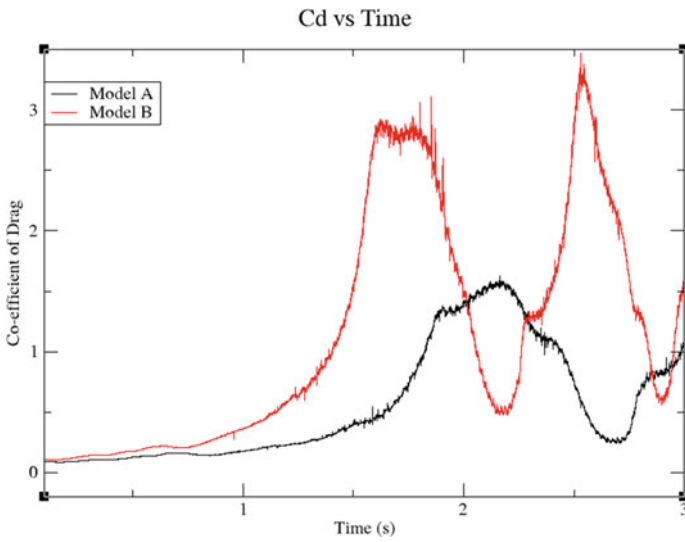**Fig. 17** C_m comparison for models A and B at 5 m/s
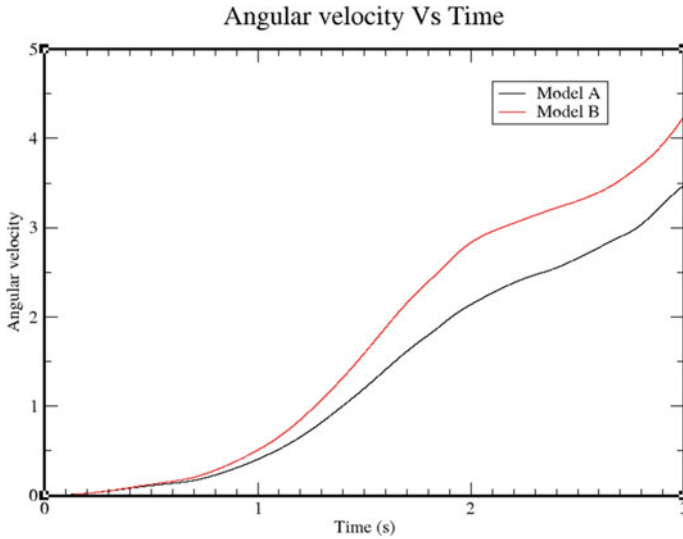

Fig. 18 Comparative drag coefficients

Fig. 19 Comparative angular velocity at 5 m/s for models A and B

References

1. IRENA (2021) Retrieved from https://www.irena.org/wind. Accessed on 10/08/2022
2. Bethi RV, Laws P, Kumar P, Mitra S (2019) Modified Savonius wind turbine for harvesting wind energy from train moving in tunnels. Renew Energy 135:1056–1063
3. Mao Z, Yang G, Zhang T, Tian W (2020) Aerodynamics performance analysis of a building-integrated savonius turbine. Energies 13:2636
4. Putri NP, Yuwono T, Rustam J, Purwanto P, Bangga G (2019) Experimental study on the effect of obstacle upstream of a Savonious wind turbine. SN Appl Sci 1:1261. https://doi.org/10.1007/s42452-019-1253-2
5. Sugiharto B, Soeparman S, Widhiyanuriyawan D, Wahyudi S (2020) Characteristics of the savonius wind using multiple guide vanes. Int J Fluid Machin Syst 13(3):606–614. https://doi.org/10.5293/IJFMS.2020.13.3.606
6. Kalluvila JBS, Sreejith B (2018) Numerical and Experimental study on a modified Savonius rotor with guide blades. Int J Green Energy 15:744–757. https://doi.org/10.1080/15435075.2018.1529574
7. Tantia P, Singh P, Prakash P, Mishra N (2021) Numerical analysis of savonius vertical axis wind turbine with dimpled blades. In: Rakesh PK, Sharma AK, Singh I (eds) Advances in engineering design: lecture notes in mechanical engineering. Springer, Singapore. https://doi.org/10.1007/978-981-33-4018-3
8. Hasan Fayaz SM, Tyagi U, Jain A, Mishra N (2021) Performance enhancement of a savonius vertical axis wind turbine with bio-inspired design modifications. In: Akinlabi E, Ramkumar P, Selvaraj M.(eds) Trends in mechanical and biomedical design: lecture notes in mechanical engineering. Springer, Singapore (2021). https://doi.org/10.1007/978-981-15-4488-0_38
9. Mishra N, Jain A, Nair A, Khanna B (2020) Mitra Experimental investigation on a ducted Savonius vertical axis wind turbine and its performance comparison with and without endplates, Renew Energy Res Applicat 1(1):1–9
10. Shouman MR, Helal MM, El-Haroun AA (2022) Numerical prediction of improvement of a Savonius rotor performance with curtaining and fin addition on blade. Alex Eng J 61:10689–10699

11. Mishra N, Jain A, Nair A, Khanna B, Mitra S (2020) Numerical and experimental investigation on a dimpled savonius vertical axis wind turbine. Int J Renew Energy Res 10(2)
12. OpenFOAM (2022) User Guide: snappyHexMesh, V 10
13. https://github.com/krajit/sixDoFDynamicMotion: Accessed on 20/08/2022
14. Laws P, Bethi RV, Kumar P, Mitra S (2020) Improved design of Savonius rotor for green energy production from moving Singapore metropolitan rapid transit train inside tunnel Proceedings of the Institution of Mechanical Engineers. Part C: J Mech Eng Sci 223–7(2426–2441)

Performance Enhancement of Solar Air Heater with Reverse NACA 0040 Profile Ribs in V-Down Orientation

Tejas Bhavsar, Kalp Patel, Sanjay V. Jain, and Vikas J. Lakhera

Abstract The primary drawback of the solar air heater (SAH) is a decreased heat transfer coefficient caused by the development of a laminar sublayer on the absorber plate's surface. This laminar sublayer can be eliminated by various methods. One of the methods is to use artificial roughened absorber plate. Artificial roughness will improve the heat transfer coefficient, but it also increases the pressure drop; therefore, the ribs must be provided in such a way that solar air heater's overall thermo-hydraulic performance is enhanced. In the current study, SAH analysis was carried out with smooth and artificially roughened absorber plate in the form of NACA 0040 profile ribs with V-down orientation with an angle of attack of 45° in the reverse manner. Experimental results were used to validate the numerically generated results in the Reynolds number (Re) range of 6000 to 18,000. The values of relative roughness pitch and relative roughness height were kept as 5 and 0.065 respectively. As compared to a smooth absorber plate, the ribs' provision improved the Nusselt number and friction factor by 37.51–59.42 and 19.89–26.22% respectively. The maximum thermo-hydraulic performance parameter (THPP) was found to be 1.48 at Re of 16,000.

Keywords Solar air heater · NACA · Heat transfer coefficient · Turbulence · Roughened plate

Nomenclature

A_1	Venturi meter inlet area [m^2]
A_2	Venturi meter throat area [m^2]
A_p	Absorber plate surface area [m^2]
C_d	Coefficient of discharge
C_p	Specific heat at constant pressure [J/kg K]

T. Bhavsar · K. Patel · S. V. Jain (✉) · V. J. Lakhera
Department of Mechanical Engineering, Nirma University, Ahmedabad, India
e-mail: sanjay.jain@nirmauni.ac.in

ρ_a	Density of air [kg/m^3]
a	Distance from start of test section [m]
ASHARE	American Society of Heating, Refrigerating and Air-Conditioning Engineers
C	Chord length [mm]
CFD	Computational fluid dynamics
D	Hydraulic diameter [mm]
e	Maximum roughness/rib height [mm]
g	Gravitational acceleration [m/s^2]
h	Heat transfer coefficient [W/m^{2}K]
k	Conductivity of air, turbulence kinetic energy [W/mK], [m^2/s^2]
L	Length of test section [mm]
NACA	National Advisory Committee for Aeronautics
Nu	Nusselt number
P	Pitch [mm]
RNG	Renormalization group
SAH	Solar air heater
T_{fm}	Air mean temperature [k]
THPP	Thermo-hydraulic performance parameter
T_{pm}	Plate mean temperature [k]
Pr	Prandtl number
ε	Turbulence dissipation rate [m^2/s^3]

1 Introduction

Every country's development path has resulted in an ever-increasing reliance on fossil fuels; consequently, environmental concerns and the rapid depletion of non-renewable resources have led to the advancement of energy solutions that are renewable and do not hurt the environment. Assets for fossil fuels are being depleted quickly. Oil, coal, and other depletable resources are starting to run out in the world; it is predicted that this will happen within the next 40 years. We must therefore look for sources of renewable energy, such as solar, hydro, wind, bio, and geothermal energy [1].

Solar energy is the heat or light the sun produces. A variety of constantly developing technologies, including solar architecture, solar thermal energy, solar heating, and photovoltaics, can be used to harness it. It is important source of renewable energy. There are two types of solar energy harvesting: active solar and passive solar [2].

Solar collectors are devices that capture solar radiation energy and convert it into the internal energy of fluid passing through it. The equipment's main idea is to use solar energy, a free and abundant energy source, to fulfil the requirement for heating, which typically requires a mechanical or other type of power supply. One of the

technological advanced, most efficient and environmentally benign inventions is the solar collector. Solar thermal technology, often known as solar air heating, uses the energy from the sun to heat air by absorbing it.

In order to increase the heat transfer co-efficient and performance of solar air heater, laminar sublayer has to be eliminated. This can be done by creating the turbulence using artificial roughened absorber plate. Many investigators have used different types of methods for design of artificial roughened absorber plate, viz. ribs of different geometry such as round, rectangular, inclined ribs, V-shaped, V-shaped discrete ribs, 3-D roughness geometries, etc. [3].

2 Literature Review

Over the years, different investigators have used different roughness profiles like transverse ribs [3], inclined ribs [4, 5], V-orientation ribs [6–9], arc-shaped ribs [10–12], transverse discrete ribs [13, 14]. Patel et al. [15] analysed solar air heater with reverse NACA 0040 profile ribs with a chord length of 10, 15, and 20 mm. Airfoil with chord length of 15 mm resulted in maximum Nusselt number (Nu) and THPP of 106.22 and 2.51 respectively. Further, by discretization of these ribs THPP was improved by 5.58% [16]. Many researchers have used different ribs in V-orientation with an angle of attack range of 30°–90° [17–19]. The V-orientation resulted in six times higher Nu than the smooth plate [20].

Many investigators have analysed the performance of solar air heater with numerical approach in order to optimize the rib profile and its orientation. Yadav et al. [21] used different turbulence models, viz. standard k-ε model, renormalization-group (RNG) k-ε model, realizable k-ε model, standard k-ω, and shear stress transport k-ω model and compared the same with Dittus–Boelter empirical relation. Among the various models, RNG k-ε model was found to be closest with the Dittus–Boelter relation. The RNG k-turbulence model was suggested by numerous other researchers for use in the investigation of solar air heaters. [22–24].

Karwa et al. [25] carried our experimental studies on SAH with rectangular ribs with various orientations like transverse, inclined, V-up continuous and V-down continuous. Among the different orientations, V-down orientation resulted in the better performance. In the present study, analysis of solar air heater was carried out with smooth plate and an artificially roughened absorber plate in the form of reverse NACA 0040 profile ribs with V-down orientation with an angle of attack of 45°. The numerical results were validated with results obtained from experiments in the Reynolds number (Re) range of 6000 to 18,000. The novelty of the work is use of three-dimensional (3-D) profile in V-down orientation. Very few researchers have used 3-D profile in V-orientation so far.

3   Numerical Simulation of Solar Air Heater

A numerical simulation for this study was carried out in ANSYS Fluent 21.0_R1 tool.

3.1   Modelling and Meshing

The three-dimensional computational model of absorber plate is as shown in Fig. 1. This model is designed in ANSYS Spaceclaim 21.0_R1 tool. The length of entry section and test section are 525 and 1000 mm respectively. The height and width of duct are 25 and 300 mm respectively. The width/height (W/H) ratio is taken 12 as per ASHRAE standard [26] which also studied by many researchers [15, 16, 22, 24]. The value of relative roughness pitch (P/e) and relative roughness height (e/D) were kept as 5 and 0.065 respectively.

For design of NACA 0040 profile rib Eq. (1) was used. The lower side of the absorber plate in the current investigation was equipped with a half-symmetric airfoil profile.

$$
\begin{aligned}
y(t) = {}& 1.4845(x)1/2\,t - 0.63(x)t \\
& - 1.758(x)2t + 1.4215(x)3t - 0.5075(x)4t
\end{aligned}
\tag{1}
$$

For meshing, ANSYS basic meshing tool with grid size of 10 mm and curvature angle of 14° was used. The total number of elements is 73,17,741 which was finalized by doing grid independency test with number of elements in the range of 43.3 to 87.4 lacs (Fig. 2).

Fig. 1 Computational model of NACA 0040 absorber plate with v-orientation
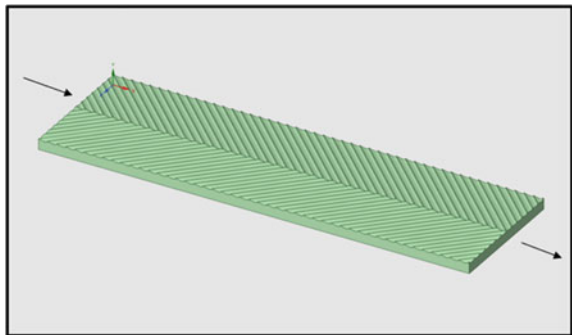
Fig. 2 Grid for v-orientation plate
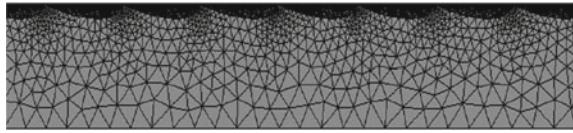
3.2 Solution Methodology and Governing Equations

At the duct's entrance, a velocity inlet was defined as the boundary condition, and at the duct's output, a pressure outlet with atmospheric pressure was employed. At the top face of the duct wall, a heat flux of 1000 W/m^2 was specified. The lower and side walls were considered as adiabatic. The details of solution method applied for the numerical work are given in Table 1.

The governing equations used for the computational analysis of SAH are given in Eqs. (2–6) [16].

Equation for conservation of mass,

$$\frac{\partial u}{\partial x} + \frac{\partial \upsilon}{\partial y} + \frac{\partial w}{\partial z} = 0 \tag{2}$$

Equations for conservation of momentum,

$$u\frac{\partial u}{\partial x} + \upsilon\frac{\partial u}{\partial y} + w\frac{\partial u}{\partial z} = -\frac{1}{\rho}\frac{\partial p}{\partial x} + \vartheta\left(\frac{\partial^2 u}{\partial x^2} + \frac{\partial^2 u}{\partial y^2} + \frac{\partial^2 u}{\partial z^2}\right) \tag{3}$$

$$u\frac{\partial \upsilon}{\partial x} + \upsilon\frac{\partial \upsilon}{\partial y} + w\frac{\partial \upsilon}{\partial z} = -\frac{1}{\rho}\frac{\partial p}{\partial y} + \vartheta\left(\frac{\partial^2 \upsilon}{\partial x^2} + \frac{\partial^2 \upsilon}{\partial y^2} + \frac{\partial^2 \upsilon}{\partial z^2}\right) \tag{4}$$

$$u\frac{\partial w}{\partial x} + \upsilon\frac{\partial w}{\partial y} + w\frac{\partial w}{\partial z} = -\frac{1}{\rho}\frac{\partial p}{\partial z} + \vartheta\left(\frac{\partial^2 w}{\partial x^2} + \frac{\partial^2 w}{\partial y^2} + \frac{\partial^2 w}{\partial z^2}\right) \tag{5}$$
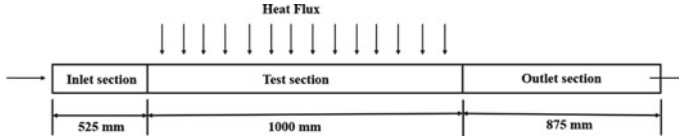
Equation for conservation of energy,

Table 1 Solution method

Parameter	Values
Turbulence model	Renormalization-group k-ε
Hydraulic diameter (D_h)	0.04615 m
Velocity range	1.97–5.87 m/s
Energy equation	ON
Near wall treatment	Viscous heating—ON Enhance wall treatment—ON Thermal effects—ON
Solution method	SIMPLE scheme
Reference value	Compute from inlet

Fig. 3 Schematic layout of experimental setup

$$u\frac{\partial T}{\partial x} + \upsilon\frac{\partial T}{\partial y} + \upsilon\frac{\partial T}{\partial z} = \alpha\left(\frac{\partial^2 T}{\partial x^2} + \frac{\partial^2 T}{\partial y^2} + \frac{\partial^2 T}{\partial z^2}\right) \tag{6}$$

The RNG k-ε model's governing equations are as follows [3].
Turbulent kinetic energy (k):

$$\frac{\partial}{\partial x_i}(\rho k u_i) = \frac{\partial}{\partial x_j}\left(\alpha_k \mu_{eff}\frac{\partial k}{\partial x_j}\right) + G_k - \rho\varepsilon \tag{7}$$

Turbulent dissipation rate (ε):

$$\frac{\partial}{\partial x_i}(\rho\varepsilon u_i) = \frac{\partial}{\partial x_j}\left(\alpha_k \mu_{eff}\frac{\partial k}{\partial x_j}\right) + C_{1\varepsilon}\frac{\varepsilon}{k}G_k - C_{2\varepsilon}\rho\frac{\varepsilon^2}{k} - R\varepsilon \tag{8}$$

3.3 Experimental Setup

The experimental setup was designed and installed in the Mechanical Engineering Department, Nirma University. Figure 3 illustrates the schematic layout of the experimental design.

An experiment setup is having major components like absorber plate, air duct, temperature sensors, air blower, air control valve, insulation box filled with glass wool, electric heater, voltmeter, ammeter, and variable autotransformer as per shown in Fig. 4.

Table 2 contains particulars of the various instruments and components employed throughout the experimental study.

3.4 Performance Parameters

The Nusselt number, friction factor, and THPP are a few of the measures that are used to analyse the performance of SAH. The following formulae were used to determine each of these parameters.

Fig. 4 Pictorial view of
experimental setup
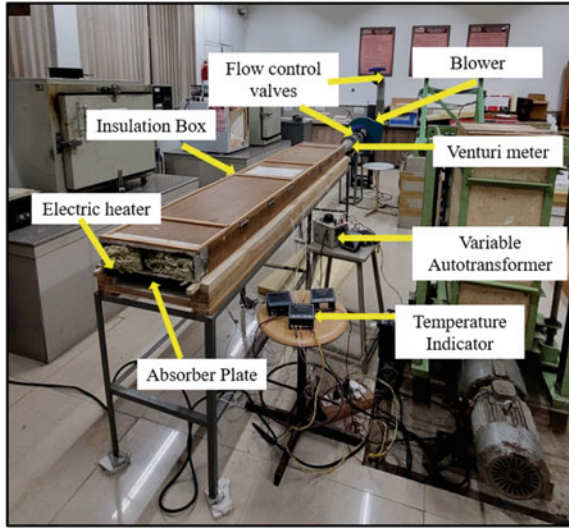
Table 2 Specifications of SAH setup

Information on the device or component	Specifications
Electric heater	Capacity: 1000 W/m^2
Absorber plate	Material: Al
Insulation	Glasswool
Temperature sensors	Type: Resistance temperature detector PT-100 Numbers: 19
Ammeter	Range: 0–2 A
Micromanometer	Make: Fluke Range: ± 400 mm of H$_2$O
Variable autotransformer	Range: 270 V
Volt meter	Range: 0–220 V

The air discharge through venturi meter was calculated as,

$$Q = \frac{c_d A_1 A_2 \sqrt{2g\,\Delta h_a}}{\sqrt{A_1^2 - A_2^2}} \tag{9}$$

where, $\Delta h_a = \left(\frac{\rho_w}{\rho_a} - 1\right) \times \Delta h_w$

The velocity of air was calculated as,

$$V = \frac{\dot{m}}{\rho_a \times A} \tag{10}$$

The friction factor was measured by tracking the amount of pressure that was lost along the test section's length.

$$f = \frac{\Delta p D}{2 L V^2 \rho_a} \tag{11}$$

The heat transfer rate to the air from absorber plate was determined as,

$$Q = \dot{m} C_p (T_o - T_i) \tag{12}$$

$$\text{Inlet temprature} \, T_i = \frac{T_{13} + T_{14} + T_{15}}{3} \tag{13}$$

$$\text{Outlet temprature} \, T_o = \frac{T_{16} + T_{17} + T_{18}}{3} \tag{14}$$

where T_{13}, T_{14}, T_{15} are inlet temperature of test section and
T_{16}, T_{17}, T_{18} are outlet temperature of test section.
The heat transfer coefficient was calculated as,

$$h = \frac{Q_a}{A_p \left(T_{pm} - T_{fm} \right)} \tag{15}$$

where $T_{pm} = \frac{T_1 + T_2 + T_3 + T_4 + T_5 + T_6 + T_7 + T_8 + T_9 + T_{10} + T_{11} + T_{12}}{12}$

$$T_{fm} = \frac{T_i + T_o}{2}$$

The Nusselt number was calculated as,

$$Nu = \frac{h L}{k} \tag{16}$$

The THPP was calculated as,

$$\text{THPP} = \frac{Nu_r / Nu_s}{(f_r / f_s)^{1/3}} \tag{17}$$

4 Results and Discussion

The numerical conclusions for the smooth duct were supported by experimental findings in this section. Results of smooth and roughened plates were contrasted in the presentation.

Figure 5 illustrates temperature contours for SAH provided without and with ribs for the selected portion of the test Sect. ($0.8485 \leq a/L \leq 0.976$) which is shown at Re = 10,000. It can be seen from Fig. 5b that the temperature is relatively higher in V-orientation than the smooth plate. Due to higher surface temperature, heat transfer from the surface to air was increased. As a result, the surface heat transfer coefficient is increased by using NACA 0040 C15 profile ribs in V-orientation.

Figure 6 shows comparison of streamlines for smooth and roughened plates. It can be seen that the provision of ribs led to vortex formation near the entrance of each rib thereby increased the turbulence created and resulted in increment in the value of heat transfer coefficient and hence Nusselt number.

The major objective of provision of ribs is to increase the turbulence. The turbulence kinetic energy (TKE) is directly proportional to turbulence. It can be observed from Fig. 7 that in the roughened plate, TKE is relatively higher than the smooth plate which resulted in increase in the heat transfer coefficient.
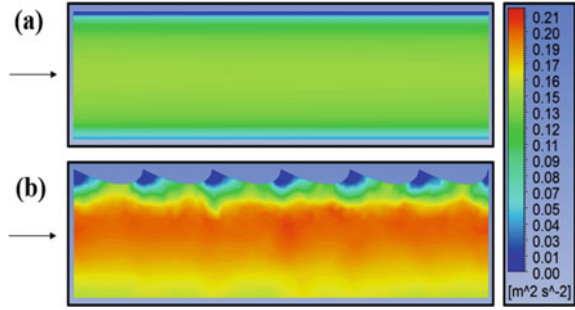

Fig. 5 Temperature contours for $0.8485 \leq a/L \leq 0.976$, **a** Smooth plate, **b** V-orientation plate
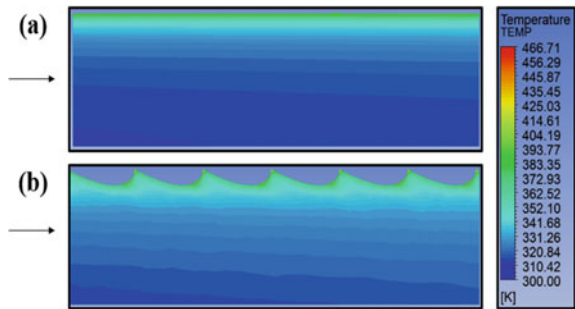
Fig. 6 Streamlines for $0.8485 \leq a/L \leq 0.976$, **a** smooth plate, **b** V-orientation plate
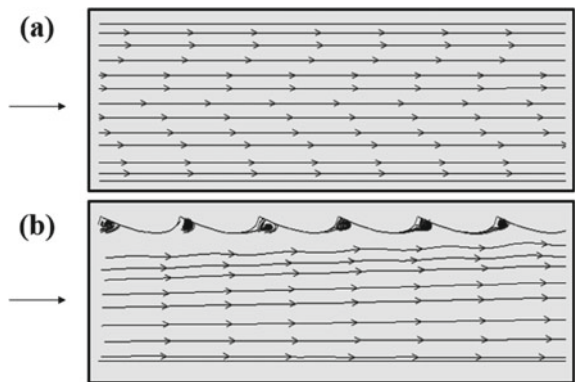
Fig. 7 TKE contours for
$0.8485 \leq a/L \leq 0.976$,
a smooth plate,
b V-orientation plate

Fig. 8 Pressure contours for
$0.8485 \leq a/L \leq 0.976$,
a smooth plate,
b V-orientation plate
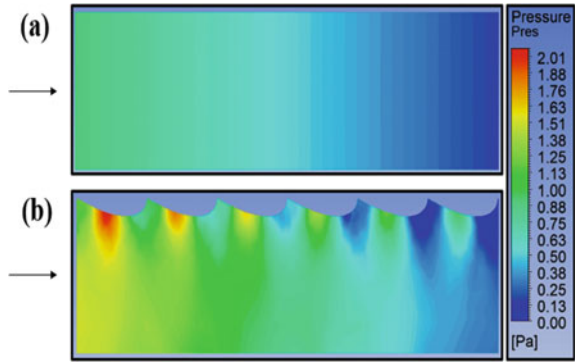
Figure 8 depicts the pressure contour comparison between the smooth and the roughened plates. It can be seen that there is higher pressure drop in the roughened plate in comparison with the smooth plate. The higher pressure drop resulted in higher friction factor as discussed in the next section.

4.1   Validation and Comparison of Results

The validation of numerical results obtained for the smooth plate was done with the experimental results and following empirical relations.

Gnielinski correlation for $6000 \leq \mathrm{Re} \leq 10,000$ [16].

$$Nu_s = \frac{\left(\frac{f}{8}\right)(Re - 1000)Pr}{1 + 12.7\left(\frac{f}{8}\right)^{\frac{1}{2}}\left(Pr^{\frac{2}{3}} - 1\right)} \tag{18}$$

where f is the Darcy friction factor calculated by,

$$f = (0.79 ln(Re) - 1.64)^{-2}$$

Dittus–Boelter equation for Re > 10,000 [16].

$$Nu_s = 0.023 Re^{0.8} Pr^{0.4} \tag{19}$$

Figure 9 shows comparison between Nusselt number versus Reynolds number for smooth and roughened plates obtained from different approaches. As can be observed, Nu increased in all the cases along with a rise in Re. For the smooth plate, the trend of Nu obtained from numerical, experimental and empirical approaches was found to be similar. Nu calculated numerically was found to be higher than Nu evaluated from experimental results. This may be due to negligence of heat losses in the numerical approach. It can also be seen that provision of artificial ribs resulted in substantial improvement in Nu in comparison with the smooth plate. Thereby, Nu was increased by 37.51% to 59.42% in Re range of 6000 to 18,000.

The comparison of f versus Re plot for smooth and roughened plates is shown in Fig. 10. It is clear that the friction factor decreased with increment in Re in all the cases. Numerically obtained f was found to deviate by 5.13% to 13.46% compared to experimental values. Due to addition of ribs, friction factor was increased by 19.89% to 26.22% in comparison with the smooth plate in Re range of 6000 to 18,000 which may be due to increase in the turbulence.

In SAH due to provision of artificial ribs, Nu increased but simultaneously f also increased. Hence, the performance of roughness element is analysed in terms of THPP as stated in Eq. (17). Figure 11 shows that THPP increased with increment in Re due to provision of NACA 0040 profile ribs in V-orientation. The highest value of THPP was found to be 1.48 at Reynold number of 16,000.

Fig. 9 Nu versus Re plot for smooth and roughened plates
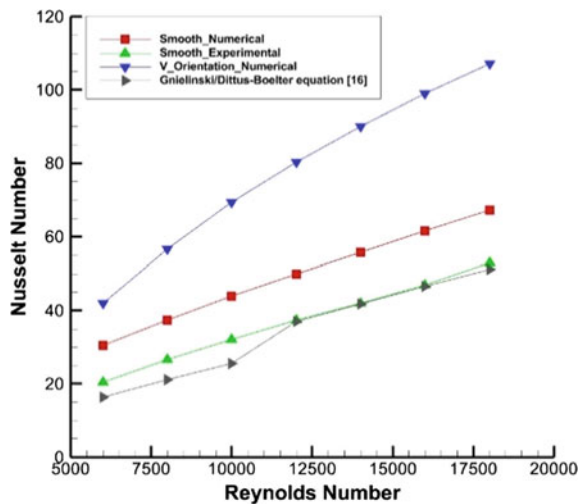
Fig. 10 Friction factor
versus Reynolds number plot
for smooth and roughened
plates
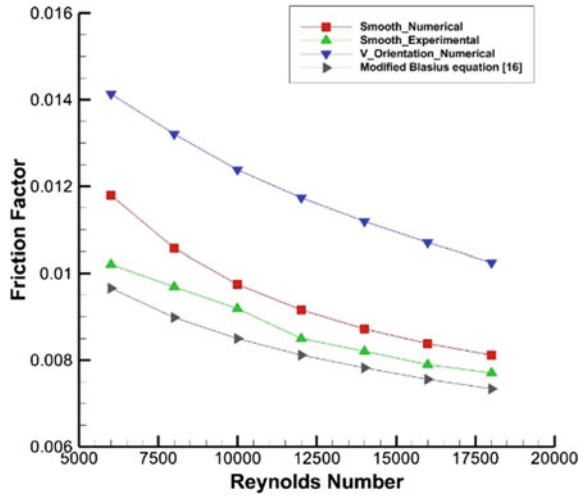
Fig. 11 THPP versus Re
plot for roughened plate
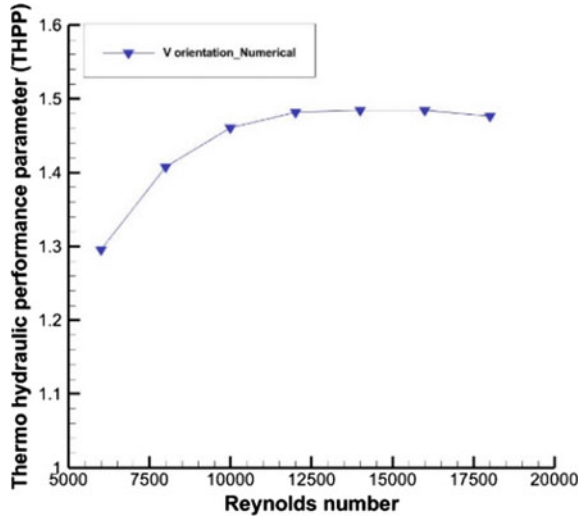
5 Conclusions

In the present study, analysis of solar air heater was done with smooth and artificially
roughened absorber plates. In order to create the roughness, NACA 0040 profile
ribs were used in V-down orientation with an angle of attack of 45° in the reverse
manner. The numerical results obtained for the smooth plate were validated with
the experimental results in the Reynolds number (Re) range of 6000 to 18,000. The
difference between the numerical and experimental results was found to be 5.13% to
13.46% for the friction factor. The provision of artificial ribs led to 37.51% to 59.42%

increment in Nu and 19.89% to 26.22% rise in the friction factor. The highest value of THPP was obtained as 1.48 at a Reynolds number of 16,000.

References

1. Ritchie H, Roser M, Rosado P (2020) "Energy", Published online at OurWorldInData.org. Retrieved from: 'https://ourworldindata.org/energy' [Online Resource]
2. Royal society of Chemistry Retrieved from https://www.rsc.org/campaigning-outreach/global-challenges/energy/, [Online Resource]
3. Kumar A, Saini RP, Saini JS (2014) A review of thermo hydraulic performance of artificially roughened solar air heaters. Renew Sustain Energy Rev 37:100–122
4. Aharwal KR, Gandhi BK, Saini JS (2009) Heat transfer and friction factor charateristics of solar air heater ducts having integral inclined discrete ribs on absorber plate. Int J Heat Mass Transf 52:5970–5977
5. Han JC, Zhang YM (1992) High performance heat transfer ducts with parallel broken and v-shaped broken ribs. Int J Heat Mass Transf 35(2):513–523
6. Taslim ME, Li T, Kercher DM (1994) Experimental heat transfer and friction in channels roughened with angled, v-shaped and discrete ribs on two opposite walls, pape no. 94-GT-163. Int Gas Turbine Aeroengine Congr Expos June 13–16, New York, USA
7. Wang L, Sunden B (2004) An experimental investigation of heat transfer and fluid flow in a rectangular duct with broken v-shaped ribs. Experiment Heat Transfer 17:243–259
8. Karwa R, Chitoshiya G (2013) Performance study of solar air heater having v-down discrete ribs on absorber plate. Energy 55:939–955
9. Singh S, Chander S, Saini JS (2011) Heat transfer and friction factor correlations of solar air heater ducts artificially roughened with discrete v-down ribs. Energy 36:5053–5064
10. Hans VS, Gill RS, Singh S (2017) Heat transfer and friction factor correlations for a solar air heater duct roughened artificially with broken arc ribs. Exp Thermal Fluid Sci 80:77–89
11. Pandey NK, Bajpai VK (2016) And varun, experimental investigation of heat transfer augmentation using multiple arcs with gap on absorber plate of solar air heater. Sol Energy 134:314–326
12. Gill RS, Hans VS, Saini JS, Singh S (2017) Investigation on performance enhancement due to staggered piece in a broken arc rib roughened solar air heater duct. Renewable Energy 104:148–162
13. Lau SC, McMillin RD, Han JC (1991) Turbulant heat transfer and friction in a square channel with discrete rib turbulators. J Turbomach 133(3):360–366
14. Singh I, Vardhan S, Singh S, Singh A (2019) Experimental and CFD analysis of solar air heater duct roughened with multiple broken transverse ribs: a comparative study. Sol Energy 188:519–532
15. Patel YM, Jain SV, Lakhera VJ (2019) Thermo-hydraulic performance analysis of a solar air heater roughened with reverse NACA profile ribs. Appl Therm Eng 146:910–920
16. Patel Y, Jain SV, Lakhera VJ (2021) Thermo-hydraulic performance analysis of a solar air heater roughened with discrete reverse NACA profile ribs. Int J Thermal Sci 167:107026
17. Momin AE, Saini JS, Solanki SC (2002) Heat transfer and friction in solar air heater duct with v-shaped rib roughness on absorber plate. Int J Heat Mass Transf 45:3383–3396
18. Sharma A, Awasthi A, Singh T, Kumar R, Chauhan R (2022) Experimental investigation and optimization of potential parameters of discrete v down baffled solar thermal collector using hybrid Taguchi-TOPSIS method. Appl Therm Eng 209:118250
19. Alam T, Saini RP, Saini JS (2014) Experimental investigation on heat transfer enhancement due to v-shaped perforated blocks in a rectangular duct of solar air heater. Energy Convers Manage 81:374–383

20. Hans VS, Saini RP, Saini JS (2014) Heat transfer and friction factor correlations for a solar air heater duct roughened artificially with multiple v-ribs. Sol Energy 84:898–911
21. Yadav AS, Bhagoria JL (2014) A CFD based thermo-hydraulic performance analysis of an artificially roughened solar air heater having equilateral triangular sectioned rib roughness on the absorber plate. Int J Heat Mass Transf 70:1016–1039
22. Kumar S, Saini RP (2009) CFD based performance analysis of a solar air heater duct provided with artificial roughness. Renewable Energy 34:1285–1291
23. Yadav AS, Bhagoria JL (2013) A CFD (computational fluid dynamics) based heat transfer and fluid flow analysis of a solar air heater provided with circular transverse wire rib roughness on the absorber plate. Energy 55:1127–1142
24. Kumar K, Prajapati D, Samir S (2017) Heat transfer and friction factor correlations development for solar air heater duct artificially roughened with 's' shape ribs. Exp Thermal Fluid Sci 82:249–261
25. Karwa R (2003) Experimental studies of augmented heat transfer and friction in asymmetrically heated rectangular ducts with ribs on the heated wall in transverse, inclined, v-continuous and v-discrete pattern. Int Commun Heat Mass Transfer 2:241–250
26. ASHRAE standard, ANSI/ASHRAE 93, 1986, (RA 91)

Measurement Techniques in Fluid Mechanics

μ-PIV/PTV Measurement of Suspensions in Symmetric Diverging-Converging Micro-Channel

Bhaskar Jyoti Medhi, Anugrah Singh, Bhaskor Jyoti Bora, Prabhakar Sharma, and Debabrata Barik

Abstract Single-camera micro-PIV and PTV measurements were performed in diverging-converging micro-channel to study the suspension flow. In micro-channel, the width of the left and right daughter branch constant at 200 μm. A small quantity of 1 μm dyed particles was mixed with the suspension to measure background fluid velocity with the micro-particle image velocimetry technique (μ-PIV), and a small quantity of dispersed particle (6 μm or 10 μm) dyed to measure particle-phase velocity profile and particle distribution using micro-particle tracking velocimetry (μ-PTV). A tip-valley-tip velocity profile was observed near the divergence, which gradually reduces to blunted profile at the outlet of the confluence section. We have qualitatively studied the concentration by using in-house developed particle counting MATLAB programme and from micro-PTV vector map. At the inlet locations of diverging section concentration profile was symmetric due to particle migration towards the centre of the channel which becomes asymmetric at the daughter branches. The profile becomes again symmetric due to additional particles migration towards the centre of daughter branches and in the outlet locations of converging sections.

Keywords Diverging-converging micro-channels · Micro-PIV/PTV · Suspension

B. J. Medhi (✉)
Department of Chemical Engineering, Assam Energy Institute Sivasagar (Centre of RGIPT Jais, Amethi), Sivasagar 785697, India
e-mail: bmedhi@rgipt.ac.in

A. Singh
Department of Chemical Engineering, Indian Institute of Technology Guwahati, Guwahati 781039, India

B. J. Bora
Energy Institute Bengaluru (Centre of RGIPT Jais, Amethi), Bengaluru 562167, India

P. Sharma
Department of Mechanical Engineering, Delhi Skill and Entrepreneurship University, New Delhi 110089, India

D. Barik
Department of Mechanical Engineering, Karpagam Academy of Higher Education, Coimbatore 641021, India

1   Introduction

Suspension transport in micro-fluidic channels with bifurcations is frequently seen in various applications like particle separation, segregation, etc. Physiological systems also experience suspension transport in bifurcating channels. Numerous bifurcation networks exist in the human body's microvascular system, particularly in the brain, aorta, and lung. The bifurcation region of the human blood circulation system is the zone predisposed to aneurysm, coronary artery illness, etc.

One of the significant problems in micro-fluidic devices handling concentrated suspensions is the jamming of particles in certain branches. Therefore, the effect of branching angle, particle concentration and flow rate on flow and particle distribution in symmetric and asymmetric bifurcation channels need to be ascertained. Recently [1] carried out experiments on different bifurcated micro-channels using particle image velocimetry (μ-PIV) and particle tracking velocimetry (μ-PTV) techniques to study the effect of branching angle, particle size on velocity and concentration profiles for diverging and converging flow in symmetric and asymmetric bifurcation channels. They observed that velocity and concentration profiles were symmetric in the intake branch, which became asymmetric as they approached the daughter branches. Profile became symmetric again at the outlet of daughter branches due to further migration of particles towards the centre of the channel.

2   Literature Review and Objective

Most of the experiments on particle migration for suspension flow reported on straight channels and pipes than bifurcating micro-channels. The particles were expected to follow the fluid motion in most investigations on bifurcating micro-channels. This makes it possible to predict the significant particle distribution using information about trajectory near the bifurcation. This behaviour would be altered by any inertial cross-streamline migration or hydrodynamic shear-induced diffusion. In a symmetric bifurcation channel having a similar length and width of daughter section, flow and particle distribution would be the same. However, at an asymmetric bifurcation channel, the particle distribution in the daughter section would be influenced by the concentration profile in the intake branch [2–4]. For an asymmetric bifurcation, the particle-rich centre in the inlet channel would split unevenly into the daughter branches as a result of the migration of particles. Paper [1] also reported that the lower performance of the micro-branching channel to separate the particles from the fluid is due to unequal distribution of particles in the asymmetric channel daughter branches, although the fluid partitioning is even. The primary cause of this behaviour is the redistribution of particles caused by shear. The effect redistribution of particles which changes the symmetric velocity and concentration to asymmetric has not been studied in detail experimentally.

The magnitudes of fluid-particle partitioning in the bifurcation channel depend upon particle size, the particle volume fraction, volumetric flow rate, and angles between the branches. Although in these experiments, particle loading seems small, it was observed that interactions between particles inside the bifurcation were considerably more common, which causes unequal distribution of particles in the bifurcation network. It was observed that their transitional velocity decreases as the particles near the apex of a bifurcation. The next particles in the upstream have time to enter the bifurcation and interact with the earlier particles. These interactions perturb the trajectory of particles near the bifurcations resulting in unequal fluid and particle partitioning in the downstream branches.

In continuation of [1] work, we have conducted similar single-camera micro-PIV, PTV experiments on single-phase Newtonian fluid and dilute suspension of two different size particles in a symmetric diverging-converging micro-channel. The flow velocity profile was measured by μ-PIV, and local concentration was measured by the image processing method and μ-PTV. This will identify and quantify the effect of particle size and channel width on the velocity and concentration profiles, providing unprecedented detail about the effect of shear-induced particle migration on an unequal distribution of the fluid and particle phases in the downstream branches. These previous observations and present work will provide better way of understanding of particle distribution in this type of diverging-converging geometry and have significant contribution for developing micro-fluidic devices for handling suspension transport in bifurcating micro-channels.

3 Materials and Methods

In Fig. 1a, we have shown the schematic drawing of the experimental arrangement. It involves a 12-bit, 1376×1040 pixel CCD camera, which is attached with an epifluorescent microscope. At a particular flow condition, 100 images were recorded with 19 fps for post-processing and to analyse the images. A fluorescence light source was used to illuminate the tracer particles. The desired flow was maintained with a syringe pump. For experiments, two different neutrally buoyant suspensions were prepared by mixing PMMA having mean diameters 6 and 10 μm with a glycerol-water mixture. In our experiment, microscope magnification of the objective lens (M = 10 X) and numerical aperture (NA = 0.25) was constant. In the test channel, the maximum (centreline) velocity was in the range of 0.0159–0.0279 cm/s. Particle and fluid flow Reynolds number (Re) was O (10^{-4}) and O (10^{-2}), respectively. In our experiment, a small quantity of dispersed particles (6 μm or 10 μm) were dyed with a rhodamine 6G to study the particle-phase behaviour by micro-particle tracking velocimetry, and a small quantity of 1 μm dyed particles were mixed with the suspension to measure background fluid velocity field with micro-particle image velocimetry technique. The concentration of tracer for micro-PIV and micro-PTV experiments was in the range of 0.012–0.026% v/v and 0.001–0.006% v/v, respectively.
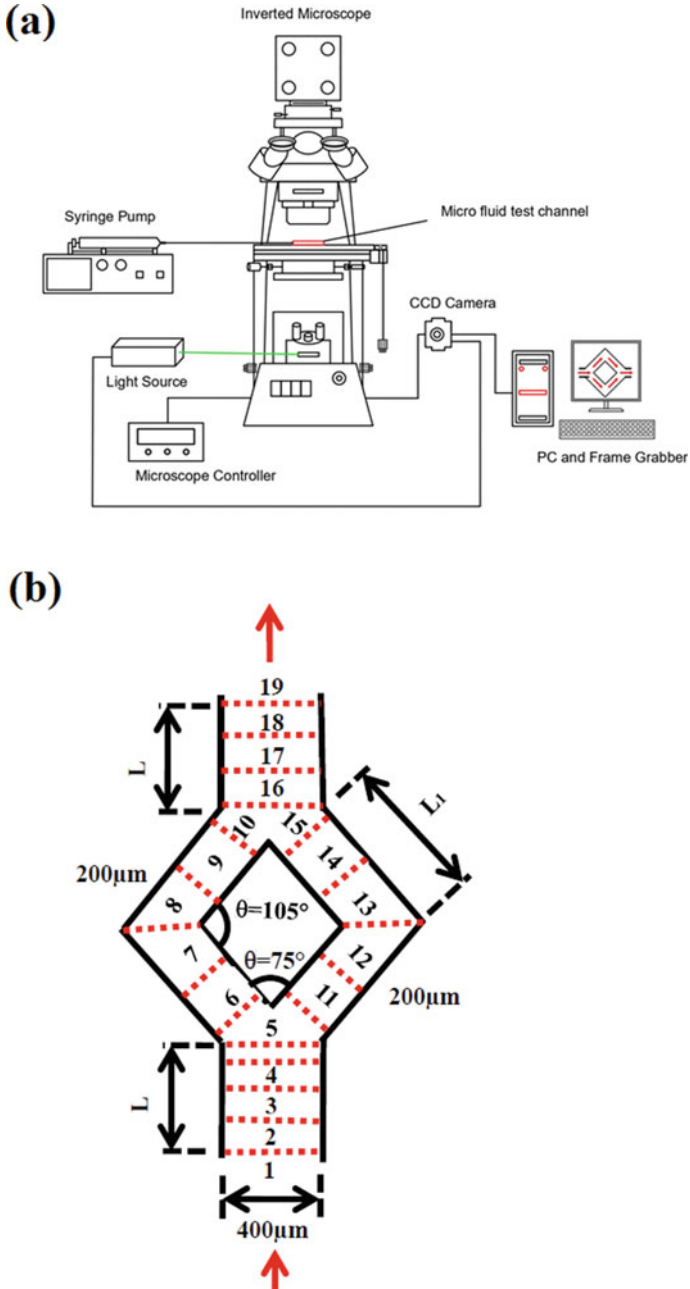
Fig. 1 Schematic diagram of the **a** experimental set-up; **b** symmetric of diverging-converging channel

In Fig. 1b, a schematic of experimental geometry with the locations where measurements were carried out is shown. The relative lengths of inlet and outlet sections were designed equal to ($L = 4$ cm), and the length of the left and right daughter branches were considered as $L_1 = 1.5$ cm. A silicon rubber pipe connected the syringe pump with the inlet of channel whose speed was varied to generate desired flow. In our work length of the rubber pipe was sufficient for a fully developed flow to establish before flow enters the inlet section of the channel. We have conducted experiments keeping particle concentration low 5% so that particle-to-particle impacts can be ignored. Moreover, at low concentration experimental variable can be precisely controlled for accurate and easier measurements.

3.1 Images Post-processing Method

In particle image velocimetry technique, post-processing of the images is necessary to generate the correct velocity and concentration profile. To remove defects such as unequal contrast and low-frequency background noise, image filtering of raw images is essential.

In this study, on the basis of particle size image separation was carried out with in-house developed MATLAB code. For the standard micro-PIV/PTV system, a particle with larger diameter is used to investigate the particle phase phenomena using μ-PTV (micro-particle tracking velocimetry), while small particles are used for measuring the background fluid velocity with μ-PIV (micro-particle image velocimetry) technique. Since in the μ-PIV volume, illumination is used, most of the separated images contain defocused particles, which creates spurious vectors during investigation. Different steps of pre-processing of μ-PIV/PTV images, separation 1 μm tracer and 10 μm test particles based on particle size, separation focused and defocused particles are described in [1].

Micro-PTV investigation was carried out for separated focused test particle image using PTVlab Beta software to get the information on particle-phase phenomena. μ-PIV analysis was carried out for the separated 1 μm tracer image using PIVlab_1.32 software to get the information about carrier fluid phase. The correlation scheme was framed 1 with 2, 2 with 3, 3 with 4 and so on. To analyse the images, it is divided into a number of grids known as interrogation windows (IWs). The size of the IW should be adequately small so that particle displacement in the area is consistent, and additionally, IW should be large enough to contain a sufficient number of particles. Here in this study, μ-PIV analysis was carried out on each of the data sets, with an IW size of 32×32 pixels and an overlap of 75% between the interrogation windows.

4 Results and Discussion

4.1 Velocity Field

In Figs. 2, 3, 4, 5, 6 and 7 mean velocity profile for Newtonian fluid, two suspensions of dispersed particle sizes 6 and 10 μm were plotted in all the locations shown in the schematic, Fig. 1b. In these plots, we have shown the outer wall location is at $x/B = +1$ and $x/B = -1$ for right and left daughter branches respectively. The magnitude of velocity (U) was normalized relative to the maximum velocity (Umax). Plotted profiles in the inlet locations 1, 2 and 3 are shown in Fig. 2. At location 1, velocity profiles were blunted, which indicates that flow was fully developed before location 1. It was observed that at location 3, there is a formation of the tip-valley-tip profile.

Figure 3 shows the relative velocity profiles of Newtonian fluid with suspensions at a location 5 mm ahead of bifurcation (location 4) and at the bifurcation point (location 5) of diverging-converging channel. At this location, the velocity profile become tip-valley-tip pattern similar to described in [1] due to distribution of fluid in the two equal daughter branch. After the divergence point, the flow moves in the left and right daughter channel.

Figure 4 shows velocity profiles of Newtonian fluid with suspensions at location 6 (left daughter branch) and at location 11 (right daughter branch). We observed a shifting velocity profile towards the outer wall direction.

Locations 8 and 13 are the end position for separating flow and the beginning of joining flow. In both the daughter branches, velocity profile tips are shifted in

Fig. 2 Velocity profiles in the inlet branch locations
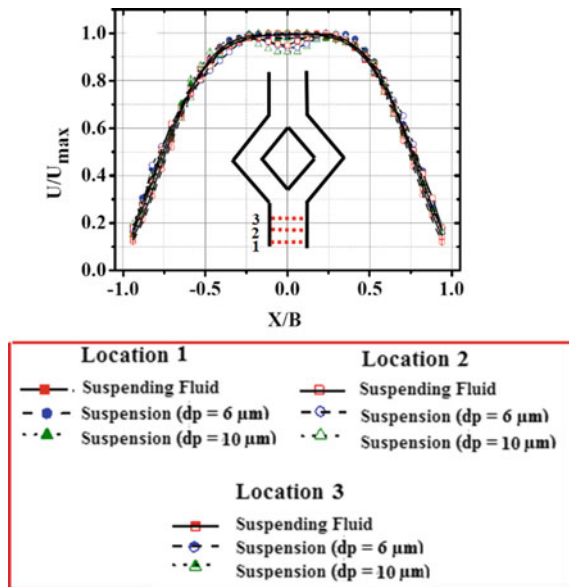
Fig. 3 Velocity profiles in the inlet branch at location 4 and location 5
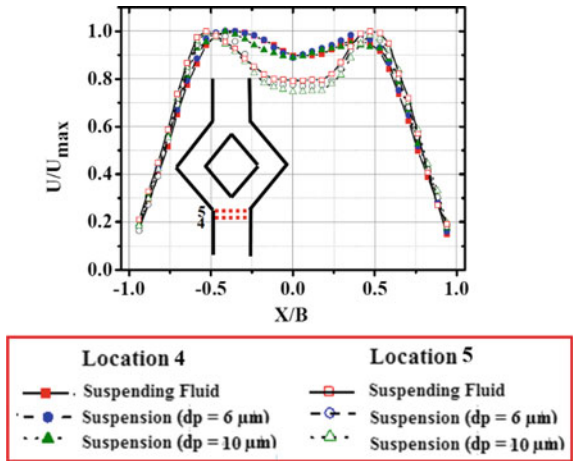
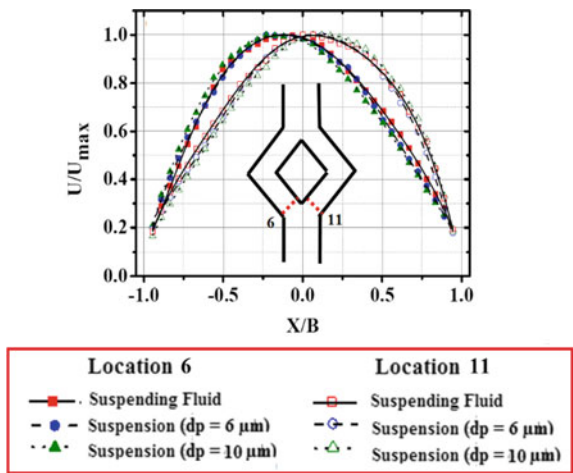**Fig. 4** Velocity profiles at location 6 (left daughter branch) and location 11 (right daughter branch)

the direction of the converging section. Here flow changes its direction in both the locations. The profile shifted more for suspension flow than the Newtonian fluid. It was detected from Fig. 5 that at locations 8 and 13, velocity profiles were almost mirror images.

The profiles at the end of the converging section, location 10 in the left daughter branch and location 15 in the right daughter branch, are shown in Fig. 6. The profile is faintly asymmetric for the 200 μm equal width channel.

Figure 7 shows the comparative velocity plot at the union of flow streams (location 16) and the outlet section (location 17, location 18 and location 19). We observed a symmetric tip-valley-tip profile. This is due to meeting two fluid streams of similar flow rates and equal volume. As the flow moves further towards downstream locations

Fig. 5 Velocity profiles at
the end of the diverging
section and beginning of the
converging section at
location 8 (left daughter
branch) and location 13
(right daughter branch)
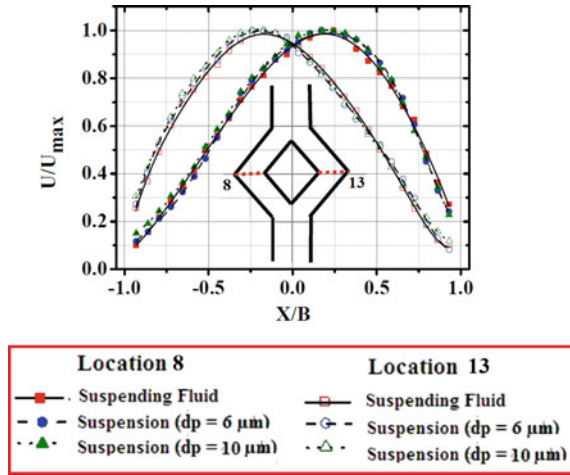
Fig. 6 Velocity profiles at
the end of the diverging
section and beginning of the
converging section at
location 10 (left daughter
branch) and location 15
(right daughter branch)
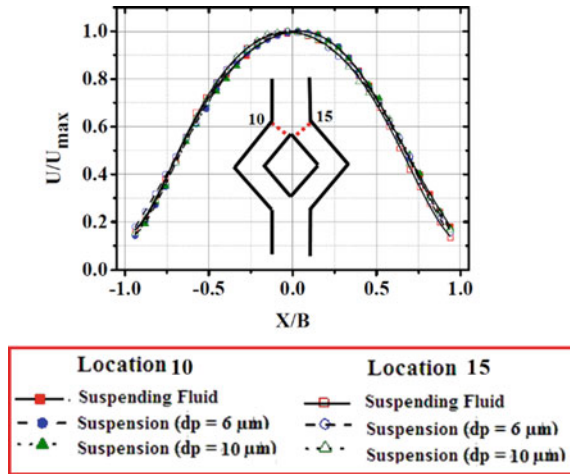
of outlet length, symmetric tip-valley-tip shape in the profile gradually disappears,
and only a blunting velocity profile appears at the last location (location 19).

4.2 Particle Concentration

Figure 8 shows the velocity vector map of 10 μm size particle in the symmetric
diverging-converging channel. It was detected from the vector map that more vectors
were located in the middle of the channel in the inlet section. This is due to shear-
induced migration phenomena where particle migrates from the wall region to the

Fig. 7 Velocity profiles at the junction point (location 16) and the outlet section, location 17, location 18 and location 19 of the diverging-converging channel
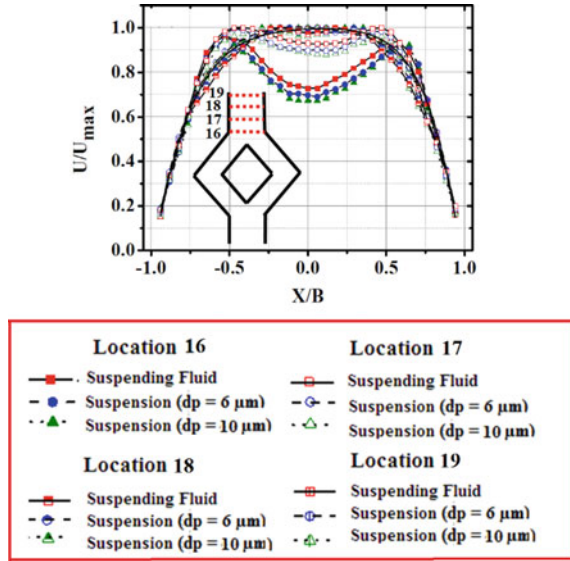
middle of the channel. After the bifurcation point, it was detected that the concentration of particles was relatively higher near the inner walls of daughter branches both in the diverging and converging section. This is because the inlet section particle has already moved to the middle of the channel and these particles favour moving closer to the inner wall of the side branches. Finally, particles from both streams meet at the converging section's confluence and come out from the outlet section. Here we have observed two separated vector streams in the outlet section. This velocity vector map of the particle phase qualitatively gave particle concentration over the whole area of diverging-converging channel.

We have qualitatively studied the concentration profile at different locations of the channel using particle counting MATLAB programme. Steps of selecting a rectangular section of the images of size 400 pixels in the velocity gradient direction and 80 pixels in the flow direction, subdividing that image into 11 equal width bins and counting particles with MATLAB programme are described in [1]. The term N_p/N_T denoted the concentration of particles in each divided bins, where N_p is the number of particles in a bin and N_T is the total number of particles present in the entire image.

Fig. 8 Velocity vector map of particle phase (10 μm size)
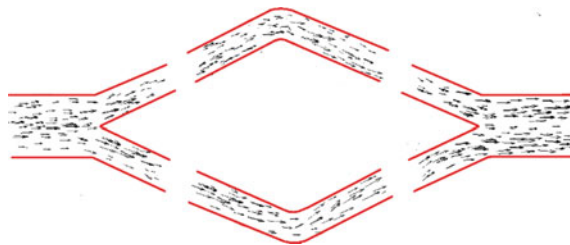
The concentration profile from locations 1 to 5 in the inlet section is shown in Fig. 9. In all the particle counts, profiles of Figs. 9, 10, 11 and 12 were normalized with the total particle count.

Fig. 9 Normalized particle count profiles in the bins at the inlet sections
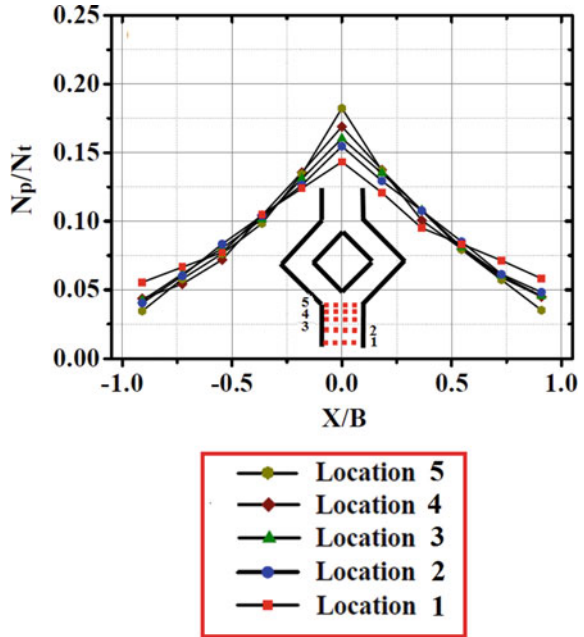
Fig. 10 Normalized particle count profiles in the bins at right daughter branch (location 11, location 12, location 13) and on the left daughter branch (location 6, location 7, location 8)
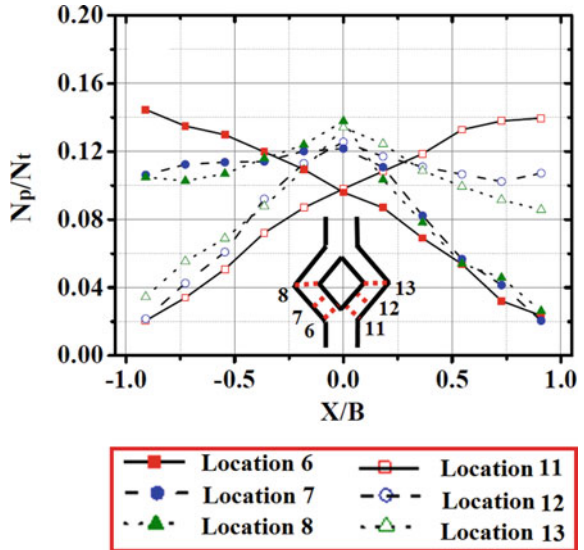
Fig. 11 Normalized particle count profiles in the bins at right daughter branch (location 14, location 15) and on the left daughter branch (location 9, location 10)
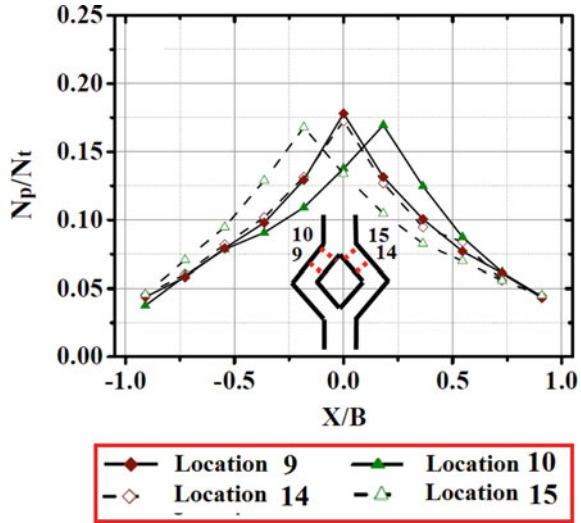
Fig. 12 Normalized particle count profiles in the bins at the outlet section (location 16, location 17, location 18 and location 19) of diverging-converging channel
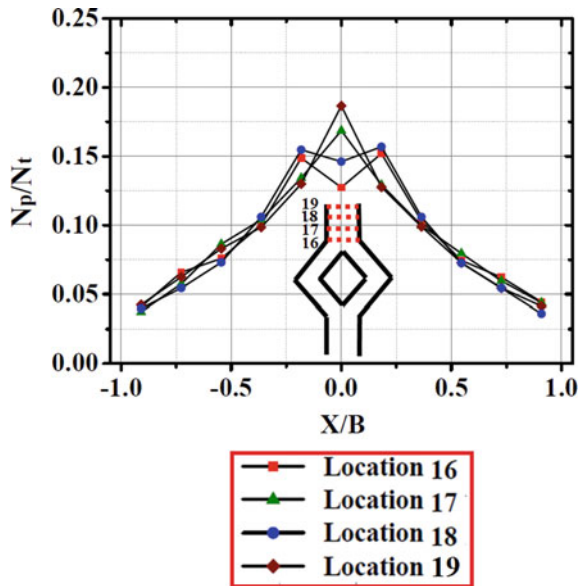
In Fig. 9, because of shear-induced migration, the particles travel from walls to the centre of the channel, which gives an upturned V-shape of the profile similar to described in [1]. Once flow moves from locations 1 to 5, the tip in concentration profiles too rises in the channel.

Figure 10 showed the profiles of normalized particle count at the daughter branches for diverging flow. The concentration of particles was maximum near the

inner wall region at location 6 of the left branch and location 11 of the right branch. As flow movers towards the downward locations, near-wall particle concentration gradually reduces, and the tip of the concentration profile shifts towards the middle of the channel. After the flow leaves the diverging section and enters the converging section at location 8 on the left and location 13 on the right branch. Here profiles were still asymmetric due to the shorter length of daughter branches in the diverging section for the fully developed symmetric profile.

Flow changes its direction in the converging section, and profiles in the middle and at the end of the converging section are shown in Fig. 11. In the converging section, redistribution of particles and migration towards the middle of daughter branches continue and finally, the asymmetric profile leaving diverging section becomes symmetric at location 9 and location 14 in the converging section. We found that at the end of daughter branches in the converging section (location 10 and location 15), the profile shifted in the downward direction as these two locations are near to the converging section.

Particle count profiles at outlet locations are shown in Fig. 12. A tip-valley-tip profiles were detected at locations 16 and 17. This is due to the merging of two unequal fluid streams at the confluence. As the flow moves towards the outlet locations, the tip-valley-tip profile gradually reduces to a symmetric single tip profile (locations 18, 19) near the middle of the channel.

5 Conclusions

To study the suspension flow, we have conducted single-camera micro-PIV and PTV measurements in diverging-converging micro-channel of daughter branch width 200 µm. A tip-valley-tip velocity profile was observed near the diverging section, which gradually reduces to blunted profile at the outlet of the converging section. We have qualitatively studied the concentration profile from the PTV analysis vector map and also by using the particle counting MATLAB programme. Due to the migration of particles towards the centre of the channel symmetric concentration profile in the inlet locations of diverging section becomes asymmetric in daughter sections. The profile becomes again symmetric due to additional particles migration towards the centre of daughter channel and in the outlet locations of converging sections.

References

1. Medhi BJ, Agrawal V, Singh A (2018) Experimental investigation of particle migration in suspension flow through bifurcating microchannels. AIChE J 64(6):2293–2307
2. Xi C, Shapley NC (2008) Flows of concentrated suspensions through an asymmetric bifurcation. J Rheol 52(2):625–647

3. Yezaz Ahmed GM, Singh A (2011) Numerical simulation of particle migration in asymmetric bifurcation channel. J Non-Newtonian Fluid Mech 166(1–2):42–51
4. Reddy MM, Singh A (2014) Flow of concentrated suspension through oblique bifurcating channels. AIChE J 60(7):2692–2704

Measurements and Diagnostics of a Gas Extraction Probe

Y. Biswal, G. M. Nayak, V. W. Ketan, B. Sayak, B. Saravanan, and P. S. Kolhe

Abstract An endeavor is made to design the intrusive emission measurement technique to predict the combustion reaction with a precise species concentration. The present study built two (P1 and P2) different orifice diameters of gas sampling probes with a water-cooled system. A laminar premixed CH_4/Air one-dimensional flame is chosen for the product concentration measurements. The flame area contraction ratio using direct images demonstrates probe-induced flame interference. The probe configuration is evaluated based on thermo-physical properties and emission measurement. The sampling velocity, quenching temperature, and residence time emphasize the understanding of aerodynamic quenching in the designed probe. The sampled gas temperature is observed to be well below the quenching temperature limit within a chemical time scale. The smaller orifice diameter of the probe, in this case, P2, is most likely to measure species concentration accurately. In addition, a higher sampling velocity and lower flame stretching can be expected. The gas sampling probe measured CO_2 concentration corroborates with the numerical solution.

Keywords Flat flame · Gas extraction probe · Aerodynamic quenching · Residence time · Emission measurement

Nomenclature

c_p Specific heat of sampled gas [kJ/kg K]
d_i Orifice diameter [m]
h Heat transfer coefficient [W/m²K]
k Thermal conductivity (W/mK)
Nu Nusselt number
m_0 Gas sampling rate [kg/s]

Y. Biswal · G. M. Nayak · V. W. Ketan · B. Sayak · B. Saravanan · P. S. Kolhe (✉)
Department of Mechanical and Aerospace Engineering, IIT Hyderabad, Kandi, Sangareddy, Telangana 502284, India
e-mail: psk@mae.iith.ac.in

M_w Equivalent molecular weight [g/mole]
P_0 Atmospheric pressure [Pa]
P_r Prandtl number
T_0 Flame temperature [K]
T_f Quenching temperature [K]
T_w Probe wall temperature [K]
Υ Specific heat ratio
μ Dynamic viscosity [Pa-s]

1 Introduction

In a real-time gas turbine application, accurate emission concentration helps to understand the combustion reactivity and efficiency. An accurate emission measurement plays a crucial role in the combustion community. It is vitally important to pay attention to in-flame emissions rather than exhaust emissions in order to regulate pollutant emissions according to global environmental emission standards. The in-flame emission measurement needs to be focused on optimizing the combustion efficiency, considering the pollutant emissions. Both intrusive and non-intrusive techniques are available to measure emissions, but the latter is more expensive and requires a complicated system. The intrusive method is much simpler to build at a low cost.

Several studies have been carried out to design the gas sampling probe, such as convective cooled probes, gas dilution probes, and quick-quench probes [1–6]. Friedman et al. [4] have demonstrated a study of the water-cooled and naturally convective cooling probe, ensuring minimum flame disturbance and quenching the chemical reaction within the probe. The probe is provided with a silver tip of an orifice size of 38 microns to avoid flame perturbation. The oxidation process of NO to NO_2 and CO to CO_2 is diagnosed through quartz micro probe by Kramlich et al. [6]. For the naturally convected probe and water-cooled probe, the specie concentrations are investigated, where the water-cooled probe exhibits a quick temperature quenching in CH_4/Air and CO/Air combustion. At the uncooled tip, it was reported that the conversion of NO to NO_2 occurs more quickly. The oxidation of NO to NO_2 is caused by the formation of HO_2 and O_3 due to temperature quenching. Furthermore, the NO_2/NO ratio, which represents the NO_x concentration, is found to be higher in water-cooled probe.

Specie concentration measurements rely primarily on the probe geometry and rate of heat removal from the gas sample. Bryson et al. [2] conducted comparison research with the water-cooled (baseline probe), quick-quench, and inert gas dilution probes. For the fast quench probe and the dilution probe, the influence of thermophysical parameters such as pressure ratio and gas dilution are reported. Aerodynamic quenching is established in a quick-quench probe, and higher specific heat capacity gases like N_2, Ar, and He are used to dilute with the hot sampled gas in

the dilution probe. N_2 dilution probe is observed to measure a higher concentration of NO_x emissions. The CO and unburnt hydrocarbon (UBHC) are measured high in dilution probe and quick quench. A similar study was conducted by Heitor et al. [5], where a direct water quenching effect is added to other basic probe configurations. The quenching effectiveness of different probe types and probe-induced flame disturbances are addressed. Due to higher suction velocity, the quick-quench probe induces in higher flame perturbation. An exclusive investigation is conducted by Colket et al. [3] on aerodynamic quenching, where the gas is sampled through a choked nozzle. The residence time, stagnation temperature, and pressure of the compressible fluid are diagnosed. According to their study, a chemical reaction can freeze at a temperature below 1000 K for a residence time of 1 ms. An analytical study of the flame quenching process is examined by Mitani et al. [7]. The friction length, convective heat transfer coefficient, and reactions inside the probes are reported in real-time applications of ramjet and scramjet engines. Blanco et al. [1] described the advantages of using the He dilution and the quick chemical quenching process by accelerating the sample at a supersonic flow in the gas sample probe. A computation model is also developed and compared with the quick-quench probe under the testing condition of "General Electric J85 Turbo Jet Engine".

The gas sampling method is less expensive and more precise in species measurements when compared to optical diagnostics techniques. The key concern of the gas sample probe is in-flame interference. Several strategies have been adopted to date in an attempt to quench the chemical reactions within the sampling system and avoid probe-induced flame disturbances. The current study aims to diagnose a gas extraction probe to design with a water-cooled convective system, where the aerodynamic quenching effect on the gas sample is expected.

2 Experimental Set Up and Geometrical Confugeration of Gas Extraction Probe

An intrusive technique is utilized in this study. The primary objective is to measure precise emitted species concentrations within the flame using a gas extraction probe. An endeavor is made to design the probe geometry to minimize flame perturbation and freeze the chemical reaction. The schematic diagram of the experimental test setup is presented in Fig. 1a. A simple one-dimensional (1D) flame of the Mckenna burner is considered in this study. All the measurements are conducted for laminar CH_4/air premixed flames. The methane flow rate is fixed at 1.5 L/min, and the airflow rate is maintained at 15.0 L/min to maintain a stable flame of an equivalence ratio (ϕ) of 0.95. The flow rate of nitrogen coflow is kept at 20 L/min as the shielding gas to minimize the ambient disturbance. The gaseous flow rates are controlled using a mass flow controller (Bronkhorst). The gas sample probe is incorporated with a water cooling system on the counter-flow heat exchange principle as shown in Fig. 1a. A counter-flow heat exchange geometry is established by providing the flow of cold

water and the hot sampled gas in opposite directions. A constant pressure chamber is maintained to provide a water flow rate of 500 ml/min for heat exchange. The sensible heat removal rate is taken into account by both the sampling gas and the flue gas present outside the probe [8]; accordingly, the flow rate of cooling water is evaluated. The flame emission is extracted using a suction energy (Vacuum pump, Rocker 410) incorporated on the probe. The product emissions are allowed to pass through the cold annulus with the help of a chiller to ensure the dry gas into the gas analyzer (AVL DIGAS 444N). In addition, a water trap is mounted at inlet of the vacuum pump. The product species are acquired at a constant central location of the burner of different heights above the burner (HAB) from 0.5 to 20 mm, where the flame instability caused by buoyancy is assumed to be negligible. The probe species measurements are compared to the numerical solution of a similar operating condition [9].

Figure 1b displays an enlarged view of gas extraction probe with the physical dimensions. The probe is made of commercially available stainless steel tubes. The probe orifice diameter is evaluated considering the Eq. (1) for a fixed mass flow rate of sampling [10]. The probe orifice dimension is evaluated from Eq. (1). Two probe configuration is used in this study, P1 and P2 of orifice diameter (d_0) of 0.8 mm and 0.7 mm, respectively. For the probe inside temperature measurement, a K-type thermocouple of 0.35 mm bead size is placed at a 41 mm distance from the tip of the probe. The corresponding location of flame temperature is measured by a C-type thermocouple.

A high-speed acquisition system (c-Daq, NI-9174) is used to acquire the temperature at a sampling rate of 5000 Hz for 5 s. The radiation affect is accounted in the temperature measurement for the location of 5–20 mm HAB. Assuming calorically perfect gas and homogeneous reaction, the energy conservation equation is deduced to Eq. (2) [11], from this equation the minimum travel distance of the gas sample inside the probe is evaluated. The suction pressure is decided by the calculation made in Eq. (3) [11].

Mass flow rate of the sampled gas,

$$m_0 = P_o \left(\frac{\pi}{4} d_0^2 \right) \left[\left(\frac{\gamma \cdot M_w}{R_g \cdot T_o} \right) \left(\frac{2}{\gamma + 1} \right)^{\frac{\gamma+1}{\gamma-1}} \right]^{\frac{1}{2}} \tag{1}$$

Minimum travel distance of sampled gas,

$$Y = e^{(-\text{Nu} \cdot X)} \tag{2}$$

where,

$$Y = \frac{T_f - T_w}{T_o - T_w}, \, Nu = \frac{h \cdot d_0}{k}, \, X = \frac{\pi \cdot k \cdot x}{m_o \cdot c_p}$$

$$\text{For } X = \frac{1}{2} \quad \text{then} \quad Y = e^{(-3.66 \cdot X)}$$

Fig. 1 Schematic representation of experimental setup (**a**), an enlarged view of gas extraction probe (**b**)
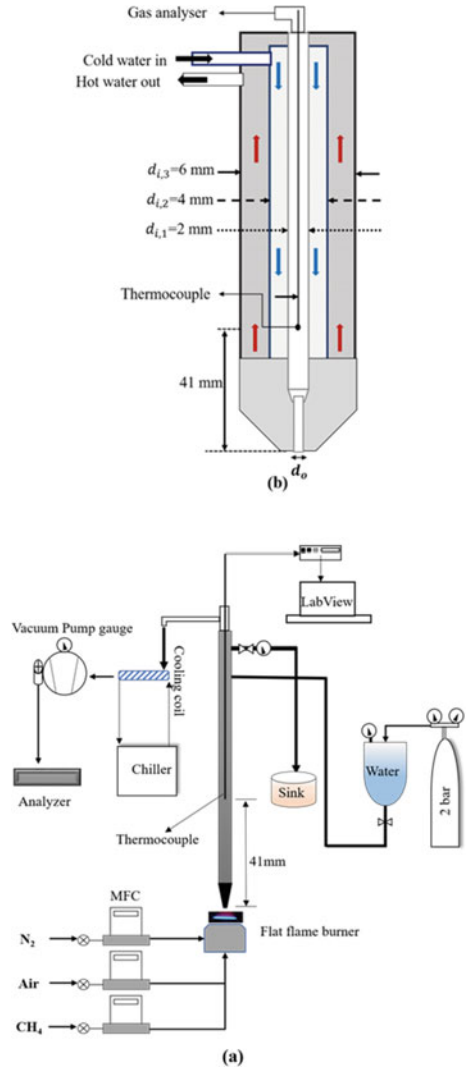
For $X = \dfrac{1}{2}$ then $Y = e^{\left(-2.95 X^{\frac{2}{3}}\right)}$

Pressure drop calculation,

$$\Delta P = \frac{\mu^2 \cdot x^2}{\rho \cdot d_0^4} \cdot \frac{\left[128 + \frac{10}{\mathrm{Pr} \cdot X} + \frac{0.185}{(\mathrm{Pr} \cdot X)^{\frac{5}{2}}}\right]}{\mathrm{Pr} \cdot X + \frac{0.36}{\mathrm{Pr} \cdot X}} \tag{3}$$

3 Results and Discussion

The current study investigates the non-intrusive technique to measure the accurate species concentration. Two different orifice diameter of probes are built to measure the in-flame gas emission measurement in 1D premixed CH_4/Air flame. An optimum probe configuration of P1 and P2 probes discussed based on thermo-physical and emission measurement.

3.1 *Thermo-Physical Properties and Measurements*

The thermo-physical properties like temperature, vacuum pressure, flow rates, and sampling velocities are evaluated in this section. The direct instantaneous image of probe tip on the flat flame is shown in Fig. 2. The probe tip on the flame varied vertically from 0.5 to 20 mm with a 0.5 mm step, above the burner. However, the direct images are shown from 2 to 5 mm above the burner, where flame front suction is noticed. The local stretch in the flame is clearly evident in both P1 and P2. The area contraction of flame for P1 is clearly distinguished at 4.5 mm, whereas P2 shows a diminished flame front contraction at the corresponding location. These flame front contraction images display that the suction strength of P1 is higher than that of P2. It should be noted that the lower suction strength is preferable in the gas extraction probe to avoid local flame stretch.

The flame area contractions of the two probes are deter- mined at 3.5 mm HAB from the direct images, as shown in Fig. 3. The flame area contraction ratio of P1 and P2 is evaluated as 1.98 and 2.23, respectively. It indicates the flue gases acceleration toward the probe tip is higher in P2 over P1. Therefore, the aerodynamic quenching is more likely to occur in P2, which eventually freezes the chemical reactions. Figure 4 displays the higher sampling velocity in P2 compared to P1. The mass and energy conservation principle are used to determine the sampling velocity, which corroborated to each other. The highest sample velocity is observed at 0.5 mm HAB owing to the higher flow rate at upstream in Fig. 5. At upstream location where lower specific volume in the preheat zone, the thermodynamic work on the system is less at a fixed power rate of suction pump. As a result, the suction pressure is observed
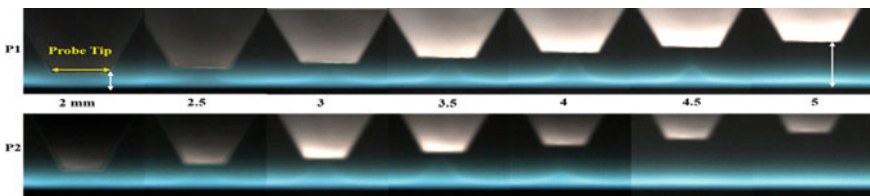
Fig. 2 Direct imaging of suction of the flame front at various suction locations for two different orifice size

as 230 and 225 mbar for P1 and P2, respectively, at 0.5 mm HAB. At downstream, flow rate and the sampling velocity drop occur due to increase in thermodynamic work on the system.

The previous studies report that the gas sample is sampled at sonic velocity (Mach number = 1) at the probe's tip inlet, which can be evaluated from the choke compressible flow Eq. 1 [1, 3, 5, 12]. Elkady et al. [12] reported that the flame temperature is assumed to be 2200 K for sonic, and the desired flow rate of the gas sample is calculated at about 3 Lpm. However, the present study reported velocities are subsonic (Mach number < 1) flows with the consideration of the flame temperature [10]. It should be noted that the flow rate of gas sampling varies with the sampled velocity and the probe's tip orifice diameter. The current work reflects the variation in-flame temperature and the corresponding flow rate at different downstream location of the flame.

Figure 6 depicts the radiation corrected temperature profile along the axial direction of the flat flame. The temperature measurements acquired at downstream location of 5–20 mm with a 5 mm step. It should be noted that the measured temperature profile clearly matches with the simulated CHEMKIN solution and previous study [9]. The temperature profile reflects the chemical reaction zone with a sharp slope of 0.5–2 mm HAB. An absolute slope of velocity and flow rate is less as compared to the slope of temperature profile. However, the decrease in velocity and flow rate profiles of P1 and P2 are observed to be similar. Besides, P2 has a steeper curve over P1 due to local flame disturbance.
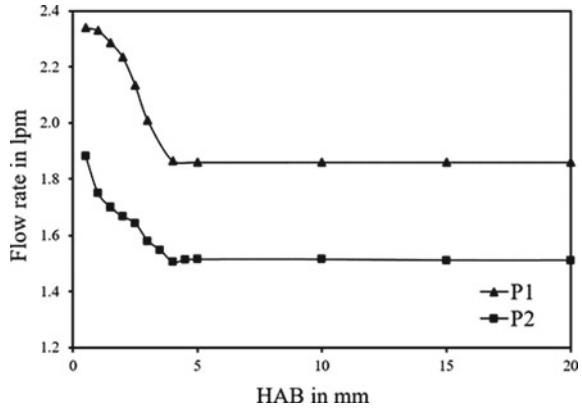

Fig. 3 Comparison of the flame contraction in between the two probes at 3.5 mm suction location
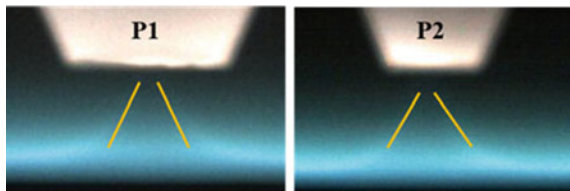
Fig. 4 Sample velocity of the flame combustion gases at different suction location
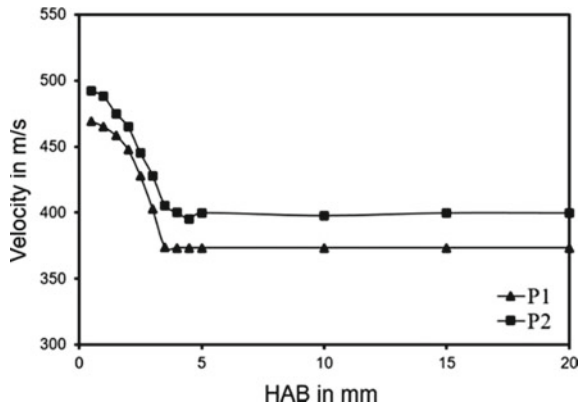
Fig. 5 Sample flow rate at different height above the burner

Fig. 6 Central flat flame temperature profile along the axial downstream location
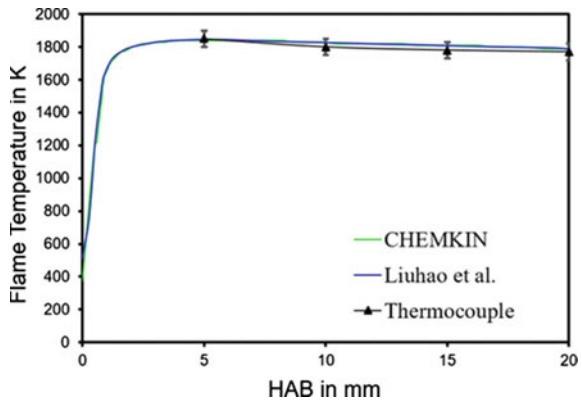
Further discussion, Fig. 7 presents the inside probe temperature of the sampled gases. The thermocouple is placed 41 mm above the probe tip. The acquired temperature is observed to be well below 1000 K for both the probes, indicating the aerodynamic quenching effect [3]. P2 exhibits a lower temperature as compared to P1, where smaller orifice size allows the higher sampling velocity to cause chemical reaction to freeze.

The residence time of probes is shown in Fig. 8. The period of a gas sample to travel from the probe's tip to the thermocouple is referred to as residence time. Colket et al. [3] reported that the quenching period must not exceed 1 ms. Figure 8 shows the residence time of both the probe at different locations is less than 1 ms, where gas sample is assumed to have undergone an aerodynamic quenching process.

The residence time in P2 is observed to be higher due to significant pressure drop. Moreover, the velocity reduction from the orifice size to sample tube size is more in P2, which results in more travel time of the sampled gas to reach the thermocouple tip.

Fig. 7 Gas sample temperature, which is residing inside the gas extraction probe at a location 41 mm from the tip probe
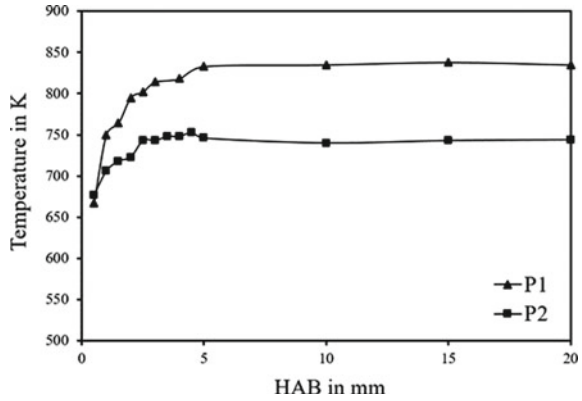
Fig. 8 Residence time of the sample
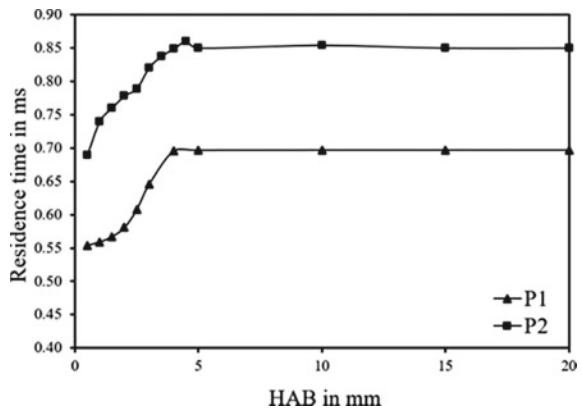
3.2 Emission Measurements

The previous section discusses the aerodynamic quenching of the sample gases in terms of thermo-physical properties of the gas extraction probe. In addition, the product species concentration measurements aid in a better understanding of the sample quenching process. The species to concentration profile of Mckenna burner signifies the combustion zone.

Figure 9 shows the measure CO_2 mole concentration at various HAB. The measured species concentration corroborates with the simulated CHEMKIN solution and literature study [9]. It can be seen that the species concentration is mostly matched in the downstream but unlikely in the upstream due to local stretching the flame. The numerical solution shows a greater in slope compared to measured concentration. Furthermore, P2 profile is steeper, indicating the miniature orifice size probes can yield precise measurements. Besides, the local flame perturbation is comparatively low in P2, as discussed in the previous section. The species concentration becomes saturated in the downstream, where complete combustion is expected. The measured

Fig. 9 Mole fraction of CO$_2$ at different suction location from the height above the burner

Mole fration CO2 / HAB in mm

Liuhao et al.
CHEMKIN
P1
P2
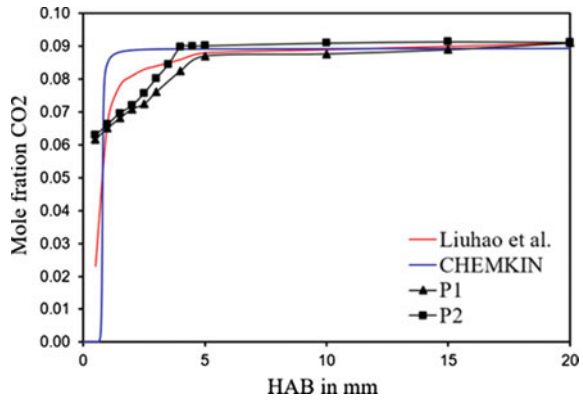
concentration identifies the flame thickness as 4.2 and 3.5 mm in P1 and P2, respectively. However, numerical solution of flame thickness is approximately found to be 3 mm.

Further discussion, Figs. 10 and 11 display the UBHC and CO concentration, respectively. A key intermediate in fuel-lean and stoichiometric combustion is CO, which is a main product in partial oxidation processes. The formation of CO$_2$ is an important channel for CO oxidation and heat release. The concentration profile of CO in P1 and P2 emphasizes the formation of CO$_2$ in Fig. 9. Besides, P2 exhibits a steeper decaying plot, with similar arguments in the previous discussions. Hence, the CO concentration measurement ensures the precision of the gas sample probe designed in this study. It is interesting to study the smaller orifice diameter of gas sampling probe at high suction energy.

Fig. 10 Concentration of unburnt hydrocarbon at different suction location from the height above the burner

UBHC in ppm / HAB in mm

P1
P2
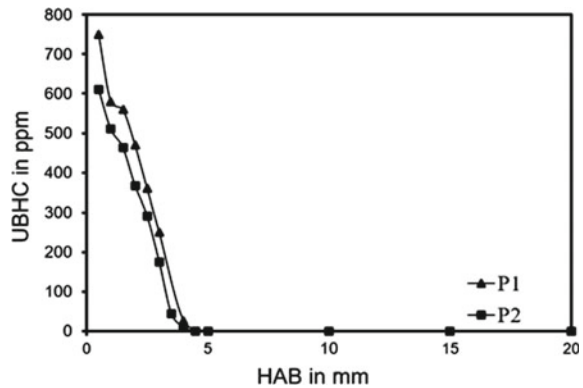
Fig. 11 Concentration of CO at different suction location from the height above the burner
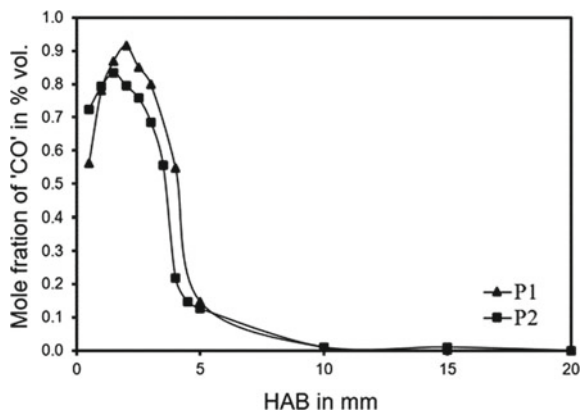
4 Conclusions

The probe geometry and the suction strength determine the precision label of the emission measurement. The following conclusion is withdrawn from this study.

- The present study builds two different orifice diameters of gas extraction probes to accurately measure the species concentration.
- The flame contraction area from the direct images reveals that the aerodynamic quenching is most likely to occur in P2, where sampling velocity is found to be higher. In addition, the inside probe temperature is observed below 1000 K.
- The measured species concentration of CO_2 corroborates with the numerical solution in the downstream location, where local flame stretch is observed in the combustion zone.
- The preservation of CO and UBHC concentration reveals that the chemical reaction inside the probe tip quenches, despite a probe-induced disturbance in the flame.

References

1. de la Rosa Blanco E, Peck J, Miake-Lye RC, Hills FB, Wood EC, Herndon SC, Annen KD, Yelvington PE, Leach T (2011) Minimizing sampling loss in trace gas emission measurements for aircraft engines by using a chemical quick-quench probe. J Eng Gas Turbines Power 133(7)
2. Bryson RJ, Few JD (1978) Comparisons of turbine engine combustor exhaust emissions measurements using three gas-sampling probe designs. Technical report, Arnold Engineering Development Center, Arnold AFB TN

3. Colket MB III, Chiappetta L, Guile RN, Zabielski MF, Seery DJ (1982) Internal aerodynamics of gas sampling probes. Combust Flame 44(1–3):3–14

4. Friedman R, Cyphers JA (1955) Flame structure studies. iii. Gas sampling in a low-pressure propane-air flame. J Chem Phys 23(10):1875–1880

5. Heitor MV, Moreira ALN (1993) Thermocouples and sample probes for combustion studies. Prog Energy Combust Sci 19(3):259–278

6. Kramlich JC, Malte PC (1978) Modeling and measurement of sample probe effects on pollutant gases drawn from flame zones. Combust Sci Technol 18(3–4):91–104

7. Mitani T (1996) Quenching of reaction in gas-sampling probes to measure scramjet engine performance. In: Symposium (International) on combustion, vol 26. Elsevier, pp 2917–2924

8. Bergman TL, Lavine AS, Incropera FP, DeWitt DP (2011) Introduction to heat transfer. Wiley

9. Ma L, Cheong K-P, Ning H, Ren W (2020) An improved study of the uniformity of laminar premixed flames using laser absorption spectroscopy and cfd simulation. Exp Thermal Fluid Sci 112:110013

10. Shapiro AH (1953) The dynamics and thermodynamics of compressible fluid flow. Ronald Press, New York

11. Taylor AMKP (1993) Instrumentation for flows with combustion. Academic Press

12. Elkady AM (2006) Experimental investigation of aerodynamics, combustion, and emissions characteristics within the primary zone of a gas turbine combustor. Ph.D. Thesis, University of Cincinnati

Characterization of the New Open Surface Recirculating Water Tunnel Facility at the Indian Institute of Technology Kharagpur

Gangadhar V. R. Pinapatruni, Rahul Ranjan, Durga Charan, Sunita Mishra, and Sunil Manohar Dash

Abstract The present study aims to characterize the free stream flow of the newly installed recirculating water tunnel facility in the BIAHR Laboratory at the Indian Institute of Technology Kharagpur. This tunnel can operate at speeds ranging from 0.05 m/s to 0.40 m/s in the test section. The dimension of the test section is 400 × 400 × 1500 mm³ in width, depth, and length respectively. An acoustic Doppler velocimetry is used to measure the instantaneous velocity in the test section at the frequency of 10 Hz with a measured accuracy of ± 1%. The flow velocity in the test section is found to vary linearly with motor speed, and the turbulence level decreases on increasing the motor speed. The average temporal stability in the tunnel is found to be less than 1%, and the maximum possible deviation in the spatial uniformity is less than ± 1.35%. Furthermore, the free stream turbulence intensity characteristics in the test section are determined at different operating velocities.

Keywords Water tunnel · Acoustic Doppler Velocimeter · Low speed · Turbulence intensity · Spatial uniformity

Nomenclature

C	Speed of sound in water (m/s)
f	Frequency or sampling rate (s^{-1})
k	Turbulent kinetic energy (m^2/s^2)
N	Number of samples
t	Time (s)
Tu	Turbulence intensity

G. V. R. Pinapatruni · R. Ranjan · D. Charan · S. M. Dash (✉)
Department of Aerospace Engineering, IIT Kharagpur, Kharagpur 721302, India
e-mail: smdash@aero.iitkgp.ac.in

S. Mishra
Department of Mining Engineering, IIT Kharagpur, Kharagpur 721302, India

| u, v, w | Velocity components along x, y, and z (m/s) |
u', v', w'	Fluctuating velocity components (m/s)
$\overline{u}, \overline{v}, \overline{w}$	Mean velocity components (m/s)
ϕ	Phase shift (rad)

1 Introduction

The experimental fluid dynamics study generally requires a controlled environment with known free stream flow characteristics. Water and wind tunnels are specially designed to achieve such a controlled fluid flow environment. The water tunnel is preferred over the wind tunnel facility for investigating the low-speed fluid flow physics. Furthermore, the water tunnel size and its overall design depend on the test section dimensions and the required free stream flow characteristics. After installing the new water tunnel research facility, a precise calibration must be performed to ascertain the free stream flow characteristics in the test section. This calibration step involves the measurement of spatial uniformity of velocity, temporal stability, turbulence intensity, etc. [1].

Recently, an open surface recirculating water tunnel facility, as shown in Fig. 1, is installed in the Bio-Inspired Aero and Hydrodynamics Research Laboratory (BIAHRL) at the Indian Institution of Technology Kharagpur. This facility is equipped with a high-speed camera, multi-axis force and torque sensor, dye injection system, flapping airfoil mechanism, Acoustic Doppler Velocimeter (ADV), and a high-end data acquisition system. Additional technical details of this water tunnel are described in Sect. 3.

The present study aims to quantify the free stream flow characteristics in the water tunnel test section. This quantification involves the measurement of spatial uniformity of velocity, temporal stability, and turbulence intensity [1]. Several techniques are available to measure the temporal data of velocity in the flow field, in which the Acoustic Doppler Velocimetry (ADV) is one of the techniques. This ADV device transmits an acoustic signal with high frequency, which is reflected by the particulate
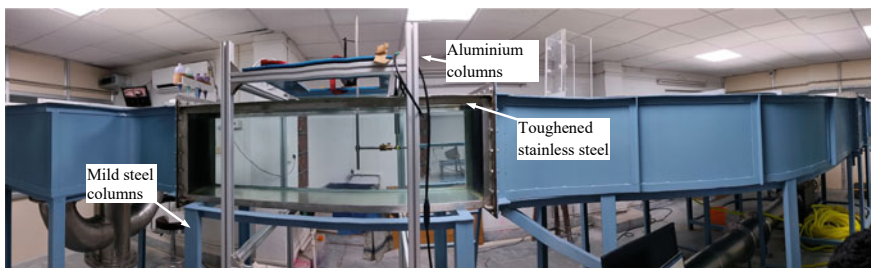
Fig. 1 Open surface recirculating water tunnel set up in BIAHR Laboratory in IIT Kharagpur (Panorama view)

in the flow field with a shift in frequency namely Doppler shift. This phase shift is proportional to the velocity of that particulate. In the following we have described the relevant literature available on the water tunnel characterization and defined objectives of the present study.

2 Literature Review and Objective

The development of water tunnel experimental facilities started to resolve the limitations of the towing tanks, where the object is forced to move in the static water channel. This technique does not support flow visualization and accurate estimation of free stream characteristics [2]. In the case of the water tunnel, the frame of reference is reversed, where the flow passes over the stationary object instead. Note that in the past, the water tunnel has been used for flow visualization and force measurement [3], developing synthetic cavitation (cavitation channels) [1, 4], Reynolds stresses estimation [5], skin friction, and boundary layers studies [6]. The design, operation, and maintenance of various water tunnels are based on the specific application [7–9]. However, all the tunnels must be calibrated to estimate their flow characteristics. Various studies [1, 4–6, 10] have reported on the methodology of characterizing the water tunnels. The common characteristics are velocity and pressure drop (for closed surface) measurements along the centre line of the test section, non-uniformity, and velocity profiles from the wall to the free surface. Park et al. [1] described that the key characterization of water tunnel setup includes the determination of spatial uniformity, temporal stability, and turbulence intensity [1, 11] in the test section. These quantities are the statistics of temporal velocity data in the free stream. Note that the instantaneous, temporal velocity measurement in the water tunnel can be performed by various instruments like Hot Wire Velocimeter (HWV) [1, 12, 13], Laser Doppler Velocimeter (LDV) [1], Acoustic Doppler Velocimeter (ADV) [14, 15], and Digital Particle Image Velocimeter (DPIV) [5, 16]. These instruments have sampling rates ranging from 10 Hz to a few hundred kHz and can measure a wide range of flow velocities. It is worth mentioning that velocity field data acquisition at high frequency is necessary to accurately determine turbulence statistics in the tunnel.

Park et al. [1] estimated the hydrodynamic characteristics of a Large Cavitation Channel using both the LDV and HWV devices. They acquired the data at a frequency of approximately 100 kHz. Sargison et al. [6] used a hot film probe and pitot probes for velocity measurements at a frequency of 30 Hz. Song and Chiew [15] employed the commercial ADV and acquired the velocity data at 25 Hz. Moreto and Liu [5] also estimated the flow quality in the water tunnel using a DPIV measurement technique and acquired the data at 5 Hz. This shows the sampling rate (frequency) does not limit the estimation of turbulence statistics. However, the energy associated with high-frequency eddies cannot be captured at a low sampling rate.

The present study determines the free stream flow characteristics in the new open surface recirculating water tunnel facility at the Indian Institute of Technology Kharagpur. For instantaneous measuring of the velocity data, an Acoustic Doppler

Velocimeter made by SonTek (FlowTracker2) is employed. The user manual [17] is followed carefully for accurate data acquisition. The effects of sampling rate, signal-to-noise ratio (SNR), and spikes in velocity data collection [15, 18, 19] are considered.

3 Recirculating Water Tunnel Facility

The schematic drawing and picture of the recirculating water tunnel located at BIAHR Laboratory at the Indian Institution of Technology Kharagpur are shown in Fig. 1 and Fig. 2, respectively. A propeller-type impeller unit is coupled with a 1.5 kW and 710 RPM three-phase induction motor to create the desired water head. A Variable Frequency Drive (VFD) is installed to control the motor RPM. The water exiting from the pump unit passes through the filter section (Fig. 2). Ahead of the filter section, the honeycomb section, coarse and fine mesh screens are installed for flow straightening and reducing turbulence intensity. The mesh sizes are appropriately chosen to limit the maximum turbulence intensity in the tunnel to 3% (design criteria). Then flow passes through the convergent section, which has a contraction ratio of 6:1 that accelerates the flow to achieve the required velocity in the test section. The test section velocity in the present water tunnel can be varied from 0 to 0.4 ms^{-1}. After the test section, a diffuser section is installed that helps to reduce the backpropagation of pressure and velocity disturbance to the test section. The recirculating pipe (dia = 300 mm) connected at the diffuser exit continues the flow recirculation in the water tunnel. An electromagnetic flowmeter of range 10 m/s is installed to measure water's average velocity and volume flow rate. An expansion bellow is attached to further reduce the flow-induced vibration in the pipeline.
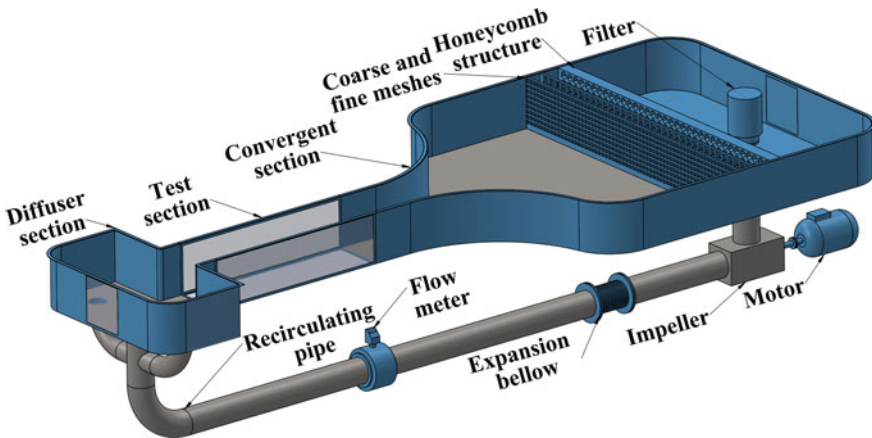
Fig. 2 Schematic drawing of the open surface recirculating water tunnel setup

Fig. 3 Water tunnel test section **a** front and **b** side views
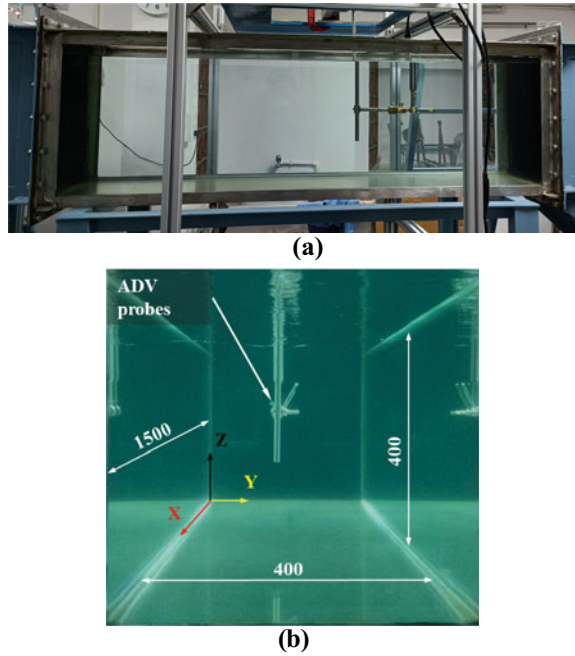
The front and side views of the water tunnel test section are shown in Fig. 3a and b, respectively. The test section dimensions are $400 \times 400 \times 1500$ mm, and it is fitted with three-sided transparent glasses and an open top surface. The structural support to the test section comes from the toughened stainless steel (see Fig. 1), supported by four mild steel columns. The aluminium columns are also arranged around the test section for resting the base plate at sufficient height over the test section. This base plate supports the mountings of the experimental specimens and instrumentations. It is worth mentioning that the test section has a draft angle of 1^0 along the length in a sideward direction. This angle compensates for the boundary layers effects such that the free stream velocity can be maintained in the test section.

4 Velocity Data Acquisition

In the present study, an acoustic Doppler velocimeter (ADV) is used to measure the time-resolved velocity in the water tunnel. The ADV is mounted, as shown in Fig. 4a. A linear actuator is fixed to the base plate with C-clamp, and the actuator permits the linear movement (along the Y-axis, refer to Fig. 3b) of ADV (Fig. 4a). The coupling and the ADV sensor probes can be seen in the zoom view in Fig. 4a. The ADV alignment is achieved by using an acrylic stand (Fig. 4b), which serves as a vertical reference plane in the tunnel. This stand's size is half the width of the

Fig. 4 **a** Mounting of ADV on the test section and **b** positioning of ADV probes using reference plane made of Acrylic sheet

(a)

(b)
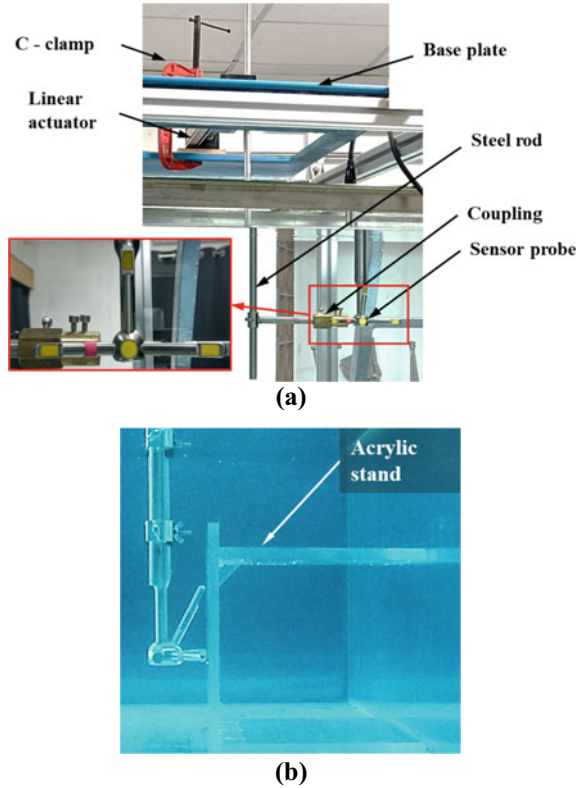
tunnel, so it facilitates the position of ADV probes in the middle of the tunnel. A steel rule is also attached to the stand to position it at the required location.

The schematic diagram of the working principle of ADV is shown in Fig. 5. The transmitting probe generates the acoustic signal with a frequency (f) of 10 MHz and passes through the sampling volume 100 mm ahead. The particulates present in the water flow reflect the signal with a shift in frequency (Doppler shift). This shift is a directly proportional velocity of that particle. For accurate measurement of Doppler shift, present ADV utilizes a coherent pulse technique [17, 18] in which two pulses from the transmitter are generated with a time lag of Δt. The receivers receive the signal reflected in the sampling volume and measure the phase (ϕ) of each signal. The change in phase is proportional to Doppler shift (Δf, see Eq. 1). Then the velocity (u) of the particle or flow can be determined using Eq. 2, where the speed of the sound 'c' in water can be determined by FlowTracker2 software using the temperature and salinity data.

$$\Delta f = \frac{\Delta \phi}{2\pi \Delta t} \tag{1}$$

Fig. 5 Acoustic Doppler Velocimetry measuring principle
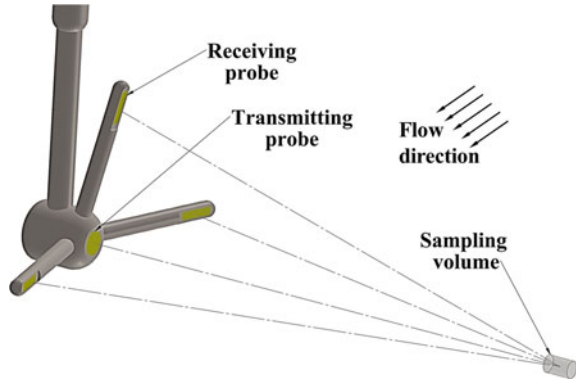
$$u = \frac{c\Delta f}{2f} \tag{2}$$

$$\sigma = \sqrt{\left(\frac{1}{N}\sum_i (u_i - \overline{u})^2\right)} \tag{3}$$

$$k = \frac{(u_i - \overline{u})^2}{2} \tag{4}$$

$$Tu = \frac{\sqrt{\left(\frac{1}{N}\sum_i (u_i - \overline{u})^2\right)}}{\overline{u}} \tag{5}$$

Note that selecting the appropriate velocity range, sampling rate, sampling time, and SNR is crucial before measuring with the ADV [18]. The velocity range in this study is defined based on the flow meter reading. The sampling rate is fixed at 10 Hz, and the total number of samples collected is 2000. The uncertainty of the ADV velocity measurement is ± 1% of the measured velocity value (pre-calibrated by the manufacturer), and the upper bound of error is 0.25 cm/s for velocity greater than 25 cm/s. However, increasing the SNR can reduce the error in the ADV velocity measurements. The ADV measurement requires an SNR of a minimum of 7 dB. Hence, the seeding particles (glass beads) are introduced into the water tunnel. These particles enhance the SNR to a maximum of 25 dB, and an average of 12 dB. The ADV FlowTracker2 software has an inbuilt quality checking operation. It performs a quality check before performing each measurement. This checking ensures no wall or obstacles near the sensor probe, SNR values and its rate of descent, and similarity in SNR receiving by receiving probes (see Fig. 5). After completion of the above ADV setting up operations, the velocity data obtained from the ADV is logged to a high-end data acquisition system for processing.

5 Results and Discussion

The free stream flow characteristics in the test section are estimated by measuring temporal velocity data in the flow field. It is worth noting that the three probes of ADV can measure the three-dimensional velocity components ($V = u\hat{i} + v\hat{j} + w\hat{k}$) in Cartesian coordinates using the FlowTracker2 software. The instantaneous velocity data is acquired at this $3 \times 3 \times 3$ spatial grid as shown in Fig. 6 at 100, 150, 200, and 250 motor RPMs. This spatial grid location is chosen in such a way that the region where the testing specimen is usually placed in the water tunnel.

The ADV can measure the velocity of the flow at a distance of 100 mm from the transmitting probe (see in Fig. 5), in a cylindrical sampling volume. The measurement of velocity is performed at 27 spatial coordinates on three x-planes ($x_1 = 500$, $x_2 = 600$, and $x_3 = 700$ mm), as shown in Fig. 6. The y-plane coordinates are 100, 150, and 200 mm, the same for the z-plane. Note the above coordinates correspond to ADV transmitting probe location, where the sampling volume lies on the same x and z coordinates, whereas in the y-direction, the sampling volume is 100 mm ahead of the ADV transmitting probe. The coordinate system of the ADV is aligned to the global coordinate system of the water tunnel. The ADV device was pre-calibrated for multiple velocity ranges like ± 0.1, ± 0.2, ± 0.5 ms^{-1}, and so on. It is necessary to select the appropriate velocity range in the software so that the flow velocity in the tunnel should fall in the selected velocity range. The flow velocity in this study ranges from 0.05 to 0.3 m/s. Hence, the software chooses the corresponding velocity ranges for precise measurement [18].

The instantaneous transient velocity data along the x-direction (u) is shown in Fig. 7, where the mean velocity and the fluctuating velocity components are $\overline{u}$ and u' respectively. Using the temporal data at all 27 spatial coordinates, the temporal stability, spatial uniformity, and turbulence intensity are determined. To estimate the temporal stability in the test section, we adopted a method slightly different from the one suggested by Park et al. [1]. The velocity data is acquired for 200 RPM of the rotor at different time instants T_2 and T_1. The statistics of measurements obtained at these two instants are shown in Table 1. The data show that the average temporal stability is 1.0% and the maximum is 1.5%.

The spatial uniformity is calculated in terms of Relative Standard Deviation (RSD) of the mean velocity data and presented in Table 2, where σ is the standard deviation shown in Eq. (3). The RSD is determined at each x-plane ($x_1 = 500$, $x_2 = 600$,

Fig. 6 Schematic view of test and the grid points represents the points of velocity measurements
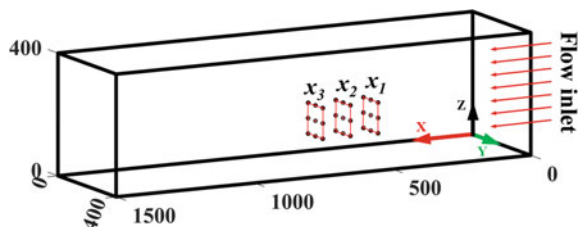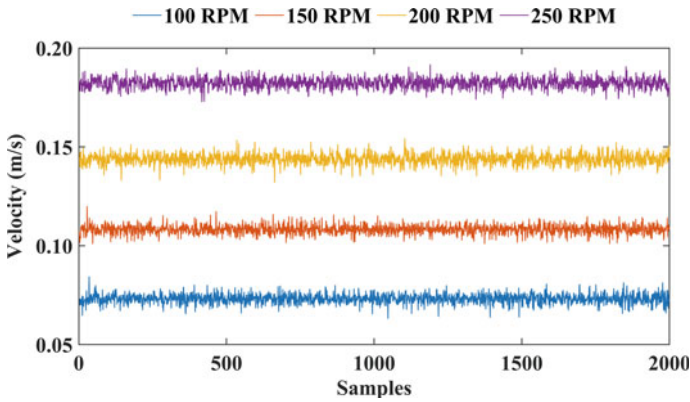
Fig. 7 Transient velocity (in *x*-direction) data at x = 600 and y = z = 150 mm, at different motor RPMs

Table 1 Mean *x*-velocity data at 200 RPM of the motor at T_1 and T_2 time instants

x = 500 mm			
y = z	x-velocity		
	$\overline{u_{T1}}$	$\overline{u_{T2}}$	$\frac{\overline{u_{T1}} - \overline{u_{T2}}}{\overline{u_{T2}}} \times 100$
100	0.1443	0.1432	0.7623
150	0.1438	0.1431	0.4868
200	0.1448	0.1444	0.2762
x = 700 mm			
y = z	x-velocity		
	$\overline{u_{T1}}$	$\overline{u_{T2}}$	$\frac{\overline{u_{T1}} - \overline{u_{T2}}}{\overline{u_{T2}}} \times 100$
100	0.1423	0.1419	0.2811
150	0.1436	0.1426	0.6964
200	0.1439	0.1418	1.4593

and $x_3 = 700$ mm), where each plane consists of nine-spatial points (see in Fig. 6). This deviation shows random nature while comparing planes at each RPM (Table 2, column 3). It also follows no relation between different motor RPMs. However, the overall RSD (calculated using all the 27 spatial points) is gradually decreasing with increasing RPM (Table 2, column 4), and it is found minimum ($\pm$ 0.61%) at 200 RPM. The maximum possible deviation is $\pm$ 1.31% at 100 RPM.

The free stream turbulence characteristics at 200 RPM of the motor are presented in Table 3. This data represents turbulence characteristics' average and standard deviation at a $3 \times 3 \times 3$ spatial grid (see in Fig. 6). The turbulence characteristics at 100, 150, and 250 RPM are given in Appendix 1. The flow field's turbulent kinetic energy (k) is calculated using Eq. (4). The acquired time domain data is transformed into the frequency domain and plotted in Fig. 8. It is worth noting that the energy

Table 2 Relative standard deviation of mean *x*-velocity in the test section at different RPMs

Motor RPM	x (mm)	Relative Standard Deviation ($\sigma/\overline{u}$) %	
		x-plane $\overline{u} \pm$ RSD % (9 coordinates) (%)	Overall $\overline{u} \pm$ RSD % (27 coordinates) (%)
100	500	0.072 ± 1.41	0.072 ± 1.31
	600	0.072 ± 0.87	
	700	0.072 ± 0.55	
150	500	0.108 ± 0.88	0.108 ± 1.02
	600	0.108 ± 0.63	
	700	0.108 ± 1.37	
200	500	0.143 ± 0.55	0.143 ± 0.61
	600	0.143 ± 0.67	
	700	0.143 ± 0.49	
250	500	0.182 ± 0.84	0.182 ± 0.78
	600	0.182 ± 0.64	
	700	0.182 ± 0.67	

associated with the high-frequency eddies in the flow field cannot be collected as the maximum sampling rate of the device is 10 Hz. This limits the understanding of more details of turbulence in the free stream. However, the sampling rate is sufficient enough (described in Sect. 2) to get the statistical mean turbulence characteristics, as shown in Table 3.

The velocity data is acquired at the central grid point ($x = 600$ mm, and $y = z = 150$ mm) from 75 to 400 motor RPM in step 25 to understand the variation of *x*-velocity and *Tu* with RPM. Figure 9 shows the characteristics of the test section velocity and *Tu* at various motor RPMs. The *Tu* is calculated from Eq. (5). The plots show a linear variation of the test section velocity with motor RPM, where *Tu* shows a decreasing trend with motor RPM. The *Tu* reduces to less than 2% for RPM of greater than 200. High levels of *Tu* (> 2%) are observed from 75 to 150 RPM regions and show a significant drop after 150 RPM.

Table 3 Free stream turbulence characteristics in the test section at 200 RPM of the motor

Turbulence parameter	Spatial average	Standard deviation
RMS$(u' + v' + w')/\overline{u}$	4.46E−02	1.83E−02
$\frac{1}{N}\sum(u')^2/\overline{u}^2$	3.60E−04	2.05E−04
$\frac{1}{N}\sum(v')^2/\overline{u}^2$	7.96E−05	2.20E−05
$\frac{1}{N}\sum(w')^2/\overline{u}^2$	3.62E−03	6.86E−03
$\left|\frac{1}{N}\sum(u'v')\right|/\overline{u}^2$	1.06E−04	4.18E−05
$\left|\frac{1}{N}\sum(v'w')\right|/\overline{u}^2$	2.77E−04	1.52E−04

(continued)

Table 3 (continued)

Turbulence parameter	Spatial average	Standard deviation
$\left\lvert \frac{1}{N} \sum (w'u') \right\rvert / \bar{u}^2$	6.00E−04	4.76E−04
$\mathrm{RMS}(u')/\bar{u}$	1.84E−02	4.57E−03
$\mathrm{RMS}(v')/\bar{u}$	8.85E−03	1.17E−03
$\mathrm{RMS}(w')/\bar{u}$	5.14E−02	3.19E−02
$\sqrt{\left\lvert \frac{1}{N} \sum (u'v') \right\rvert}/\bar{u}$	1.01E−02	1.83E−03
$\sqrt{\left\lvert \frac{1}{N} \sum (v'w') \right\rvert}/\bar{u}$	1.62E−02	3.81E−03
$\sqrt{\left\lvert \frac{1}{N} \sum (w'u') \right\rvert}/\bar{u}$	2.34E−02	7.43E−03
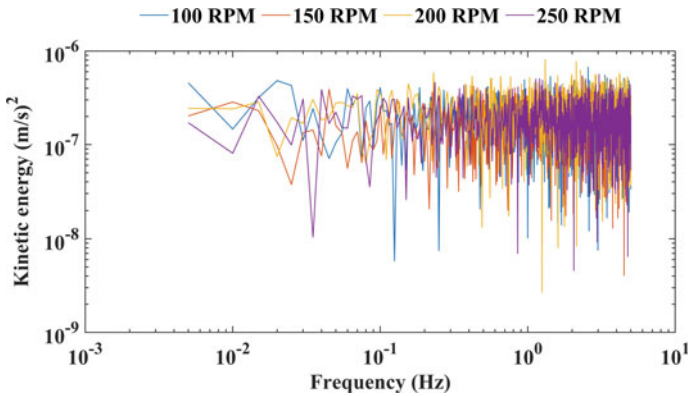
Fig. 8 Turbulent kinetic energy in the frequency domain at different motor RPMs (sampling rate is 10 Hz)
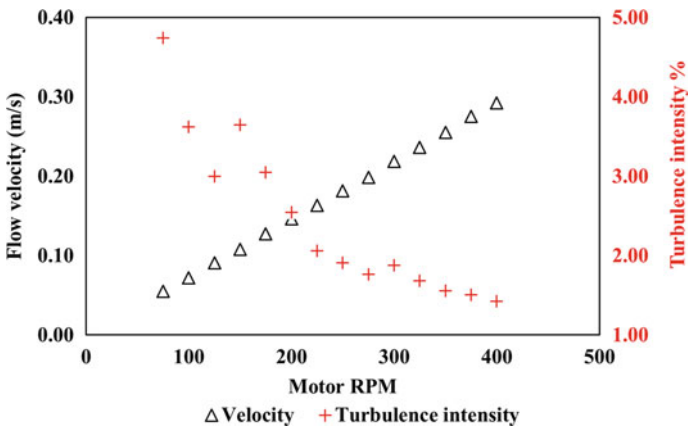
Fig. 9 Flow velocity (*x*-direction) and turbulence intensity at the centre of the water tunnel

6 Conclusions

The characterization of the new open surface recirculating water tunnel facility at the Indian Institute of Technology Kharagpur is carried out successfully. Using the SonTek Flowtracker2 Acoustic Doppler Velocimeter, the instantaneous velocity data at $3 \times 3 \times 3$ spatial grid points in the test section is acquired. The temporal stability of the free stream flow in the test section is found to be less than 1%. The spatial uniformity is found to be a function of the motor RPM. It is observed that the spatial non-uniformity is higher at lower RPM. The free stream turbulence characteristics are also estimated at the working test section velocities.

Appendix 1

See Table 4.

Table 4 Free stream turbulence characteristics in the test section at various RPM of the motor

Turbulence parameter	Standard deviation (motor RPM)		
	100	150	250
RMS $(u' + v' + w')/\overline{u}$	3.55E−02	2.29E−02	3.10E−02
$\frac{1}{N} \sum (u')^2 /\overline{u}^2$	5.66E−04	2.60E−04	3.22E−03
$\frac{1}{N} \sum (v')^2 /\overline{u}^2$	3.21E−05	2.20E−05	2.43E−04
$\frac{1}{N} \sum (w')^2 /\overline{u}^2$	9.36E−02	8.05E−03	5.74E−02
$\left| \frac{1}{N} \sum (u'v') \right| /\overline{u}^2$	1.09E−04	5.29E−05	8.12E−04
$\left| \frac{1}{N} \sum (v'w') \right| /\overline{u}^2$	2.64E−04	2.04E−04	8.86E−04
$\left| \frac{1}{N} \sum (w'u') \right| /\overline{u}^2$	9.35E−04	6.83E−04	3.25E−03
RMS $(u')/\overline{u}$	8.08E−03	5.35E−03	2.58E−02
RMS $(v')/\overline{u}$	1.65E−03	1.36E−03	5.67E−03
RMS $(w')/\overline{u}$	1.23E−01	3.74E−02	1.02E−01
$\sqrt{\left| \frac{1}{N} \sum (u'v') \right|}/\overline{u}$	3.43E−03	2.29E−03	1.24E−02
$\sqrt{\left| \frac{1}{N} \sum (v'w') \right|}/\overline{u}$	5.28E−03	4.86E−03	1.23E−02
$\sqrt{\left| \frac{1}{N} \sum (w'u') \right|}/\overline{u}$	1.05E−02	9.13E−03	2.56E−02

References

1. Park JT, Cutbirth JM, Brewer WH (2005) Experimental methods for hydrodynamic characterization of a very large water tunnel. J Fluids Eng 127(6):1210–1214
2. Howe JW, McNown JS (1946) The characteristics and utilization of the David W. Taylor model basin circulating water channel. In: Proceedings of the third hydraulics conference: June 10–12, 1946. State University of Iowa, Iowa City
3. Dash SM, Lua KB, Lim TT, Yeo KS (2018) Enhanced thrust performance of a two dimensional elliptic airfoil at high flapping frequency in a forward flight. J Fluids Struct 76:37–59
4. Arakeri VH, Sharma SD, Mani K, Govinda Ram HS (1988) The high speed water tunnel facility at the Indian Institute of Science. Sadhana 13(4):223–235
5. Moreto JR, Liu X (2020) SDSU water tunnel test section flow quality characterization. In: AIAA Scitech 2020 Forum. American Institute of Aeronautics and Astronautics, Reston, Virginia
6. Sargison JE, Barton AF, Walker GJ, Brandner PA (2009) Design and calibration of a water tunnel for skin friction research. Aust J Mech Eng 7(2):111–124
7. Zahari M, Dol SS (2015) Design and development of low-cost water tunnel for educational purpose. IOP Conf Ser Mater Sci Eng 78:012040
8. Zhang H. The water tunnel/channel design and applications in Beihang University. In: The 14th Asian symposium on visualization. Beijing
9. Haynes AMC Operation and maintenance of a high-speed water tunnel. Masters Thesis, University of Gerogia, Athens, Georgia
10. Elbing BR, Daniel L, Farsiani Y, Petrin CE (2018) Design and validation of a recirculating, high-Reynolds number water tunnel. J Fluids Eng 140(8)
11. Park JT, Cutbirth JM, Brewer WH Hydrodynamic performance of the large cavltatlon channel (LCC). West Bethesda
12. Spedding GR, Hedenström A, Johansson LC (2009) A note on wind-tunnel turbulence measurements with DPIV. Exp Fluids 46(3):527–537
13. Nader G, dos Santos C, Jabardo PJS, Cardoso M, Taira NM, Pereira MT Characterization of low turbulence wind tunnel. In: XVIII IMEKO world congress on environmental science, engineering
14. Voulgaris G, Trowbridge JH (1998) Evaluation of the acoustic Doppler velocimeter (ADV) for turbulence measurements. J Atmos Oceanic Tech 15(1):272–289
15. Song T, Chiew YM (2001) Turbulence measurement in nonuniform open-channel flow using acoustic Doppler velocimeter (ADV). J Eng Mech 127(3):219–232
16. Scharnowski S, Bross M, Kähler CJ (2019) Accurate turbulence level estimations using PIV/PTV. Exp Fluids 60(1):1
17. FlowTracker2 User's Manual 1.7. San Diego: SonTek- a Xylem brand.
18. Fan X (2019) FlowTracker2 Lab ADV: SNR, Sampling rate and velocity range effects on data
19. Goring DG, Nikora VI (2002) Despiking acoustic Doppler velocimeter data. J Hydraul Eng 128(1):117–126

On the Instability of a Flow Past a Spherical Cap Body

Ragavendiran Muniyammal, Shyam Sunder Gopalakrishnan, Sanjay Kumar, and Alakesh Chandra Mandal

Abstract We have performed an experimental flow visualization for a flow over an axisymmetric body which has a spherical shape. To explain the flow visualization images, we have also carried out the global stability analysis. The aspect ratio (χ) of the spherical shape body is defined as $\chi = 2W/D$, where W and D are the width and the base diameter, respectively. We present here some flow visualization and stability calculations for $\chi = 0.6$. We used Laser-Induced Florescence (LIF) technique for flow visualization. The flow speed has been set such that the Strouhal number is found to be 0.12, which is similar to the vortex shedding frequency of a sphere. The wake structure is compared with the global Eigen modes obtained from the stability analysis.

Nomenclature

D	Base diameter of the model (m)
W	Width of the model
ρ	Density of water (kg/m^3)
μ	Dynamic viscosity (Kg/m s)
χ	Aspect ratio (2*W/D) –
$U\infty$	Free-stream velocity (m/s)
Re	Reynolds number
f	Shedding frequency (Hz)
St	Strouhal number = fD/u

R. Muniyammal (✉) · S. Kumar · A. C. Mandal
Department of Aerospace Engineering, IIT Kanpur, Kanpur 208016, India
e-mail: ragav@iitk.ac.in

S. S. Gopalakrishnan
Department of Mechanical Engineering, IIT Kanpur, Kanpur 208016, India

LIF   Laser-induced fluorescence
PIV   Particle image velocimetry
$\hat{u}_z$ Axial velocity
$\hat{u}_r$ Radial velocity
$\hat{u}_\theta$ Azimuthal velocity

1 Introduction

Flow over a circular/rectangular cylinder, or sphere mimics a simple model of many engineering and real-life applications. Therefore, flows over bluff bodies received a considerable attention in the past. Several works were carried out experimentally using the flow visualization and the hot-wire anemometry techniques. Similarly, many numerical simulations were also carried out using direct numerical simulation (DNS), large eddy simulation (LES) and Reynolds averaged Navier–Stokes (RANS) simulation. Some works were also carried out to investigate the global stability characteristics of these bluff-body flows.

Experimentally, Moller [11] studied the flow over a sphere to find the vortex shedding frequency using the flow visualization technique. He showed that two Strouhal numbers exist for $10^3 < \text{Re} < 10^4$; here, Re is the Reynolds number based on the diameter of the sphere. Later, for the same Reynolds number range, Cometta [5] confirmed the same phenomenon using the hot-wire measurements. Further, Achenbach [1] found the high-frequency mode of Strouhal number same as Moller [11] using both flow visualization and hot-wire measurements. Kim and Durbin [8] studied the wake of a sphere for $5 \times 10^2 < \text{Re} < 6 \times 10^4$, and they showed small-scale instabilities associated with two distinct modes of unsteadiness and high frequency was detected downstream of the immediate wake of a sphere for Re > 800. Later, flow visualization of immediate wake formation after flow separation from the sphere was studied by Taneda [14]. He observed flow over a sphere with oil coated, smoke flow and tufts visualizations. He found that the Strouhal number is 0.2 in the range of Reynolds numbers $10^4 < \text{Re} < 3 \times 10^5$.

The global linear stability analyses of bluff-body wakes have been carried out extensively in the literature. Such an analysis allows one to obtain information on the Eigen mode structures which reveal the regions of the flow where perturbations are susceptible to grow. Earlier Zebib [15] studied the instability of flow past a circular cylinder. Similarly, Jackson [6] studied flows past an ellipse, a flat plate and an isosceles triangle. Using the linear stability analysis of a flow past some axismetric shapes (sphere and disc), Natarajan and Acrivos [12] found that bifurcations are associated with the destabilization of global modes. The flow over an axismetric blunt body has a higher critical Reynolds number for high aspect ratios [2]. Jimenez et al. [7] studied the flow over stream-wise rotating axismetric bodies of the cylinder with a hemispherical nose.

Most recently, Chiarini et al. [3] computed the flow past a rectangular cylinder and proposed different scaling for critical Reynolds number. Also, Chiarini et al. [4] extended the same scaling for different shapes like triangular, elliptical and diamond to assess generality of the scaling.

Linear stability analyses of flows past two-dimensional bodies with cross-sections like rectangular, triangular, elliptical and diamond (Chiarini et al. [4]) and three dimensional axisymmetric bodies like spheres [7, 12, 13], discs, long cylinder with hemispherical cap [9, 10], were carried out in the past to find the critical Reynolds number. Experimentally many studies have been carried out to find the shedding frequency of flow over a sphere in different range of Reynolds numbers. However, to the best of our knowledge, flows past a spherical cap shape and an elliptical cap shape are not explored in the literature. We investigated the global insatiability of flows past a spherical/elliptical cap, hemisphere and elliptic nose using both the linear stability analysis and the LIF technique.

This paper is organized as follows. In Sect. 2, we describe the problem geometry and experimental method for the present study. Flow visualization and frequency measurement are discussed in Sect. 3. Concluding remarks are given in Sect. 4.

2 Experimental Details

2.1 Water Tunnel

All the experiments reported here were performed in a water tunnel. It has a test section of 180 mm in depth, 250 mm in width and 460 mm in length. A schematic of the present experimental setup is shown in Fig. 1. The flow speed can be varied from 10 mm/s to 100 mm/s. The model was placed in middle of the test section with a support sting of diameter 10 mm. It was connected to the centre of the base of the model. The tunnel has an external motor control. Hence, desired tunnel speed was set by the external motor system.
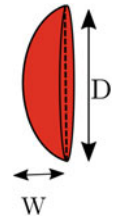
2.2 Models

Figure 2 shows the experimental model. As mentioned, the aspect ratio is defined as $\chi = 2W/D$, where W is the width of the spherical/elliptical cap and D is the base diameter. Reynolds number is defined as $Re = \rho U_\infty D/\mu$, where ρ is the density of the fluid, U_∞ is the free-stream velocity and μ is the dynamic viscosity of the working fluid.
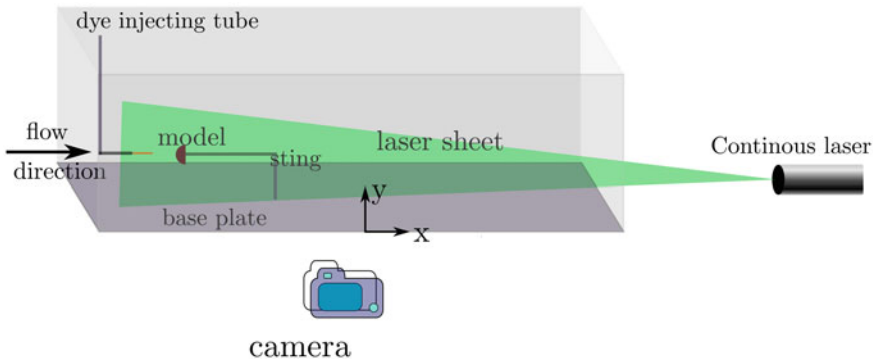
Fig. 1 Schematic of LIF visualization technique

Fig. 2 Spherical cap model
$\chi = 0.6$

2.3 PLIF Visualization

Flow around the spherical cap model in the water channel was visualized using Rhodamine dye. The Rhodamine dye injection system was located approximately 10D upstream of the model. Since the dye injection stainless tube is small in diameter ($\approx$ 1 mm), the dye injection system maintains the attached flow and the test section maintains a uniform flow. A green LED light source was used to illuminate the Rhodamine dye. It was placed on the rear side of the test section. A DSLR camera (3820 pixels $\times$ 2460 pixels) was used to acquire the images at 30 frame per second (fps) for a region of interest of 200 mm $\times$ 100 mm. The acquired images were processed using the MATLAB image processing tool. The vortex shedding frequency for a model at a given Reynolds number was calculated using the time series of the grey scale of the images.

3 Results and Discussion

In this section, we presented results of flow visualization and frequency calculation of a spherical cap model with an aspect ratio of $\chi = 0.6$. It was ensured that the tunnel speed was rightly set such that Re $= 221$, and the injected dye from the dye injection system was aligned with streamlines of the free-stream flow.

Figure 3 shows some instantaneous snapshots of vortex shedding behind a spherical cap body at an interval of 1 s. The dye was introduced at the upstream flow of the model. The dye follows a uniform stream and flows around the spherical cap. Due to the sharp edge, the flow separates at the end of the model and forms a re-circulation region leading to eventual vortex shedding in the wake. Figure 4 shows five different locations where the time series of the grey scale of the images were collected.

Figure 5 shows the frequency spectra of the vortex shedding as measured from the dye intensity. For finding the shedding frequency, the image intensity was collected at five different locations (see Fig. 4) downstream of the model to calculate the shedding frequency. Same frequency was found at all locations, as shown in Fig. 5. Power spectra (Fig. 5) and flow visualizations (Fig. 3) suggest that hairpin-shaped vortices appear periodically in the wake of the model. The non-dimensional frequency, i.e. the Strouhal number, is found to be 0.12.

A numerical study was also carried out for the spherical shape bodies. Briefly, a steady base flow was obtained by solving the steady Navier–Stokes equations.
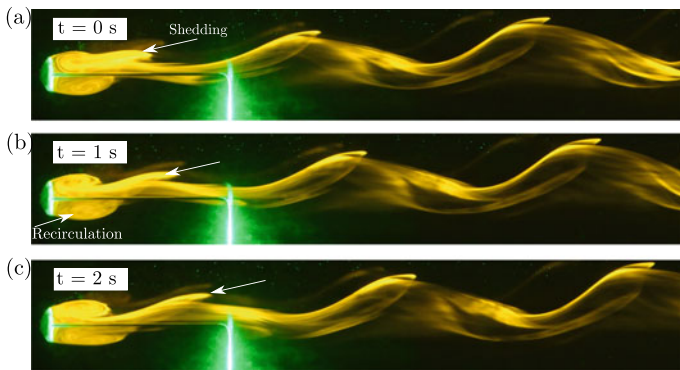
Fig. 3 Wake of the spherical cap model $\chi = 0.6$ at Re $= 221$ for different time instants. (**a**) At $t = 0$ s, (**b**) at $t = 1$ s and (**c**) at $t = 2$ s
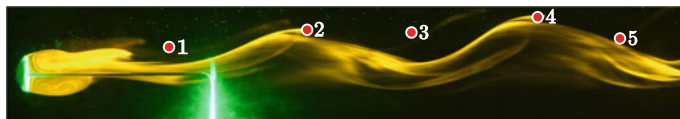
Fig. 4 Locations where image grey intensity used for frequency calculation

Fig. 5 Vortex shedding
frequency $f = 0.23$ Hz for χ
$= 0.6$ at different locations
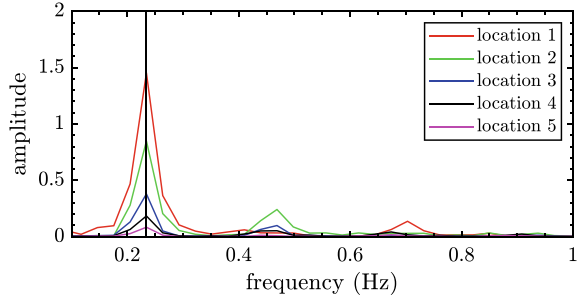
A normal mode of the disturbance led the linearized Navier–Stokes equation to an
eigenvalue problem, which was solved for the given base flow. These computations
were carried out using an open source code, FreeFEM++. The global mode shape
corresponding to the most unstable eigenvalue, as obtained from the global stability
analysis for the aspect ratio $\chi = 0.6$, is shown in Fig. 6. This shows that the flow is
globally unstable and the vortex shedding is the result of this global instability of the
flow.
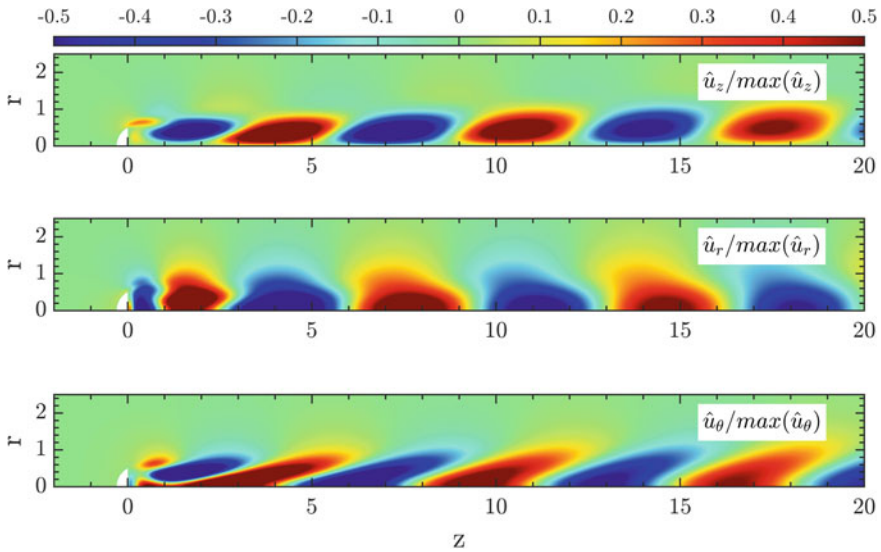
Fig. 6 Leading global mode at the bifurcations. Real part of $\hat{u}_z$, $\hat{u}_r$ and $\hat{u}_\theta$ velocity components
(from top to bottom) of the unstable mode for Hopf bifurcation at Re $= 155.5$ for $\chi = 0.6$ of
azimuthal mode $m = 1$

4 Conclusions

In this paper, we report an experimental investigation of the flow past a spherical cap model with an aspect ratio (χ) = 0.6. From the flow visualization image sequence, the shedding frequency was calculated. The periodic vortex shedding is clearly found to exist at Re = 221. The Strouhal number for the present case is found to be 0.12. This initial study shows that the vortex shedding behind a spherical shape body is due to the global instability. It is an ongoing study, and further investigations are being carried out using the LIF visualization and the Particle Image Velocimetry (PIV) techniques for different models.

References

1. Achenbach E (1974) Vortex shedding from spheres. J Fluid Mech 62(2):209–221
2. Bohorquez P, Sanmiguel-Rojas E, Sevilla A, Jimenez-Gonzalez JI, Martınez-Bazan C (2011) Stability and dynamics of the laminar wake past a slender blunt-based axisymmetric body. J Fluid Mech 676:110–144
3. Chiarini A, Quadrio M, Auteri F (2021) Linear stability of the steady flow past rectangular cylinders. J Fluid Mech 929
4. Chiarini A, Quadrio M, Auteri F (2022) On the frequency selection mechanism of the low-re flow around rectangular cylinders. J Fluid Mech 933
5. Cometta C (1957) An investigation of the unsteady flow pattern in the wake of cylinders and spheres using a hot wire probe. Div. engineering technical report, Brown University, Tech. Rep. WT-21
6. Jackson CP (1987) A finite-element study of the onset of vortex shedding in flow past variously shaped bodies. J Fluid Mech 182:23–45
7. Jimenez-González JM, Manglano-Villamarın C, Coenen W (2019), The role of geometry on the global instability of wakes behind streamwise rotating axisymmetric bodies. Eur J Mech B Fluids 76:205–222
8. Kim HJ, Durbin PA (1988) Observations of the frequencies in a sphere wake and of drag increase by acoustic excitation. Phys Fluids 31(11):3260–3265
9. Le Clainche S, Li JI, Theofilis V, Soria J (2015) Flow around a hemisphere-cylinder at high angle of attack and low Reynolds number. Part I: Experimental and numerical investigation. Aerosp Sci Technol 44:77–87
10. Le Clainche S, Rodriguez D, Theofilis V, Soria J (2015) Flow around a hemisphere-cylinder at high angle of attack and low Reynolds number. Part II: Pod and dmd applied to reduced domains. Aerosp Sci Technol 44:88–100
11. Moller W (1938) Experimentelle untersuchung zur hydromechanick der hugel. Phys Z 35:57–80
12. Natarajan R, Acrivos A (1993) The instability of the steady flow past spheres and disks. J Fluid Mech 254:323–344
13. Pier B (2008) Local and global instabilities in the wake of a sphere. J Fluid Mech 603:39–61
14. Taneda S (1978) Visual observations of the flow past a sphere at Reynolds numbers between 104 and 106. J Fluid Mech 85(1):187–192
15. Zebib A (1987) Stability of viscous flow past a circular cylinder. J Eng Math 21(2):155–165

Turbulence Measurement Over Rough and Smooth Bed in Open-Channel Flow

Kirti Singh and Kesheo Prasad

Abstract A 3D Acoustic Doppler velocimeter was used in the current investigation to quantify the mean and turbulence characteristics in non-uniform open-channel flows. Results are obtained from studies done in laboratory, analysing the behaviour of sand particles under turbulent open-channel flow conditions flowing through rough, porous beds. Data obtained from ADV is used to calculate turbulent flow characteristics, Reynolds stresses and turbulent kinetic energy. Theoretical formulations for the distribution of Reynolds stress and the vertical velocity have been constructed using the Reynolds equation and the continuity equation of 2D open-channel flow. Measured Reynolds stress profile and the vertical velocity are comparable with the derived expressions. This study uses the Navier–Stokes equations for analysing the behaviour of the vertical velocity profile in the dominant region of full-fledged turbulent flows in open channels, and it gives a new origination of the profile. For both wide and narrow open channels, this origination can estimate the time-averaged primary velocity in the turbulent boundary layer's outer region.

Keywords Turbulence · Bed roughness · Logarithmic law · Shear stress correlations · ADV · Reynolds shear stress

Nomenclature

U	Average mean velocity (cm/s)
AR	Aspect ratio –
R	Shear stress correlation coefficient –
u	Instantaneous velocity in x-direction (cm/s)
v	Instantaneous velocity in y-direction (cm/s)
$K.\,E$	Kinetic energy
P	Density of fluid

K. Singh (✉) · K. Prasad
Department of Civil Engineering, IIT-BHU, Varanasi 221005, India
e-mail: Kirtisingh.rs.civ19@itbhu.ac.in

K   Turbulent kinetic energy
η   Bulk viscosity
υ   Coefficient of kinematic viscosity of fluid
$\zeta(x, z)$ Reynolds shear stress $(= -\rho\overline{u'v'})$

1   Introduction

Turbulence is characterized by irregularity, diffusivity, rotationality and dissipation. Turbulence can be viewed as instability of laminar flow due to increase in Reynold's number. Unlike the laminar flow, where the fluid moves parallelly in layers or smoothly flowing channels, turbulent flow experiences fluctuations in the fluid or non-uniform mixtures. In a turbulent flow, the amplitude and direction of the fluid's speed are constantly shifting. In fluid dynamics, irregular flows including eddies, vortices, and flow instabilities are referred to as a turbulent regime. On the other hand, the laminar regime develops when a continuous flow takes place in parallel layers.

For both engineers and scientists, the behaviour of small suspended sediments in riverine systems, particularly, their inclination to settle down and deposit, poses important issues and difficulties. The sediment that is available for transport at the local scale is determined by the river channel, which serves as an interface between channel flow and subsurface sediments. Presence or lack of bed-forms affects the bed surface topography when the channel contains a movable bed.

Particle Image Velocimetry (PIV), Laser Doppler Velocimetry (LDV), and Acoustic Doppler Velocimetry (ADV) were widely employed to detect liquid velocities in various fluid dynamic experiments to determine the mean and turbulence features in an open channel [1–3].

Due to its numerous practical uses, the distribution of the velocity in vertical direction across the cross section of the channel has been the subject of several studies for many years [3–6]. A logarithmic law (log law) has been proposed by Nikuradse [7] to explain the vertical distribution of the main velocity. This law has been enhanced by Coles [8] by including the wake function.

2   Literature Review and Objective

2.1   *Theoretical Background*

This study focuses on fully turbulent flows having a composite turbulent boundary layer made up of inner and outer regions.

1. **Inner Region**—A turbulent boundary layer has a substantially smaller inner region as compared to an outer region. Its thickness makes up 10–20% of the total thickness of the boundary layer [9]. The formulation of turbulent kinetic energy is greater than the rate of dissipation in this region. Depending upon the texture of the wall being smooth or rough, the behaviour varies [1–3, 10].

Smooth Wall—A viscous sublayer, the area next to the wall, a transitional area in the central, and a fully turbulent zone makes up the inner region. In the viscous sublayer, the viscosity is centric and the mean velocity distribution is assumed as (U):

$$\frac{U}{u*} = \frac{u * y}{\nu} = y^+ \tag{1}$$

Here, y is the perpendicular distance measured from the bottom, $u*$ is the shear velocity and ν is the kinematic viscosity. This linear distribution is applicable for $y^+ \leq 5$ [11]. In the full-fledged turbulent zone of the inner region, the vertical distribution of the velocity is calculated by the logarithmic law:

$$\frac{U}{u*} = \frac{1}{\kappa} \frac{u * y}{\nu} + B \tag{2}$$

where, κ being the von Karman constant and integration constant is represented by B. These parameters are studied by various researchers. The κ value is taken as 0.41, a constant which is universally taken disregarding the flow configuration [11]. On the contrary, the value of constant B may vary based on the flow properties and Fig. 1 showcases the variation for the values for constant B procured from various studies.

Rough Wall—The following relationship determines the velocity distribution across the area around the wall [12]:

$$\frac{U}{u*} = \frac{1}{\kappa} \ln \frac{y}{y_0} \tag{3}$$

2. **Outer Region**—Following equation can determine the velocity behaviour across the outer region [13]:

$$\frac{U}{u*} = \frac{1}{\kappa} \ln\left(\frac{z}{ks}\right) + B_s + w(\xi)$$

having

$$w(\xi) = \frac{2\pi}{\kappa} \sin\left(\frac{\pi}{2}\xi\right) \tag{4}$$

Here, $w(\xi)$ is the wake function that Coles [8] proposed to adjust the log-law additively. Equation 4 is applicable to both smooth and rough surfaces.
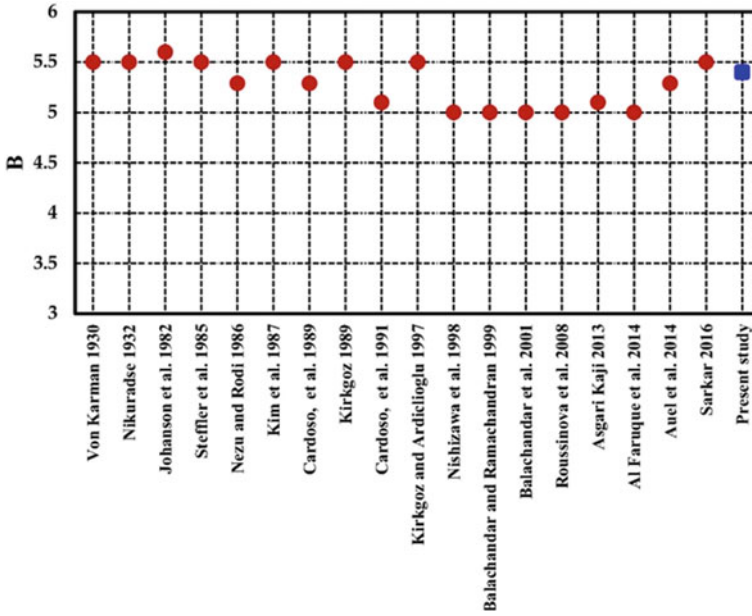
Fig. 1 Heterogeneous values of the integration constant (B) in the logarithmic law obtained by various studies

3 Mathematical Modelling

Direct numerical simulation and Reynolds-averaged Navier–Stokes are two mostly used numerical approaches for resolving turbulent flows.

The immediate velocity components (u, v) in two dimensions (x, y), as well as the instantaneous pressure intensity 'p', are decomposed in the following manner:

$$u = \overline{u} + u'; \, v = \overline{v} + v'; \, p = \overline{p} + p' \tag{5}$$

Here an overline represents time-averaged quantity and a prime represents variations in time-averaged quantity; and t is time.

Time-averaged velocity component is defined as:

$$\overline{u} = \frac{1}{\Delta t} \int\limits_{t}^{t+\Delta t} u.dt \tag{6}$$

The continuity equation in most general form is written as

$$\frac{\partial \rho}{\partial t} + \nabla.(\rho u) = 0 \tag{7}$$

Because it includes extra variables known as Reynold's stresses (or turbulent stresses), the momentum equation is changed concerning laminar flow.

$$\frac{\partial \rho u}{\partial t} + \nabla.(\rho u \otimes u) - \nabla.(\mu_{\text{eff}} \nabla u) = -\nabla p' + \nabla.(\mu_{\text{eff}} \nabla u)^T + B \qquad (8)$$

Here B represents the summation of body forces, μ_{eff} is defined as the effective viscosity and p' denotes the modified pressure represented as

$$p' = p + \frac{2}{3}\rho k + \nabla.u\left(\frac{2}{3}\mu_{eff} - \eta\right) \qquad (9)$$

The continuity equations for fluctuating and time-averaged velocity components are

$$\frac{\partial \overline{u}}{\partial x} + \frac{\partial \overline{w}}{\partial z} = 0; \; \frac{\partial u'}{\partial x} + \frac{\partial w'}{\partial z} = 0 \qquad (10)$$

And the RANS equation is

$$\overline{u}\frac{\partial \overline{u}}{\partial x} + \overline{w}\frac{\partial \overline{u}}{\partial z} = -\frac{1}{\rho}\frac{\partial \overline{p}}{\partial x} + \upsilon\frac{\partial^2 \overline{u}}{\partial z^2} - \frac{\partial \overline{u'^2}}{\partial x} + \frac{1}{\rho}\frac{\partial \zeta}{\partial z} + g\sin\beta \qquad (11)$$

$$\overline{u}\frac{\partial \overline{w}}{\partial x} + \overline{w}\frac{\partial \overline{w}}{\partial z} = -\frac{1}{\rho}\frac{\partial \overline{p}}{\partial z} + \upsilon\frac{\partial^2 \overline{w}}{\partial x^2} - \frac{\partial \overline{w'^2}}{\partial z} + \frac{1}{\rho}\frac{\partial \zeta}{\partial x} - g\cos\beta \qquad (12)$$

where ρ = density of fluid; k = turbulent kinetic energy; η = bulk viscosity; υ = coefficient of kinematic viscosity of fluid; $\zeta(x,z)$ = Reynolds shear stress ($= -\rho\overline{u'v'}$); and g = gravitational acceleration.

4   Experimental Setup and Materials

A 9.2 m in length, 0.3 m in width and 0.55 m in depth water recirculating channel having steady slope of bed of 0.001% was used for the experiments. A man-made channel bed that ran the entire working length of the channel served as support for the porous bed material layer. The trials were conducted in a bigger flume facility that employed a water-recirculation and sediment feeding system. The channel's steady, uniform, and subcritical flow characteristics were used for all of the trials.

For all three trials, the flow depth was maintained at 14 cm across the sections that are used for test, which was 4.5 m down the channel inlet. In order to guarantee sufficient 2D flow and independence from wall effects in the channel's inner region, this resulted in a width to depth ratio of 2.14.

Flow depth ratio, i.e. B/H was confined to 2.0–3.2 due to the narrow width of the visualization channel, that is less than the crucial magnitude of B/H = 5 needed for two-dimensional turbulent flow [14, 15].

The tests were conducted with a constant flow rate, which maintained the comprehensive average flow velocity constant at roughly 28.5 cm/sec. Hence, the flow Reynolds number, based upon the flow depth & the average velocity, was maintained to approximately 39,700 throughout all trials.

Boundary Roughness—The hydraulically rough and smooth boundary conditions were obtained by sheathing the channel bed using fibre sheet and 2 mm Ganga sand and Sonbhadra sand. Figure 2 depicts the schematic arrangement of water channel.

Flow depth for experiments conducted is kept constant. In Table 1, mean flow and roughness parameters are reported. Mean height of roughness above base plate is mentioned.

Grading characteristics of soil, i.e. uniformity coefficient and coefficient of curvature for different sand are calculated in Table 2. With the help of grading curve of soil.
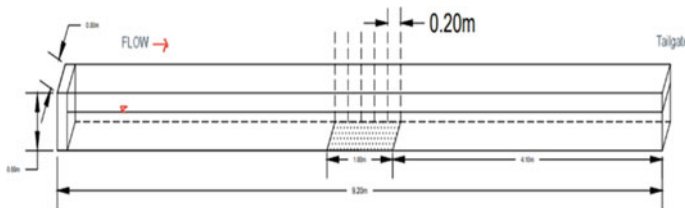
Fig. 2 Schematic arrangement of water channel

Table 1 Mean flow and bed roughness parameters

Experiments	Flow depth (cm)	Height of velocity origin above bed plate (cm)	Mean height of rough tops above bed plate, k (cm)	Kinematic viscosity, v cm^2/s
Fibre sheet	14	0.1	0.1	0.008
Ganga sand	14	0.4	0.3	0.008
Sonbhadra sand	14	0.2	0.1	0.008

Table 2 Properties of sand used

| Sand used	Shear velocity	D_{60}	D_{10}	Relative density
Ganga sand	0.037 m/s	1.882	0.504	2.62
Sonbhadra sand	0.037 m/s	1.035	0.301	3.01

5   Results and Discussion

Mean Flow and Turbulence Measurements At several downstream sample locations inside each channel, the SonTek three-component ADV measured the mean and changing flow velocities. The ADV was used for all measurements, with the velocity limit set to 1.0 cm/s and the sampling rate is set to maximum of 25 Hz. According to SonTek ADV standards, random noise limit applicable for the above conditions has an estimation of result in 1% inaccuracy in the measurements of velocity, or up to 1 cm/s. In order to gather instantaneous measurements at each height for an approximate duration of at least 120 s, or a time series of more than 3,000 individual data measurements, the analysed sample volume (0.25 cm^3) was placed at several aspects inside the flow above the bed surface. Analysing these time-series measurements resulted in the generation of pointwise mean velocity and turbulence characteristics. By placing the sample volume 10 cm from the probe transducers, measurements may be taken quite near to the bed surface. This setup, meanwhile, also made it impossible to measure under the outer flow region since the probe receivers weren't completely immersed. Up to 250 instantaneous measurements that were gathered throughout a sample period of 300 s were used to calculate the pointwise mean velocities. ADV records carrying instantaneous observations of the flow velocity parameters at a specific place in the flow are used to generate vertical flow velocities, time-averaged longitudinal velocities, Reynolds' shear stress, and the turbulence. The curves for shear velocity and mean velocity are demonstrated in Figs. 3 and 4.

Turbulence Intensity The turbulence intensity distributions across the different streams are shown in Fig. 5. To eliminate any further errors associated with scaling parameters with computed quantities, the scales for the length and the velocity are respectively derived from directly measured variables such as the maximum velocity and the depth of flow. Figure 5 clearly depicts that, for all surfaces, streamwise turbulence intensity reaches to the maximum when extremely near to the bed. The smooth bed profile exhibits the strongest turbulence just next to the bed.

Fig. 3 Mean velocity profiles
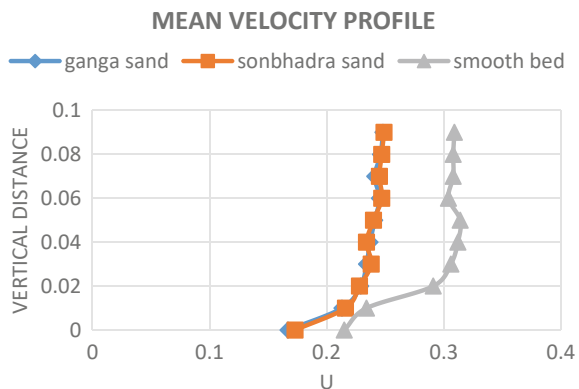
Fig. 4 U/U_T versus ($U_T y/\nu$)
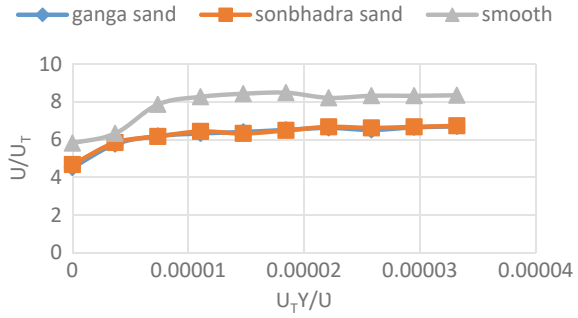
Fig. 5 Streamwise turbulence intensity for flow over different bed conditions
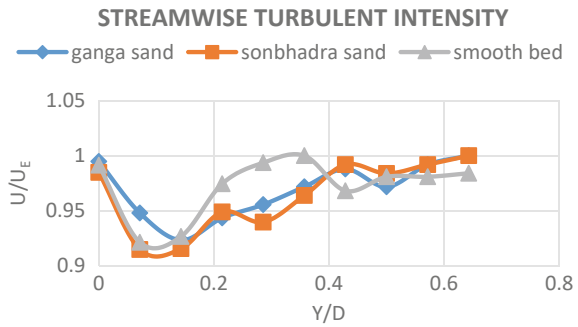
Shear Stress Correlation Coefficient Figure 6 displays the correlation coefficient distribution for shear stress ($R = \frac{-\overline{uv}}{u \times v}$) for the various channel conditions. The degree of linear correlation between the vertical and streamwise turbulence intensity can be described using the shear stress correlation coefficient, which is a normalized covariance. Local statistics of R can be used to determine whether flow structures exist or do not exist at a specific location.

Fig. 6 Distribution of shear stress correlation coefficient for flow across different bed conditions
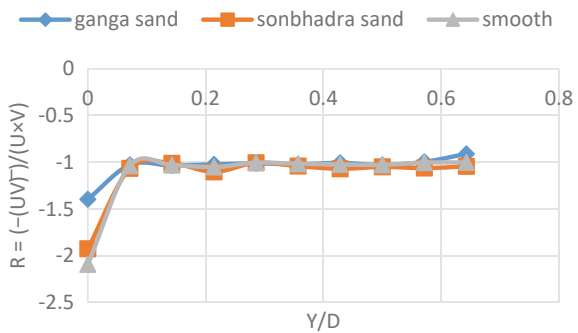
Fig. 7 Proportion of vertical flux of the turbulent kinetic energy for flow across different bed conditions
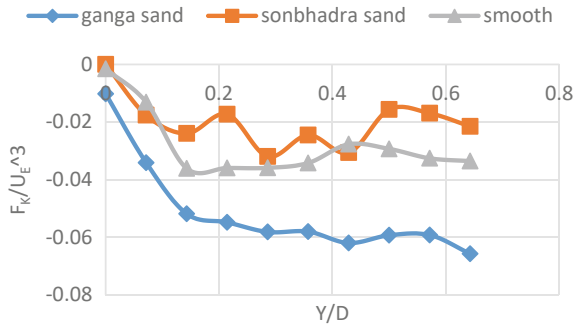
Vertical Flux of the Turbulent Kinetic Energy Figure 7 demonstrates dependency of the vertical flux of the turbulent kinetic energy (F_{kv}) on the rough and the smooth beds. F_{kv} is usually calculated as $0.5(\overline{v^3} + \overline{vu^2})$ for a two-dimensional flow.

As the size of roughness decreases, turbulent intensity increases and more turbulence occurs near the bed surface. The streamwise turbulence intensity profile's tendency is visible in the variation of vertical turbulence as well [16].

6   Conclusions

The aim behind this study was for understanding the magnitude of the effect of various roughness occurring by sand and Reynolds number on turbulence, mean velocity, shear stress correlation coefficient & vertical flux of turbulent kinetic energy in an open-channel flow. Further to this, three various types of bed surface conditions were adopted in the study. The present results seem to be fairly comparable with that of the previous research. The variation of mean velocity profile with the roughness is clearly evident through most of the flow depth with the distributed roughness presenting the maximum deviation from the smooth profile. In order to create the rough bed conditions, different sand grain is used and the variation in turbulence intensity behaves as the clear indicator that turbulence structure do varies depending on the extent of the roughness. The difference in shear stress correlation coefficient, R for the outer layer and the near-wall is a sign of the variation in flow structures between the two regions, which is clearly contrary to Nezu and Nakagawa's (1993) observation that the distribution of R is universal irrespective of the mean flow properties and the wall roughness. Sand with different densities has different effects on changing behaviour of the correlation coefficient.

References

1. Antonia RA, Krogstad PA (2000) Effect of different surface roughnesses on a turbulent boundary layer. J Braz Soc Mech Sci 22:1–15
2. Kirkgöz MS (1989) Turbulent velocity profiles for smooth and rough open channel flow. J Hydraul Eng 115(11):1543–1561
3. Kirkgoz BMS (1990) Turbulent velocity profiles for smooth and rough open channel flow vol. 115, no. 11, pp. 1543–1561
4. Sharma KVN, Lakshminarayana P, Lakshmana Rao NS (1983) Velocity distribution in smooth rectangular open channels. J Hydraul Eng 109(2):270–289. https://doi.org/10.1061/(ASCE)0733-9429(1983)109:2(270)
5. Qi M, Li J, Chen Q, Zhang Q (2018) Roughness effects on near-wall turbulence modelling for open-channel flows. J Hydraul Res 56(5):648–661. https://doi.org/10.1080/00221686.2017.1399931
6. Salih KM, Mehmet A (1997) Velocity profiles of developing and developed open channel flow. J Hydraul Eng 123(12):1099–1105. https://doi.org/10.1061/(ASCE)0733-9429(1997)123:12(1099)
7. Nikuradse J (1950) Laws of flow in rough pipes. J Appl Phys 3:399 [Online]. Available: http://scholar.google.com/scholar?hl=en&btnG=Search&q=intitle:LAWS+OF+FLOW+IN+ROUGH+PIPES#0
8. Coles D (1956) The law of the wake in the turbulent boundary layer. J Fluid Mech 1(2):191–226
9. Rubinstein R (2005) Tuncer Cebeci: analysis of turbulent flows. Theor Comput Fluid Dyn 19(4):301–302. https://doi.org/10.1007/s00162-005-0168-2
10. Al Faruque MA (2009) Smooth and rough wall open channel flow including effects of seepage and ice cover
11. Schlichting H, Kestin J, Street RL (1980) Boundary-layer theory (seventh edition). J Fluids Eng 102(1):125. https://doi.org/10.1115/1.3240614
12. Townsend AAR (1976) The structure of turbulent shear flow. Cambridge University Press
13. Jiménez J (2004) Turbulent flows over rough walls. Annu Rev Fluid Mech 36(1):173–196. https://doi.org/10.1146/annurev.fluid.36.050802.122103
14. Krogstad P-Å, Antonia RA, Browne LWB (1992) Comparison between rough- and smooth-wall turbulent boundary layers. J Fluid Mech 245:599–617. https://doi.org/10.1017/S0022112092000594
15. Krogstad P-Å, Andersson HI, Bakken OM, Ashrafian A (2005) An experimental and numerical study of channel flow with rough walls. J Fluid Mech 530:327–352. https://doi.org/10.1017/S0022112005003824
16. Afzal B, Al Faruque M, Balachandar R (2009) Effect of Reynolds number, near-wall perturbation and turbulence on smooth open-channel flows. J Hydraul Res 47(1):66–81. https://doi.org/10.3826/jhr.2009.3113

High-Speed Schlieren Imaging as a Tool for Identifying Vortices in Dragonfly Flight

Amit Ashok Pawar, Kumar Sanat Ranjan, Arnab Roy, and Sandeep Saha

Abstract Bio-inspired aerodynamics has amazed the scientific community for decades now. It has inspired researchers and innovators to identify solutions to several fundamental and advanced problems in academia and industry. Insight into temporally evolving vortical structures developing in the near field of a beating wing will be helpful to interpret better the aerodynamic forces generated by the flap cycle of an insect. In the present study, high-speed Schlieren imaging is implemented to capture vortex structures on the wings of Pantala flavescens in the tethered arrangement. The method discussed here helps identify various vortical structures like leading edge vortex and trailing edge vortex. A physics-based optical flow method is also implemented to quantify the flow field and interpret the jump in the nature of vorticity during wing rotation at the end of the stroke. It is also demonstrated that this method has the potential to capture the vortex structure. The present study illustrates how this method is not limited to presenting flow visualization or qualitatively complementing the force measurement tests but also has the potential to provide a quantified velocity field.

Keywords Insect aerodynamics · Schlieren technique · Physics-based optical flow · Flow visualization · Vortex structure

1 Introduction

Insect flight has invoked curiosity in the scientific community, and significant advances have been made over the past decades on the frontier of understanding insect flight aerodynamics. Until the early twentieth century, the potential of unsteady mechanisms for lift generation was not realized. Biologists quickly adopted the quasi-steady assumptions-based approach to study insect flight. Later more intensive research [1, 2] helped the research community realize that the insect flight is a

A. A. Pawar (✉) · K. S. Ranjan · A. Roy · S. Saha
Department of Aerospace Engineering, IIT Kharagpur, Kharagpur, West Bengal 721302, India
e-mail: amit.pawar@iitkgp.ac.in

more complex transient phenomenon [1–3]. In the last few years, higher computational resources and high-speed imaging coupled with various force measurement and flow field quantification experiments have accelerated understanding insect flight aerodynamics.

The flow field around an insect is a complex vortex-dominated field. These vortices play a significant role in the generation of aerodynamic forces in a flapping cycle of insect flight. In particular, the leading edge vortex (LEV) is responsible for fulfilling major lift requirements for all modes of insect flight. Additionally, recent studies have highlighted the role of phasing between different wings and the quick wing rotation at the end of strokes in aerodynamic force generation.

Due to the highly transient nature of the flow field and the complex wing-wake and wing-wing interactions, interpreting the results of force measurement experiments is not trivial. Visualizing the vortical structures will provide significant insights into insect fight aerodynamics. It will also help identify the wing kinematics of the particular flap cycle and its associated forces. Additionally, access to the vorticity map of the near field while performing force measurement tests will work as a wrapper of additional details to better interpret the acquired force measurements.

The present study uses Schlieren imaging to capture these vortical structures. The captured images are further quantified using physics-based optical flow techniques to quantify these images and produce a velocity field.

2   Methodology

A high-speed, single mirror, double-pass Schlieren setup demonstrated by Taylor and Waldram [4] was used for the present study. A white LED (Godox S60) was used as a light source. A pinhole in front of the light source is used to project a diverging beam on the 8-inch spherical mirror. The projected and the reflected, both diverging and converging rays, traverse through the test region. The reflected beam is redirected to the knife edge using a 50/50 (reflection/transmission ratio) beam splitter. A knife edge is placed at the focusing point of this reflected beam to produce the Schlieren images. A high-speed camera (Mini AX50, Photron) placed in front of this knife edge is used to capture the Schlieren images. Figure 1 presents a schematic of the present study's setup. The test objects (insects in this case) are placed close to the mirror to reduce the deflection angle and achieve double sensitivity compared to a single-pass system [5].

Pantala flavescens used in the experiment were obtained at the IIT Kharagpur campus by capturing them using an aerial net. The captured insects were transported from the field to the lab in Ziploc bags and kept to rest for around 60 min. The insects were cold immobilized by keeping them in a refrigerator at around 5°C for 1 min. An aluminum rod of 2.5 mm diameter and approximately 200 mm long is used as a tether. The immobilized insects are attached to this rod using a cyanoacrylate ester. The tethered insects are left for recovery from cold immobilization for a recovery interval of around 20 min. Isopropyl alcohol has been used for similar experiments to
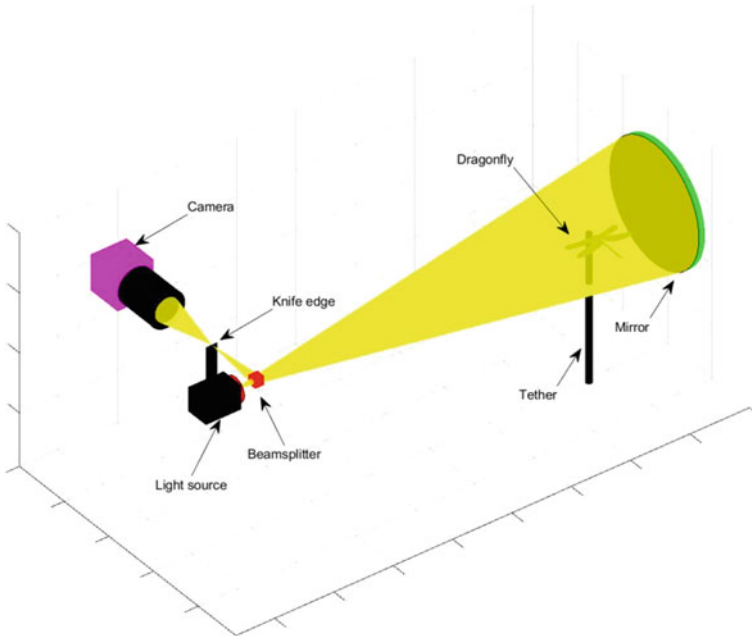
Fig. 1 Schematic of the Schlieren setup

capture the vortical structures developing around an insect's flapping wing; Schmidt number has been reported of order one [6], making it a good candidate for a passive scalar, which is primary for such experiments.

Isopropyl alcohol is coated on the dragonfly's wing using a brush before starting the experiment. The vapors from the wing are entrained by the unsteady three-dimensional vortical structures developing on the wing. The Schlieren imaging setup picks up the presence of vapors in the vortical structures. The images are acquired at a rate of 3000 frames per second. The acquired images help identify different vortical structures evolving in the near-field region. These images are further processed to obtain the velocity field using the physics-based optical flow method [7] using Matlab.

3   Results and Discussion

3.1   Vortical Structures in the Near Field

The method illustrated in the previous section was implemented to capture the vortical structures in the near field region of the dragonfly. Figure 2 presents the captured vortical structures. These are snapshots from different flap sequences captured at different framing speeds. Figure 2a shows the leading edge vortex developed over

the forewing during the start of the upstroke of the forewing. Figure 2b and c highlight the trailing edge vortex and the root vortex developed over the hindwing during the upstroke. Root vortex is the vortex developed in the root region of the wing near the thorax of the insect's body. Figure 2d presents the tip vortex and the vortex loop comprising of the tip, root and trailing edge vortex on the hindwing during the downstroke. Figure 2a and b are captured at a framing speed of 3000 frames per second whereas Fig. 2c, d and e are captured at 2000 frames per seconds.

Figure 2d is a snapshot from instants before the loop is shed at the onset of supination, whereas Fig. 2e captured shows the sequence after the supination (6 ms later the Fig. 2d) where the vortex loop has been shed, and the trailing edge vortex can be seen developing at the onset of the upstroke.

3.2 Quantified Velocity Field

Figure 3 illustrates the data acquired using the setup described in Sect. 2. This snippet is from a sequence of flap cycles captured during a downstroke. The images were calibrated and processed using the physics-based optical flow technique to obtain quantified flow field data. The area enclosed in the red box is selected as a region of interest (ROI) as the test case for quantifying the velocity field.

Figure 4a presents the masked ROI of 15 mm × 8 mm processed for demonstration of the methodology. Figure 4b illustrates the streamlines obtained using the computed velocity field for a mean flow averaged over 12 frames, i.e., 3.6 ms.

Figure 5 shows vorticity contours around a hindwing performing a flapping cycle. The sequence presented here is as follows: (i) upstroke (a-b); (ii) quick wing rotation (c) and (iii) downstroke (d-f). This information helps identify the nature of flow in the near field during a flapping cycle.

During the upstroke, LEV is visible on the wing. At pronation (Fig. 5c), the LEV is absent. As the downstroke begins (Fig. 5d), the LEV and starting vortex are visible on the wing. In Fig. 5f, the wing has covered half of the downstroke, and the starting vortex has shed. All this findings are similar to various observations reported in literature [6, 8–10].

Unlike the case presented in Fig. 4, the sequence presented in Fig. 5 spans over 11.3 ms. The flow is highly three-dimensional and transient with strong spanwise velocities. In this sequence, rapid wing rotation also happens at the end of the upstroke. The methodology implemented in this study can be advanced further to capture the out-of-plane motion, i.e., the spanwise evolution of the flow, by building a Schlieren imaging setup placed orthogonal to the existing setup. Three-dimensional image reconstruction can then be applied further to developing the vortical structures. Nevertheless, the existing method presented in this study provides additional qualitative details as presented in Fig. 5, which highlights the presence of vortices developed during the upstroke; the change in nature of vorticity during rapid wing rotation; the LEV developing on the leading edge during the downstroke and the vortex shed at the end of the upstroke.

(a)

(b)

(c)

(d)

(e)
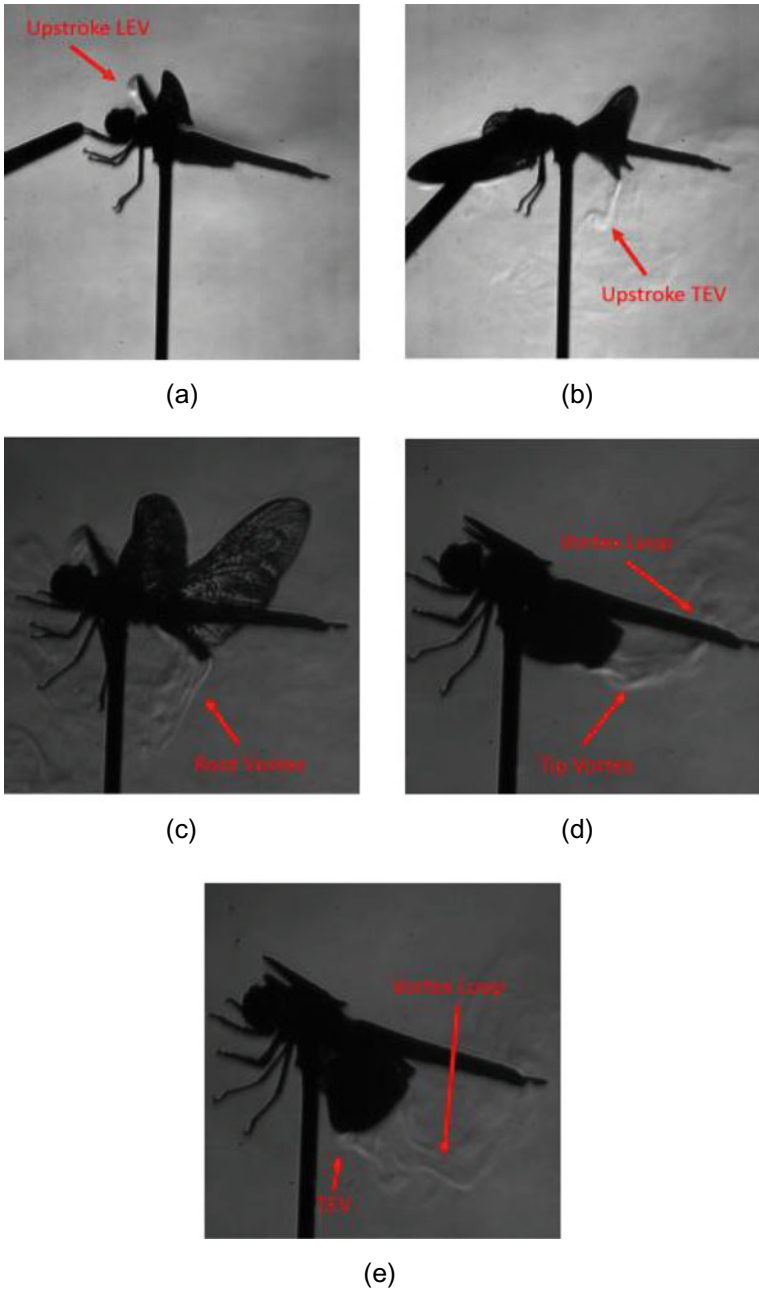
Fig. 2 Vortical structures in the near field

Fig. 3 Schlieren image captured during a flap cycle
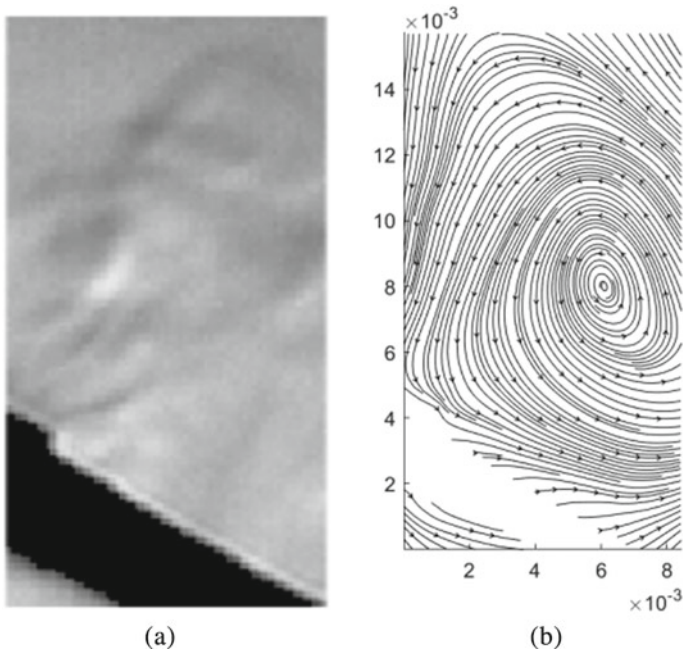
Fig. 4 a Masked image of ROI; **b** Streamlines obtained using the physics-based optical flow technique

(a) t = 0 ms

(b) t = 3 ms

(c) t = 4.67 ms

(d) t = 6.3 ms

(e) t = 9.3 ms

(f) t = 11.3 ms

-1000   -500   0   500   1000
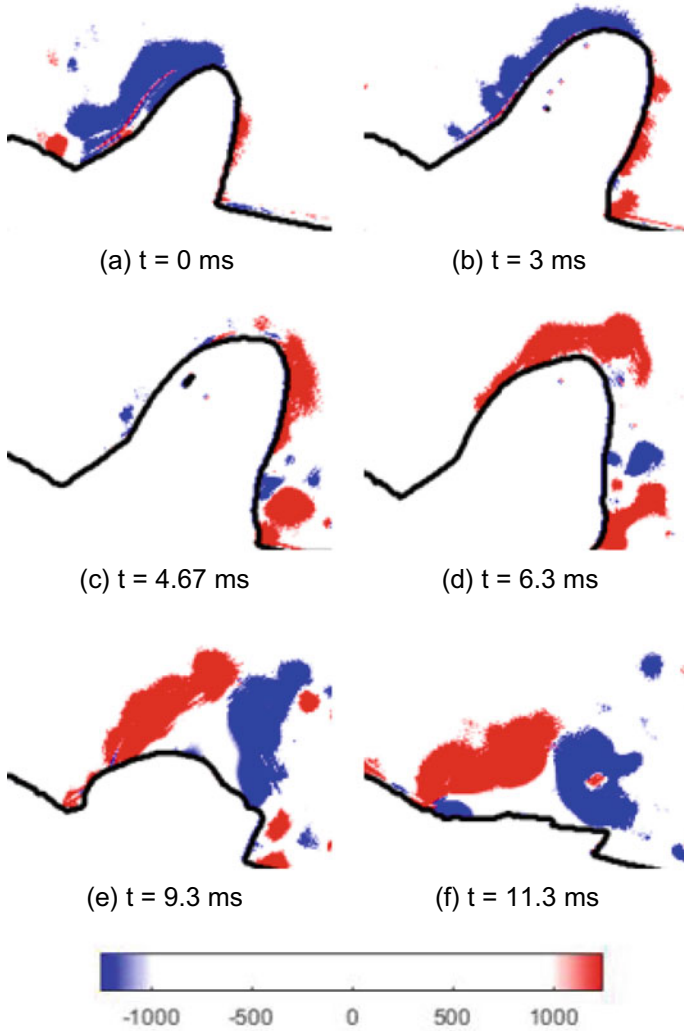
Fig. 5 Vorticity contour over a wing in motion

4 Conclusions

High-speed Schlieren imaging of the flap cycle of a Pantala flavescens highlights vortical structures developing on the wing and the near-field region. This method can give great insights into the wing-wake and wing-wing interactions also. These details can help better interpret the force measurement tests. It is demonstrated that the Schlieren approach is not limited to flow visualization, but implementing the physics-based optical flow method can quantify the flow field. This can help identify vortices

and vorticity regions associated with the wing kinematics. The Schlieren method, though limited in the case of highly three-dimensional cases, is still demonstrated in this study how this can help understand the aerodynamics associated with the flight of a dragonfly.

Ethical Clearance Authors had obtained approval from the Institute animal ethics committee (IAEC of IIT Kharagpur) for performing the experiments on dragonflies. For the purposes of this paper, no dragonflies were harmed, and all of them were released back to their habitat in IIT Kharagpur.

References

1. Norberg RÅ (1975) Hovering flight of the dragonfly Aeschna juncea L., kinematics and aerodynamics. In: Swimming and flying in nature. Springer, pp 763–781
2. Weis-Fogh T (1973) Quick estimates of flight fitness in hovering animals, including novel mechanisms for lift production. J Exp Biol 59(1):169–230. ISSN: 0022-0949, 1477-9145
3. Rayner JM (1999) Estimating power curves of flying vertebrates. J Exp Biol 202 (Pt 23):3449–3461
4. Taylor HG, Waldram JM (1933) Improvements in the Schlieren method. J Sci Instrum 10(12):378
5. Settles GS (2001) Schlieren and shadowgraph techniques: visualizing phenomena in transparent media. Springer Science & Business Media, p 20180198
6. Liu Y et al (2018) Schlieren photography on freely flying hawkmoth. Biol Lett 14(5)
7. Liu T, Shen L (2008) Fluid flow and optical flow. J Fluid Mech 614:253–291
8. Christoffer Johansson L et al (2013) Multiple leading edge vortices of unexpected strength in freely flying hawk-moth. Sci Rep 3(1):1–5
9. Hedenstrom A, Christoffer Johansson L (2015) Bat flight: aerodynamics, kinematics and flight morphology. J Exp Biol 218(5):653–663
10. Hefler C et al (2020) Aerodynamic performance of a free-flying dragonfly—a span-resolved investigation. Phys Fluids 32(4):041903

Smoke Flow Visualization of Dragonfly *Pantala Flavescens* in Tethered Flight

Kumar Sanat Ranjan, Amit Ashok Pawar, Arnab Roy, and Sandeep Saha

Abstract Dragonflies use unsteady mechanisms, like leading-edge vortex (LEV) and trailing-edge vortex (TEV), to generate high lift in a few wing beats to perform flight maneuvers and hunt smaller insects. We qualitatively study flow field and topology using smoke flow visualization and high-speed imaging over dragonfly species *Pantala flavescens*. We observed LEV, TEV, stagnation point, saddle point, and a vortex loop in the wake formed by the interaction of LEV and TEV. We observe that LEVs remain attached to the wings at very high angles of attack due to active control of the flexibility of the wings.

Keywords Dragonfly · Smoke flow visualization · LEV · TEV · Vortex loop

1 Introduction

Dragonflies are very agile fliers; they can perform typical maneuvers, e.g., hovering, gliding, turning, and long-distance flying during migration. Their different flying modes can be categorized as follows [16]:

(1) Gliding: no wing beating
(2) Hovering: wings beat in counterstroke, i.e., forewings and hindwings are 180° out of phase
(3) Cruising: wings beat in 90° phase difference and
(4) Turning: wings beat in phase.

Dragonflies use different types of lift-generating mechanisms depending on the requirement, and they are termed; (1) classical, (2) supercritical, (3) vortices, and (4) vortex shedding [16]. Classical lift is required to remain afloat in the air, and it is the lift associated with circulation. A supercritical lift is a very high lift generated for a short period. It is generated using very short strokes with the wing oriented above the critical angle. The attached vortices on the wings enhance the steady-state

K. S. Ranjan (✉) · A. A. Pawar · A. Roy · S. Saha
Department of Aerospace Engineering, IIT Kharagpur, Kharagpur, West Bengal 721302, India
e-mail: ranjan.sanat@iitkgp.ac.in

lift. The shed vortices interact with the hindwings to produce extra lift. Dragonflies use unsteady phenomena like leading-edge vortex (LEV) to generate high lift, which contributes significantly to lift generation during flight [5]. While LEV is formed, a peak is observed in the lift [4]. During the flight, at the leading edge, the flow separates over the wings and reattaches before the trailing edge, forming an LEV. A 2-D experimental analysis by Dickinson and Gotz [8] has estimated that flow generally separates at an angle of attack above 9°. LEV is a separation structure that is open U-shaped and spans from the tip of the wing on one side to the tip of the wing on another side, passing over the thorax. At tips, tip vortices are formed, and between tips, the axis of LEV is parallel to the wing leading edge [19]. Besides translational mechanisms, dragonflies rotate their wings in specific ways to generate lift. Pronation is the sharp rotation of wings at the end of the upstroke. Similarly, the rotation at the end of the downstroke is called supination [3]. These rotations of the wings keep the angle of attack positive in both upstroke and downstroke, resulting in lift generation in both strokes [17]. In the present paper, we use smoke flow visualization to understand the aerodynamics associated with dragonflies from a qualitative perspective. We also describe flow topology using critical points formed in the flow field [18, 19].

2 Methodology

2.1 Smoke Flow Generation Setup

Smoke flow visualization experiments were performed in the low-speed, open-return wind tunnel at the Aerodynamics laboratory, IIT Kharagpur. A smoke flow setup was developed to create a sheet of smoke that can be passed over the dragonfly wing to visualize the flow field, which was illuminated using a 500 W halogen light source. A 3000 W, 20,000 cfm fog generator was used for generating the smoke. It uses water and glycerol-based fluid for smoke generation. For the injection of smoke into the wind tunnel, a symmetric airfoil-shaped smoke injector was used (Fig. 1). At the trailing edge of the airfoil, several small-diameter stainless steel tubes were fixed. These tubes were connected to a pipe that ran through the span of the airfoil carrying smoke. Direct feeding of smoke into the pipe induces turbulence, evident in the flow at the exit of the smoke generator. Two settling chambers were used upstream of the pipe to eliminate incoming turbulence, and a blower was used to maintain the feed of smoke. The smoke is first passed through one of the settling chambers, reducing the smoke generator's incoming turbulence. Then the blower sucks the smoke out and feeds it to the other settling chamber, which reduces the turbulence generated by the blower, and then it is fed to the pipe inside the smoke injector. This arrangement helped in creating a streamlined sheet of smoke.
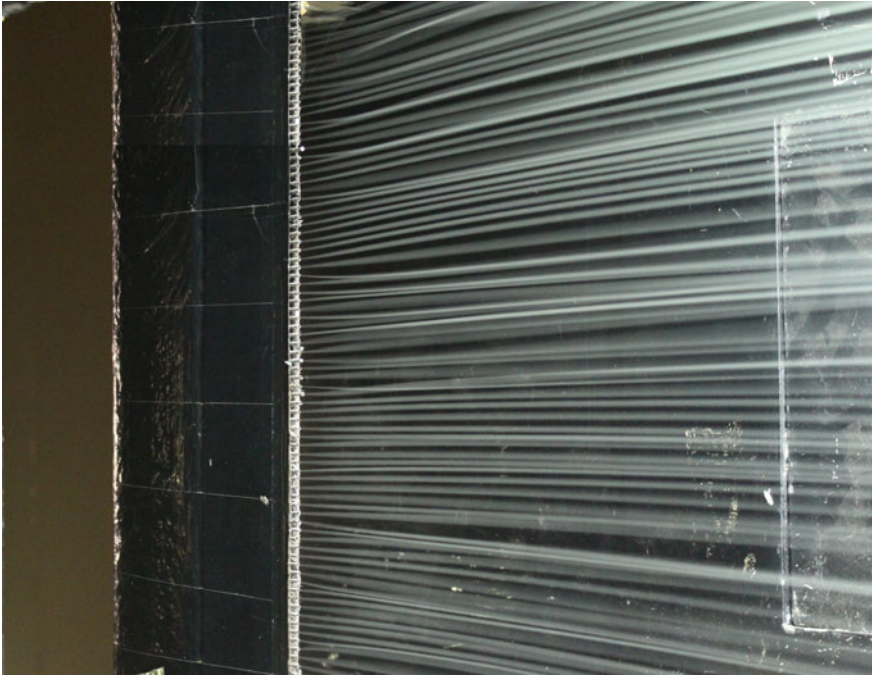
Fig. 1 Smoke coming out in the free stream

2.2 *Dragonfly Capturing and Flow Visualization in Wind Tunnel*

Dragonfly, *Pantala flavescens*, for the experiments, was captured at the IIT Kharagpur campus; at the beginning of the monsoon, they are abundantly available. Experiments were carried out on the same day as of capture. Dragonflies were sedated by putting them in a refrigerator, a usual practice for sedating dragonflies [11]. Dragonfly was tethered to a 2.5 mm rod at its thorax using cyanoacrylate adhesive [19]. The flow velocity for the experiments was 2 m/s. The flow field was visualized using a Photron AX50 high-speed monochrome camera. The images were acquired at 500fps.

3 Results and Discussion

3.1 Smoke Flow Visualization Over Dragonfly

Smoke flow visualization is an excellent experimental tool for capturing the flow field generated by insects, which can help understand aerodynamics associated with their flight. It has been suggested that the lift generated by the dragonflies and other insects can be explained using conventional aerodynamics with attached flows [1, 2, 20], with the assumption that the lift coefficient is in the similar range as for the dragonfly wings measured in steady flows [10, 13, 14, 20]. However, even if conventional aerodynamics can explain the lift generation to some extent, it certainly does provide enough evidence of dragonflies not using unconventional aerodynamics [19]. Smoke flow gives qualitative insight into the actual flow. The topological information in qualitative and quantitative flow visualizations are the same [7, 15]. Smoke is introduced into the flow field, where flow structures are formed due to vorticity. Smoke acts as a passive tracer in the flow and generates the flow structures as they form. Identifying critical points using smoke visualizations can provide insight into local analytical solutions to the Navier–Stokes equations. This identification can help understand different flow separation types, and their link to the formation of the LEV [6, 19]. Interpretation of smoke visualization needs utmost care as depending on the flow being steady or unsteady, it can be taken as streamlines or only streaklines [19]. In the present, smoke flow visualization is done on a tethered live dragonfly. Two sets of image capturing were done during the work, and analysis of those images provides excellent insight into dragonfly aerodynamics.

3.2 Flow Over Non-flapping Dragonflies

Figure 2a shows the flow around the stationary insect when the flow hits the wing at the midpoint. Some vortices can be seen in the wake of the non-flapping wings; these are periodic and form a Karman vortex street. This vortex pattern indicates that wings offer resistance to the flow by maintaining some angle of attack. Formation of the such pattern shows that steady flow over static insect wings, like flat plates, can get separated at low angles of attack, and the angles can even be less than $2°$, positive or negative [9, 21]. The separated flows are time-dependent, and shear layer instabilities make the wake oscillates, resulting in Karman vortex street formation [19]. In Fig. 2b, in the wake of the wings, the smoke lines are symmetrical, and the flow is attached, which indicates that the wings are at zero or very close to zero angles of attack. In Fig. 2b, it can be seen that the freestream flow is not disturbed even as the hindwing is fully stretched, indicating that the dragonfly actively controls its wing position even when it is not flapping.

(a) Karman Vortex Street   (b) No flow disturbance
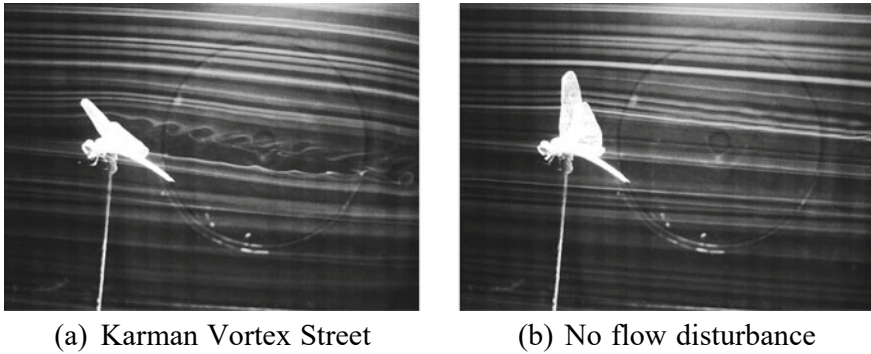
Fig. 2 Smoke flow over Dragonfly during non-flapping

## 3.3   Locating Critical Points in Smoke Flow Visualization

Figures 3 and 4 show sequence of images of smoke flow over tethered dragonfly. The dragonflies are in flapping mode and various critical points formed are evidently visible and identified. The critical points visible here are the stagnation point and the saddle point. A critical point in a flow field can be seen only when individual smoke lines impact exactly at a critical point, which is luckily happening in this case. Smoke particles are advected with the flow; hence, if there is a bifurcation of the smoke line, it indicates splitting of the streamline at that point [19]. At the critical point, the smoke line bifurcates, the slope of the streamline is undefined, and the velocity of the flow is: smoke line bifurcation are markers of the position and nature of a critical point [19]. In Fig. 3, green arrows show stagnation points. Stagnation points are one of the simplest critical points to identify as it appears in the form of bifurcation in the smoke lines. It forms when a smoke line impacts the wings or the insect head and in the wake of reattachment location of the LEV near the trailing edge. The blue arrows in the figure show the LEVs on the forewing and hindwing. The LEV on the forewing can be seen attached even when there is a quick rotation of the wing.

Figure 4 shows another critical point in the flow topology, the saddle point, pointed by yellow arrows. A saddle point is created by the interaction of downwash and upwash of LEV formed and shed in the downstroke of consecutive flap cycles [19].

LEVs form whenever there is a sharp increase in the angle of attack of the forewings and the hindwings. Similarly, a sharp decrease in the angle of attack results in vortex shedding [19].
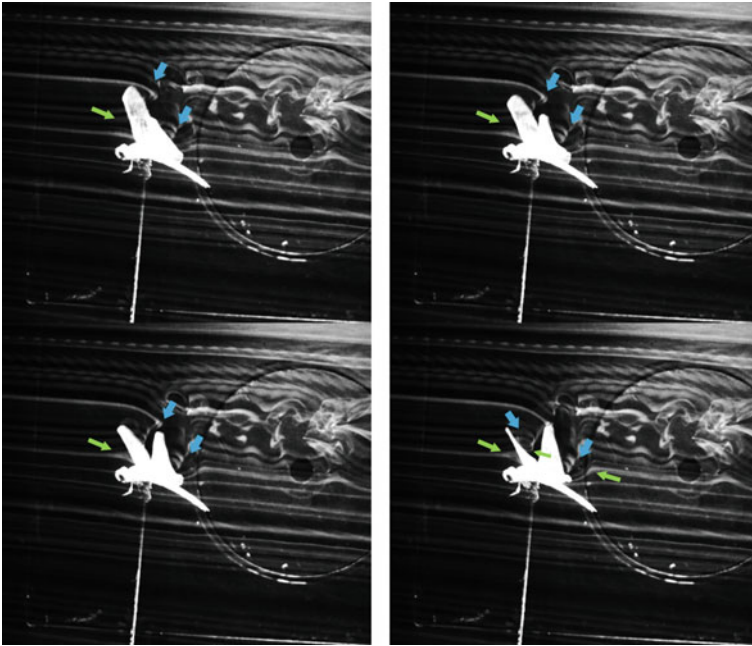
**Fig. 3** Stagnation point in smoke flow over dragonfly
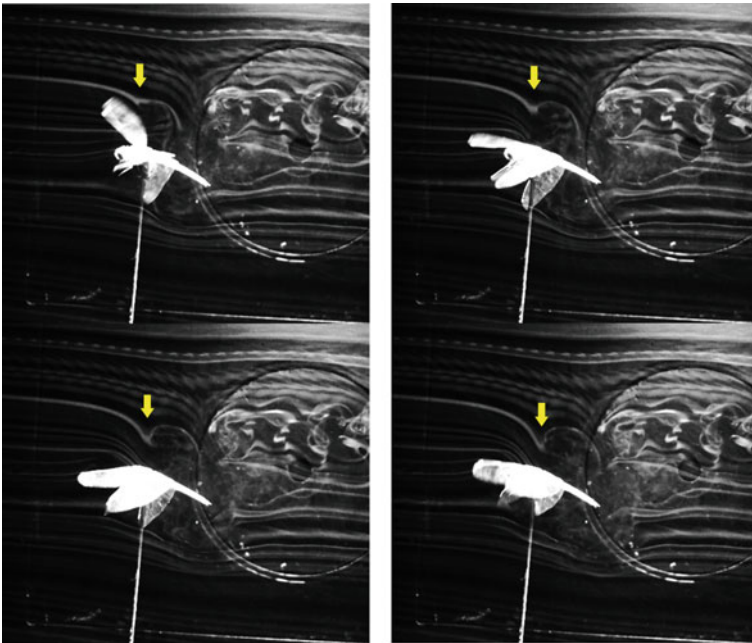
Fig. 4 Saddle point in smoke flow over dragonfly

3.4 Leading-Edge Vortex and Trailing-Edge Vortex Formation

Figure 5 shows the formation of the leading-edge vortex (LEV) over the forewing of the dragonfly as it undergoes the flap cycle, indicated by blue arrows. As the wing starts downstroke, it moves down and forward, and a circulation is created, resulting in the formation of an LEV. The LEV grows as the wing moves and remains attached to the wing until it reverses and starts upstroke. This attachment of LEV at such high angles explains the generation of high amounts of lift in dragonflies. LEV formation can also be seen on the hindwing as marked by blue arrows. Also, it can be seen that the forewing and hindwing are counter-stroking, indicating that it is trying to create a forward cruising motion [16]. The LEV formation, growth, and stabilization are dependent on angle of attack. Dragonflies change the angle of attack slowly while translating and rapidly during wing rotation.

In Fig. 6, the trailing-edge vortex (TEV) shedding from the forewing at the start of a downstroke can be seen; red arrows indicate it. As the upstroke ends and the wing pronate to start the downstroke, it sheds a vortex in the wake from its trailing edge.

Figure 7 shows the development of a pair of counter-rotating vortices consisting of a shed TEV (red arrow) and a shed LEV (blue arrow) from the hindwing of the
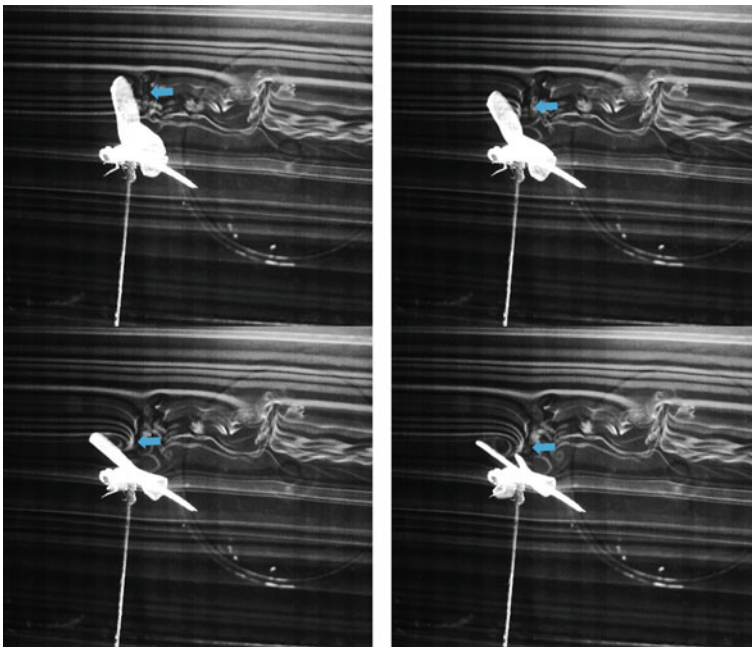
Fig. 5 LEV formation in smoke flow over dragonfly
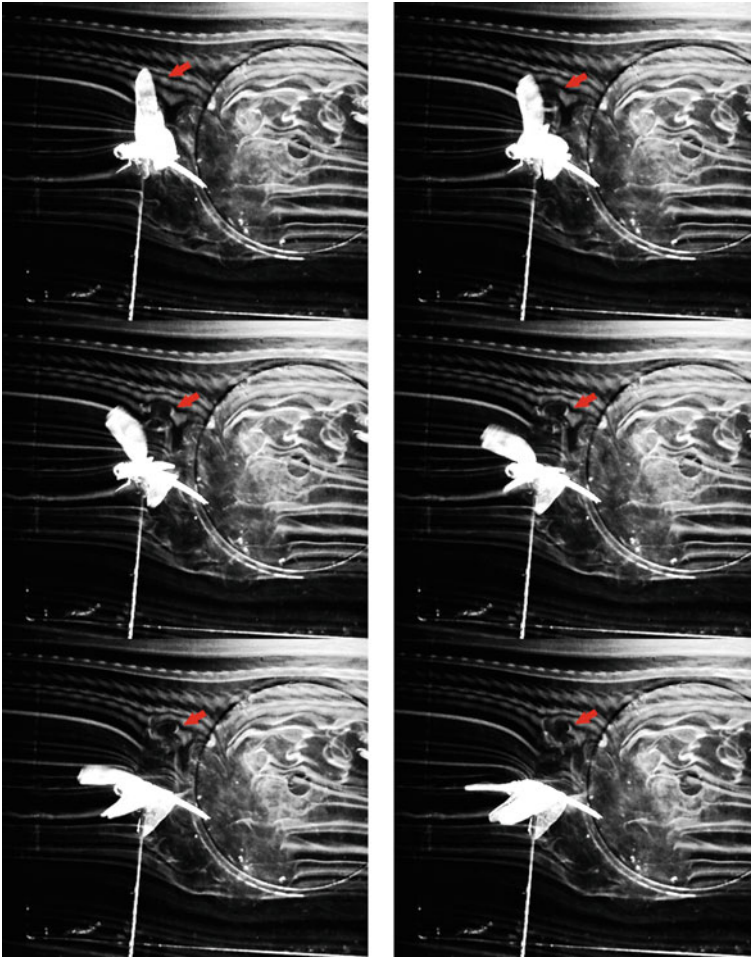
Fig. 6 TEV in smoke flow over dragonfly

dragonfly. At the start of the downstroke, the hindwing sheds a TEV of counter-clockwise sense, which travels downstream and grows. During the downstroke, an LEV is formed over the hindwing, which gets shed at the start of the upstroke. The rotation sense of the LEV is counter-clockwise. The shed vortex moves downstream and grows to form a vortex loop with the earlier shed TEV. The vortex loop observed here is not limited to dragonflies, but it has also been observed in hawkmoths [12]. Figure 7 also shows the shedding of TEV from and formation of LEV on the forewing. Also, green arrows point to the various stagnation points in the flow field.
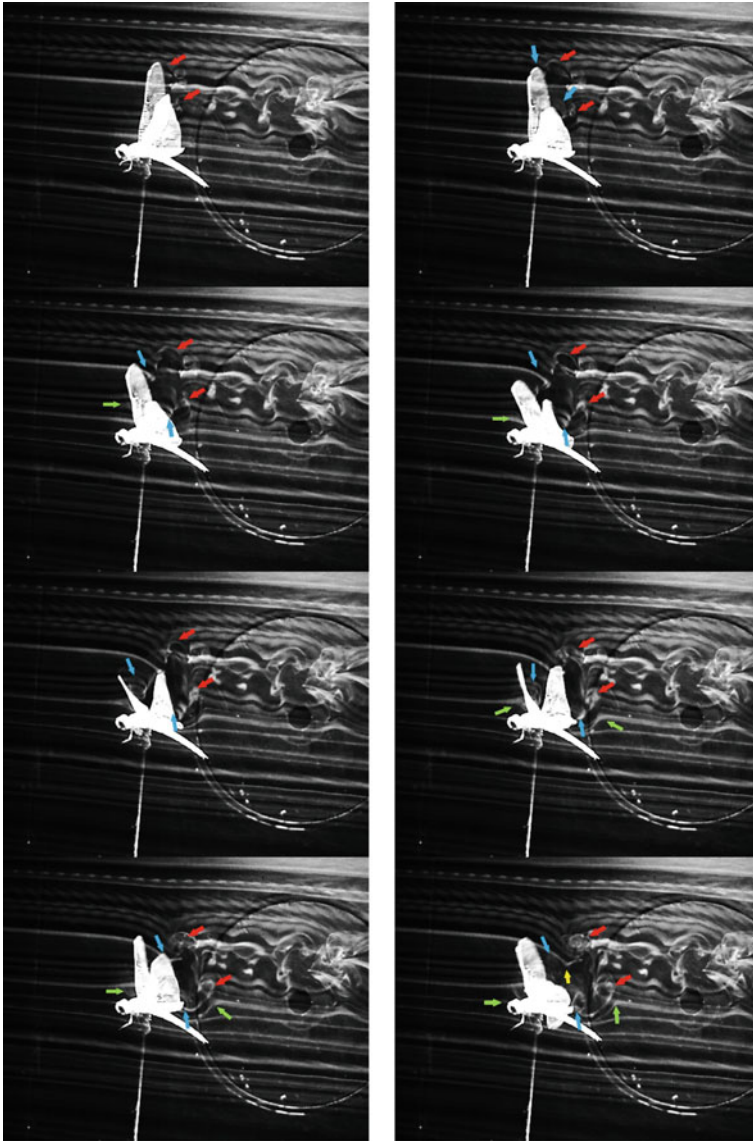
Fig. 7 Vortex loop in smoke flow over dragonfly

4 Conclusions

From the high-speed imaging of smoke flow over the tethered dragonfly, we get a good insight into flow topologies, such as the formation of LEV and TEV which are critical in explaining the lift generation in insect flight.

From the flow structures, we could identify critical points of the flow field, which represent local analytical solutions of the Navier–Stokes equation. We also identified

a vortex loop which seems to be an integral part of the flow field in the wake of at least large insects, as it has been observed for dragonflies and hawkmoths.

Ethical Clearance
Authors have obtained approval from the Institute animal ethics committee (IAEC of IIT Kharagpur) for the experiments on dragonflies. For the purposes of this paper, no dragonflies were harmed, and all of them were released back to their habitat in IIT Kharagpur.

References

1. Azuma A, Watanabe T (1988) Flight performance of a dragonfly. J Expir Biol 137:221–252
2. Azuma A, Azuma S, Watanabe I, Furuta T (1985) Flight mechanics of a dragonfly. J Exp Biol 116(1):79–107
3. Bergou AJ, Xu S, Jane Wang Z (2007) Passive wing pitch reversal in insect flight. J Fluid Mech 591:321–337
4. Birch JM (2003) The influence of wing-wake interactions on the production of aerodynamic forces in flapping flight. J Exp Biol 206(13):2257–2272
5. Bomphrey RJ, Lawson NJ, Harding NJ, Taylor GK, Thomas ALR (2005) The aerodynamics of Manduca sexta: digital particle image velocimetry analysis of the leading-edge vortex. J Exp Biol 208(Pt 6):1079–1094
6. Chong MS, Perry AE, Cantwell BJ (1990) A general classification of three-dimensional flow fields. Phys Fluids A: Fluid Dyn 2(5):765–777
7. Délery JM (2001) Robert Legendre and Henri Werlé: toward the elucidation of three-dimensional separation. Ann Rev Fluid Mech 33(1):129–154
8. Dickinson MH, Gotz KG (1993) Unsteady aerodynamic performance of model wings at low Reynolds numbers. J Exp Biol 174(1):45–64
9. Katz J, Plotkin A (2001) Low-speed aerodynamics, vol 13. Cambridge University Press
10. Kesel AB (2000) Aerodynamic characteristics of dragonfly wing sections compared with technical aerofoils. J Exp Biol 203(Pt 20):3125–3135
11. Li Q, Zheng M, Pan T, Su G (2018) Experimental and numerical investigation on dragonfly wing and body motion during voluntary take-off. Sci Rep 8(1):1–16
12. Liu Y, Roll J, Van Kooten S, Deng X (2018) Schlieren photography on freely flying hawkmoth. Biol Lett 14(5):20180198
13. Newman BG (1977) Model tests on a wing section of an Aeschna dragonfly. In: Scale effects in animal locomotion
14. Okamoto M, Yasuda K, Azuma A (1996) Aerodynamic characteristics of the wings and body of a dragonfly. J Exp Biol 199(Pt 2):281–294
15. Perry AE, Chong MS (1987) A description of eddying motions and flow patterns using critical-point concepts. Ann Rev Fluid Mech 19(1):125–155
16. Rowe RJ, Tree of life web project: dragonfly flight
17. Sane SP (2003) The aerodynamics of insect flight. J Exp Biol 206(Pt 23):4191–4208
18. Srygley RB, Thomas ALR (2002) Unconventional lift-generating mechanisms in free-flying butterflies. Nature 420(6916):660–664
19. Thomas ALR, Taylor GK, Srygley RB, Nudds RL, Bomphrey RJ (2004) Dragonfly flight: free-flight and tethered flow visualizations reveal a diverse array of unsteady lift-generating mechanisms, controlled primarily via angle of attack. J Exp Biol 207(Pt 24):4299–4323
20. Wakeling JM, Ellingtion CP (1997) Dragonfly flight I. Gliding flight and steady-state aerodynamic forces. J Exp Biol 200:543–556
21. Werlé H et al (1974) Le tunnel hydrodynamique au service de la recherche ae´rospatiale

3D-PTV Measurements
of an Axisymmetric Synthetic Jet

Kamal Raj Sharma, Malkeet Singh, Jyoti Gupta, and Arun K. Saha

Abstract The present study aims to measure the volumetric flow field of a circular synthetic jet using three-dimensional particle tracking velocimetry (3D-PTV). The statistical flow characteristics of the synthetic jet have been discussed using ensemble-averaged velocities and their fluctuations. The 3D-PTV data is compared with the 2D-PIV data for the same formation number. The jet width is different in both cases, which owes to the difference in the orifice configuration in the two measurement cases. The streamwise velocity and root mean square velocity dominates the flow owing to the induced velocity of the vortex rings. The transverse velocity and its fluctuations are more than the vertical velocity and its fluctuation. The time evolution of the circular vortex ring has also been shown for two actuation cycles using isosurfaces plots of the normalized vorticity magnitude, which infers that the induced velocity of the vortex ring remains nearly the same throughout the flow field. The streamwise turbulence decreases along the downstream direction, but the ring loses its coherence in the far field due to persisting vertical and transverse turbulence.

Keywords Synthetic jet · Vortex ring · Three-dimensional particle tracking velocimetry (3D-PTV) · Ensemble average · Vorticity magnitude

Nomenclature

υ	Kinematic viscosity of water [m^2/s]
U_o	Average blowing velocity [m/s]
f_a	Actuation frequency [Hz]
T	The time of an actuation cycle s
L	Formation number –
f	Acquisition frequency [Hz]

K. R. Sharma (✉) · M. Singh · J. Gupta · A. K. Saha
Department of Mechanical Engineering, IIT Kanpur, Kanpur 208016, India
e-mail: ksharma1@me.iitr.ac.in

D	Diameter of the synthetic jet orifice [mm]
U, V, W	Streamwise, vertical, and transverse velocity [m/s]
$U_{rms}, V_{rms}, W_{rms}$	Root mean square streamwise, vertical, and transverse velocities [m/s]
$\overline{\omega}, \omega$	Ensemble-averaged and instantaneous vorticity magnitude [1/s]
ω/ω_{max}	Normalized instantaneous vorticity magnitude –
Q/Q_{max}	Normalized Q-criteria –

1 Introduction

The synthetic jet produces a train of vortex rings, a complex three-dimensional flow with many engineering applications like modifications of bluff body aerodynamics, control of lift and drag of airfoils, reduction of skin friction in planar boundary layers, and heat transfer enhancement [1–4]. A synthetic jet is produced by an alternating fluid suction and ejection from an orifice maintaining a zero net mass flux but transferring linear momentum to the surrounding fluid. The jet is formed entirely from the fluid in which it is employed. Hence, the actuator can be integrated into the flow surface without needing extra fluid supply, making it feasible for external and internal flow control. The synthetic jet actuator contains an orifice on one side and a diaphragm on the other side of a cavity. There are a few performance factors of the actuator based on the given application, like maximum jet velocity, jet spreading rate, and mass flow rate.

A flow starts to form around the orifice edge when the diaphragm starts to move. The initially thin boundary layer separates at the nozzle edge, causing a vortex to spiral up and forms a closed vortical structure called vortex ring by entraining surrounding irrotational fluid. As the diaphragm stops pushing the fluid the induced velocity of the vortex ring advects the ring downstream. The synthetic jet flow is dominated by three regions [5], first is the near field which is dominated by the formation and advection of the time-periodic vortex rings. Characteristic length scale and celerity of the discrete vortex rings depend upon the orifice size, amplitude, and period of the diaphragm motion. The impulse the diaphragm provides to the vortex ring should be larger than the suction and frictional forces. The second region is a transitional region in which the vortex rings entrain the ambient fluid, and the third is a far-field region in which the vortex rings slow down, lose coherence as they break down into smaller vortical structures, and eventually, the flow becomes turbulent.

2   Literature Review and Objective

Many studies have revealed the flow structure of the circular synthetic jet both experimentally and numerically. It has been shown that the axisymmetric synthetic jet development and evolution of vortex rings are mainly affected by two primary dimensionless numbers, namely stroke length and Reynolds number [6], as shown in Eqs. 1 and 2, respectively, where U_o is the time-averaged expulsion velocity over one actuation cycle, shown in Eq. 3. At the same time, the Stokes number and Strouhal number determine the formation criteria of the synthetic jet, shown in Eqs. 4, 5, and 6. K is the jet formation constant of 0.16 for axisymmetric synthetic jets [7].

$$L = \frac{L_o}{D} = U_o/f_a D \tag{1}$$

$$Re = U_o D/\upsilon \tag{2}$$

$$U_o = \frac{1}{T} \int_0^{T/2} u(t)\mathrm{d}t \tag{3}$$

$$St_K = D\sqrt{\frac{f_a}{\upsilon}} \tag{4}$$

$$St = \frac{f_a D}{U_o} \tag{5}$$

$$\frac{1}{St} = \frac{Re}{St_k^2} > K \tag{6}$$

Apart from the actuation and fluid parameters, the effect of geometrical parameters on the performance of the synthetic jet has also been studied in the literature. The effect of orifice shape, edge configurations, orifice depth, and cavity size significantly impacts the evolution of the vortex rings. The higher aspect ratio of the orifice gives rise to the phenomenon of axis-switching and bifurcation [8, 9]. The other geometric parameters also affect the maximum jet exit velocity [10].

Among the experimental methods used in the literature to characterize the flow phenomenon of the synthetic jet, planar particle image velocimetry (2D-PIV) has been extensively used. The planar-PIV measuring technique offers several benefits, like non-intrusive flow field measurement in an instant, but it has also been noted in the literature that it overestimates a few turbulent flow properties [11]. Additionally, the light sheet illumination determines the particle's out-of-plane location in both classic planar and stereoscopic PIV approaches. Since a volumetric flow measurement technique illuminates the volume so the depth position of the particle cannot be assumed. Three-dimensional flow structures of the synthetic jet have been

reported using stereoscopic PIV in the literature recently [12, 13]. The evolution of circular and non-circular vortex rings has been shown in these studies. Volumetric studies on the flow problem are very rare. 3D-PTV offers more accuracy and spatial resolution than cross-correlation-based volumetric flow measuring techniques like tomographic PIV [14]. The present study enriches the experimental database with the 3D-PTV measurement of a circular synthetic jet showing various three-dimensional flow parameters.

2.1   Materials and Methods

The present study was conducted in the water tunnel facility in the Department of Mechanical Engineering, IIT Kanpur. The synthetic jet was installed in a rectangular quiescent water tank of $1000 \times 500 \times 500$ mm. The cavity of the synthetic jet, having an inner diameter of 70 mm, was fixed at the center of one side of the tank, as shown in Fig. 1. The diaphragm was attached to one side of the cavity, and the orifice plate was on the other. The diaphragm was actuated with a cam-follower arrangement powered by a brushless DC motor. The orifice plate has an outer diameter of 90 mm and a thickness of 2 mm. The orifice was extended up to the nearest possible field of view of the cameras by a nozzle of 70 mm and inner diameter, $D = 8$ mm. The Reynolds number based on U_o (average blowing velocity per actuation cycle) and D was kept at 1075. All the non-dimensional numbers related to the study are shown in Eqs. 1–6, and their concerned values in the study are shown in Table 1. The non-dimensional numbers used in the study ensure the proper vortex roll-up as the value of $Re/St_k{}^2$ (Eq. 6) in the present study is higher than the jet formation constant for the axisymmetric jet case. The actuation frequency (f_a) of the synthetic jet was kept at 5.6 Hz.

The 3D-PTV experimental setup consisted of three Phantom VEO 340 L cameras (2560×1600 pixels) fitted with 135 mm Zeiss lenses. The cameras were arranged in a linear array, as shown in Fig. 1, and focused on the measurement volume with a nominal magnification of 0.44. The capture rate was kept at 25 Hz. The cameras were positioned using a 2D traverse system (ISEL, Germany) to capture the field of view with half resolution (1280×800 pixels). Polyamide tracer particles were used with a mean diameter of 50 μm. A dual head Nd: YLF laser (Photonics DM-50-527DH) was used as the illumination source, which passed through a light arm and a series of light sheet optics that created illumination volume.

The final measurement volume of the overlapped cameras was $60 \times 40 \times 40$ mm. The laser and cameras were synchronized with a synchronizer (610036) with a timing precision of 250 ns. The calibration was performed by traversing a single plane calibration target using a 1D traverse at 21 different positions spaced 2 mm apart in the depth of the measuring volume. The mapping functions for projections and back projections were obtained. The calibration image processing and 3D-PTV were accomplished using INSIGHT V3V-4G software. The two independent image frames were separated by a short time interval ('Δt') equal to 3000 μs in the present study.
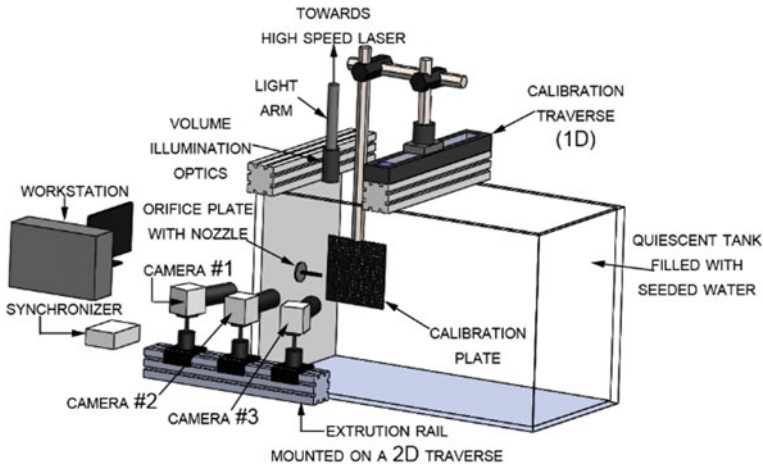
Fig. 1 Schematic of the experimental setup

Table 1 Important flow parameters of the study

Important parameters	Value
Formation number (L)	2.73
Characteristic velocity (U_o in m/s)	0.12
Reynolds number (Re, based on U_o and D)	1075
Stokes number (St_k)	19.84
Strouhal number (St)	0.37

The ensemble-averaged 3D vectors were obtained using 50 instantaneous fields. A total of $30 \times 20 \times 19$ vectors were obtained in the X, Y, and Z directions after velocity interpolation with 50% overlap, giving the spatial resolution of 2 mm. The projection error of less than 1 pixel was observed from calibration for all three apertures, along with a mean dewarping error of fewer than 20 μm.

Figure 2a shows the evolution of all three non-dimensional velocity components over the experimental time. Nearly ten cycles of the synthetic jet were captured. The streamwise velocity (U) plot shows the periodic behavior occurring at the actuation frequency of the synthetic jet actuator ($f_a = 5.6$ Hz), as shown in the FFT of the streamwise velocity (U) in Fig. 2b. The vertical (V) and transverse (W) velocity components show marginal fluctuations.
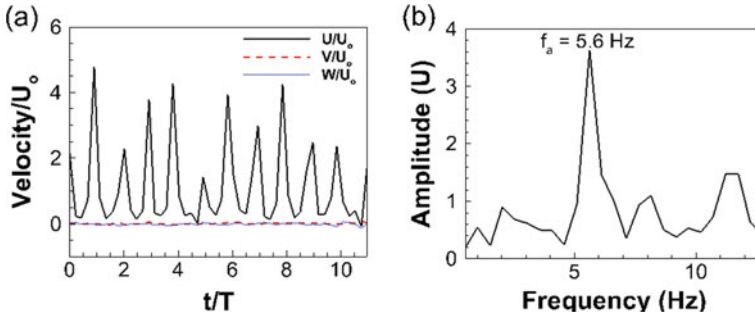
Fig. 2 **a** Temporal evolution of non-dimensional velocity components (U, V, and W) obtained near the jet orifice at $X/D = 1.25$, $Y/D = Z/D = 0$ and **b** FFT of the streamwise velocity (U)

3 Results and Discussion

3.1 Ensemble-Averaged Flow Field

The present section shows the ensemble-averaged 3D vector field of an axisymmetric synthetic jet with $L = 2.73$ and Re $= 1075$ for 50 instantaneous flow fields obtained using 3D-PTV. The origin ($X/D = Y/D = Z/D = 0$) of the 3D vector flow field is taken at the nozzle orifice. The comparison of the 2D-PIV and 3D-PTV data for the nearly same formation number but two different Reynolds numbers has been shown in Fig. 3. The data obtained from the two measurement techniques have been compared for two streamwise locations, $X.D = 2$ and 6. It can be seen from the figure that the velocity profiles do not agree as far as the jet width is concerned. This may be because the 2D-PIV data is for planar orifice configuration, whereas 3D-PTV data is for the extended nozzle case. The vortex roll-up at the exit of the orifice is different in both cases. Hence, there is a difference in the jet spread. However, the velocity extents fairly match both the techniques, and the near jet discrepancies are due to the difference in the Reynolds number in the two cases.

Figure 4a compares ensemble-averaged non-dimensional streamwise and vertical velocities obtained from 2D-PIV and 3D-PTV along the centerline in the downstream direction. The velocities obtained from both techniques agree, but the 3D-PTV data shows early decay of the vortex ring at $X/D = 5$. The streamwise velocity obtained by 3D-PTV shows a few peaks as the vortex ring develops on its size and self-induced velocity due to statistically dependent data. During this period, the vortex ring entrains more ambient fluid and increases the mass flow rate. After reaching the maximum, the mass flow rate slowly decreases due to viscous dissipation of the ring and eventually reduces to zero far downstream. The centerline vertical velocity remains almost constant up to $X/D = 2.2$ and becomes slightly negative, then remains constant. The negative centerline velocity has a negligible magnitude to cause flow asymmetry. Figure 4b shows the ensemble-averaged non-dimensional streamwise and vertical velocity fluctuations in the downstream directions obtained from the
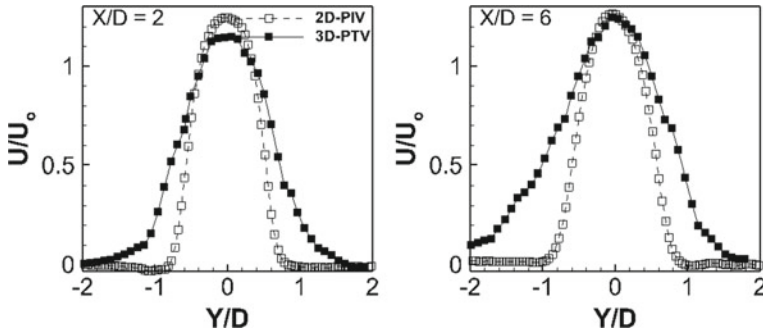
Fig. 3 Comparison of ensemble-averaged 2D-PIV ($L = 2.6$ and Re $= 470$) and 3D-PTV ($L = 2.73$ and Re $= 1075$) data of circular synthetic jet at two downstream locations

two measurement techniques. The velocity fluctuation is higher in the case of 3D-PTV may be because of the higher Reynolds number. The streamwise flow fluctuation reaches a peak at a similar streamwise location to the first peak of the streamwise centerline velocity due to the maximum entrainment of the surrounding fluid. The vertical flow fluctuation increases initially and remains nearly constant throughout the downstream location.

Figure 5 shows the non-dimensional velocity components in the *XY* plane at $Z/D = 0$ for (a) streamwise and (b) vertical velocities and (c) streamwise and (d) transverse velocities in the *XZ* plane at $Y/D = 0$. The corresponding non-dimensional standard deviation in the velocities is also shown in the figure for three streamwise locations $X/D = 2$, 4, and 6. The streamwise velocity and streamwise root mean square velocity is almost similar in both the *XY* and *XZ* planes, as seen in the figure. The maximum streamwise velocity remains the same along the streamwise direction, but the jet width increases streamwise. Whereas the streamwise root mean square velocity decreases along the streamwise direction. The results are in accordance with the literature showing mitigation of the normal and shear stresses along the
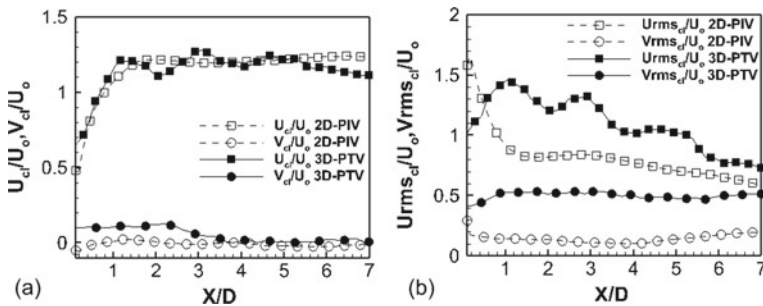
Fig. 4 Ensemble-averaged **a** non-dimensional streamwise and vertical velocity and **b** non-dimensional streamwise and vertical velocity fluctuations obtained along the centerline in *XY* plane at $Z/D = 0$

streamwise direction [12]. The transverse velocity (W) is more than the vertical velocity (V) in the near jet region. However, in the far jet region, both velocities are comparable. The transverse velocity fluctuation dominates the vertical velocity fluctuation, as noticed in the figure.
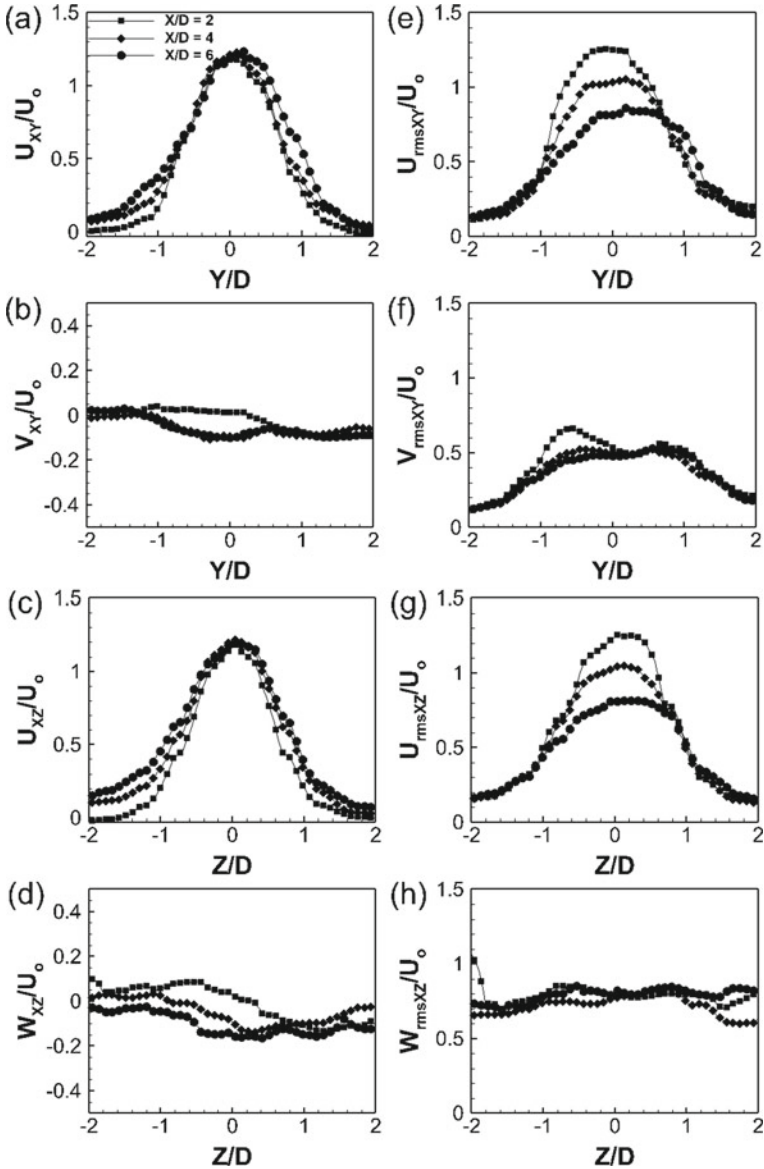
Figure 6 shows the ensemble-averaged non-dimensional vorticity magnitude distribution on three YZ planes at $X/D = 0.5$, 3.5, and 7. The spatial changes in the structure of the vortex ring can be seen in the figure. Near the orifice location ($X/D = 0.5$), the vortex ring starts developing by entraining the surrounding fluid. Hence, there is a non-uniformity in the plane. Whereas, at the mid-volume location or origin location ($X/D = 3.5$), the vortex ring gains its coherence showing the uniform vortex strength along the vortex core. At the exit of the measurement volume ($X/D = 7$), the vortex ring diffuses in the radial direction, and the surface of the ring shows dissipation, due to which the vortex ring loses its coherence.

### 3.2 Instantaneous Flow Structures

The instantaneous topology of a vortex ring is shown in Fig. 7 at $t/T = 0.225$, along with the three-dimensional velocity field. The isosurfaces of non-dimensional streamwise velocity (Fig. 7a) show that the jet is nearly axisymmetric. Figure 7b presents the isosurfaces of the normalized vorticity magnitude $\left(\frac{\omega}{\omega_{\max}} = 0.4\right)$, which defines the structure of the vortex ring. The cross section of the vortex is shown in Fig. 7c, with the streamwise velocity on the YZ plane located at $X/D = 3.1$. The figure also shows the trail of a vortex ring that just crossed the measurement volume. The vortex ring topology has also been presented using normalized Q-criterion $\left(\frac{Q}{Q_{\max}} = 0.01\right)$. The positive value of the criterion represents the vortex roll-up of the ring due to circulation filtering the shear effects.

Figure 8a–e shows the five consecutive instantaneous Z-vorticity fields in the XY plane at $Z/D = 0$. The areas of intense vorticity represent the location of the vortex ring. The vorticity of the ring is higher near the orifice, as seen in Fig. 8a, but as the vortex ring evolves, its vortex strength decreases downstream and remains limited to the ring core region, as seen in the far field of Fig. 8d. The possible reason for this is persisting vertical and transverse turbulence, as shown in Fig. 5, due to which the vortex ring loses its coherence. The complete cycle of the vortex ring evolution can be seen in the figure. It can also be noticed from the figures that the celerity of the vortex ring remains nearly the same as it advects downstream as the distance covered by the ring in the near orifice region is nearly the same as in the far stream region.

Figure 9 depicts the normalized vorticity magnitude isosurfaces (value 0.4) for the reconstructed flow structures of the circular synthetic jet shown in Fig. 9a–e. The vorticity field is normalized by the maximum value of the vorticity magnitude. One actuation cycle of a vortex ring evolution has been shown in Fig. 9a–e, where all the instantaneous reconstructions are 0.04 s ($t/T = 0.225$) apart. One cycle of the synthetic jet is nearly $T = 0.18$ s; hence, almost four instantaneous flow fields have

Fig. 5 Ensemble-averaged non-dimensional velocity component plots in the *XY* plane at *Z*/*D* = 0 for **a** streamwise and **b** vertical velocities and non-dimensional **c** streamwise and **d** transverse velocities in the *XZ* plane at *Y*/*D* = 0; along with the corresponding standard deviations of the velocity components at the three streamwise locations *X*/*D* = 2, 4, and 6
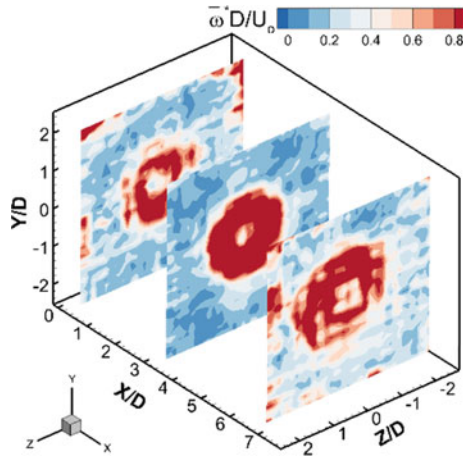
Fig. 6 Ensemble-averaged non-dimensional vorticity magnitude ($\overline{\omega}D/U_o$) distribution on three *YZ* planes at $X/D = 0.5$, 3.5, and 7
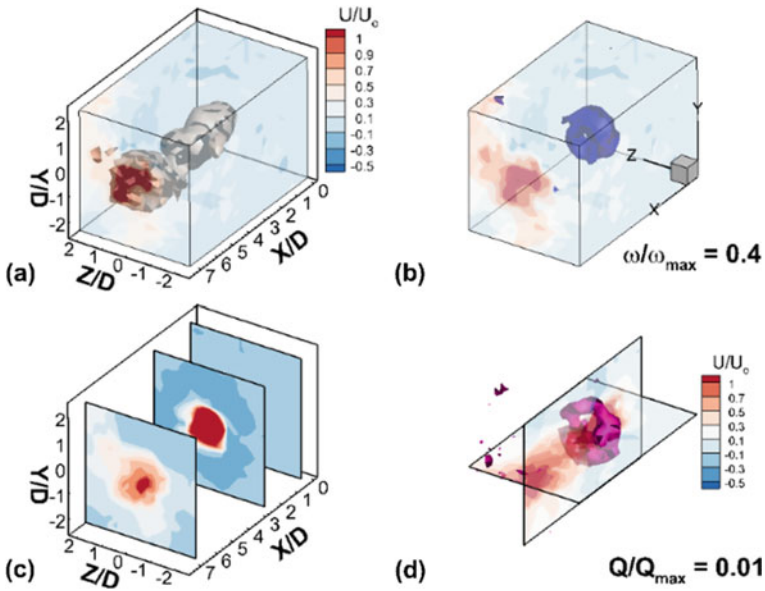
Fig. 7 Instantaneous vortex ring topology ($t/T = 0.225$) shown as **a** isosurfaces of non-dimensional streamwise velocity, **b** isosurface of normalized vorticity magnitude $\left(\frac{\omega}{\omega_{max}} = 0.4\right)$, **c** non-dimensional streamwise velocity at three different *YZ* planes, and **d** isosurfaces of normalized Q-criterion $\left(\frac{Q}{Q_{max}} = 0.01\right)$
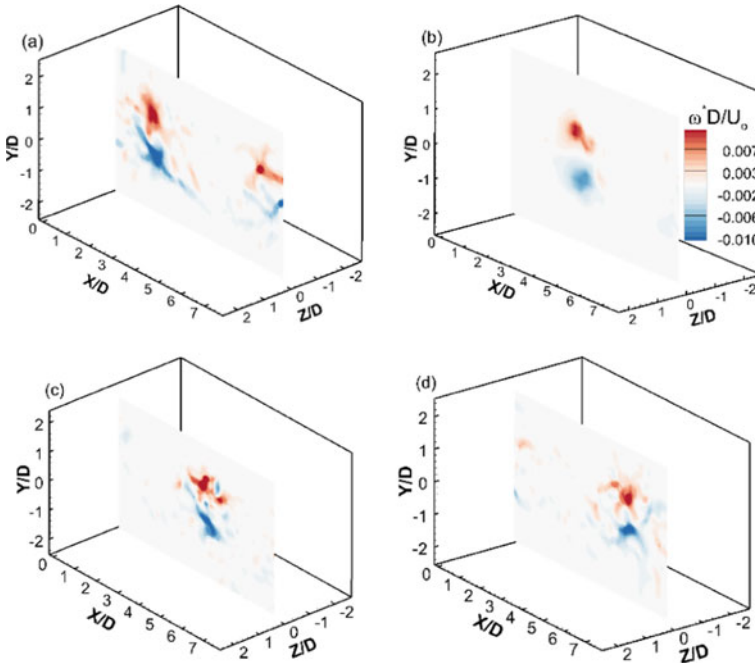
Fig. 8 Instantaneous non-dimensional spanwise vorticity ($\omega_z D/U_o$) for five consecutive fields for $L = 2.73$ and Re = 1075: **a** $t/T = 0$ s; **b** $t/T = 0.225$; **c** $t/T = 0.45$; **d** $t/T = 0.67$

been captured per cycle in this study. It can be seen from the figures that the vortex rings remain parallel to the nozzle plane. The vortex ring remains unchanged in the near jet region and loses coherence in the far jet region, as shown in Fig. 9d, e which owes to persisting vertical and transverse turbulence. The two successive vortex rings can also be seen in Fig. 9a, e. The distance between the two successive vortex rings is constant, which owes to the fixed formation number ($L = 2.73$). Figure 10a–c shows the evolution of the vortex ring with time for another actuation cycle. The vortex ring remains unchanged during the advection up to mid-measurement volume. The ejection of another vortex ring from the synthetic jet orifice and its evolution with time can also be seen in Fig. 10d, e.

4 Conclusions

The 3D-PTV experiment was carried out to investigate an axisymmetric synthetic jet flow for the formation number (L) = 2.73 and Re = 1075. The ensemble-averaged velocity line graphs followed the conventional velocity profiles of the circular synthetic jet. The similarities and differences in the velocity profiles obtained from the 3D-PTV and 2D-PIV measurement techniques have been presented for the
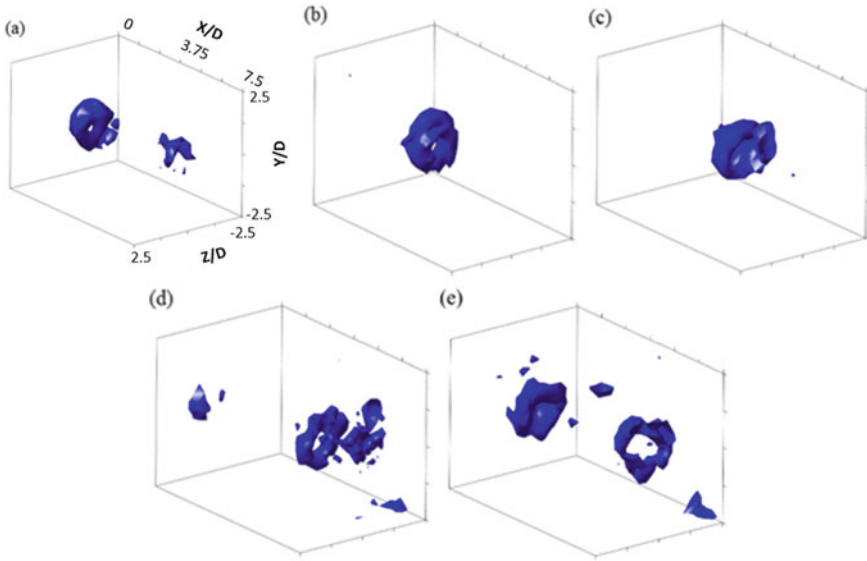
Fig. 9 Evolution of the circular synthetic jet vortex ring, illustrated by the isosurfaces of normalized vorticity magnitude ($\omega/\omega_{max} = 0.4$) for $L = 2.73$ and Re = 1075: **a** $t/T = 0$; **b** $t/T = 0.225$; **c** $t/T = 0.45$; **d** $t/T = 0.67$; **e** $t/T = 0.90$
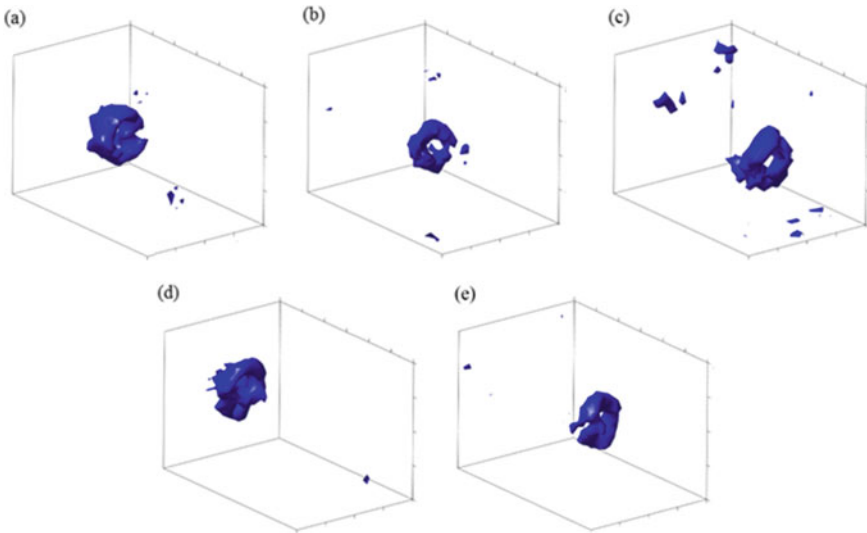
Fig. 10 Evolution of the circular synthetic jet vortex ring, illustrated by the isosurfaces of normalized vorticity magnitude ($\omega/\omega_{max} = 0.4$) for $L = 2.73$ and Re = 1075: **a** $t/T = 5.28$; **b** $t/T = 5.5$; **c** $t/T = 5.84$; **d** $t/T = 6.06$; **e** $t/T = 6.5$

same stroke length. The streamwise velocity showed similar magnitude and variations along the streamwise direction both in *XY* and *XZ* planes. The present study showed the importance of three-dimensional flow measurements as the magnitude of the transverse velocity (*W*) (which is generally ignored in the 2D flow measurements) was found to be more than that of the vertical velocity (*V*). The transverse root mean square velocity was also found to dominate the vertical root mean square velocity. The evolution of reconstructed instantaneous vortex rings with time was also shown in the study with the help of isosurfaces of normalized vorticity magnitude for two actuation cycles. The streamwise dissipation of the vortex rings was noticed in the far flow field, which owed to the persisting vertical and transverse turbulence along the downstream. The limitation of the study was the spatial resolution of the 3D vector field owing to the medium particle density of raw images.

References

1. Feng LH, Wang JJ (2014) Modification of a circular cylinder wake with synthetic jets: vortex shedding modes and mechanism. Eur J Mech B: Fluids 43:14–32
2. You D, Moin P (2008) Active control of flow separation over an airfoil using synthetic jets. J Fluids Struct 23:1349–1357
3. Smith DR (2002) Interaction of synthetic jet with crossflow boundary layer. AIAA J 40(11):2277–2288
4. Chaudhary M, Puranik B, Agarwal A (2010) Heat transfer characteristics of synthetic jet impingement cooling. Int J Heat Transf 53(5):1057–1069
5. Glezer A, Amitay M (2002) Synthetic jets. Annu Rev Fluid Mech 34:503
6. Glezer A (1988) The formation of vortex rings. Phys Fluids 31(12):3532–3542
7. Holman R, Utturkar Y, Mittal R, Smith BL, Cattafesta L (2005) Formation criteria for synthetic jets. AIAA J 43(10):2110–2116
8. Krishnan G, Mohseni K (2009) An experimental and analytical investigation of rectangular jets. J Fluids Eng 131:121101
9. Wang L, Feng LH, Wang JJ, Li T (2017) Parametric influence on the evolution of low-aspect-ratio rectangular synthetic jets. J Visualization 21:105
10. Jain M, Puranik B, Agarwal A (2011) A numerical investigation of effects of cavity and orifice parameters on the characteristics of a synthetic jet flow. Sens Actuators A 165:351–366
11. Panigrahi PK, Schroeder A, Kompenhans J (2008) Turbulent structures and budgets behind permeable ribs. Exp Therm Fluid Sci 32(4):1011–1033
12. Wang L, Feng LH, Wang JJ, Li T (2018) Characteristics and mechanism of mixing enhancement for noncircular synthetic jets at low Reynolds number. Exp Therm Fluid Sci 98:731–743
13. Shi XD, Feng LH, Wang JJ (2019) Evolution of elliptical synthetic jets at low Reynolds number. J Fluid Mech 868:66–96
14. Kähler CJ, Scharnowski S, Cierpka C (2012) On the uncertainty of Digital PIV and PTV near walls. Exp Fluids 52(6):1641–1656

On Hydrodynamics of Dry Granulation of LD/BOF Slag Using Spinning Disc Atomizer: Choice of Experimental Methodology

D. S. Kushan, G. Chakraborty, B. Maiti, S. K. Dash, A. K. Samantaray, and S. K. Singha

Abstract The iron and steel industry produces a waste product called slag. The Dry Spinning Disc Granulation (DSDG) process has been experimentally tried, widely, for the granulation of Blast Furnace (BF) slag with the recovery of heat from the high temperature slag. To study this phenomenon, the fabrication of an experimental setup, of the scale of laboratory level, has been done in the institute of the authors. Various experiments were performed on the setup. Stage-wise modifications were performed on the experimental setup on the basis of the limitations found in the previous stages of the experimental setup. In this paper, the methodology, that was adopted to perform the experiments in literature has been studied. Further, the methodology chosen for the current experimental setup has been discussed with each system, its subsystem, and the respective components. Finally, the chosen methodology for the current experimental setup has been compared with the methodologies of the experimental setups stated in the literature. The use of the current experiment methodology has been satisfactorily justified with reference to the literature surveyed. The Air Flow System (AFS) is a novel system that has been used in the current experimental setup of Spinning Disc Atomization (SDA).

Keywords Experimental hydrodynamics · Dry spinning disc granulation (DSDG) · Linz-Donavitz/basic oxygen furnace (LD/BOF) slag · Spinning disc atomizer (SDA) · Two phase flow · Experimental methodology

D. S. Kushan (✉) · G. Chakraborty · B. Maiti · S. K. Dash · A. K. Samantaray
Department of Mechanical Engineering, IIT Kharagpur, Kharagpur 721302, India
e-mail: dskushan@iitkgp.ac.in

S. K. Singha
Assam Energy Institute (Centre of Rajiv Gandhi Institute of Petroleum Technology), Sivasagar 785697, India

1 Introduction

The LD/BOF slag, in its granulated form, has many applications in construction industry, as reviewed by Das et al. [1], like roads, railway track ballasts, road stones, etc. Two broadly classified methods of slag granulation, as discussed by Jahanshahi et al. in 2011 [8] and in 2012 [7], are wet and dry granulation methods. Between these, the Dry Slag Granulation (DSG) methods, as discussed by Zhou et al. [24] and Li et al. [14], are currently under rigorous research, because it is advantageous, when compared on the basis of environmental aspects.

Of all the DSG methods, Centrifugal Granulation methods, discussed by Rutland and Jameson [17] and Eisenklam [4] are relatively economical. The Spinning Disc Atomization (SDA), studied by Dixon et al. [3], Emslie et al. [5], Kamiya and Kayano [9], Frost [6], Kawase and De [10], Purwanto et al. [16], Wang et al. in 2014 [20] and in 2016 [19], Dhirhi et al. [2], Wu et al. [22], Wang et al. [21] and Peng et al. [15], among the Centrifugal Granulation methods, is the most plain and uncomplicated process. This is because the fabrication of a disc is convenient.

The process of SDA is such that liquid slag, in its hot molten state, is slowly dropped over a high-speed spinning disc. After this, the molten slag flows outwards from the centre because of the force in the centrifugal direction and surface tension. The working process of atomization could be simply described as, slag spins out a thin film over the disc surface. This expands from the edge of the disc, radially. Researchers have used high-speed photography to show that the slag, in its hot molten state, initially, flows over the disc surface as a film. This film, at the edge of the disc, disintegrates into equal diameter bodies of liquid shaped like fingers or regular involute branches of liquid. These branches are called ligaments, as discussed by Wu et al. [23], Peng et al. [15] and Sahoo et al. [18]. In the end, the formed ligaments disintegrate and, due to the action of shearing stresses due to the flow of air, form droplets. The analytical modelling of this phenomenon has been performed by Kushan et al. [11].

To study this phenomenon, the fabrication of an experimental setup, of the scale of laboratory level, has been done in the institute of the authors. Various experiments were performed on the setup. Stage-wise modifications were performed on the experimental setup, on the basis of the limitations found in the previous stages of the experimental setup.

In this paper, the methodology, that was adopted to perform the experiments, in literature, has been studied. Further, the methodology, chosen for the current experimental setup, has been discussed, with each system, its subsystem and the respective components. Finally, the chosen methodology for the current experimental setup has been compared with the methodologies of the experimental setups stated in the literature.

In the ultimate industry prototype, slag, in its hot molten form, strikes the spinning disc. Further, the slag spreads on the disc surface, radially, in the outward direction. Moreover, when the slag reaches the edge, due to centrifugal force, it is thrown out of the disc. In an optimum speed of rotation of disc and an optimum rate of flow of

liquid, ligament-formation mode occurs and the slag, as ligaments, come out of the disc. In the end, the slag might hit the outer vessel walls.

2 Experimental Methodologies in Literature

In this section, the experimental methodologies stated in the literature have been discussed in detail.

2.1 Methodology of Frost [6]

In 1981, Frost [6] studied the phenomenon of rotary atomization occurring in the ligament formation mode.

He used aqueous solutions of glycerol and Agral surfactant, a proprietary wetting agent, as the working liquid. It is also mentioned that he used a feed tube to feed the liquid over the rotating disc.

He used Aluminium Alloy as the material for the disc. Thickness of the disc was taken as 6 mm. A 45 degrees bevel was added to the disc edge. The disc diameters, considered, were 40, 60, 80, 100 and 120 in mm. A central well was designed on the disc with diameter 8 mm and depth 0.5 mm. This central well was effective in accommodating slight eccentricities in position of feed tube. The use of an electric motor and a rubber belt has also been stated to rotate the disc.

Short duration spark photography, a high-speed photography technique, developed by Lake [13], has been used in this experiment. In this, camera, digital timer, Fresnel condensing lenses, Spark unit, Turner flash unit and Xenon tubes have been used.

2.2 Methodology of Kawase and De [10]

Kawase and De [10], in 1982, studied ligament-type disintegration pertaining to non-Newtonian fluid for the SDA process.

They used a compressor, feed tank, valve and nozzle to deliver the liquid over the rotating disc.

A stainless steel disc of 100 mm diameter was used. The disc edge has a bevel of 45 degrees. A variable speed DC motor with a V-belt has been used to rotate the disc.

Camera and micro-flash has been used for photography.

2.3 Methodology of Wang et al. [19]

In the year 2016, Wang et al. [19] investigated the dynamics of ligament formation of thin film of viscous liquid at the edge of a spinning disc. They have accurately defined three systems in their experimental setup. These include the Liquid Supply System, the Atomizing System and the Controlling System.

The Liquid Supply System includes pump, storage tank, valve, flow-meter, collector, connecting tubes and a circular nozzle of Nominal Diameter = 8 mm.

The Atomizing System consisted of two different discs of diameters 0.05 and 0.1 m and thickness 4 mm. The discs were of AISI 304. The Ra observed was 1.6 microns and the roundness range was 0.025 mm.

The Controlling System included the high-speed camera, additional light source, data receiver and computer. The camera used was Phantom V7.3. The acquisition frame rate was 4000 fps. The resolution, considered, was 800 × 600 pixels.

2.4 Methodology of Dhirhi et al. [2]

Later, in the same year, Dhirhi et al. [2] studied the dry granulation unit experimentally for its regimes of operation and analysed the size of particles and a potential of scale up.

The liquid that they used was the Rosin–Paraffin (RP mixture) with mass ratio 4:1. A PID controller was used to control the flow of the liquid and deliver it through an outlet. An enclosure was made so that the RP mixture does not spill off and the samples are not lost. The enclosure was made of MS. The top portion was cylindrical with diameter, 1000 mm, and height, 150 mm. The bottom portion of the enclosure was a frustum. The frustum had an upper diameter of 1000 mm, a lower diameter of 160 mm and height, 180 mm. The cylinder and the frustum were welded together at lower end of the cylinder. The top edge of the cylinder was covered with an MS sheet, with an opening diameter of 500 mm.

Three aluminium discs were chosen of thickness 10 mm each. The diameters of these discs were chosen as 60, 75 and 90 mm. An aluminium shaft of diameter 30 mm and height 18 mm was chosen. A motor with a Variable Frequency Drive (VFD) controller was used to rotate the shaft and, in turn, the disc.

The data was collected after the experiment was done, i.e. after the RP mixture solidified.

2.5 Methodology of Wu et al. [22]

Wu et al. [22] chose 2017 to report the experiment of centrifugal granulation of slag in a cold-type experiment using the rotary atomizer and studied the impact

of configuration of atomizer on droplets formed. The setup was, distinctly, divided into three systems, namely the Liquid Supplier, the Granulation System and the Visualization System.

The Liquid Supplier was stated to be consisting of pipes and pump.

The Granulating System comprised of rotary atomizers, shaft and electric motor.

The Visualization System consisted of a high-speed video camera, LED light and computer. The camera used was the i-Speed TR, Olympus.

2.6 Methodology of Wang et al. [21]

Wang et al. [21], in the same year, investigated, experimentally, the disintegration of slag particles in ligament formation mode in an SDA. The experimental setup had, noticeably, three systems, Working Medium Heating and Supply System,[1] Granulation System and Controlling System.

The Working Medium Heating and Supply System used a melting pot to melt the RP mixture of mass ratio 4:1.

The Granulation System consisted of spinning disc, AC motor and frequency converter.

The Controlling System had a high-speed camera, additional light source, data receiver and computer. The high speed camera used was Phantom Miro M320S.

2.7 Methodology of Peng et al. [15]

In 2018, Peng et al. [15] studied the molten slag granulation of the ligament-type for various configurations of the rotating disc. The experimental setup was, conveniently, divided into three systems, the Liquid Supply System, the Granulation System and the Visualization System.

The Liquid Supply System consisted of a fusion pot, electric heater, valve, ultrasonic flow-meter and connecting tubes. The liquid used was RP mixture of mass ratio 4:1.

The Granulation System had 8 different rotary discs, with different surface configurations. AISI 304 was chosen as the material for the disc. Thickness of the disc was 3 mm. AC powered motor with a frequency converter was used to rotate the disc.

The Visualization System included a high-speed camera and a cold light source. The high-speed camera chosen was Phantom Miro R320S with an Acquisition rate of 1700 fps. The resolution, chosen for videography, was 1024×1024.

This literature survey is limited to the available and accessible literature, mainly focusing on Spinning Disc Atomizer for slag granulation. Hence, the experimental

---

[1] The authors named the system as 'Working Medium Heated and Supply System'.

methodology of other types of atomizers and other types of granulators, however significant, have not been considered.

Motivated by the experimental methodology used in the above stated literature, the methodology of the current work of the authors has been chosen.

3   The Current Experimental Methodology

In this section, the chosen methodology of the experimental setup, fabricated by the authors of the current study in their laboratory, has been discussed in detail.

3.1   Detailed Methodology of the Experimental Setup

The experimental setup comprises various systems. Each of the systems comprises various components. The system and its respective components will be enlisted here.

- Liquid Flow System (LFS)

The LFS, as the name suggests, is the system in the experimental setup that engages in the flow and the measurement of liquid flow in the experiment. The schematic of LFS could be seen in Fig. 1.

It has the following components:

- Liquid Re-circulation Tank (LRT)
- Centrifugal pump
- Nozzle
- Measuring tank.

The liquid, from the LRT, is pumped and allowed to strike onto the rotating disc through a nozzle. The rotating disc, then, spreads the liquid towards the container vessel. The liquid, then, flows to the measuring tank via flexi-pipes. Further, the liquid drops into the LRT via gravity when the control valve is opened.

Fig. 1 Schematic of the Liquid Flow System (LFS)
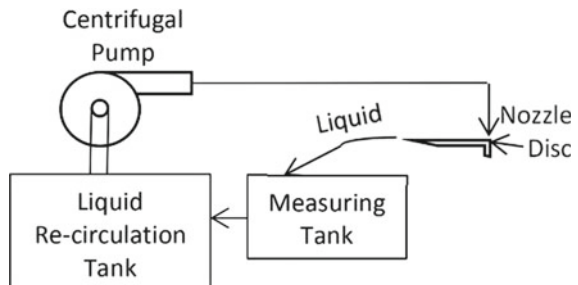
Table 1 Properties of Wacker Metroark DM Silicone Fluid 50 M CTSK

Property	Value	Unit
Kinematic viscosity (at 25 °C)	50	$mm^2 s^{-1}$
Dynamic viscosity (at 25 °C)	48	mPa s
Density at (25 °C)	0.96	$g\ cm^{-3}$
Surface tension (at 25 °C)	20.8	$mN\ m^{-1}$
Refractive index (at 25 °C)	2.71	–

Fig. 2 Schematic of the air flow system (AFS)

The working liquid, chosen, is Wacker 50 CST Silicone oil. The properties have been mentioned in Table 1.
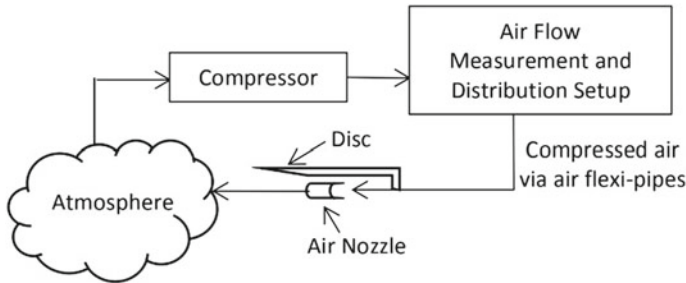
- Air Flow System (AFS)

Similarly, the AFS is the system in the experimental setup that indulges in the flow and the measurement of air flow in the experiment, from the atmospheric air to the compressed air in the system. The schematic of AFS could be seen in Fig. 2.

The AFS has the following components:

- Compressor
- Air Flow Measurement and Distribution Setup (AFMDS)
- Air nozzles.

The air, from the atmosphere, is compressed. Then, the compressed air is transferred to the Air Flow Measurement and Distribution Setup (AFMDS). The schematic of the AFMDS has been shown in Fig. 3.

The AFMDS has the following components:

- Rotameter
- Air Distributor Block (ADB).

AFMDS, as the name suggests, constitutes of a Flow Measurement Subsystem (FMS), which is a rotameter here, and a Flow Distribution Subsystem (FDS), which is the Air Distributor Block (ADB).

Fig. 3 Schematic of the air flow measurement and distribution setup (AFMDS)
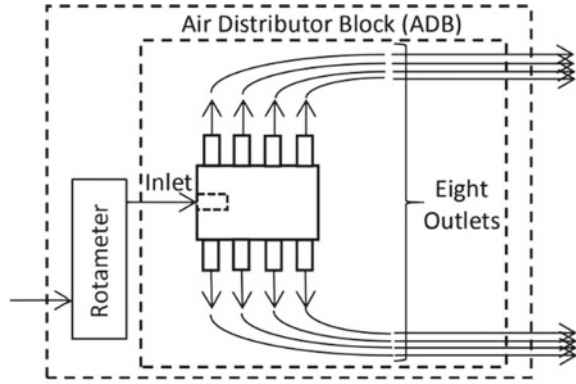
The air nozzles are positioned under the spinning disc, in the direction parallel to the surface of the disc and the direction of the nozzle making an angle of inclination with the direction of the tangent of the circular edge of the disc.

- Disc Rotation System (DRS)

The LFS and the AFS are the systems that carry the fluids: the liquid, and the atmospheric air, in compressed form in the system, respectively. The DRS, on the other hand, is the electro-mechanical system of our experimental setup. As the name suggests, this is the system that powers and controls the rotation of disc. The schematic of DRS could be seen in Fig. 4.

The MSS is the electrical subsystem. The AC power source is used to rotate the motor shaft. The variac is used to control the rotary speed of the motor and hence, the disc.

- Rotating Disc Subsystem (RDS)

The RDS has the following components:
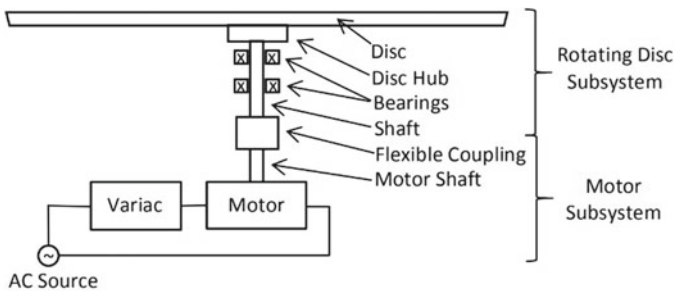
- Disc
- Disc hub

Fig. 4 Schematic of the disc rotation system (DRS)

- Bearings
- Shaft.

The RDS is the mechanical subsystem.

- Flexible coupling

The motor shaft rotates the coupling, which is a flexible coupling. The coupling is the unit that joins the MS and the RDS and combines them together to form the electromechanical system, the DRS. The flexible coupling has been used to transmit rotary power from motor shaft to the disc shaft.

- Tachometer System (TS)

The TS has the following components:

- AC source
- Proximity sensor
- Display.

An NPN inductive proximity sensor with a calibrated LED Indicator had been used as a tachometer or an RPM counter for the experimental setup.

- Camera-Light System (CLS)

This system, as the name suggests, incorporates the photography and video recording elements of our study and the necessary lighting for the same.
The CLS has the following components:

- AC source
- High-speed camera
- Laptop
- 1000 W Halogen light.

Phantom V7.3 camera with three (3) high-powered (70 W) LED as light source have been used for the current study.

The developments in the experimental setup, upto the current stage, have been studied by Kushan et al. [12].

After the discussion of the experimental methodology of the authors, a comparison between the old and the new is of need.

4   Comparison

In this section, the comparison between the experimental methodology discussed in the literature and the experimental methodology followed by the authors in their laboratory has been discussed.

Most of the authors in the literature have divided their experimental setup into three separate systems, naming them differently as per their choices. But, the authors

of the current work have five systems in the experimental setup. Hence, for the comparison of the systems, the systems of the authors' experimental setup need to be refined and joined together, first, so that they can be comparable.

Hence, for the same, the LFS and the AFS could be combined together to form a new head, called the Fluid Flow Head (FFH). The TS and the CLS can be combined together to form another new head, called the Data Acquisition Head (DAH). Hence, the current experimental setup has five systems. Four of these systems are under two heads and one, the DRS, is a standalone system.

The experimental setups in the literature, for SDA, have not used any provision for air blast. Hence, their FFH cuts down to LFS. Therefore, Frost [6] had an LFS that used the Glycerol-Agral aqueous solution as the working liquid, and feed tube as the delivery unit. Kawase and De [10] had an LFS which consisted of compressor, feed tank, valve and nozzle. Wang et al. [19] had an LFS, that they named as Liquid Supply System (LSS) that consisted of pump, storage tank, valve, flow-meter, collector, connecting tubes and nozzle. Dhirhi et al. [2] had an LFS that consisted of RP mixture as the working liquid, PID controller, outlet and enclosure. Wu et al. [22] had an LFS, that they termed as Liquid Supplier (LS), which comprised of pipes and pump. Wang et al. [21] had an LFS, that they called as Working Medium Heated and Supply System (WMHSS), that formed of RP mixture and melting pot. Finally, Peng et al. [15] had an LFS, that they termed as LSS, that had fusion pot, electric heater, valve, ultrasonic flow-meter and connecting tubes.

The experimental setup of the authors, in the current work, has an FFH, which consists of LFS and AFS. The LFS consists of LRT, pump, nozzle, and measuring tank with connecting pipes. The AFS consists of compressor, AFMDS and air nozzles. The AFS is the novel system of the current experimental setup.

Similarly, for the likes of DRS, Frost [6] had a disc with a central well, electric motor and rubber belt. Kawase and De [10] had a DRS consisting of a disc with a bevel, variable speed DC motor and V-belt. Wang et al. [19] had a DRS, that they named as Atomizing System (AS), consisting of two different sized discs. Dhirhi et al. [2] had a DRS consisting of three different sized discs, shaft, motor and VFD controller. Wu et al. [22] had a DRS, that they termed as the Granulating System (GS), that comprised of rotary atomizers, shaft and electric motor. Wang et al. [21] had a DRS, that they termed as Granulation System (could also be shortened to GS), consisting of a spinning disc, AC motor and frequency converter. Finally, Peng et al. [15] had a DRS, that they termed as GS, that had 8 rotary discs with different surface configurations, AC motor and frequency converter.

The experimental setup of the authors, in the current work, has DRS. The DRS consists of disc with hub, shaft, bearings, flexible coupling, motor and variac.

Additionally, for the likes of DAH, Frost [6] used Short Duration Spark Photography (SDSP) technique by Lake [13]. Kawase and De [10] had a DAH similar setup, consisting of camera and micro-flash. Wang et al. [19] had a system equivalent to the DAH, which they termed as controlling system, that comprised of high-speed camera, light source, data receiver and computer. Dhirhi et al. [2] did not have a DAH, as the data was collected post-experiment. Wu et al. [22] had a DAH-like system, which they called the Visualization System (VS), that consists of high-speed video

camera, LED light and computer. Wang et al. [21] had a DAH-like system, which they called the Controlling System (CS), that consists of high-speed camera, light source, data receiver and computer. Finally, Peng et al. [15] had a DAH-like system, which they called the VS, that consists of high-speed camera and cold light source and computer.

The experimental setup of the authors, in the current work, has DAH. The DAH consists of TS and CLS. The TS consists of proximity sensor and display. The CLS comprises high-speed camera, laptop and Halogen light.

Hence, after the study of the literature, the use of FFH as the combination of LFS and AFS, DRS and DAH as a combination of TS and CLS can be justified, satisfactorily.

5   Conclusions

The iron and steel industry produces a waste product called slag. The Dry Spinning Disc Granulation (DSDG) process has been experimentally tried, widely, for the granulation of Blast Furnace (BF) slag with the recovery of heat from the high temperature slag. To study this phenomenon, the fabrication of an experimental setup, of the scale of laboratory level, has been done in the institute of the authors. Stage-wise modifications were performed on the experimental setup on the basis of the limitations found in the previous stages of the experimental setup.

In this paper, the methodology that was adopted to perform the experiments in the literature has been studied. Further, the methodology chosen for the current experimental setup with each system, its subsystem, and the respective components has been discussed. Finally, the chosen methodology for the current experimental setup has been compared with the methodologies of the experimental setups stated in the literature. The FFH, in the current experimental setup, has been divided into the LFS and the AFS. The LFS has been compared to the supply systems of liquid of various literature and found fit. The AFS in the FFH is the novelty in the current experimental setup. The DRS in the current setup is motivated from various systems mentioned the literature to rotate the disc. The DAH has been divided into CLS and TS in the current setup.

The choice of the current experimental methodology has been, satisfactorily, justified with respect to the literature survey.

References

1. Das B, Prakash S, Reddy PSR, Misra VN (2007) An overview of utilization of slag and sludge from steel industries. Resour Conserv Recycl 50(1):40–57

2. Ravindra Dhirhi, Kali Prasad, Ajay Kumar Shukla, Sabita Sarkar, T. Renganathan, S. Pushpa-vanam, and Marutiram Kaza, Experimental study of rotating dry slag granulation unit: Oper-ating regimes, particle size analysis and scale up, Applied Thermal Engineering 107 (2016), 898–906.

3. BE Dixon, AAW Russell, and JEL Swallow, Liquid films formed by means of rotating disks, British Journal of Applied Physics 3 (1952), no. 4, 115.

4. Eisenklam P (1964) On ligament formation from spinning discs and cups. Chem Eng Sci 19(9):693–694

5. Alfred G Emslie, Francis T Bonner, and Leslie G Peck, Flow of a viscous liquid on a rotating disk, Journal of Applied Physics 29 (1958), no. 5, 858–862.

6. Frost AR (1981) Rotary atomization in the ligament formation mode. J Agric Eng Res 26(1):63–78

7. Sharif Jahanshahi, Yuhua Pan, and Dongsheng Xie, Some fundamental aspects of the dry slag granulation process, 9th International Conference on Molten Slags, Fluxes and Salts (Molten12), Beijing, 2012, pp. 27–31.

8. Sharif Jahanshahi, Dongsheng Xie, Yuhua Pan, Phil Ridgeway, and John Mathieson, Dry slag granulation with integrated heat recovery, 1st Int. Conf on Energy Efficiency and CO2 Reduction in the Steel Industry (EECR Steel 2011), vol. 27, 2011.

9. Kamiya T, Kayano A (1972) Film-type disintegration by rotating disk. J Chem Eng Jpn 5(2):174–182

10. Kawase Y, De A (1982) Ligament-type disintegration of non-newtonian fluid in spinning disk atomization. J Nonnewton Fluid Mech 10(3):367–371

11. Maiti B. Dash S.K. Samantaray A.K. Kushan D.S., Chakraborty G., On hydrodynamics of dry slag granulation of ld/bof slag: Analytical modeling, Proceedings of the 16th International Conference on Heat Transfer, Fluid Mechanics and Thermodynamics & the Editorial Board of Applied Thermal Engineering (HEFAT-ATE), Aug 2022, pp. 828–833.

12. Maiti B. Dash S.K. Samantaray A.K. Singha S.K. Kushan D.S., Chakraborty G., On hydrody-namics of dry slag granulation of ld/bof slag: Developments for new liquid, Proceedings of the 16th International Conference on Heat Transfer, Fluid Mechanics and Thermodynamics & the Editorial Board of Applied Thermal Engineering (HEFAT-ATE), Aug 2022, pp. 834–838.

13. Lake JR (1979) An apparatus for photographing sprays. J Agric Eng Res 24(2):215–218

14. Guangqiang Li and Hongwei Ni, Recent progress of hot stage processing for steelmaking slags in china considering stability and heat recovery, Proceedings of the Second International Slag Valorisation Symposium: The Transition to Sustainable Materials Management, Leuven, Belgium, 2011.

15. Peng H, Shan X, Ling X, Wang D, Li J (2018) Ligament-type granulation of molten slag in different rotary disk configurations. Appl Therm Eng 128:1565–1578

16. Purwanto H, Mizuochi T, Akiyama T (2005) Prediction of granulated slag properties produced from spinning disk atomizer by mathematical model. Mater Trans 46(6):1324–1330

17. Rutland DF, Jameson GJ (1970) Droplet production by the disintegration of rotating liquid jets. Chem Eng Sci 25(8):1301–1317

18. Sahoo K, Kumar S (2021) Atomization characteristics of a spinning disc in direct droplet mode. Ind Eng Chem Res 60(15):5665–5673

19. Wang D, Ling X, Peng H, Cui Z, Yang X (2016) Experimental investigation of ligament formation dynamics of thin viscous liquid film at spinning disk edge. Ind Eng Chem Res 55(34):9267–9275

20. Wang D, Peng H, Ling X (2014) Ligament mode disintegration of liquid film at the rotary disk rim in waste heat recovery process of molten slag. Energy Procedia 61:1824–1829

21. Na Wang, Hao Peng, Xiang Ling, Jingqi Kang, and Minghao Xu, Experimental investigation of slag particles of ligament mode disintegration in spinning disk atomizing, Energy Procedia 105 (2017), 622–627, 8th International Conference on Applied Energy, ICAE2016, 8–11 October 2016, Beijing, China.

22. Jun-Jun Wu, Hong Wang, Xun Zhu, Qiang Liao, and Kai Li, Cold experiment of slag centrifugal granulation by rotary atomizer: Effect of atomizer configuration, Applied Thermal Engineering 111 (2017), 1557–1564

23. Xiang-Sen Wu, Yong Luo, Guang-Wen Chu, Ying-Chun Xu, Le Sang, Bao-Chang Sun, and Jian-Feng Chen, Visual study of liquid flow in a spinning disk reactor with a hydrophobic surface, Industrial & Engineering Chemistry Research 57 (2018), no. 22, 7692–7699.
24. Yang Min Zhou, Chao Li, Li Li Xu, Si Yi Luo, and Chui Jie Yi, The experimental study of molten blast slag dry granulation, Advanced Materials Research, vol. 356, Trans Tech Publ, 2012, pp. 1882–1885.

Wake of a Circular Cylinder in Flowing Soap Films

K. Manoj, Izhar H. Khan, Sanjay Kumar, and Kamal Poddar

Abstract Flow past a stationary circular cylinder is studied experimentally in an inclined flowing soap film. Experiments are conducted in the low Reynolds number regime (Re < 200). Images acquired using a high-speed camera are used to study the global wake structure of the circular cylinder for different Reynolds numbers. Both the near-wake and the far-wake are closely observed for the variation of wake characteristics such as recirculation bubble length, shedding frequency of the vortices, and the intervortex spacing of von Karman vortex street with the soap solution's volumetric flow rate. As the flow rate rises, the wavelength of the vortices first increases, reaches a maximum, and then decreases. The 'b/a' ratio (the ratio of the distance between clockwise and counterclockwise vortices to the distance between two successive vortices in the same row) remains constant for large parts of the flow regime studied.

Keywords von Karman vortex street · Wake · Wavelength · Soap film

Nomenclature

a	Distance between two consecutive vortices
B	Distance between two rows of vortices
D	Cylinder diameter
Re	Reynolds number
St	Strouhal number

K. Manoj (✉) · I. H. Khan · S. Kumar · K. Poddar
Department of Aerospace Engineering, IIT Kanpur, Kanpur 208016, India
e-mail: mano1883@gmail.com

1 Introduction

For more than a century, the wake of a circular cylinder has been studied and is a classic problem in fluid mechanics. At a very low Reynolds number (Re), the wake is laminar and a unique and continuous relationship exists between the Reynolds number and the Strouhal number (St). As Re increases, the near-wake undergoes two separate three-dimensional transitions, and these transitions show up as discontinuities in the St–Re curve. And the two 3D transitions are labelled as 'mode A' and 'mode B' instability and occur at Re = 180–190 and Re = 230–260 [1]. Results from direct numerical simulations (DNS) demonstrate that 'mode A' is initiated by a subcritical bifurcation and 'mode B' by a supercritical bifurcation [2]. A study of the flow past circular cylinders in horizontal and vertical soap film tunnels shows that these 3D transitions disappear. And as Re increases, St increases monotonically, approaching the 2D asymptote of 0.2417 [3].

Horvath et al. [4] performed experiments using a cylindrical rod of 1 mm in diameter in a vertical flowing soap film channel of 6 cm in width. They tried to find the critical velocity at which the shedding of vortices begins. The flow rate was gradually increased and the critical velocity at which the shedding of vortices commences was observed. And then, when they reduced the flow rate, they noticed that the vortices were continuously shed even at velocities slightly less than the critical velocity. Hence, they concluded that hysteresis exits at the start of vortex shedding. Roushan and Wu [5] performed experiments using a tapered circular rod in a flowing soap film channel of 10 cm in width. The velocity of the soap film was fixed at 120 cm/s and the variation of shedding frequency with the diameter of the cylinder was determined. High-speed flow visualization data was used to measure the frequency. Based on their observations of the vortex street structure, they proposed a new relationship between St and Re. This new relationship applies to both bulk fluids and 2D soap films. They also observed that the shedding of the vortices starts at Re = 11 ± 2. Jiang and Cheng [6] performed 2D and 3D DNS to study the wake of a circular cylinder for Re ≤ 1000. They discovered that the wake Strouhal number for 2D and 3D flows agrees up to Re = 270.

Chikkam and Kumar [7] used high-speed flow visualization and particle image velocimetry to study the wake of a rotating circular cylinder of 10 mm in diameter in an inclined flowing soap film channel of 12 cm in width. The soap film channel is inclined at an angle of 6.3°. The experiments were performed at Re ~ 200 and 250 and for cylinders of varying degrees of hydrophobicity and angular velocity. The Strouhal number was found to be less for hydrophobic cylinders than for non-hydrophobic cylinders, and it also decreases as the hydrophobicity increases. Khan et al. [8] studied the characteristics of the wake of a rotationally oscillating cylinder in an inclined, flowing soap film channel. The experiments were conducted for Re ~ 145, and three different levels of oscillating amplitude, $\theta = \pi$, $\pi/2$ & $\pi/4$ rad. The oscillating frequency is varied from 0 to 35 Hz. They observed that close to the resonant frequency, the 'b/a' ratio of the wake decreases.

In the present investigation, the characteristics of the wake of a circular cylinder in a flowing soap film are studied for Re < 200. The flow rate is varied, and the corresponding changes in wake properties, such as length of recirculation zone, vortex shedding frequency, and wavelength of von Karman vortex street, are observed.

2 Experimental Setup

The experiments were carried out in an inclined, flowing soap film tunnel. A reservoir at the top holds the soap solution, and its flow is regulated via a glass rotameter. The test section is 12 cm in width and 120 cm in length and is inclined at an angle of 6.30°. The flow of the soap film is propelled by gravity. The illustration of the experimental setup is shown in Fig. 1. A soap solution with 2% surfactant solution by volume in water is used in the experiment. Full details of the experimental setup can be found in Khan et al. [8].

Images of the flow field downstream of the cylinder acquired by a high-speed camera (IDT, Inc.) are used to find the shedding frequency of the vortices. The camera was fixed on a manually operated linear slide that allowed it to view the soap film at nearly right angles and traverse parallel to it. The image acquisition rate was set at 730 Hz and the exposure time at 1366 µs. Images captured were of 2304 × 1728-pixel size and covered a 20 × 15 cm^2 physical area, corresponding to 115.20 pixel/cm resolution.

The vortex shedding frequency is calculated by measuring the time required for ten pairs of vortices to pass through a section 50 diameters downstream of the cylinder. The Reynolds number is determined using an approach followed by Gharib and Derango [9]. In this empirical method, the Strouhal number is computed by using the measured values of flow velocity and shedding frequency. Then, Re is obtained from the St-Re curve [10]. As shown in Fig. 2, intervortex spacing is calculated for vortices located between sections 30 and 45 diameters downstream of the cylinder.

Fig. 1 Schematic of the experimental setup
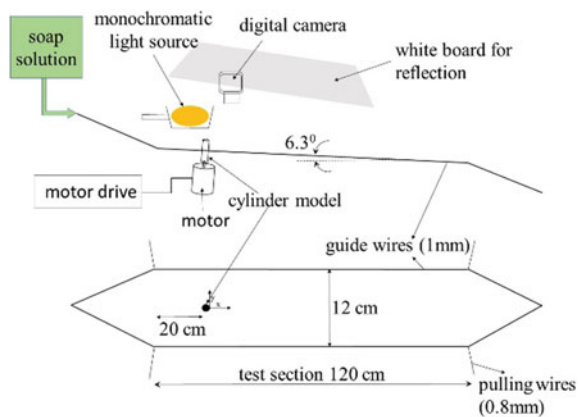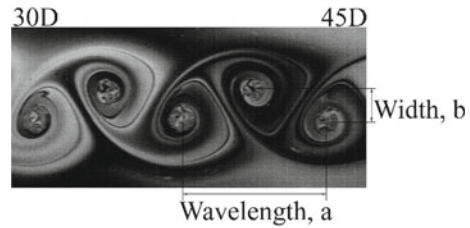
The length 'a' is the wavelength of the von Karman vortex street, and 'b' is defined
as the distance between two vortex rows.

3 Results and Discussion

Figures 3 and 4 show the wake of a cylinder of 8 mm in diameter in an inclined,
flowing soap film for different volume flow rates for Re < 200. The numbers in
each image represent the volumetric flow rate (in mL/min) of the soap solution. The
temperature of the soap solution used is 35 °C and remains constant throughout the
experiments. At 14 mL/min flow rate, a steady structure of the wake is observed
with two vortices that remain in their positions. Initially, as the flow rate rises, the
length of the recirculation bubble also increases. As the flow rate is increased further,
the flow behind the cylinder becomes unstable, and the vortices peel off and shed,
alternately flowing downstream. As shown in Fig. 3, the shedding of vortices is
intermittent for flow rates ranging between 21 and 23 mL/min. At 23.5 mL/min flow
rate, a proper von Karman vortex street is seen. As the flow rate is further increased,
the recirculation zone vanishes, and the vortex formation length reduces. It is also
observed that, with the rise in flow rate, the size of the vortices also increases.

Figure 5 depicts the relationship between shedding frequency and flow rate for
a cylinder of 8 mm in diameter. The vortex shedding frequency is calculated by
measuring the time required for ten pairs of vortices to pass through a section 50
diameters downstream of the cylinder. The shedding of vortices becomes intermittent
for volumetric flow rates below 23.25 mL/min. And a regular von Karman vortex
street is observed for flow rates above 23.25 mL/min (see the image in Fig. 5). There
is a marginal increase in the shedding frequency as the flow rate is increased from 24
to 28 mL/min. It is also observed that as the flow rate increases from 28 to 36 mL/
min, the shedding frequency gradually increases.

Figure 6 depicts the relationship between wavelength and flow rate for a cylinder
of 8 mm in diameter. Values of wavelength 'a' and the 'b/a' ratio shown in Figs. 6
and 7 are calculated by taking an average of 10 values. As the flow rate increases, the
wavelength of the vortices first increases, reaches a maximum, and then decreases.
There is a sharp increase in wavelength as the flow rate increases from 23.25 to
24 mL/min and, consequently, the frequency reduces (see Fig. 5). For flow rates
between 24 and 27 mL/min, the wavelength gradually increases with flow rate. And

Fig. 3 Wake of a cylinder of 8 mm in diameter in an inclined, flowing soap film for different volume flow rates. The numbers in each image represent the volume flow rate in mL/min
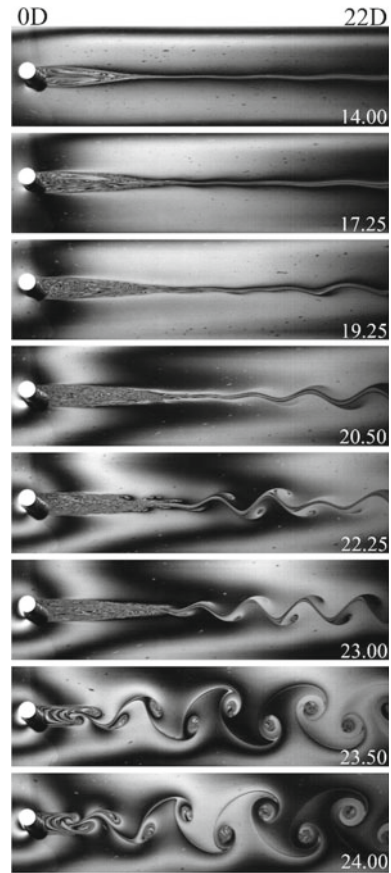

this increase in wavelength causes the frequency to remain constant. The wavelength remains almost constant for flow rates between 27 and 28.5 mL/min. With a further increase in flow rate, the wavelength shows a decreasing trend.

The b/a ratio is important from the stability characteristics point of view and was found to be equal to 0.281 [11, 12] and is represented by the horizontal line in Fig. 7. Figure 7 shows the variation of the 'b/a' ratio with flow rate for a cylinder of 8 mm in diameter. The b/a ratio first decreases and then remains almost constant for increasing flow rates, and then again shows an increasing trend beyond 35 mL/min flow rate. There is a sharp decrease in the b/a ratio as the flow rate rises from 23.25 to 24 mL/min. This is a consequence of the large increase in wavelength (see Fig. 6). For flow rates between 24 and 32 mL/min, for any changes in flow rate, both 'b' and 'a' vary proportionally, and hence their ratio remains almost constant. With a further increase in flow rate, the length 'b' decreases and reaches its minimum value at 35 mL/min. Thus, the minimum value of the b/a ratio is found at this flow rate.

Fig. 4 Wake of a cylinder of 8 mm in diameter in an inclined, flowing soap film for different volume flow rates. The numbers in each image represent the volume flow rate in mL/min
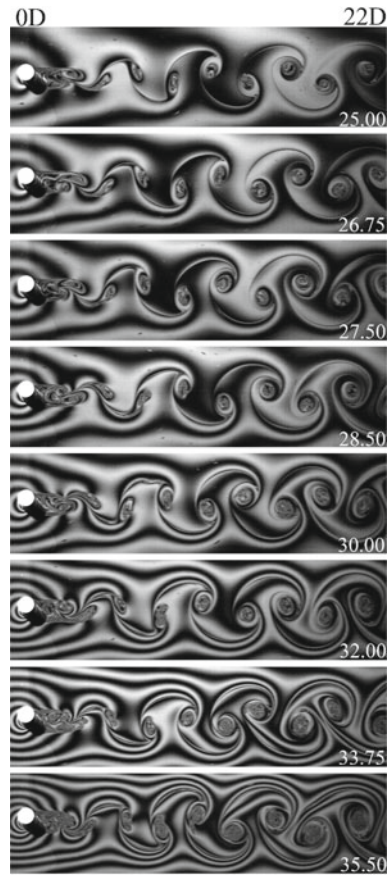
Fig. 5 Variation of shedding frequency with the flow rate of soap solution for a cylinder of 8 mm in diameter. The first image shows that the shedding of vortices becomes intermittent when the flow rate of soap solution drops below 23.25 mL/min. And the second image shows a significant increase in the wavelength as the flow rate increases from 23.25 to 24 mL/min
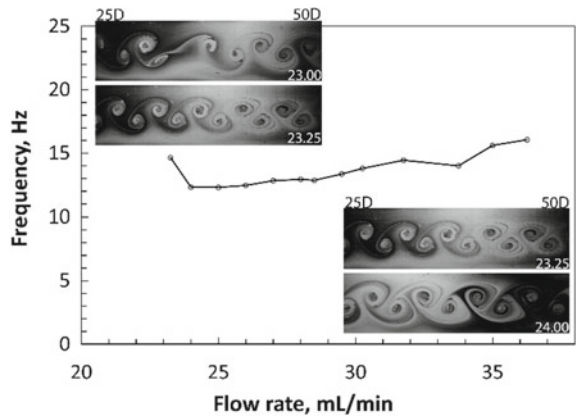
Fig. 6 Variation of wavelength with the flow rate for a cylinder of 8 mm in diameter. The image shows the considerable drop in the wavelength when the flow rate rises from 35 to 36.25 mL/min
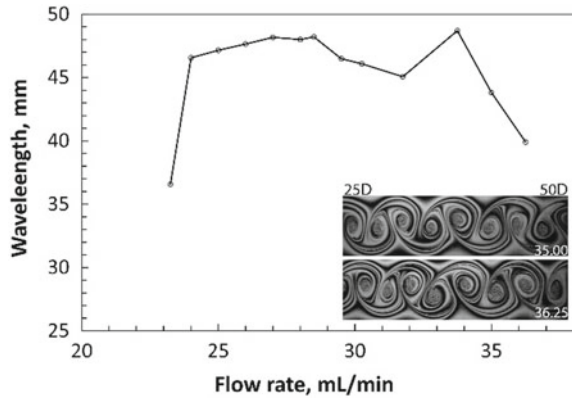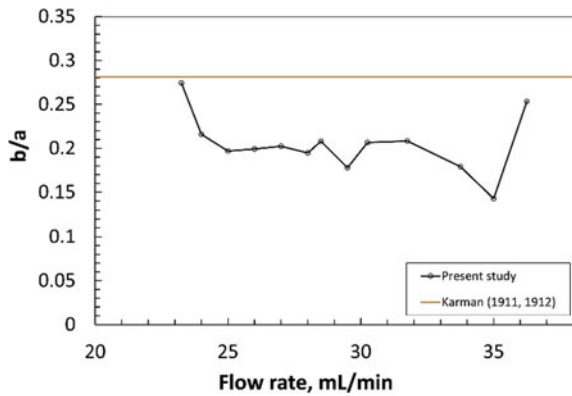

Fig. 7 Variation of b/a ratio with flow rate

4 Conclusions

In the current study, flow past a cylinder in an inclined, flowing soap film is experimentally studied using high-speed flow visualization (Re < 200). Images of the near-wake for different volume flow rates of soap film are shown. The variation of characteristics of the wake, such as the recirculation bubble length, the shedding frequency of the vortices, and the intervortex spacing of vortex street with the flow rate of soap film are presented. With increasing flow rate, the vortex shedding frequency initially remains constant and then gradually increases. The wavelength first increases, reaches a maximum, and then decreases. As the flow rate is varied, the 'b/a' ratio remains constant for large parts of the flow regime studied.

References

1. Williamson CHK (1996) Vortex dynamics in the cylinder wake. Annu Rev Fluid Mech 28:477–539
2. Ronald D (1997) HENDERSON, *Nonlinear dynamics and pattern formation in turbulent wake transition.* J Fluid Mech 352:65–112
3. Wen CY, Lin CY (2001) Two-dimensional vortex shedding of a circular cylinder. Phys Fluids 13:557–560
4. Horvath VK, Cressman JR, Goldburg WI, Wu XL (2000) Hysteresis at low Reynolds number: onset of two-dimensional vortex shedding. Phys Rev E 61:R4702–R4705
5. Pedram Roushan and X. L. Wu, *Structure-based interpretation of the strouhal-reynolds number relationship*, Phys. Rev. Lett. 94 (2005), 054504.
6. Jiang H, Cheng L (2017) Strouhal-Reynolds number relationship for flow past a circular cylinder. J Fluid Mech 832:170–188
7. Navya Geethika Chikkam and Sanjay Kumar (2019) Flow past a rotating hydrophobic/nonhydrophobic circular cylinder in a flowing soap film. Phys. Rev. Fluids 4:114802
8. Izhar H. Khan, Manoj K, Sanjay Kumar, and Kamal Poddar, *An experimental study of the near wake characteristics of a rotationally oscillating cylinder in a flowing soap film*, AIAA AVIATION 2022 Forum, 2022.
9. Gharib M, Derango P (1989) A liquid film (soap film) tunnel to study two-dimensional laminar and turbulent shear flows. Physica D 37:406–416
10. Williamson CHK (1989) Oblique and parallel modes of vortex shedding in the wake of a circular cylinder at low Reynolds numbers. J Fluid Mech 206:579–627
11. von Karman Th (1912) Uber den mechanismus des wiederstandes, denein bewegter korper in einer flussigkeit erfahrt, Nachrichten von der Gesellschaft der Wissenschaften zu Gottingen, Mathematisch- Physikalische Klasse 1912:547–556
12. Th. von Karman, *Uber den mechanismus des widerstandes, den ein bewegter korper in einer fl ussigkeit erfahrt*, Nachrichten von der Gesellschaft der Wissenschaften zu Gottingen, Mathematisch-Physikalische Klasse 1911 (1911), 509–517

Droplet Impact on a Hydrophilic Flexible Surface

Bibek Kumar, Gaurav Upadhyay, and Rajneesh Bhardwaj

Abstract We study impact of water-glycerol droplets on a flexible surface, in particular the effect of viscosity on the overall system's dynamics. We experimentally analyzed the impact dynamics and cantilever response of the system. A thin hydrophilic cantilever beam, made of copper, was used as a flexible substrate. During impact, the viscosity of a droplet damps the substrate's vibration by dissipating the system's energy. However, we observed that the initial dynamics of the droplet also contribute to the damping of the cantilever. An analytical model was presented to predict the motion of a cantilever beam, which was shown to be in good accord with our experimental findings.

Keywords Droplet impact · Oscillations · Viscous damping

Nomenclature

ρ Droplet density [kg/m^3]
μ Droplet viscosity [Pa s]
γ Surface tension [mN/m]
D_0 Initial diameter of droplet [mm]
V_0 Impact velocity [m/s]
K Cantilever stiffness, $K = 3EI/L^3$ [N/m]
E Young's modulus [GPa]
I Moment of inertia [m^4]
m_b Mass of cantilever [kg]
m_d Mass of droplet [kg]
ω_0 Cantilever frequency, $\omega_0 = 2\pi f_0$ [rad/s]
We Weber number, $\rho V_0^2 D_0/\gamma$

B. Kumar · G. Upadhyay · R. Bhardwaj (✉)
Department of Mechanical Engineering, IIT Bombay, Mumbai 400076, India
e-mail: rajneesh.bhardwaj@iitb.ac.in

t_b Time period of cantilever [ms]
t_d Time period of droplet [ms

1 Introduction

Droplet impact over flexible surfaces has application in agricultural spray, rain drops with micro air vehicles'/insects, and biotechnology [1–3]. Droplet impact over solid surfaces and the subsequent interaction dynamics has been studied comprehensively. However, not all droplet impact scenarios involve solid rigid surfaces and in those cases, substrate compliance becomes a vital parameter to consider. As a result, it is essential to comprehensively study the interplay between the elastic substrate and impacting droplets. The varied timescales of flexible substrates and liquid droplets present a novel avenue to manipulate the impact dynamics as per demand without fabricating complex micro/nanostructures.

Pepper et al. [4] study droplet dynamics on the elastic membrane at large velocities. They showed that splashing could be delayed to higher velocities by appropriately tuning the membrane's stiffness. Soto et al. [5] deciphered two different regimes based on the droplet and substrate timescales for impacts on flexible cantilever beams. Gart et al. [2] used Euler–Bernoulli analysis to get the temporal variation of the beam's dynamics. Weisensee et al. [6] and Vasileiou et al. [7] showed that droplets' contact time on superhydrophobic surfaces can be reduced by employing flexible substrates. They performed experiments with water droplet impact on the cantilever and simply supported and proposed limiting conditions for contact time reduction in terms of impact velocity. Huang et al. [8] studied drop impact on hydrophilic cantilever resulting in large deformation. A theoretical model was presented by employing energy balance analysis. Recently, Upadhyay et al. [9] showed that the contact time could be varied in a wide range from higher to lesser than that on the rigid substrates. The study highlighted the importance of cantilever's and droplet's timescales in determining the contact time, maximum cantilever displacement, rebound height, and energy transfer. A simple forced harmonic model was developed to corroborate the experimental findings.

Studies mentioned above on droplet impact on a flexible substrate did not consider the effect of viscosity of the droplet on the substrate and the droplet dynamics. A droplet with higher viscosity has less energy available for rebound due to viscous dissipation [10]. Vasileiou et al. [11] in their work highlighted the effect of substrate flexibility on enhancing the repellency of highly viscous droplets. They proposed a model based on energy conservation considering the viscosity of the droplet to predict rebound and contact time. However, recently, Alam and Dickerson [12] showed that the viscous drops damp the cantilever oscillation. The optimum value of viscosity that damps the cantilever depends on the substrate's stiffness. They also employed an energy balance analysis to quantify the energy dissipation due to drop sloshing.

The above studies demonstrated only droplet dynamics on superhydrophobic flexible substrates and cantilever damping due to droplet sloshing.

To date, theoretical models and experiments have not addressed the viscosity's effect on the overall system's dynamics and how it affects the oscillation of a flexible beam. The present work examines experimentally and theoretically the effect of viscosity to develop a comprehensive understanding of the fluid–structure interaction.

2 Methodology

2.1 Experiments

A copper piece of dimension 10×10 cm^2 was cut from a sheet with an average thickness of 40 μm. It was cleaned sequentially with deionized water isopropanol and deionized water. In order to vary the viscosity of the droplet, we have used pure water, water-glycerol mixture (50% V/V), and pure glycerol droplet.

The experimental setup used to study the droplet, and cantilever dynamics after droplet impact on the cantilever is shown in Fig. 1. The droplets of diameter 2.7 $\pm$ 0.05 mm are produced by using a syringe pump (New era pump systems, Inc.) and exit through a 21G needle released from a height of 10 cm resulting in impact velocity (V_0) 1.4 m/s. An elastic strip made of copper ($20 \times 10 \times 0.04$ mm) is clamped rigidly from one end to make a cantilever configuration. The syringe was adjusted such that the drop impacts the cantilever symmetrically in a spanwise direction, and the impact point was 5 mm away from the free end to ensure no end effects. A high-speed camera (NXA3S3, IDT, Inc.) with a short-distance working objective (Qioptiq Inc.) was used to capture the droplet and cantilever dynamics. The experiments were performed for at least 3 different samples under the same ambient conditions (temperature: 25 °C, relative humidity: 60%) to check the repeatability of the data. The images were processed in MATLAB using custom-built image processing tools to obtain the time-varying deflection of the cantilever and the droplet dynamics.

To assess the wettability of the copper substrate, we measured the static contact angle of different liquids by gently placing 5 μL droplets on the surface using a micropipette (Biosystem diagnostics Inc.). The static contact angle of water, water-glycerol mixture (1:1 v/v), and glycerol on a copper sheet are 80 $\pm$ 5°, 75 $\pm$ 5°, and 70 $\pm$ 5° respectively. A summary of droplet parameters is depicted in Table 1. In order to understand the droplet-cantilever dynamics, we investigated the impact of droplets of different viscosity on a cantilever of length 20 mm and stiffness (K).
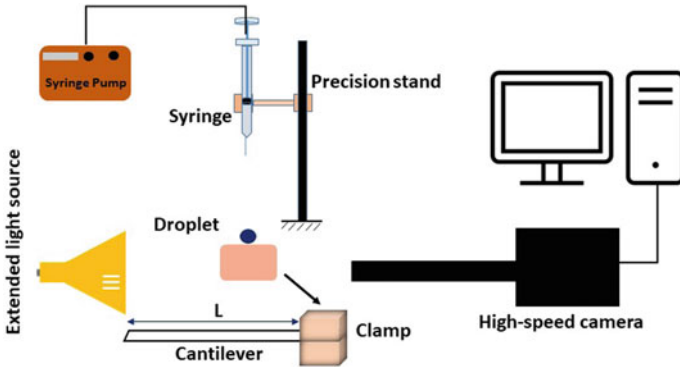
Fig. 1 Schematic representation of the experimental setup

Table 1 Thermophysical properties of liquid droplet parameters

	ρ (kg/m^3)	μ (Pa-s)	γ (mN/m)
Water	1000	1.0×10^{-3}	72
Water-glycerol	1139	6.8×10^{-3}	67
Glycerol	1250	9.0×10^{-1}	63

2.2 Theoretical Model of Cantilever Response

The motion of the beam clamped at one end can be described using a second-order differential equation (Euler–Bernoulli beam theory) as follows [13]

$$\ddot{\delta} + 2\zeta\dot{\delta} + \omega_0^2\delta = 0, \tag{1}$$

where $\ddot{\delta}$ $\dot{\delta}$, and δ are the cantilever tip acceleration, velocity, and displacement, respectively. ζ is damping factor that can be obtained by fitting experimental data and ω_0 ($\omega_0 = 2\pi f_o$) is natural vibration frequency of the system. The general solution of Eq. 1 is as follows [13]

$$\delta = e^{-\zeta\omega_0 t}\left(A \sin\sqrt{1-\zeta^2}\omega_0 t + B \cos\sqrt{1-\zeta^2}\omega_0 t\right), \tag{2}$$

where A and B are constants that can be obtained by applying initial boundary conditions. At time $t = 0$, the cantilever is at rest ($\delta(0) = 0$), gives $B = 0$. Also at $t = \pi/2\omega_0$, i.e., the cantilever is at maximum deflection (δ_0) gives the final expression

$$\delta = e^{-\zeta\omega_0 t}\left(\frac{\delta_0}{e^{-\frac{\pi}{2}\frac{\zeta}{\sqrt{1-\zeta^2}}}} \sin\sqrt{1-\zeta^2}\omega_0 t\right), \tag{3}$$

where (δ_0) is the maximum deflection of the cantilever, which can be determined by experiments. Before impact, the droplet has mass md at velocity V_0 and the cantilever of mass m_b at rest. When a droplet impacts the cantilever, it sticks to the cantilever, resulting in a system of mass ($m_d + m_b$) vibrating at its natural frequency and is given by [13],

$$f_0 = \frac{3.52}{2\pi} \sqrt{\frac{EI}{mL^3}}, \qquad (4)$$

where m is the total mass of the system. The cantilever tip displacement can be obtained by using Eqs. 3 and 4.

3 Results and Discussion

Here, we present results for the impact dynamics of the droplet-cantilever and compare the measured cantilever response with the model presented in Sect. 2.2.

Figure 2 shows the time frames of water droplets (Fig. 2a), water-glycerol mixture (Fig. 2b), and glycerol (Fig. 2c) impacting on the cantilever beam of length $L = 20$ mm ($K = 2.56$ N/m) with impact velocity 1.4 m/s. The motion of the droplet and the cantilever beam is depicted in the picture as a red and blue arrow respectively. Since the cantilever beam is hydrophilic, the droplet generally adheres to the beam surface and starts oscillating with the beam. In the case of a water droplet, when the time $t = 0$, i.e., just before the impact, the droplet's shape is spherical, as shown in Fig. 2. The typical features of droplet impact dynamics over the flexible surface are as follows. After the impact, the droplet starts spreading, converting initial total energy into surface energy and the cantilever bending energy, as a result, the cantilever starts moving downward. In succession, when $t = 4.5$ ms, 5.75 ms, and 5 ms for water, water-glycerol, and glycerol respectively, the cantilever attains its maximum deflection. Subsequently, the droplet starts receding and converting parts of its surface energy back to its kinetic energy and oscillates with the cantilever. In the later time frames, we observe that the droplet oscillation time for water, water-glycerol, and glycerol are 20 ms, 18 ms, and 16 ms respectively. However, the maximum spreading time is almost the same in all three cases, $t_{spread} \sim 4$ ms.

Figure 3 illustrates the variation of droplet contact diameter $D(t)$ normalized with initial droplet diameter D_0, i.e., spreading factor (β), for all the three liquids. We observed that droplet viscosity influences droplet spreading. If a droplet impacts on solid surface, the maximum spreading factor D_{max}/D_0 scaled as, $\beta_{max} \sim We^{0.25}$ [2] which results $\beta_{max} = 2.9$ for the present case. The experimental value of β_{max} is 2.6, which is smaller than the impact on a solid surface. This can be understood as some part of the droplet kinetic energy transfers to the cantilever, resulting in a lower value of the maximum spreading factor. The glycerol droplet does not follow the above scaling law for the spreading factor and is required to rescale the β by considering
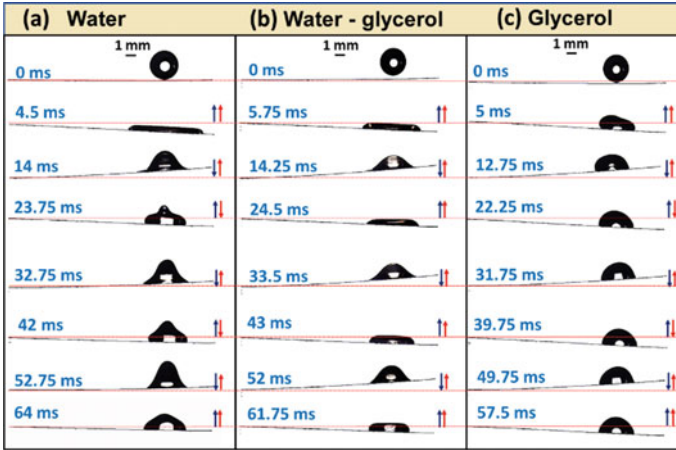
Fig. 2 Time frames of droplets impacting on the cantilever beam of length $L = 20$ mm: **a** water, **b** water-glycerol mixture, and **c** glycerol

liquid viscosity. As the viscosity increases, more energy is lost in dissipation, which further decreases the spreading factor, as shown in Fig. 3.

Further, we provide the cantilever oscillation for droplets with different viscosity. Figure 4 shows a plot depicting the beam tip deflection ($L = 20$ mm and $K = 2.56$ N/m) versus time for water (Fig. 4a), water-glycerol (Fig. 4b), and glycerol (Fig. 4c) droplet. The maximum tip deflection in all the cases is approximately the same ($\sim$ 1 mm) and can be explained as the droplets having the same impact velocity and comparable mass. We also have plotted an analytical solution for cantilever deflection discussed in Sect. 2.1, which agrees with our experimental data. It can be seen that there is quick decay in the amplitude of the cantilever for the case of pure water droplet followed by water-glycerol mixture and pure glycerol. The reason for the

Fig. 3 Temporal evolution of the spreading factor $D(t)/D_0$ for droplets on the cantilever
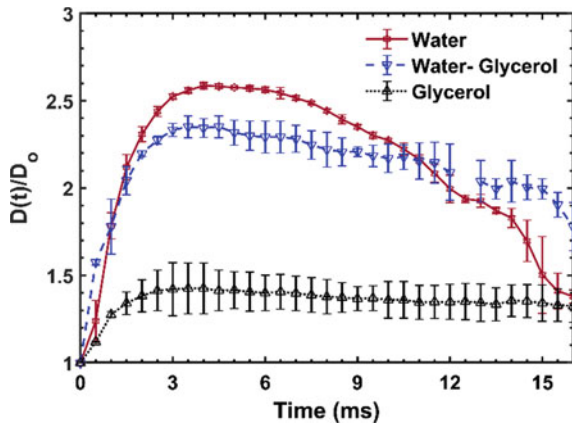
Fig. 4 Experimental and analytical cantilever beam deflection versus time for **a** water, **b** water-glycerol, and **c** glycerol droplet on beam length of $L = 20$ mm
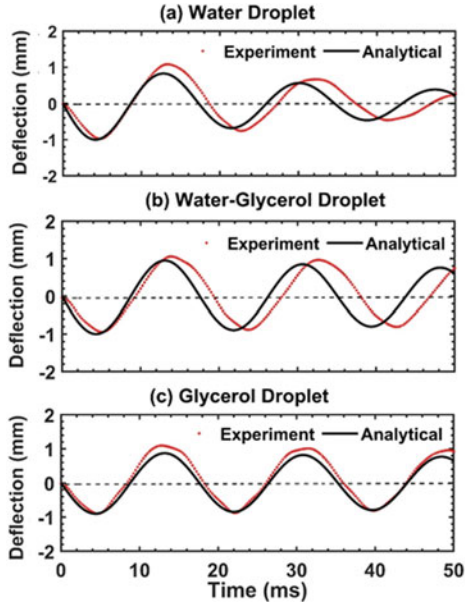

same can be the comparable time scales of water droplet oscillation and cantilever oscillation. The cantilever time period of oscillation, $t_b = 1/f_0 \sim 16$ ms and water droplet oscillation time, $t_d = \sqrt{\rho D_0^3/\gamma} \sim 16.5$ ms. This can be calculated by balancing inertial forces with the capillarity of the droplet [14, 15].

For the water-glycerol mixture and glycerol droplet, the viscosity also comes into play while scaling the oscillation time. This is perhaps the cause of less damping in the case of viscous droplets. The frequency response of cantilever tip deflection versus time is shown in Fig. 5 obtained using the FFT technique. The measured frequencies for water, water-glycerol, and glycerol droplets are 50.5 Hz, 51.5 Hz, and 53.5 Hz, respectively. These findings can be strengthened by tuning the time scale viscous droplet and cantilever to understand the droplet-cantilever system's coupled dynamics.

4 Conclusions

We performed different viscosity droplet impact experiments on the cantilever and captured the dynamics using high-speed visualization. We showed cantilever oscillation and droplet spreading. The cantilever's vibration frequencies were measured using the FFT of a signal. We also compare cantilever oscillation with simple theoretical modeling for different droplets. We discovered that less viscous droplets, i.e., water droplets, damped the cantilever more than highly viscous droplets. Further,

Fig. 5 Frequency response
of cantilever after the impact
of **a** water, **b** water-glycerol,
and **c** glycerol droplet
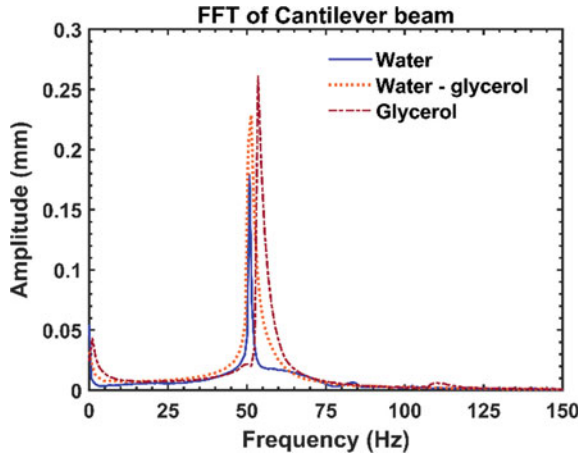
our results demonstrate that the damping depends not only on the droplet's viscosity
but also on the cantilever and droplet's oscillation time scales. These findings may
provide a foundation to design the engineered system where liquid damping plays a
vital role, such as sensors, robotic flyers, and aerial vehicles.

References

1. Josserand C, Thoroddsen ST (2016) Drop impact on a solid surface. Ann Rev Fluid Mech 48:365–391
2. Gart S, Mates JE, Megaridis CM, Jung S (2015) Droplet impacting a cantilever: a leaf-raindrop system. Phys Rev Appl 3(4):044019
3. Kumar B, Chatterjee S, Agrawal A, Bhardwaj R (2021) Evaluating a transparent coating on a face shield for repelling airborne respiratory droplets. Phys Fluids 33(11):111705
4. Pepper RE, Courbin L, Stone HA (2008) Splashing on elastic membranes: the importance of early-time dynamics. Phys Fluids 20(8):082103
5. Soto D, De Lariviere AB, Boutillon X, Clanet C, Quéré D (2014) The force of impacting rain. Soft matter 10(27):4929–4934
6. Weisensee PB, Tian J, Miljkovic N, King WP (2016) Water droplet impact on elastic superhydrophobic surfaces. Sci Rep 6:30328
7. Vasileiou T, Gerber J, Prautzsch J, Schutzius TM, Poulikakos D (2016) Super hydrophobicity enhancement through substrate flexibility. Proc Natl Acad Sci 113(47):13307–13312
8. Huang X, Dong X, Li J, Liu J (2019) Droplet impact induced large deflection of a cantilever. Phys Fluids 31(6):062106
9. Upadhyay G, Kumar V, Bhardwaj R (2021) Bouncing droplets on an elastic, superhydrophobic cantilever beam. Phys Fluids 33(4):042104
10. Mao T, Kuhn DCS, Tran H (1997) Spread and rebound of liquid droplets upon impact on flat surfaces. AIChE J 43(9):2169–2179
11. Vasileiou T, Schutzius TM, Poulikakos D (2017) Imparting icephobicity with substrate flexibility. Langmuir 33(27):6708–6718
12. Alam E, Dickerson AK (2021) Sessile liquid drops damp vibrating structures. Phys Fluids 33(6):062113

13. Thomson WT (2018) Theory of vibration with applications. CRC Press
14. Richard D, Clanet D, Quéré D (2002) Contact time of a bouncing drop. Nature 417(6891):811–811
15. Schiaffino S, Sonin AA (1997) Molten droplet deposition and solidification at low weber numbers. Phys Fluids 9(11):3172–3187

Development of a New Instrumented Structure for the Measurement of Avalanche Impact Pressure

Rakesh K. Aggarwal, Ranjan Das, and Hemen dra S. Gusain

Abstract Accurate knowledge of avalanche impact pressure is vital for the design of avalanche control middle-zone and run-out zone structures. Very little database is available in this regard. With the motivation to fill the knowledge gaps in this area and to develop comprehensive database towards improved guidelines for the avalanche impact pressures on the avalanche control structures, an instrumented structure of size 1.0 m height and 0.65 m width has been developed and installed on a 61 m long experimental facility snow chute located at Field Research Station, Dhundhi (near Manali, Himachal Pradesh), India, for avalanche impact pressure measurement. Four equally spaced piezoelectric force sensors are fitted in the centre of the structure. The measured data has been analysed and compared with the theoretically estimated avalanche impact pressures acquired using the Voellmy–Salm model, and both are found in reasonably good agreement with each other. The obtained results portray that the maximum avalanche impact pressure varies in the range of approximately 15–40 kPa, and the present theoretical predictions are accurate within 20.4% with respect to the experimental observations.

Keywords Impact pressure · Drag coefficient · Avalanche · Snow chute · Experimentation · Theoretical model

Nomenclature

b Width of snow chute [m]

R. K. Aggarwal · H. S. Gusain
Defence Geoinformatics Research Establishment, DRDO, Chandigarh 160036, India

R. K. Aggarwal · R. Das (✉)
Department of Mechanical Engineering, Indian Institute of Technology Ropar, Rupnagar, Punjab 140001, India
e-mail: ranjandas@iitrpr.ac.in; ranjandas81@gmail.com

H. S. Gusain
Institute of Technology Management, DRDO, Mussorie, Uttarakhand 248179, India

C_d	Drag coefficient [–]
d_p	Flow depth [m]
d_s	Depth of deposited snow [m]
g	Acceleration due to gravity [m/s^2]
h	Fracture depth of snow in hopper [m]
L	Length of starting zone [m]
P_s	Avalanche impact pressure [N/m^2]
Q	Discharge [m^3/s]
R	Hydraulic radius [m]
S	Avalanche run-out distance [m]
t	Time [s]
V	Volume of snow in hopper [m^3]
V_p	Velocity at end of track zone [m/s]
$V_{p,m}$	Avalanche velocity striking at the instrumented structure [m/s]
V_s	Velocity at end of starting zone [m/s]
θ_p	Average slope inclination (°)
θ_s	Starting zone angle (°)
μ	Dynamic friction coefficient [–]
ξ	Turbulent friction coefficient [m/s^2]
ρ	Snow density [kg/m^3]

1 Introduction

Simple hydraulics-based relations are insufficient to accurately estimate avalanche impact pressure on the structures. It seems quite logical that the avalanche impact pressure can be measured by doing experiments on a real scale avalanche site. However, due to complexity in quantifying the snow properties and hazardous nature of avalanches, it is a challenging task to measure accurately the avalanche impact pressures on the avalanche control structures. Further, due to size of the avalanche terrain in the order of few kilometres, it is not possible to conduct these type of measurements at a large number of avalanche sites, and thus generalize the values of avalanche impact pressures. However, this problem can be fairly solved by doing experiments on a small scale experimental facility like snow chute, where a large number of "real avalanche like" experiments can be conducted with better accuracy and relative ease, as compared to experiments on a real terrain. Further, the measured values can be repeated and generalized.

Pedersen [1] reported a 2-D model for the prediction of avalanche impact forces on an arbitrary structure and compared the model results with the reported experimental values. An error of 21% was reported by the authors between the simulated and experimental results. However, details were not provided about the measurement system employed. Dent and Lang [2] demonstrated the correspondence between the physical and computer simulated impact processes. Using experiments, total force

on the target was recorded by the output of the four-active-arm strain-gage bridge displayed on a storage oscilloscope, and the trace photographed. The authors reported an average force value during the time period between 100 and 250 m s as 11.0 N experimentally, and 9.8 N through simulations. However, corresponding impact pressure values were not provided. McClung and Schaerer [3] measured avalanche impact pressures at Rogers Pass in the Selkirk Mountains of British Columbia using five 645 mm^2 disc-shaped surface load cells mounted on 5.2-m-high steel frame and a large circular aluminium plate 0.5 m in diameter. From the analysis of the data, the authors found that the large plate gives lower avalanche impact pressure values by roughly an order of magnitude for the wet avalanche and in the order of magnitude of 2 for the moist avalanche. Nakamura et al. [4] did measurements of avalanche impact pressure and some other parameters on a 25-m-long and 1-m-wide chute. They used six load cells with capacities of 1.96 and 9.80 kN installed from the bottom to 0.823 m high post. They found the maximum observed values of the impact pressure against a post due to snow blocks hitting at a speed of about 12 m/s, in the range of 77–740 kPa. Sovilla et al. [5] analysed the avalanche impact pressures and velocity of five Vall'ee de la Sionee measurements. They made the measurements on a 20 m high tubular pylon with high-frequency pressure transducers and optoelectronic velocity sensors. Based on the measurements, they derived the relationship between impact pressure and Froude Number. Naaim et al. [6] emphasized on the significance of impact pressure values in the design of avalanche control structures and estimated the variation of drag coefficient with avalanche flow parameters. Baroudi et al. [7] measured impact pressures of dry and wet snow avalanches at the Swiss Valle'e de la Sionne experimental test site using piezo and cantilever sensors set-up at different faces of the 20-m-high pylon in the avalanche flow. They found significant variations in the impact pressure values of dry snow and wet snow avalanches. ODA et al. [8] applied a two-phase flow model to simulate snow avalanche motion for 8.0-m-long and 0.8-m-wide experimental chute facility and compared the simulated avalanche impact pressures with the measured values. Thibert et al. [9] quantified the measured avalanche impact pressures on the flat surface of an instrumented structure by experiments performed at full scale. An inverse analysis was used to reconstruct the pressure applied on the obstacle from the deformations recorded during the impact. Sovilla et al. [10] found that the shape and size of the measuring force sensors have a profound effect on the impact pressure values. Maggioni et al. [11] performed measurements of impact forces and pressures due to avalanches at Seehore set-up situated in Aosta Valley, Italy. By performing tests at Vallée de la Sionne test facility, Sovilla et al. [12] demonstrated variations of impact pressure with respect to space and time and their relationship with avalanche geometry and flow regimes. Recently, Kyburz et al. [13] developed a numerical scheme namely, discrete element method for assessing the response of avalanche with a rigid body and the variation of impact pressure on the shape and size of the body.

It can be very well observed from the work done in the past that measurement of avalanche impact pressures has been done by different authors under different real terrain and laboratory conditions. However, few details have been provided about the kind of measurement systems used, their accuracy and other allied aspects. Further,

no comprehensive database has been generated for the measured impact pressure values which can act as a significant guideline for design of different avalanche control structures. The present work has been attempted to fill these knowledge gaps in this area.

2 Methodology

One Avalanche Impact Force Measurement System (AIFMS) has been developed for measuring avalanche impact pressure of the flowing snow avalanche pressures up to 250.0 kPa on a 61-m-long snow chute at Dhundhi, Himachal Pradesh, India. The location of the system on snow chute is shown in Fig. 1.

2.1 Experimental Methodology

The block diagram of the system designed is shown in Fig. 2. The system comprises basically of four single axis piezoelectric load cells fitted at an interval of 0.20 m on a stainless steel plate of size 1.00 m × 0.25 m. Two mild steel side plates each of 0.20 m width were additionally attached to this steel plate on its left and right sides. The vertical load of the complete impact plate assembly is transferred to four reinforced concrete cement (RCC) pillars through a mild steel base frame, and shear load is taken by a rigid mild steel structure fitted on the back of plate assembly. The RCC concrete pillars, each of size 0.3 m × 0.3 m × 2.5 m and corresponding foundation measuring 1 m deep for the system, were designed and constructed by considering
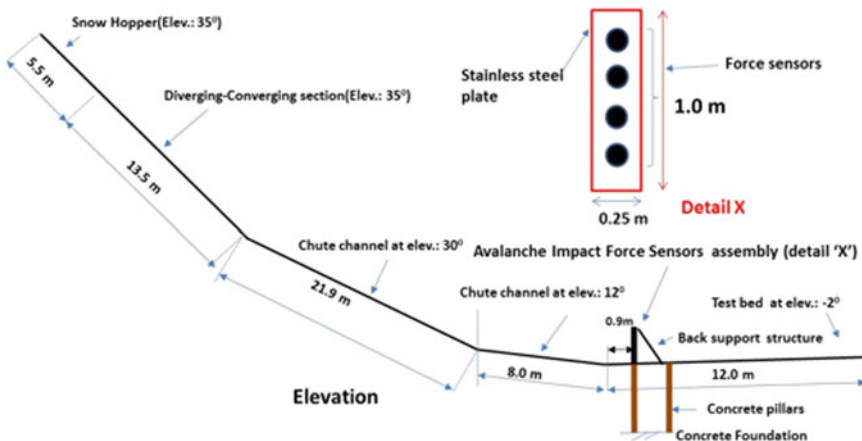

Fig. 1 Set-up of the avalanche impact force measurement system

both static load as well as bending force due to oblique avalanche forces. Overall, the system is designed to measure maximum 250 kPa avalanche impact pressure. In order to isolate the sensor assembly from the noise and vibrations coming from the snow chute body, a uniform gap of 10 mm was provided all around between the base frame and snow chute plates. The force sensors were calibrated in their laboratory by PCB Inc., USA. Before fitting sensors on the plate, the functioning of the force sensors was affirmed by putting some known load on them and noting the output of the sensor through data acquisition and display system. Each load cell is capped with a circular-shaped steel shroud of area 314.28 mm^2. Neoprene washers were provided around each force sensor to prevent ingress of snow/ice through the front plate of the impact assembly. In order that force sensors measure avalanche impact force proportionate to its top surface area, the top surfaces of the four force sensors were ground-flushed with the instrumented plate. This ensures accurate translation of avalanche impact force values to the corresponding avalanche impact pressures.

The output of the four piezoelectric load cells is connected via 20-m-long four co-axial low noise cables to a signal conditioner which converts the received charge from the sensors into voltage. Signal conditioner is further interfaced to the Data Acquisition System (DAQ). Signal conditioner is given AC power supply while DAQ is powered by an accurate DC power supply source. Because of the ambient temperature at the site going below sub-zero temperatures, some of the temperature sensitive components of the system like DAQ, signal conditioner and DC power supply are kept inside a temperature control enclosure which can maintain the desired air temperature around these components. Finally, the output of the DAQ is interfaced with a "Laptop" in which a customized Labview code was installed for data acquisition, display, storage and analysis of the data.

After selecting/developing various components of the system as per the desired avalanche loads, these were transported to Dhundhi site for assembly, installation
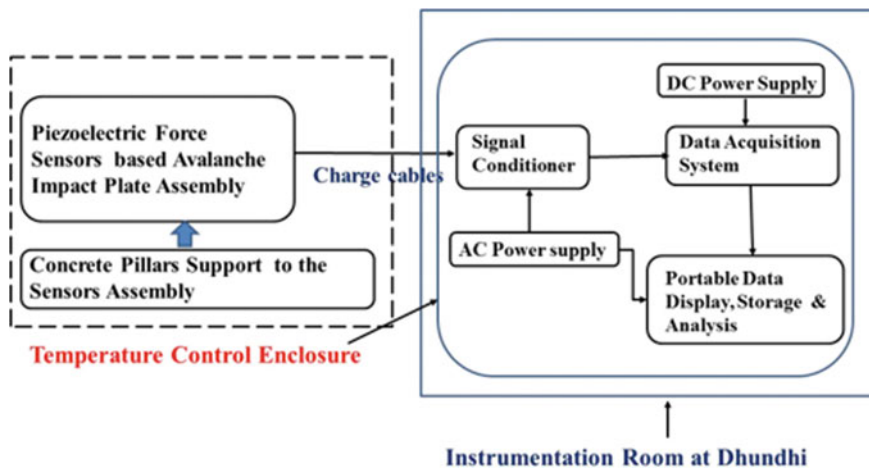

Fig. 2 Block diagram of avalanche impact force measurement system

and testing on the test bed of snow chute. Before installation, it was ensured that foundation and all the four supporting RCC pillars were cured and ready to take the load. Brief installation details of the AIFMS are shown in Fig. 3, whereas the complete is displayed in Fig. 4.

Fig. 3 Installation details of the avalanche impact force measurement system, **a** foundation, **b** removal of snow chute sheets and casings, **c** casting of concrete pillars, **d** pulling of mild steel base frame, **e** erection of base frame **f** inspection of piezoelectric force sensors
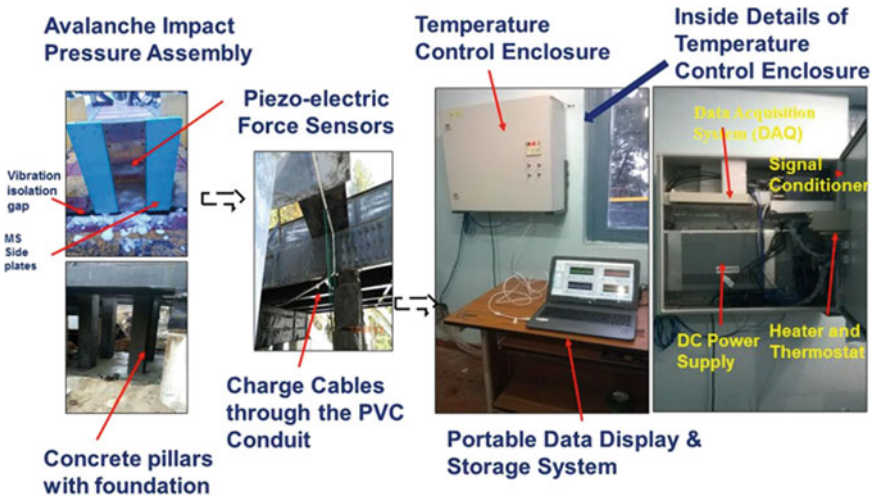
Fig. 4 Complete assembly of the avalanche impact force measurement system

2.2 Simulation Methodology

In the present paper, Voellmy–Salm model [14] has been employed for the theoretical avalanche velocity and impact pressure values. For calculating velocity V_s at the end of the starting zone, i.e. hopper and trapezoidal section combined together, following equation is used [14],

$$V_s = \sqrt{\xi h (\sin \theta_s - \mu \cos \theta_s)} \tag{1}$$

Here μ and ξ are the coefficient of Coulomb friction and turbulent friction, respectively. Based on the experimental work done by Verma et al. [15], the value of μ has been taken as 0.11, and ξ as 700 m/s^2. Moreover, h is the fracture depth of the snow, i.e. height of snow in the hopper, and θ_s is the starting zone angle which is 35° in the present case. After calculating velocity V_s, time taken t by the avalanche mass to cross the starting zone is calculated as the ratio of the total length L of the starting zone i.e., 19 m in the present case and the velocity V_s. Discharge Q of avalanche mass is then computed as the ratio of the volume V of snow in the hopper and time taken t to cross the starting zone. As per the present model, terminal velocity V_p at the end of the track of avalanche can be calculated by the following equation [14],

$$V_p = \sqrt{\xi R (\sin \theta_p - \mu \cos \theta_p)} \tag{2}$$

Here, R is the hydraulic radius, and θ_p is the average slope inclination of track. In this case, it is taken as the average of 30° and 12° slopes. In order to compute the avalanche flow depth d_p, discharge Q is equated to $b \times d_p \times V_p$, where, b is the width of the snow chute in the track section which is 2.0 m in this case. The value of d_p is iterated by trial and error method in a such a manner that the total discharge of the snow mass remains the same in the starting and track zones with an accuracy of $\pm$ 0.02. Corresponding to one of the experiments, the flow depth value d_p was estimated as estimated as 0.36 m, while velocity at end of track V_p as 7.76 m/s. The avalanche run-out distance can be calculated as [14],

$$S = \frac{d_s \xi}{2g} \ln \left[1 - \frac{V_p^2}{d_s \xi (\sin \theta - \mu \cos \theta)} \right] \tag{3}$$

Here, d_s is the depth of snow deposited in run-out zone having slope $- 1.8°$ and this can be estimated as below [14],

$$d_s = d_p + \frac{V_p^2}{10g} \tag{4}$$

Run-out distance S as estimated with Eq. (3) in case of one test done comes out to be 9.40 m (from the beginning of test bed). However, the distance between the start of the test bed and AIFMS is 0.92 m. Interpolating the avalanche velocity striking at the instrumented structure, $V_{p, m}$ with respect to run-out distance S, the value comes out to be 7.00 m/s. The same procedure is followed in the computation of run-out distance, and velocity for all experiments. Avalanche impact pressure at the instrumented structure, P_s is now estimated from the following equation [14],

$$P_s = \frac{1}{2}\rho C_d V_{p,m}^2 \tag{5}$$

where ρ denotes snow density, and $C_d = 2.0$ denotes drag coefficient of flowing snow and structure [16]. Following the work of Thibert [16], this is justified 2.0 as the geometry of AIFMS is similar to a flat-plate perpendicular to flow considered in this paper for Froude number of around 5.0.

3   Results and Discussion

After complete installation of the system, a total of four tests were done on the AIFMS to ascertain its proper functioning and measure impact pressure values (Figs. 5 and 6). For the tests, undisturbed snow was manually filled in the hopper from the surrounding area. Maximum snow filling capacity of the hopper is 11.0 m^3. Before opening gate of the hopper, snow temperature and density were noted at three points in the hopper. These values of temperature and density of snow were averaged before use in the computations.
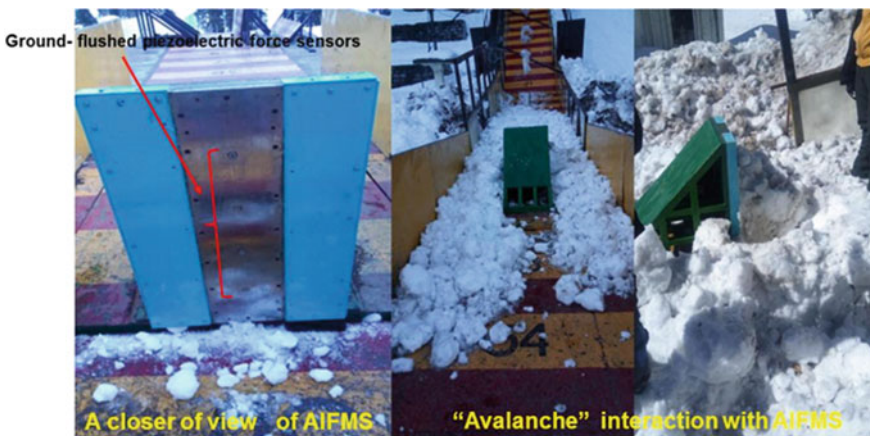
Fig. 5 View of ground-flushed piezoelectric force sensors along with release of snow from the hopper and avalanche hitting the instrumented obstacle
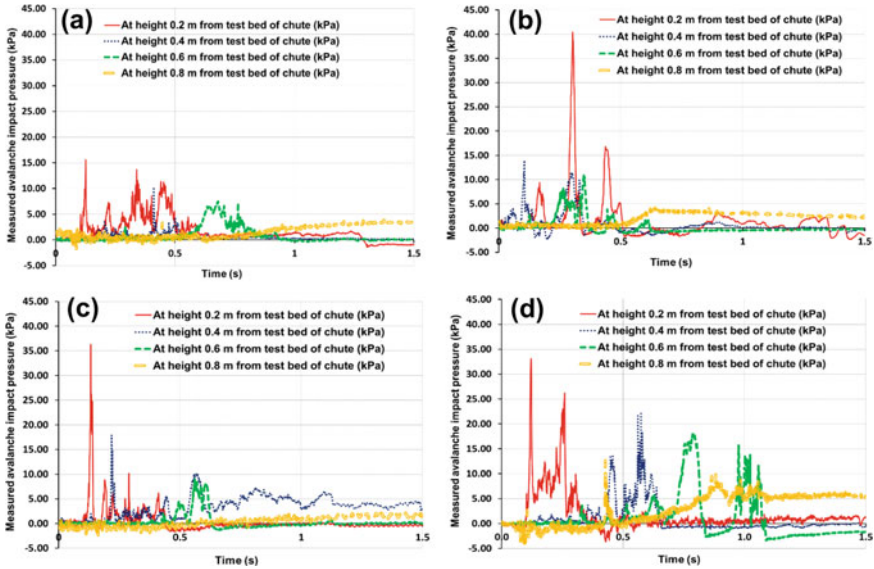
Fig. 6 Variation of instantaneous avalanche impact pressures during experiments, **a** Experiment-1, **b** Experiment-2, **c** Experiment-3, and **d** Experiment-4

Figure 6 shows the instantaneous peak avalanche impact pressures recorded by the AIFMS. Pressures are recorded at four points with an interval of 20 cm, starting from the test bed of the snow chute. These pressures are recorded with the help of piezoelectric load cells. These load cells are suitable for dynamic load measurements. Variation in the values is mainly attributed to the snow variability in terms of density, microstructure, and densification of snow. Interaction between the snow mass and the AIFMS remains for about 2 s. A summary of the experimental tests and the corresponding model computations is given in Table 1. The results indicate that the maximum avalanche impact pressure varies nearly between 15 and 40 kPa, and theoretical predictions are accurate within 20.4% with respect to the experimental values. So, there seems to be reasonably satisfactory conformity between the average measured pressures and estimated avalanche impact pressure using Voellmy–Salm model. This proves the suitability of the AIFMS for avalanche impact pressure measurements. In the near future, more such measurements will be done using this system to develop a comprehensive database for the impact pressure values.

Table 1 Comparison of experimental and theoretical results of the avalanche flow parameters

S. No.	Snow volume V, (m^3)	Snow height, h (m)	Density of snow in hopper, ρ (kg/m^3)	Theoretical estimate of avalanche parameters		Impact pressure measured by AIFMS, P_s (kPa)
				Velocity at AIFMS, $V_{p,m}$ (m/s)	Impact pressure, P_s (kPa)	
1	7.15	0.65	313.0	7.00	15.36	15.31
2	11.0	1.0	470.0	8.52	34.10	33.08
3	11.0	1.0	443.0	8.52	32.14	40.40
4	10.0	0.91	473.0	8.18	31.65	36.27

4   Conclusions

One avalanche impact pressure measuring experimental facility has been successfully developed, installed, and tested on snow chute, Dhundhi, Himachal Pradesh. Limited experiments conducted have proven the capability of the system to measure avalanche impact pressure of the avalanches on small scale. Theoretical predictions of avalanche impact pressure indicate reasonably good accuracy with the experimentally measured values. In the near future, the setup is expected to be a useful tool to calibrate and validate the avalanche dynamics models. Further, simulations can be attempted to simulate transient variation of the avalanche impact pressure using computational fluid dynamics techniques which will give a better insight into the point-to-point variations in the impact pressures.

References

1. Pedersen RR (1979) Forces on structures impacted and enveloped by avalanches. J Glaciol 22(88):529–534
2. Dent JD, Lang TE (1980) Scale modelling of snow-avalanche impact on structures. J Glaciol 26(94):189–196
3. McClung DM, Schaerer PA (1985) Characteristics of flowing snow and avalanche impact pressures. Ann Glaciol 6:9–14
4. Nakamura T (1987) A newly designed chute for snow avalanche experiments. International Association of Hydrological Sciences (IAHS) Publication, 162, pp 441–451
5. Sovilla B, Schaer M, Kern M, Bartlelt P (2008) Impact pressures and flow regimes in dense snow avalanches observed at the Vall'ee de la Sionne Test Site. J Geophys Res 113:1–14

6. Naaim M, Faug T, Thibert E, Eckert N, Chambon G, Naaim F, Bellot H (2008) Snow avalanche pressure on obstacles. In: Whistler 2008 international snow science workshop, 21–27 Sept 2008, Whilster, B.C., Canada
7. Baroudi D, Sovilla B, Thibert E (2011) Effects of flow regime and sensor geometry on snow avalanche impact-pressure measurements. J Glaciol 57(202):277–288
8. Oda K, Moriguchi S, Kamiishi I, Yashima A, Sawada K, Sato A (2011) Simulation of a snow avalanche model test using computational fluid dynamics. Ann Glaciol 52(58):57–64
9. Thibert E, Faug T, Bellot H, Baroudi D (2013) Avalanche impact pressure on a plate-like obstacle. In: International snow science workshop, 7–11 Oct 2013, Grenoble-Chamonix, France
10. Sovilla B, Faug T, Köhler A, Baroudi D, Fischer J, Thibert E (2016) Gravitational wet avalanche pressure on pylon-like structures. Cold Reg Sci Technol 126:66–75
11. Maggioni M, Barbero M, Barpi F, Borri-Brunetto M, De Biagi V, Freppaz M, Frigo B, Pallara O, Chiaia B (2019) Snow avalanche impact measurements at the Seehore test site in Aosta Valley (NW Italian Alps). Geosciences 9:471 (1–20)
12. Sovilla B, Kyburz M, Ligneau C, Fischer JT, Schaer M (2020) Spatial and temporal variability of snow avalanche impact pressure and its importance for structural design, Paper No. 813, 22nd EGU General Assembly conference abstracts, Online, 4–8 May 2020
13. Kyburz ML, Sovilla B, Gaume J, Ancey C (2022) Physics-based estimates of drag coefficients for the impact pressure calculation of dense snow avalanches. Eng Struct 254:113478 (1–17)
14. Bartelt P, Salm B, Gruber U (1999) Calculating dense-snow avalanche runout using a Voellmy-Fluid model with active/passive longitudinal straining. J Glaciol 45(150):242–254
15. Verma SC, Kumar A, Panesar GR, Shukla AK, Mathur P (2004) An experimental study of snow avalanche friction parameters using snow chute. In: International symposium on snow monitoring and avalanches (ISSMA), Manali, India, 12–16 April 2004

On Hydrodynamics of Dry Granulation of LD/BOF Slag Using Spinning Disc Atomizer: Effect of Change in Disc Rotation Direction with Air Blast on Liquid Flow Characteristics

D. S. Kushan, G. Chakraborty, B. Maiti, S. K. Dash, A. K. Samantaray, and S. K. Singha

Abstract The iron and steel industry produces a waste product, slag. Dry Spinning Disc Granulation (DSDG) process has been experimentally tried, widely, for the granulation of Blast Furnace (BF) slag, with the recovery of heat from the high temperature slag. To study this phenomenon, the fabrication of an experimental setup, of the scale of laboratory level, has been done in the institute of the authors. Various experiments were performed on the setup. Stage-wise modifications were performed on the experimental setup, on the basis of the limitations found in the previous stages of the experimental setup. In this study, the experimental setup with all its systems has been elaborated. Then, after the setup is acquainted, a study has been performed to find the effect of change in disc rotation direction with air blast on liquid flow characteristics. Finally, the results have been discussed and the conclusions drawn.

Keywords Experimental hydrodynamics · Dry spinning disc granulation (DSDG) · Linz-Donavitz/basic oxygen furnace (LD/BOF) slag · Spinning disc atomizer (SDA) · Two phase flow

1   Introduction

The LD/BOF slag, in its granulated form, has many applications in construction industry [1], like roads, rail-way track ballasts, road stones, etc. Two broadly classified methods of slag granulation [2] are wet and dry granulation methods. Between these, the Dry Slag Granulation (DSG) methods [2–5] are currently under rigorous

D. S. Kushan (✉) · G. Chakraborty · B. Maiti · S. K. Dash · A. K. Samantaray
Department of Mechanical Engineering, IIT Kharagpur, Kharagpur 721302, India
e-mail: dskushan@iitkgp.ac.in

S. K. Singha
Assam Energy Institute (Centre of Rajiv Gandhi Institute of Petroleum Technology),
Sivasagar 785697, India

research, because it is advantageous, when compared on the basis of environmental aspects. Of all the DSG methods, Centrifugal Granulation methods [6, 7] are relatively economical. The Spinning Disc Atomization (SDA) [8–12] among the Centrifugal Granulation methods, is the most plain and uncomplicated process. This is because the fabrication of a disc is convenient.

The process of SDA is such that liquid slag, in its hot molten state, is slowly dropped over a high speed spinning disc. After this, the molten slag flows outwards from the centre because of the force in the centrifugal direction and surface tension. The working process of atomization could be simply described as, slag spins out a thin film over the disc surface. This expands from the edge of the disc, radially. Researchers have used high speed photography to show that the slag, in its hot molten state, initially, flows over the disc surface as a film. This film, at the edge of the disc, disintegrates into equal diameter bodies of liquid shaped like fingers or regular involute branches of liquid. These branches are called ligaments [13–15]. In the end, the formed ligaments disintegrate and, due to the action of shearing stresses due to the flow of air, form droplets. The analytical modelling of this phenomenon has been done by Kushan et al. [16].

To study this phenomenon, the fabrication of an experimental setup, of the scale of laboratory, has been done in the institute of the authors. Various experiments were performed on the setup. Stage-wise modifications were performed on the experimental setup, on the basis of the limitations found in the previous stages of the experimental setup.

In this study, the experimental setup with all its systems has been elaborated. Then, after the setup is acquainted, a study has been performed to find the effect of change in disc rotation direction with air blast on liquid flow characteristics. Finally, the results have been discussed. Silicon liquid, with 50 cSt Kinematic Viscosity, has been considered as the working liquid for the experiments. The developments performed in the setup have been discussed by Kushan et al. [17].

In the ultimate industry prototype, slag, in its hot molten form, strikes the spinning disc. Further, the slag spreads on the disc surface, radially, in the outward direction. Moreover, when the slag reaches the edge, due to centrifugal force, it is thrown out of the disc. In an optimum speed of rotation of disc and an optimum rate of flow of liquid, ligament-formation mode occurs and the slag, as ligaments, come out of the disc. In the end, the slag might hit the outer vessel walls.

The following study is concentrated on the study of ligament formation in a continuum of liquid, when the liquid is dropped at a uniform flow rate over a spinning disc that is circular and flat. Hence, the study has been diminished to, purely, a hydro-mechanical one, without any regard towards thermodynamic concerns.

2 Methodology

In this section, the detailed schematic of the experimental setup has been discussed.

Fig. 1 Schematic of the liquid flow system (LFS)
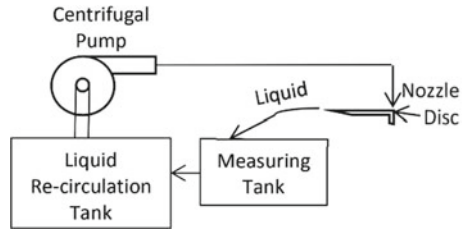
A. Detailed Schematic of the Experimental Setup

The experimental setup comprises various systems. Each of the systems comprises of various components. The system and its respective components will be enlisted here.

- Liquid Flow System (LFS)

The LFS, as the name suggests, is the system in the experimental setup that engages in the flow and the measurement of liquid flow in the experiment. The schematic of LFS could be seen in Fig. 1.
It has the following components:

- Liquid Re-circulation Tank (LRT)
- Centrifugal pump
- Nozzle
- Measuring tank.

The liquid, from the Liquid Re-circulation Tank (LRT), is pumped and allowed to strike onto the rotating disc through a nozzle. The rotating disc, then, spreads the liquid towards the container vessel. The liquid, then, flows to the measuring tank via flexi-pipes. Further, the liquid drops into the LRT via gravity when the control valve is opened.

The working liquid, chosen, is Wacker 50 CST Silicone oil. The properties have been mentioned in Table 1.

The LRT is a stainless steel (SS) cylindrical tank with the axis perpendicular to the ground having an opening at the top flat side with mild steel (MS) stands and MS top supports. The pump is a half (1/2) HP Kirloskar centrifugal pump.

Table 1 Properties of Wacker Metroark DM Silicone Fluid 50 M CTSK

Property	Value	Unit
Kinematic viscosity (at 25 °C)	50	$mm^2 s^{-1}$
Dynamic viscosity (at 25 °C)	48	mPa s
Density at (25 °C)	0.96	$g\ cm^{-3}$
Surface tension (at 25 °C)	20.8	$mN\ m^{-1}$
Refractive index (at 25 °C)	2.71	–

The container vessel is a hemispherical aluminium container vessel with locally fabricated Acrylic (Per-spex) flat base, supported over the LRT top by MS support stands. The pipeline material is chosen to be PVC, if the material requirement is hard, and flexi-pipe, if the pipe is needed to be flexible, supported over the container by MS stands.

- Air Flow System (AFS)

Similarly, the AFS is the system in the experi-mental setup that indulges in the flow and the measurement of air flow in the experiment, from the atmospheric air to the compressed air in the system. The schematic of AFS could be seen in Fig. 2.

The AFS has the following components:

- Compressor
- Air Flow Measurement and Distribution Sys-tem (AFMDS)
- Air nozzles.

The air, from the atmosphere, is compressed using a compressor. Then, the compressed air is transferred to the Air Flow Measurement and Distribution Setup (AFMDS). The schematic of the AFMDS has been shown in Fig. 3.

The AFMDS has the following components:
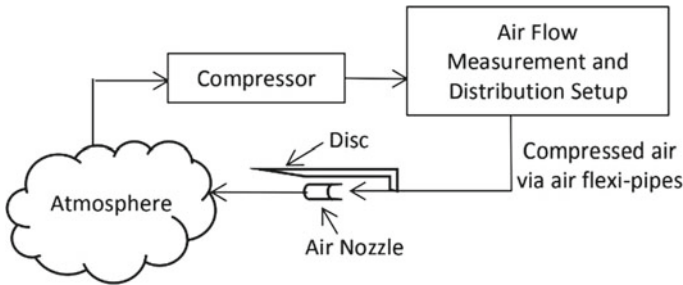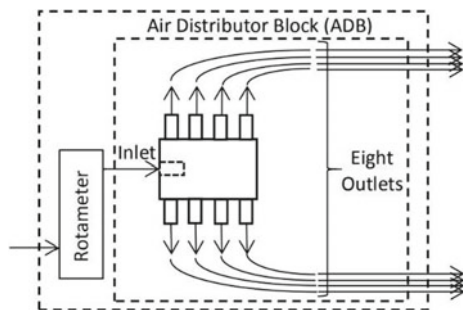
- Rotameter

Fig. 2 Schematic of the air flow system (AFS)

Fig. 3 Schematic of the air flow measurement and distribution setup (AFMDS)

- Air Distributor Block (ADB).

AFMDS, as the name suggests, constitutes of a Flow Measurement System (FMS), which is a rotameter here, and a Flow Distribution System (FDS), which is the Air Distributor Block (ADB).

The air nozzles are positioned under the spinning disc, in the direction parallel to the surface of the disc and the direction of the nozzle making an angle of inclination with the direction of the tangent of the circular edge of the disc.

The compressor is a medium capacity air compressor. The AFMDS consists of a 50 L Per Minute (LPM) FILFABS Air Rotameter and a novel 1:8 ADB with 1 inlet and 8 outlets to 8 nozzles under the rotating disc. The ADB is a rectangular Acrylic (Perspex) block with inlet and outlets drilled, tapped and pipes connected using Araldite.

The inlet is a 1/4 inches copper connector. The out-lets are 4 mm stainless steel pipes. The air nozzles under the disc are stainless steel pipes built-into Acrylic (Perspex) nozzles holder fabricated locally.

- Disc Rotation System (DRS)

The LFS and the AFS are the systems that carry the fluids: the liquid, and the atmospheric air, in compressed form in the system, respectively. The DRS, on the other hand, is the electro-mechanical system of the experimental setup. As the name suggests, this is the system that powers and controls the rotation of disc. The schematic of DRS could be seen in Fig. 4.

The DRS has the following subsystems:

- Motor Subsystem (MSS)

The MSS has the following components:
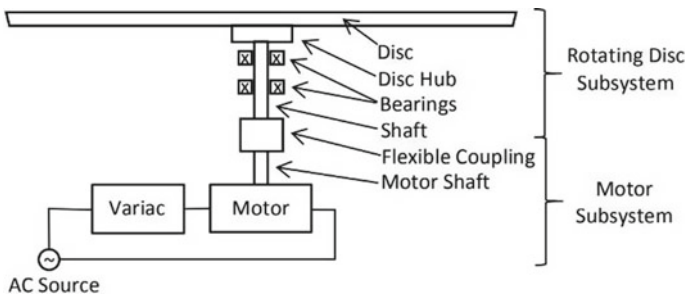
- AC source
- Variac
- Motor
- Motor shaft.

Fig. 4 Schematic of the disc rotation system (DRS)

The MSS is the electrical subsystem. The AC power source is used to rotate the motor shaft. The variac is used to control the rotary speed of the motor and hence, the disc. The motor is a one-eighth HP DC motor.

Rotating Disc Subsystem (RDS)

The RDS has the following components:

- Disc
- Disc hub
- Bearings
- Shaft.

The RDS is the mechanical subsystem. The disc shaft, in support of bearings, rotates the disc hub and the disc. The disc is chosen to be of Acrylic (Perspex). The disc hub is also of Acrylic. The shaft is an 8 mm SS shaft. The bearings are 8 mm ID bearings. The bearings were held in an acrylic cylinder. This acrylic cylinder was fixed on two places:

- The stationary disc, on which the air nozzles outlets were built-in
- Acrylic base of the hemispherical container vessel.

The bearings and the shaft were assembled under press-fit conditions.

- Flexible coupling

The motor shaft rotates the coupling, which is a flexible coupling. The coupling is the unit that joins the MS and the RDS and combines them together to form the electro-mechanical system, the DRS. The flexible coupling has been used to transmit rotary power from motor shaft to the disc shaft. The flexible coupling is an aluminium coupling with rubber coupler mesh.

- Tachometer System (TS)

An NPN sensor detects a near metallic object and then, based on that, declares and shows the counts per minute as RPM. The sensor uses the induction phenomenon to detect a metallic object in its proximity. Therefore, the sensor used is called an NPN inductive proximity sensor. On the other hand, a PNP sensor detects the discontinuities in optics in the form of a slit or a paint stripe made on the shaft periphery, parallel to the axis of the shaft. This type of sensor uses Infrared rays for its optical aid and a sensor detects the reflected ray from the shaft surface. If any discontinuity is detected by the sensor, it is reflected on the counter screen per minute as RPM.

The TS has the following components:

- AC source
- Proximity sensor
- Display.

An NPN inductive proximity sensor with a calibrated LED Indicator had been used as a tachometer or an RPM counter for the experimental setup.

- Camera-Light System (CLS)

This system, as the name suggests, incorporates the photography and video recording elements of our study and the necessary lighting for the same.

The CLS has the following components:

- AC source
- Camera
- Laptop
- 1000 W Halogen light.

Phantom V7.3 camera with three (3) high-powered (70 W) LEDs as light source have been used for the current study.

B.   The Experimental Setup.

Figure 5 shows the experimental setup. The major components, the water recirculation tank, which is now the LRT, the Nozzle Height Adjuster, the Flow Control valve, the Measuring Tank, the Pump (bottom right), the Variac and Controller unit, and the wires and pipelines, are visible in the figure.

Figure 6 shows the novel air nozzles placed below the rotating disc, directed parallel to the disc in an inclination to the tangent of the disc.
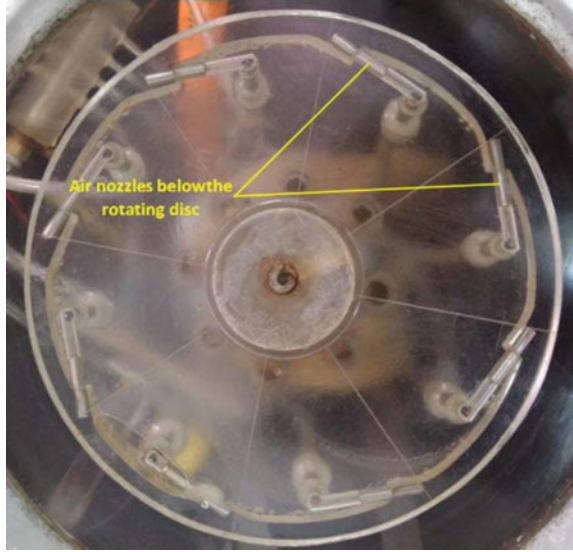
C.   The Experiment.

Atomization is the primary objective of the study. Here, a study has been performed to find the effect of change in disc rotation direction with air blast on liquid flow characteristics. The data recording for Liquid Flow Rate (LFR) and Air

Fig. 5 Experimental setup arrangement

Flow Rate (AFR) was fuzzy at this stage of the experiment. Hence, a medium LFR and a medium AFR were considered. The Disc Angular Velocity (DAV) has been kept as 600 RPM.

3   Results and Discussion

In this section, the effect of change in disc rotation direction with air blast on liquid flow characteristics has been discussed. The results have been mentioned and, then, discussed.

Effect of Change in Disc Rotation Direction with Air Blast on Liquid Flow Characteristics

The objective of the current study is to find out the direction in which atomization occurs. The formation of droplets and the breakup of ligaments into droplets is the desired outcome of the study. First, the direction of disc rotation has been kept opposite to the direction of air flow, i.e. clock-wise in the Fig. 7. Then, the direction of disc rotation has been kept the same as the direction of air flow, i.e. anticlock-wise in the Fig. 8.

When the disc rotation is in the opposite direction of air flow, as visible in Fig. 7, mist formation is seen instead of ligaments breaking into droplets. However, droplet formation is noticed, after the ligament breakup with the assistance of the air blast, when both the air flow and disc rotation directions are same, as seen in Fig. 8. Since, the droplet formation is observed when the air flow direction and the disc rotation direction are same and droplet formation is the desired phenomenon for slag
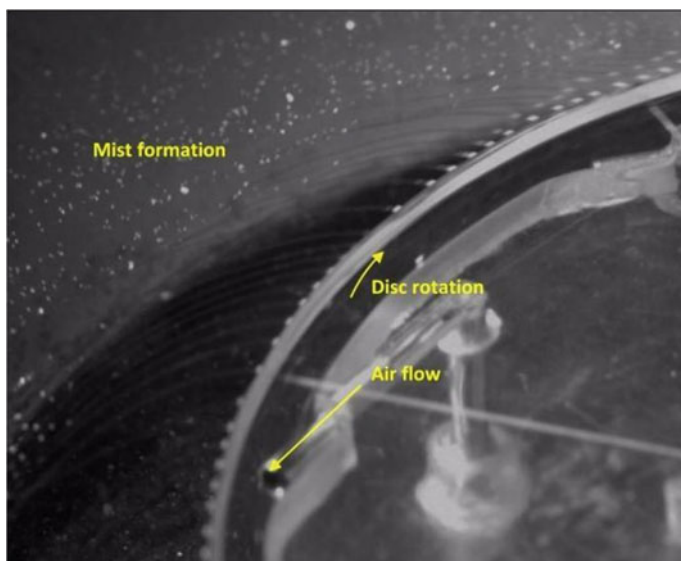
Fig. 7 Disc rotation direction is the opposite of the air flow direction at 600 RPM
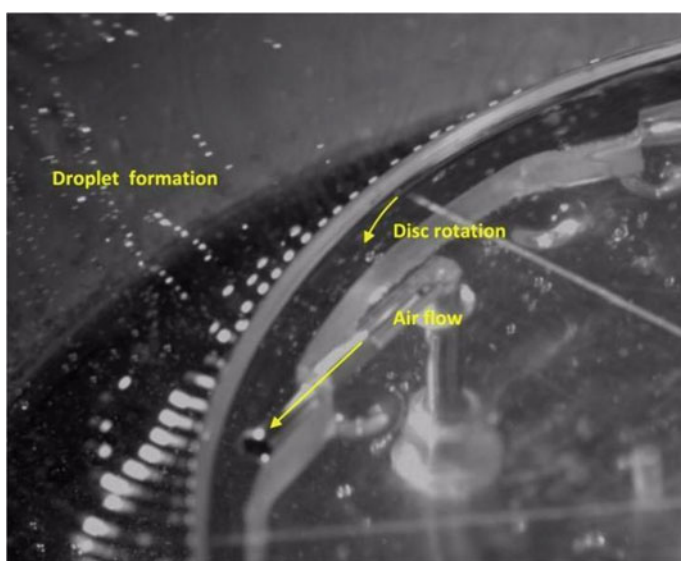
Fig. 8 Disc rotation direction is the same as the air flow direction at 600 RPM

granulation, therefore, for all further experiments, the latter configuration has been maintained.

4 Conclusions

The iron and steel industry produces a waste product, slag. Dry Spinning Disc Granulation (DSDG) process has been experimentally tried, widely, for the granulation of Blast Furnace (BF) slag, with the recovery of heat from the high-temperature slag. To study the phenomenon of granulation, the fabrication of an experimental setup, of the scale of laboratory, has been done in the institute of the authors. Various experiments were performed on the setup. Stage-wise modifications were accomplished on the experimental setup, on the basis of the limitations found in the previous stages of the experimental setup.

In this paper, the experimental setup with all its systems has been elaborated. Then, after the setup is acquainted, a study has been performed to find the effect of change in disc rotation direction with air blast on liquid flow characteristics. It could be concluded that when the disc rotation is in the opposite direction of air flow, mist formation is seen instead of ligaments breaking into droplets. However, droplet formation is noticed when both the air flow and disc rotation directions are same. Therefore, for all further experiments, the latter configuration, i.e. both the air flow and disc rotation directions are same, has been maintained as droplet formation is the desired phenomenon for slag granulation.

References

1. Das B, Prakash S, Reddy PSR, Misra VN (2007) An overview of utilization of slag and sludge from steel industries. Resour Conserv Recycl 50(1):40–57
2. Jahanshahi S, Pan Y, Xie D, Some fundamental aspects of the dry slag granulation process. In: 9th International conference on molten slags, fluxes and salts (Molten12), Beijing, 2012, pp 27–31
3. Jahanshahi S, Xie D, Pan Y, Ridgeway P, Mathieson J (2011) Dry slag granulation with integrated heat recovery. In: 1st International conference on energy efficiency and CO_2 reduction in the steel industry (EECR steel 2011), vol 27, 2011
4. Li G, Ni H (2011) Recent progress of hot stage pro-cessing for steelmaking slags in china considering stability and heat recovery. In: Proceedings of the second international slag valorisation symposium: the transition to sustainable materials management, Leuven, Belgium, 2011
5. Zhou YM, Li C, Xu LL, Luo SY, Yi CJ (2012) The experimental study of molten blast slag dry granulation. Adv Mater Res 356:1882–1885
6. Eisenklam P (1964) On ligament formation from spinning discs and cups. Chem Eng Sci 19(9):693–694
7. Rutland DF, Jameson GJ (1970) Droplet production by the disintegration of rotating liquid jets. Chem Eng Sci 25(8):1301–1317
8. Dixon BE, Russell AAW, Swallow JEL (1952) Liquid films formed by means of rotating disks. Br J Appl Phys 3(4):115

9. Emslie AG, Bonner FT, Peck LG (1958) Flow of a viscous liquid on a rotating disk. J Appl Phys 29(5):858–862
10. Kamiya T, Kayano A (1972) Film-type disintegration by rotating disk. J Chem Eng Jpn 5(2):174–182
11. Purwanto H, Mizuochi T, Akiyama T (2005) Prediction of granulated slag properties produced from spinning disk atomizer by mathematical model. Mater Trans 46(6):1324–1330
12. Wang D, Peng H, Ling X (2014) Ligament mode disintegration of liquid film at the rotary disk rim in waste heat recovery process of molten slag. Energy Procedia 61:1824–1829
13. Peng H, Shan X, Ling X, Wang D, Li J (2018) Ligament-type granulation of molten slag in different rotary disk configurations. Appl Therm Eng 128:1565–1578
14. Sahoo K, Kumar S (2021) Atomization characteristics of a spinning disc in direct droplet mode. Ind Eng Chem Res 60(15):5665–5673
15. Wu X-S, Luo Y, Chu G-W, Xu Y-C, Sang L, Sun B-C, Chen J-F (2018) Visual study of liquid flow in a spinning disk reactor with a hydrophobic surface. Ind Eng Chem Res 57(22):7692–7699
16. Maiti B, Dash SK, Samantaray AK, Kushan DS, Chakraborty G (2022) On hydrodynamics of dry slag granulation of LD/BOF slag: analytical modeling. In: Proceedings of the 16th international conference on heat transfer, fluid mechanics and thermodynamics & the editorial board of applied thermal engineering (HEFAT-ATE), Aug 2022, pp 828–833
17. Maiti B, Dash SK, Samantaray AK, Singha SK, Kushan DS (2022) On hydrodynamics of dry slag granulation of LD/BOF slag: developments for new liquid. In: Proceedings of the 16th international conference on heat transfer, fluid mechanics and thermodynamics & the editorial board of applied thermal engineering (HEFAT-ATE), Aug 2022, pp 834–838